FAM49B:
First negative regulator of the Scar/WAVE complex
–
From Evolution to an *in vivo* analysis

Loïc Fort

Thesis submitted in fulfilment of the requirements for the Degree of Doctor of Philosophy

October 2017

Cancer Research UK – Beatson Institute
University of Glasgow

Abstract

Cell migration is present throughout the life of all organisms, starting during the first stages of development and is crucial later for physiological functions during adulthood, such as wound healing, immune response, among others. It primarily relies on the ability of the actin cytoskeleton to polymerise and depolymerise, resulting in the emergence of dynamic protrusions.

Understanding the regulation of the actin cytoskeleton has been an exciting challenge for every scientists working in this field. Decades of research established a pathway involving the small Rho GTPase family, the Scar/WAVE complex and the Arp2/3 complex. Tight regulation of each other protein's activity and localisation allows actin polymerisation and pseudopods formation. Polarisation of these protrusive arms is crucial for cell steering and efficient migration. However, mechanisms dictating where a protrusion forms are largely unknown. This decision requires the cells to constrain the activity of the actin machinery at specific locations while excluding it elsewhere.

A protein-protein interaction screen aiming to find new partners of the Scar/WAVE complex identified FAM49 as a putative candidate in proximity to the complex. Sequence analysis revealed an extremely good conservation across evolution and also a shared domain, uniquely found in CYFIP, a member of the Scar/WAVE complex involved in Rac1-mediated complex activation. Using a combination of biochemistry and imaging approches, we show that FAM49B binds specifically to the active form of Rac1 and buffers the GTPase activity. We hypothesise that recruitment to the membrane is driven by a combination of myristoylation and palmitoylation events that regulate the spatio-temporal activity of the protein.

Cancer and normal cells genetically depleted in FAM49B are unable to form defined pseudopods resulting in the formation of a large lamellipodium that correlates with a higher Rac1 activity. Migration and invasion of these cells is increased, although invasion was restricted to cancer cells, as it was not observed in non-cancerous cells types migrating in 3D. We also demonstrate that FAM49B is crucial during cyst formation in 3D culture and depends on Rac1 activity. This observation links the role of Rac1 during cell polarisation and its spatial downregulation required for generating signals to appropriate effectors.

Based on mathematical modelling, it is our hypothesis that FAM49B functions as a local inhibitor, which is crucial for narrowing the diffusion of the Scar/WAVE complex by direct binding to Rac1. Here, we propose that FAM49B acts as the first Scar/WAVE complex inhibitor by competing for the binding to Rac1 and negatively regulates protrusion formation. Understanding the full mechanism of FAM49B activation is among one of the most exciting questions to follow up in this project.

Author's declaration

I, Loïc Fort hereby declare that all of the work in this thesis was performed personally, with the following exceptions mentioned below. No part of this thesis has been submitted for other degree or award at this or another university.

Loïc Fort

Chapter 3:

- CLICK chemistry experiments corresponding to Figures 3-2 (E-F) and 3-3 were performed in collaboration with Dr. Jennifer Greaves from Prof. Luke Chamberlain's laboratory *(University of Strathclyde)*
- Quantification of FLAG-tag and F-actin staining (Figure 3-4 C) was performed by Dr. Luke Tweedy from Prof. Robert Insall's laboratory *(Cancer Research UK – Beatson Institute)*

Chapter 4:

- Biacore data (Figure 4-6) was processed by Dr. Peter Brown from the Drug Discovery Unit (*Cancer Research UK – Beatson Institute)*

Chapter 6:

- All Drosophila crosses and lines were maintained by Dr. Marcos Vidal and his student Miss Christin Bauer *(Cancer Research UK – Beatson Institute)*
- Confocal imaging of TubG4>UAS-LifeAct-GFP/RNAi haemocytes (Figure 6-11) was performed by Miss Christin Bauer *(Cancer Research UK – Beatson Institute)*
- Live ligh sheet imaging of hmlG4>UAS-GFP/RNAi larvae (Figure 6-14) was performed by Miss Christin Bauer and Dr. Alessandro Scopelliti *(Cancer Research UK – Beatson Institute)*

Chapter 10:

- Phylogenetic tree (Appendix 2) was produced by Prof. Laura Machesky and Prof. Robert Insall

Acknowledgment

First of all, I would like to thank my supervisor, Laura Machesky for giving me the opportunity to start a PhD in her lab. I feel myself more accomplished after these four years under her supervision, learning so much from her and listening to her advice. Laura got to know me and adapt herself to my character and my way of doing science. Not only professionally but also personally, I could get her support during this "rollercoaster PhD" like I used to call it. As this project was a real collaboration with Robert Insall so his input has been extremely important to me. I hope to keep seeing you at the gym, although you will have to increase your pace at some point, because I'm coming back on the treadmill!! Laura and Robert share nothing in common in Science but as a student, you get this extraordinary energy from both sides that always pushes you further in your scientific reflexion and as a person.
Thank you to my two advisors, Kurt Anderson and David Bryant for being so patient and for guiding me in my projects. We tend to underestimate the luck we have discussing with other PIs but both of you really helped me a lot.

I would also like to thank Cancer Research UK for funding my PhD and together with the Beatson Institute for giving me the opportunity to work and learn in such a great environment. I want spend some time to thank all the on-site facilities starting with the molecular technology service (Billy and Andy) for making my work a bit easier with the hundreds of clonings required for this project. Colin and his group at the histology platform are doing a wonderful job – We cannot expect more from you guys. Thank you to all the BSU/BRU staff for looking after my mice and for doing such a wonderful job in a great atmosphere. Thank you to IT for their support during this PhD and to the central units for their company early in the morning and all the help they provide. Finally, a special thank you goes to Margaret O'Prey for the hours she spent training me on the various microscopes. I will really miss our nice morning chats in the dark room, although it might sound a bit creepy said that way but you know what I mean.
My PhD would have not been possible without all of you – So thank you!

As every PhD student would agree: A PhD is a life-experience. You learn about yourself and you meet people who were here to support and guide you along. I would like to start with all former and current R2/R6/M22 members, as well as Chloe, the MSc student who did some work with me. We shared more than 10h/day as a colleagues together – However the feeling I perceived was more like a big family, helping each other, discovering new

places in Glasgow, the UK, and abroad. This camaraderie was celebrated with an incredible amount of cakes, sweets and sometimes alcohol – I'm lucky I had not become diabetic by the end of this experiment. Special thanks go to Heather and Peter for their guidance and for their energy to organise the lab! Heather, four years have passed and I'm always surprised by the untidiness of your bench! But like you used to say, "a tiny bench is an empty mind". Peter, we spend so much time together, at Tinderbox talking about life, thinking about our future and about science of course… But this amount of calories uptake had to be balanced by our regular runs together! I'm happy to say I found a real friend.
When your colleague is also your flatmate, things could have turned difficult rapidly. With Clelia, we went through it all, although we had our mis-understandings sometimes, what I get out from these 4 years together is a wonderful friendship. You are one of the most caring person I have met and I'm sure you will succeed wherever science takes you for your Post-doc. I also want to thank my others flatmates, Yvette and Matthew and his girlfriend Christin for their help and patience during our year living together and for their continued friendship during this PhD. I will never forget our trips to Lisbon and Barcelona!
I also want to thank Amelie. The first day I arrived, it was a real relief to find a french fellow sitting beside me and showing me the ropes. I have no doubt about the successful scientist you will be in a near future. A massive "thank you" goes to Jose for having initiated this amazing project, Olivia and Nikki for their energy in life and in the lab, so much good laugh with you girls, Kirsty for your help/patience with FRET, and also to Jamie, my "FAM49B-buddy" for all the great fun and chat we have been having since you joined the lab. Finally, thank you every one for proofreading my PhD thesis and for your helpful comments.

Being abroad is a difficult challenge when you share a strong relationship with your friends. Despite the distance, they have always been present for me, showing their support and cheering me up during difficult times. Thank you Baptiste/Alyson, Laura/Mathieu, Gael, Thomas (The Ginger one :p) and the other Thomas for your visits to sunny Glasgow. Thank you to Julien, despite the nearly 5000 km between us, we maintain this strong friendship. Looking forward to seeing you in Montreal again! Faustine, even when we independently decided to move away from France, we ended up on the same island! Thank you so much for being so supportive for the last 26 years! We definitively have a special link and let's see where the next step will take us.

My mum, dad, brother, little niece, grandparents, auntie and uncle were so important to me during these four years. I took so much energy from them, calling up whenever I was down

and trying to get the bright side out from them. Despite the kilometres between us, I now feel a stronger link and I want to thank you all for your support and belief.

Maman, Papa, Damien et Elyna, Mémé, Grand-père, Marie-Paule et Richard, vous avez été si important durant ces 4 années. Vous représentez une incroyable source d'énergie pour moi, même si j'ai toujours tendance à le cacher. Dans ces moments difficiles que chaque étudiant en thèse connait, je pouvais vous appeler à n'importe quelle heure et vous avez toujours été present pour me remonter le moral afin que je reste optimiste. Malgré les kilometres qui nous séparent, je sens un lien encore plus fort et je veux tous vous remercier pour votre support et votre confiance en moi.
Maintenant, vous savez (presque) tout de ma "mystérieuse protéine".

Juste pour info, il m'a quasiment pris autant de temps pour écrire ces 8 lignes que le reste de ma thèse !

I would like to dedicate this work
to the grandmother, who was taken from our family before I get the chance to know her,
Yvette Fort (8.06.1931 – 22.09.1984)
and to my grandfather who passed away in the middle of my research
and was one of the most joyful person,
Jean Chamalot (14.08.1932 – 31.05.2014).

Believe me, one day, we will beat cancer!

Je voudrais dédicacer ce travail de thèse
à la grand-mère emportée par la maladie avant d'avoir la chance de la connaitre
Yvette Fort (8.06.1931 – 22.09.1984)
et à mon grand-père, décédé durant ma thèse
et qui était l'une des personnes les plus joyeuses que j'ai pu rencontrer
Jean Chamalot (14.08.1932 – 31.05.2014).

Ayez confiance en moi, un jour, nous battrons le cancer!

Publications

Fort, L. *, Batista, J. *, Thomason P., Spence H. J., Greaves J., Martin K. J., Anderson K. I., Brown P., Lilla S., Neilson M. P., Tafelmeyer P., Zanivan S., Ismail S., Tomkinson N. C. O., Chamberlain L. H, Insall R. H. * and Machesky L. M. * **CYRIPS (FAM49) proteins are local inhibitors of Rac1 and Scar/WAVE induced lamellipodia.** Under review (Nat. Cell Biol.) (* Authors contributed equally) – bioRxiv preprint https://doi.org/10.1101/164905

Giampazolias E., Zunino B., Dhayade S., Bock F., Cloix C., Cao K., Roca A., Lopez J., Ichim G., Proïcs E., Rubio-Patiño C., Fort L., Yatim N., Woodham E., Orozco S., Taraborrelli L., Peltzer N., Lecis D., Machesky L., Walczak H., Albert M. L., Milling S., Oberst A., Ricci J. E., Ryan K. M., Blyth K., Tait S. W. G. **Mitochondrial permeabilization engages NF-κB-dependent anti-tumour activity under caspase deficiency**. Nat. Cell Biol. 2017 Sep;19(9):1116-1129. doi: 10.1038/ncb3596

Morris H. T., Carey F. A., Spence H. J., Fort L., Patel R., Vincent D. F., Park J. H., Snapper S. B., Sansom O. J., Machesky L. M.
Loss of N-WASP drives early progression in an Apc model of intestinal tumourigenesis. Submitted (J. Pathol.)

Abbreviations

°C: Celsius degree

∅: Diameter

∞: Infinite

A

2D: 2-dimension

3D: 3-dimension

Abi: Abl interactor

ABS: Actin-binding site

ADF: Actin depolymerizing factor

ADP: Adenosine diphosphate

αSMA: Alpha smooth muscle actin

AMIS: Apical membrane initiation site

APC: Antigen-presenting cell

Arc: Actin-related complex

Arf: ADP ribosylation factor

Arp: Actin-related protein

ArpC: Actin-related protein complex

Arpin: Actin-related protein inhibitor

ATP: Adenosine triphosphate

Ax3: Axenic 3

B

bp: Base pair

BrdU: 5-bromo-2'-deoxyuridine

BSA: Bovine serum albumin

C

c-Myc: Cellular myelocytomatosis

CAP: Cyclase-associated protein

CCK: Cholecystokinin

CDC42: Cell division control protein 42

cDNA: complementary DNA

ChiP: chromatin-immunoprecipitation

cm: centimeter

CoA: Coenzyme-A

Cre-ER: Estrogen receptor-dependent Cre

CRE: Causes recombination

CRIB: Cdc42 Rac1 Interacting Binding

Ctr: Control

$CuSO_4$: Copper(II) sulfate pentahydrate

Cyfip1: Cytoplasmic FMR (fragile X mental retardation)-interacting protein

D

Da: Dalton

DAB: 3,3'-Diaminobenzidine

DCT: dopachrome tautomerase

DIC: Differential interference contrast

DIP: mDia interacting protein

DMEM: Dulbecco's Modified Eagle Medium

DMSO: Dimethyl sulfoxide

DNA: Deoxyribonucleic acid

DNaseI: Deoxyribonuclease I

DUF1394: Domain of unknown function 1394

E

E: embryonic day

eCFP: enhanced Cyan fluorescent protein

ECL: Electrochemiluminescence

ECM: Extra cellular matrix

EGF: Epidermal growth factor

EGFP: Enhanced green fluorescent protein
EHT1864: 5-(5-(7-(Trifluoromethyl)quinolin-4-ylthio)pentyloxy)-2-(morpholinomethyl)-4H-pyran-4-one dihydrochloride
eIF4E: Eukaryotic translation initiation factor 4E
EM: Electron microscopy
EMT: Epithelial to mesenchymal transition
Ena: Enabled
ERAAP: Endoplasmic reticulum aminopeptidase associated with antigen processing
EV: Empty vector

F

FA: Focal adhesion
FAAI: Focal adhesion alignment index
FAAS: Focal adhesion analysis server
FAK: Focal adhesion kinase
FAM49: Family of unknown function 49
FBS: Fetal bovine serum
FDR: False discovery rate
FGF: Fibroblast growth factor
FH: Formin homology
FLIM: Fluorescence lifetime imaging microscopy
FRAP: Fluorescence recovery after photobleaching
FRET: Förster resonance energy transfer

G

g: gram
Gadkin: Gamma-A1-adaptin and kinesin interactor
GAL4: Galactose-responsive transcription factor 4
GAP: GTPase activating protein
GDP: Guanosine diphosphate
GEF: Guanine nucleotide exchange factor
GMF: Glial maturation factor
gp135: Glycoprotein 135
GppNHp: 5'-Guanylyl imidodiphosphate
GSH: Glutathione
GST: Glutathione S-tramsferase
GTP: Guanosine triphosphate
GTPγS: Guanosine 5'-O-(3-thiotriphosphate)

H

h: hour
H/E: Haematoxylin/Eosine
Het: Heterozygote
Hml: Hemolectin
HMM: Hidden Markov models
Hom: Homozygote
Hscp300: Heamatopoietic stem/progenitor cell protein 300

I

i-TASSER: Iterative Threading ASSEmbly Refinement
IHC: Immunohistochemistry
IPTG: Isopropyl β-D-1-thiogalactopyranoside
IRSp53: insulin receptor substrate protein of 53kDa
IVF: *In vitro* fecundation

J ----------

JMY: Junction-mediating and regulatory protein

K ----------

kb: kilo base

K_d: Dissociation constant

KO: Knockout

L ----------

L: Liter

L1/2/3: Larval stage 1/2/3

LB: L-Broth

LC-MS/MS: Liquid chromatography–tandem mass spectrometry

LIMK1: Lin11 Isl-1 & Mec-3 domain kinase 1

LoxP: Locus of crossover in P1

LSFM: Light Sheet fluorescent microscopy

LSL: Lox-STOP-Lox

M ----------

M: Molar

MAPK: Mitogen-activated protein kinases

MDCK: Madin-Darby Canine Kidney

MEF: Mouse epithelial fibroblast

MES: 2-(N-morpholino)ethanesulfonic acid

mg: milligram

Mg^{2+}: Magnesium $^{2+}$

MHC: Major histocompatibility complex

min: minute

MITF: Micropthalmia Transcription Factor

mL: milliliter

ML141: 4-[4,5-Dihydro-5-(4-methoxyphenyl)-3-phenyl-1H-pyrazol-1-yl]benzenesulfonamide

mM: Milli molar

mm: millimeter

MMP: Metalloproteinase

MOPS: 3-(N-morpholino)propanesulfonic acid

mRNA: messenger RNA

MT: Microtubules

MT1-MMP: Membrane type 1-matrix metalloproteinase 1

MTOC: Microtubule organisation centre

mTOR: Mechanistic target of rapamycin

N ----------

N-WASP: Neuronal Wiskott-Aldrich syndrome protein

Na_3VO_4: Sodium orthovanadate

NaF: Sodium fluoride

NaN_3: Sodium azide

Nap1: Nck-associated protein 1

NCBI: National Center for Biotechnology Information

Ndrg1b: N-myc downstream-regulated gene 1b

Neg: Negative

NHS: Nance-Horan syndrome

nM: nano molar

NMT: N-myristoyl-transferase

NPF: Nucleation promoting factor

n.s.: non significant

NSC23766: N^6-[2-[[4-(Diethylamino)-1-methylbutyl]amino]-6-methyl-4-

pyrimidinyl]-2-methyl-4,6-quinolinediamine trihydrochloride

NTA: nitrilotriacetic acid

O

OD: Optical density

OHT: hydroxytamoxifen

P

P-Rex1: phosphatidylinositol-3,4,5-trisphosphate-dependent Rac exchange factor 1

PanIN: Pancreatic intraepithelial neoplasia

Par: Parental

pb: pair base

PBD: PAK binding domain

PBS: Phosphate buffer saline

PCR: Polymerase chain reaction

PDAC: Pancreatic ductal adenocarcinoma

PDB: Protein database

PDGF: Platelet-derived growth factor

Pdx1: Pancreatic and duodenal homeobox 1

Pdx1: Podocalyxin

PFA: Paraformaldehyde

Pfam: Protein family

PH: Pleckstrin-homology

Pi: Inorganic phosphate

PI3K: Phosphoinositide 3-kinase

PICK1: Protein interacting with C kinase 1

PIP_3: Phosphatidylinositol-3,4,5-trisphosphate

PIR121: p53-inducible mRNA

PKC: Protein kinase C

PMFS: Phenylmethylsulfonyl fluoride

Pos: Positive

PTEN: Phosphatase and Tensin homologue

PTM: Post-translational modification

px: pixel

Q

qRT-PCR: Quantitative reverse transcription polymerase chain reaction

R

Rab: Ras-associated proteins in brain

Rac1: Ras-related C3 botulinium toxin substrate 1 precursor

Ran: Ras-related nuclear protein

Ras: Rat sarcoma protein

RBD: Rac binding domain

rcf: relative centrifugal force

Rho: Ras homolog gene family

RhoGDI: Rho GDP-dissociation inhibitor

RIPA: Radioimmunoprecipitation assay buffer

RNA: Ribonucleic acid

rpm: rotation *per* minute

S

Scar: Suppressor of cAMP receptor

SD: Standard deviation

SDS-PAGE: sodium dodecyl sulfate polyacrylamide gel electrophoresis

sec: second

S.E.M: Standard error to the mean

sgRNA: single guide RNA

SH3: Src-homology domain 3

shRNA: short hairpin RNA
SILAC: Stable isotope labeling with amino acids in cell culture
siRNA: small interference RNA
smTIRF: single molecule total internal reflection fluorescence
SPIN90: SH3 protein interacting with Nck, 90kDa
SPR: Surface plasmon resonance
Sra: Specifically Rac1-associated protein
sREACh: Super resonance energy-accepting chromoprotein

T

TAE: Tris base, Acid acidic and EDTA
TBS-T: Tris-buffered saline-Tween
Th: Thesla
TMR: Tetramethylrhodamine-5-Maleimide
Tub: Tubulin

U

UAS: Upstream activating sequence
UV: ultra violet

V

VASP: Vasodilator-stimulated phosphoprotein
VCA: Verpolin Cofilin Acidic domain
vs: versus

W

w/v: weight/volume
WASH: WASP and Scar homologue complex
WASP: Wiskott-Aldrich syndrome protein
WAVE: WASP-family verpolin homoly protein
WH2: Wiskott-Aldrich homology domain 2
WHAMM: WASP Homologue associated with actin, membranes and microtubules
WIRS: WRC interacting receptor sequence
WISH: WASP interacting SH3 protein
Wnt: Wingless-related integration site
WRC: WAVE regulatory complex
WT: Wild type

µ

µg: microgram
µL: microliter
µM: Micro molar
µm: micrometer

Table of Contents

List of Figures

List of Table

1 Introduction

1.1 Overview of cell migration in biology: From a developmental to a pathological point of view

In this exciting period of high-throughput screening, development of new immunotherapeutic approaches and advances in our understanding of epigenetic modifications of the genome, investigations into basic processes such as cell migration tend to be underrated. However, this kind of fundamental knowledge is at the root of most, if not all, biological phenomena and is required for more translational studies.

Although the first observation of cell movement was made in the middle of the 19th, Michael Abercrombie is considered as the pioneer in the modern history of cell migration (Abercrombie et al., 1970) but at this time, the complexity of the processes involved was of course unknown. Cells move throughout the body in order to achieve critical functions: From development to wound healing and immune response, cell migration is fundamental throughout the lifespan of an organism and underlying molecular mechanisms have just started to emerge. For example, during avian gastrulation, cells respond to FGF (Fibroblast growth factor) signalling inducing EMT (Epithelial to mesenchymal transition) and regulating downstream pathways such as somatic mesoderm migration (Yang et al., 2002). Examples of early requirements of cell migration and actin regulation during embryogenesis are numerous: Using *Drosophila* as a model, Martin et al (Martin et al., 2009) and Mason et al (Mason et al., 2013) unravelled some important mechanisms leading to apical constriction, which is thought to be important for sheet invagination and early organ formation. In their studies, they show that constriction of the apical end of a cell follows a pulsed pattern dependent on Twist and Snail transcriptional factors, which are pacing the frequency of the acto-myosin network constriction. This was shown to be dependent on the polarisation and differential activation of RhoGEF across the cell.

In physiology, cell migration is crucial during immune response. Indeed, immune cells are specialized in scanning their environment and migrating to specialized compartments upon recognition of foreign antigens. This complex mechanism involves different types of environment, different cell-cell interactions and this is reflected by different behaviours in term of cell motility. For example, naive T-cells migrate within the lymph node and follow a random walk, mostly guided by a reticular network and using a haptokinetic-mode of migration based on a ligand-receptor mechanism. Cells alternate between fast and slow migration, reflecting the heterogeneity of the environment (Gerard et al., 2014). Upon activation, T-cell migration is highly skewed by a chemotactic gradient produced by the

antigen-presenting cells (APC), resulting in the swarming and the clustering of T-cells, allowing differentiation and immune memory. At this point, activated T-cells are functional and are attracted to the site of injury by APC in order to trigger the immune boost and clear out the infection (Krummel et al., 2016). This specific example clearly demonstrates the complexity of cell migration under normal conditions.

However, when the regulation of cell motility goes askew, the potency of its mechanisms can lead to serious and life-threatening effects. Among them, the most studied is cancer metastasis. Similar to embryonic cells during gastrulation, most cancer cells arise within an epithelium and re-activate some proliferation and EMT pathways, leading to tumour growth, increasing motility and seeding to a distant metastatic site. Better understanding in cancer biology and drug efficiency allows improved survival upon early diagnosis in most cases (Quaresma et al., 2015). However, if spreading from the primary tumour has already occurred, the survival of the patient drops significantly and clearly reflects a lack of understanding of underlying mechanisms. In line with those numbers, over 90% of cancer-related deaths are linked to metastasis and this is directly related to the failure of treatment to recognise and stop cells from spreading.

These dramatic statistics emphasise the need to gain a deeper understanding of how cancer cells use cytoskeletal remodelling to spread. Some molecules are already in use for different cancer treatment strategies. For instance, the most famous one, Paclitaxel (Taxol®), an anti-mitotic molecule that stabilises microtubule polymers and blocks them from disassembly (Schiff et al., 1979). This molecule has led to a significant improvement in combined cancer treatments, although clinicians are aware of considerable side effects due to the lack of specificity. Indeed, healthy cells must also divide to maintain the pool required for their physiological functions and these cells also get targeted following the treatment delivery in a cancer patient.

Since cancer cells are particulary motile, especially driven by actin-based protrusions, actin cytoskeleton would make an ideal target for inhibition. However, actin and actin-related proteins have been difficult to target because of their abundance and essential functions in healthy cells, such as muscle fibre contraction. This has progressively changed over the years as new molecules targeting the actin cytoskeleton have come out and show greater specificity for actin-based motility. For example, Stehn *et al* (Stehn et al., 2013) developed a specific tropomyosin inhibitor called TR100. This inhibits the high levels of tropomyosin that are present in motile metastatic tumour cells but affinity is weak enough to not affect

much lower levels found in healthy cells. This area of inhibitors is in its infancy but opens an encouraging avenue for researchers to continue their work and obtain a clearer picture of the different effectors driving cancer progression.

Cell migration is a very plastic event and although cells have their default type of migration (mesenchymal mode used by stromal cells, collective migration used by epithelial cells just to cite a few) they can switch from one type to the other in order to adapt to their environment (Friedl and Wolf, 2010) and this adaptation might also be involved in drug-resistance..

1.2 Biology and mechanisms of actin polymerisation and cell spreading

1.2.1 Cytoskeleton, major architect of the cell

Cells need a rigid internal skeleton to maintain their shape and move over a surface but also have the ability to dynamically modify the length and the stability of their internal cytoskeleton. The cytosketon of mammalian cells comprises 3 main fibrous structures (**Figure 1-1**) and all are organised as polymers forming networks able to respond to external and internal cues, such as pressure (Thamilselvan and Basson, 2005), damage (Gefen and Weihs, 2016) and oxidation (Wilson and Gonzalez-Billault, 2015).

Microtubules are composed of 13 protofilaments of alpha-beta tubulin dimers, organised radially from the centrosome. During interphase, they act as dynamic trails facilitating the trafficking of molecular motors along the filaments. As cell division starts, they profoundly modify their organisation and form a radial spindle, aligned at the place of the future cleavage furrow. This assures the equal distribution of the genetic material to each daughter cell. Thus, microtubules are highly dynamic and polarised structures and are characterised by their ability to undergo successive cycles of polymerisation-depolymerisation called dynamic instability. Detailed characterisation of microtubule dynamics and their regulation is beyond the scope of this thesis and has been extensively reviewed (Akhmanova and Steinmetz, 2015; Conde and Caceres, 2009).

Intermediate filaments are probably the least well described and understood cystosketal structures within the cell. They also represent a whole family of diverse proteins, which makes their characterisation more difficult but they have been divided as cytoplasmic or nuclear. Similarly to microtubules and actin filaments, members of this family show cell and tissue specificity and are involved in a large variety of functions, all related to physical

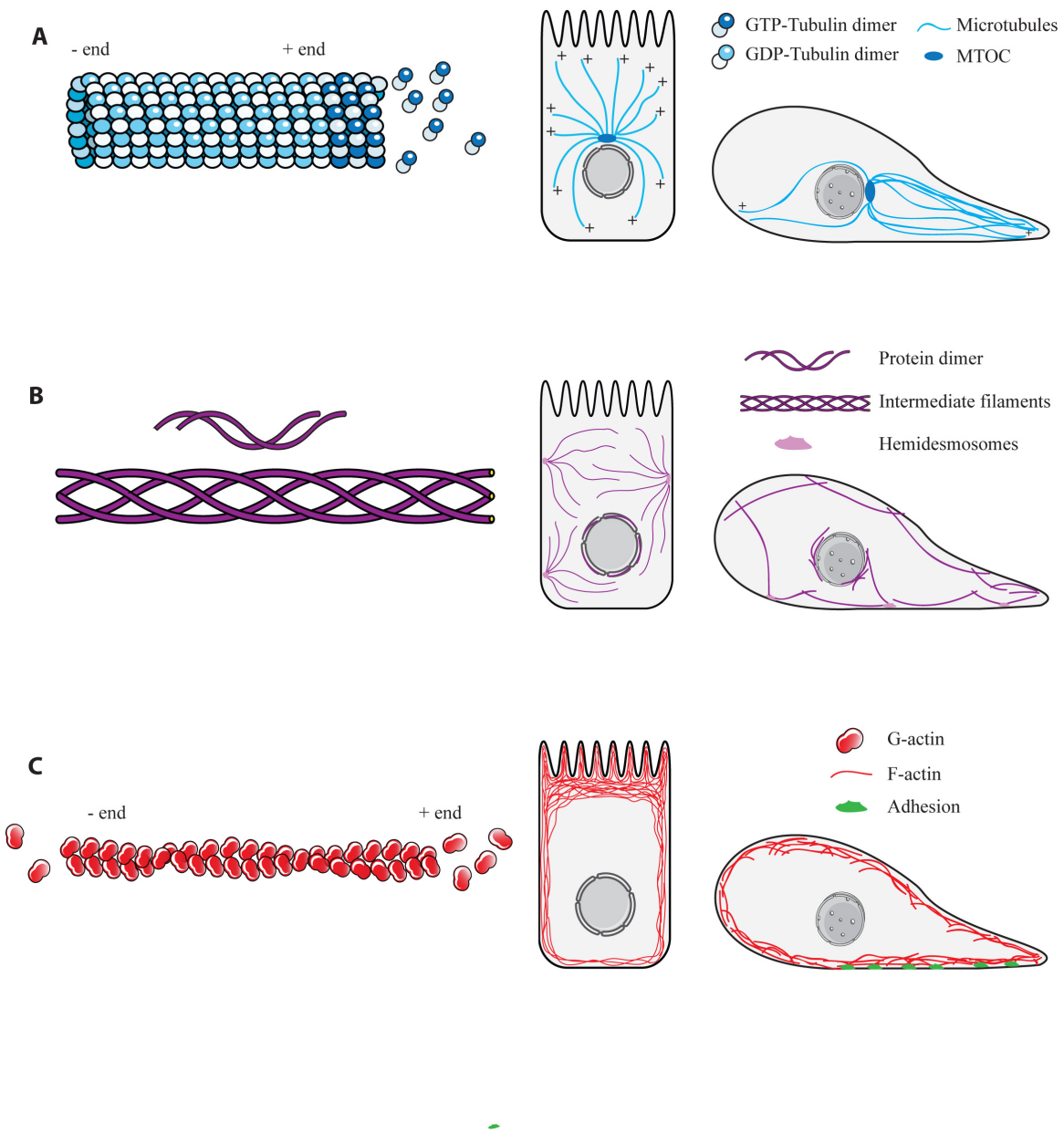

Figure 1-1: The cytoskeleton: Components and organisation
A – Tubulin dimers are the major units for the organisation of the microtubules. They associate as protofilaments that wind together to form a microtubule. Microtubules are polarised with a dynamically growing plus end, rich in GTP-Tubulin and a GDP-Tubulin enriched minus end that emerges from a microtubule organisation centre (MTOC) in a cell during interphase. The MTOC is usually located next to the nucleus but moves significantly during cell migration.

B – Intermediate filaments can be found in the cytosol and inside the nuclear membrane. There are 4 types of intermediate filaments, named according to the main protein (Keratin, Desmin/Vimentin, Neurofilaments, Laminin). Monomers associate to each other by their central rod domain and form a final rope-like structure involved in nuclear organisation, cell-cell and cell-ECM adhesion, to highlight a few.

C – Actin filaments (F-actin) are polarised structures with a barbed end (= Plus end) and a pointed end (= Minus end). F-actin is enriched below the cell cortex and at the cell protrusions. They link intracellular forces to the environment using adhesive structures. To note, the nature of the nucleotide (ATP or ADP) is not mentioned in this simple schematic and will be fully addressed in section 1.2.3.

forces and tension. Because of their different nature, they adopt different organisations (homo/heteropolymers and homo/heterodimers) and can associate along side to each other. Unlike nuclear intermediate filaments forming the nuclear membrane, which are relatively stable (except during cell division), cytoplasmic intermediate filaments are very dynamic throughout the cell cycle. They represent a whole area of research and more details about their organisation and regulation can be found elsewhere (Herrmann et al., 2007; Herrmann et al., 2009).

Like intermediate filaments, the presence of nuclear and cytosolic actin is now accepted in the field of actin dynamics. However, nuclear actin has been difficult to study and its functions within this compartment remain largely unknown (de Lanerolle and Serebryannyy, 2011; Sharili et al., 2016). My thesis has focussed on cytoplasmic actin; so nuclear actin will not be discussed further.

Actin was initially visualised at the end of the 19th century by a British physiologist, William Halliburton but the discovery was co-attributed to Straub and Szent-Gyorgyi after the Second World War (Szent-Gyorgyi, 1945). Similarly to microtubules, actin exists as a monomeric form (known as globular actin or more simply as G-Actin) and as polymers (known as F-actin). Actin filaments are polarised structures and are defined by a barbed end (plus end) and a pointed end (minus end) (**Figure 1-1**). This distinction is purely qualitative and is based on the shape of the filament ends obtained from electro-microscopy pictures. This is related to the presence of the myosin head, which binds to the actin filaments in a polarised way. However, in contrast with microtubules, there is no specific organisation centre where filaments originate. Indeed, actin nucleation only requires a sufficient concentration of G-actin. Once initiated and under the right conditions, actin displays a steady polymerisation and depolymerisation referred to as treadmillling (see section 1.2.3) (Heuser and Kirschner, 1980; Wegner, 1976).

This was a brief overview of the main components of the cytoskeleton. Together, those 3 structures maintain a defined cell shape, allowing the cell to resist and react to the environment. These are also at the base of specific structures driving cell motility and I will next focus on the different types of actin-based protrusions resulting from actin nucleation.

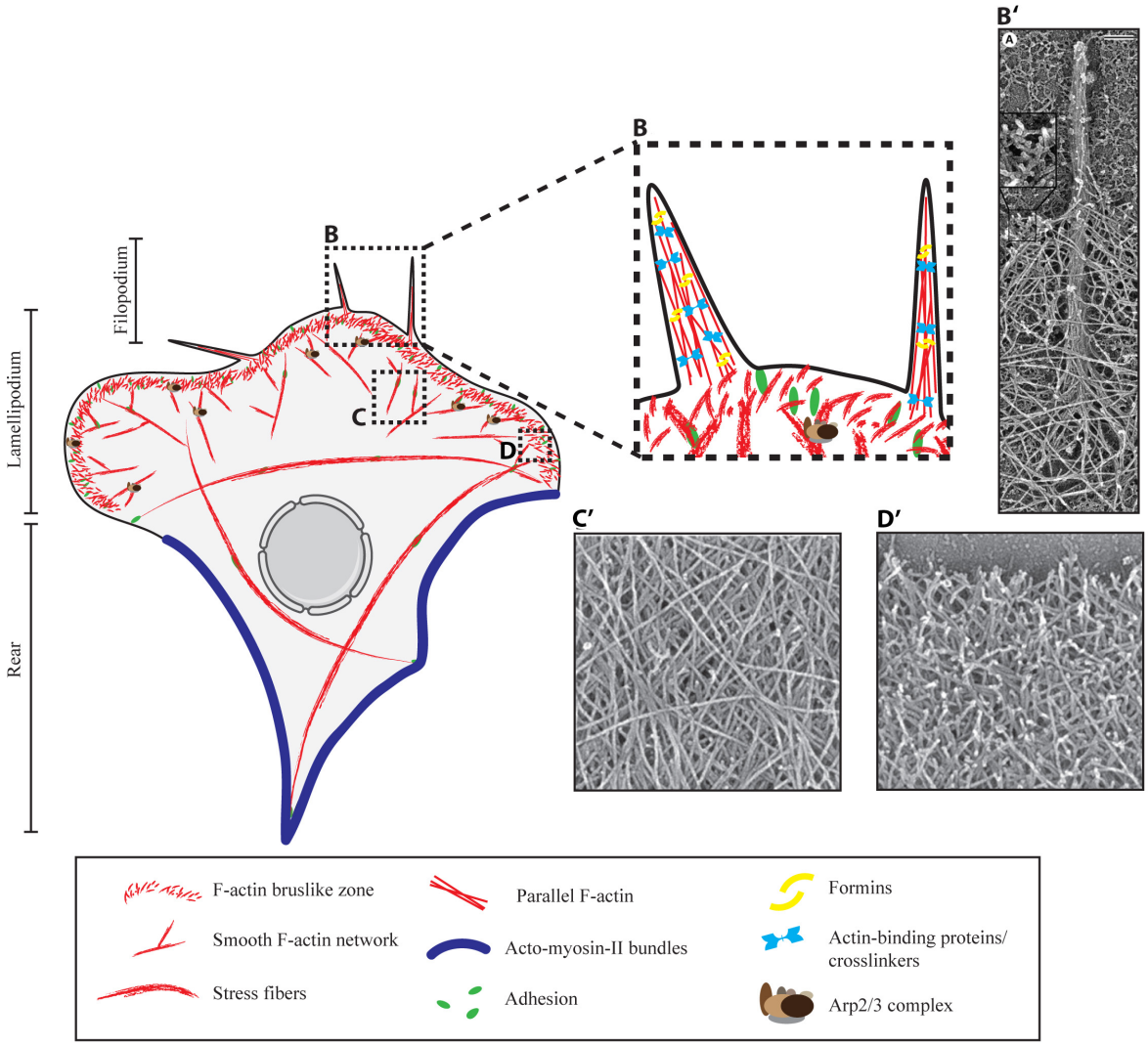

Figure 1-2: Morphological features of an mesenchymal cell in 2D
A - Graphical representation of the actin cytoskeleton during cell migration. In 2D, the cell front is dominated by a motile lamellipodium composed by a tight network of branched F-actin, underneath the plasma membrane. Filopodia emerge from the lamellipodium with a distinct actin organisation, mainly dominated by thick actin bundle. Focal adhesions (green) are physical linkers between the internal cytoskeleton and the extra-cellular matrix. The cell rear is the place of high activity of the acto-myosin network.

B – Schematic representation of a filopodium protruding from the front of the lamellipodium. This highlights the structural differences between actin filaments. Indeed, F-actin in filopodia are long, straight and parallel. This reflects the activity of different actin nucleators and actin-binding proteins. B' Platinum replicate EM picture representing a filopodium protruding outside the lamellipodium of a B16F1 cell. Reprinted with permission from Rockefeller University Press: [J. Cell Biol.], (Svitkina et al., 2003), copyright (2003).

C-C' & D-D' – EM pictures of detergent-extracted keratocyte lamellipodium. Within the lamellipodium, difference of the density of branched actin can be observed between the smooth actin network (C-C') and the brushlike zone at the edge of the cell (D-D'). Reprinted with permission from Rockefeller University Press: [J. Cell Biol.], (Svitkina et al., 1997), copyright (1997).

1.2.2 Actin-based protrusions, drivers of the cell motility

1.2.2.1 Lamellipodium, filopodium and cell rear

Within a cell, actin filaments can adopt different organisations depending on the local environment. Most of the early cell migration studies have used cells migrating on planar 2-dimensional (2D) surfaces. Although not physiologically relevant for all cell types, it is a relatively easy system to study basic mechanisms involved during cell migration. Under those conditions, many cells type adopt distinct features and become polarised with a defined front and rear (**Figure 1-2**). The front of the cell is dominated by a highly motile flat-sheet structure called a lamellipodium, characterised by a rich network of branched-actin localised just underneath the plasma membrane. The lamellipodium contains all the elements required for Arp2/3-dependent actin polymerisation and its regulation (see section 1.2.3). It is also an important compartment where forces are generated that allows cells to pull themselves forward (Shahapure et al., 2010). Indeed, growing actin filaments point their barbed end toward the plasma membrane and create a flow able to transmit intracellular forces directly to the focal adhesions during cell protrusion (Hoffmann and Schafer, 2010).

Coming out from the lamellipodium, filopodia are finger-like protrusions characterised by parallel actin filaments. Filaments are organised as tight bundles by specific crosslinkers, a major one being Fascin (Vignjevic et al., 2006) (**Figure 1-2**). Precise information about Fascin will be detailed in chapter 8 but briefly, it functions as an actin-bundling protein. Fascin contains 2 actin-binding sites that mediate parallel orientation of actin filaments within filopodia (Jansen et al., 2011). This specific organisation also reflects the activity of different actin nucleation proteins, among them the formin family (Peng et al., 2003; Romero et al., 2004). Formins are large multidomain proteins characterised by a FH2 domain that binds to the barbed end enabling insertion of G-actin and prevent the association of capping proteins, which could inhibit actin polymerisation. The FH1 domain acts to deliver G-actin (in complex with profilin) to the growing end, stimulating filament elongation even further (Goode and Eck, 2007).

Because of their high motility and their localisation pointing outside the cell, filopodia have been seen as signalling hubs, able to sense the surrounding environment and deliver information (Prols et al., 2016). Taking the example of the zebrafish embryo, molecules from the Wnt-pathway can form clusters (signalosomes) and mediate signalling from stable filopodia (Stanganello et al., 2015). Similarly, specific proteins involved in

EGF/FGF signalling are recruited at the filopodium but their clear functions remain elusive (Prols et al., 2016).

The cell rear in contrast is highly contractile due to the localisation of strong actomyosin-II bundles (Yam et al., 2007). Frequently, a retraction tail can be observed and is connected to the front by thick stress fibres, allowing for good coordination and helping the cell to pull itself forward. It is mostly an area with high actin depolymerisation and focal adhesions disassembly (Parsons et al., 2010).

1.2.2.2 Invadopodia and other degradative structures.

Over the years, scientists have been developing new tools to study cell migration using more physiological systems than glass. When a cell is plated on an extracellular matrix (ECM), it forms specialised structures known as invadopodia (cancer cells) and podosomes (macrophages, osteoclasts, dendritic cells, amongst others) (Linder, 2007; Murphy and Courtneidge, 2011) (**Figure 1-3**). They are actin-rich patches protruding out from the ventral face (in 2D) of the cell directly toward the ECM. They possess the main components required for actin polymerisation and are composed by a mix of parallel and branched F-actin (Schoumacher et al., 2010). They are sites of active secretion of proteases, leading to the degradation and the remodelling of the underlying ECM (Clark et al., 2007; Gawden-Bone et al., 2010). Differences between invadopodia and podosomes have remained subtle for a long time but a proper nomenclature has been adopted to characterise these structures (Murphy and Courtneidge, 2011). They mostly differ by the duration of turnover, ranging from few minutes for podosomes to hours for invadopodia. Also, podosomes tend to be localised at the periphery of a normal cell whereas invadopodia are often contained below the nucleus of cancer cells.
Finally, as well as their role in cell attachment (see section 1.2.2.3), focal adhesions have been shown to be a site of degradation mediated by an indirect interaction between FAK and the protease MT1-MMP (Wang and McNiven, 2012). This raised questions about how these various structures (podosome, focal adhesion and invadopodia) share common properties and work together to promote cancer dissemination. These structures allow ECM remodelling and cell migration and together promote cell invasion and metastasis, which has been classified as a hallmark of cancer (Hanahan and Weinberg, 2011).

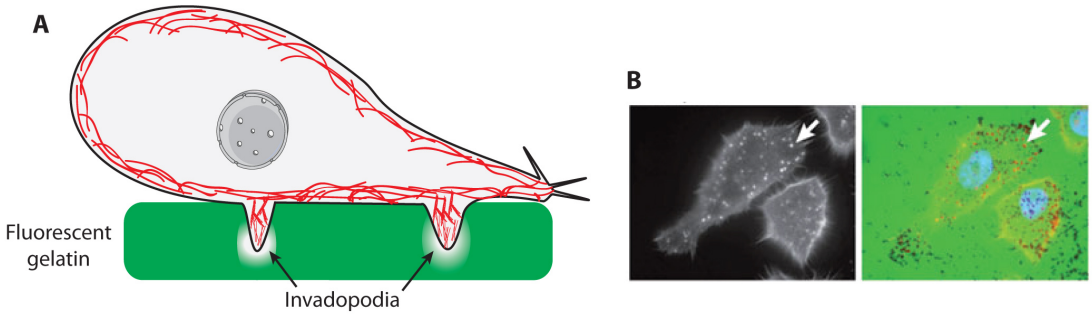

Figure 1-3: Invadopodia and ECM degradation
A – Cell migrating on a thin layer of labelled ECM. Invadopodia are actin-rich structures composed by a mix of branched and parallel actin filaments (Red). Local delivery of proteases at the site of the invadopodia leads to degradation of the ECM.

B – Representative picture of an invadopodia assay. SCC61 cells (head and neck squamous carcinoma cells) were plated on a fluorescent matrix and stained for F-actin. Degradation can be visualised by the appearance of black spots, colocalising with an actin-rich structure and reflects the presence of an invadopodia (white arrow). Reprinted with permission from Nature Publishing Group: [Nat. Rev. Mol. Cell Biol], (Murphy and Courtneidge, 2011), copyright (2011).

1.2.2.3 Coupling actin protrusions to adhesion

In order to generate movement and transmit forces, protrusions interact with the surrounding matrix using focal adhesions. Focal adhesions represent an interface between the environment and the cells and contain multi-molecular complexes, known as the "adhesome" (**Figure 1-4**). Focal adhesions are considered as a signalling hub mediating the transmission of information regarding matrix composition, environmental cues, activation state of intracellular signalling, in a bi-directional way (the so-called inside-out and outside-in signalling). They are also characterised by their ability to assemble and disassemble within a few minutes. This high turnover reflects the importance for the cell to maintain a dynamic pool of focal adhesion and adjust to the environment. Defects in adhesion dynamics or failure to form functional adhesions can lead to different diseases, such as cancer, inflammation, cardiovascular diseases, dystrophies to cite only a few (Winograd-Katz et al., 2014).

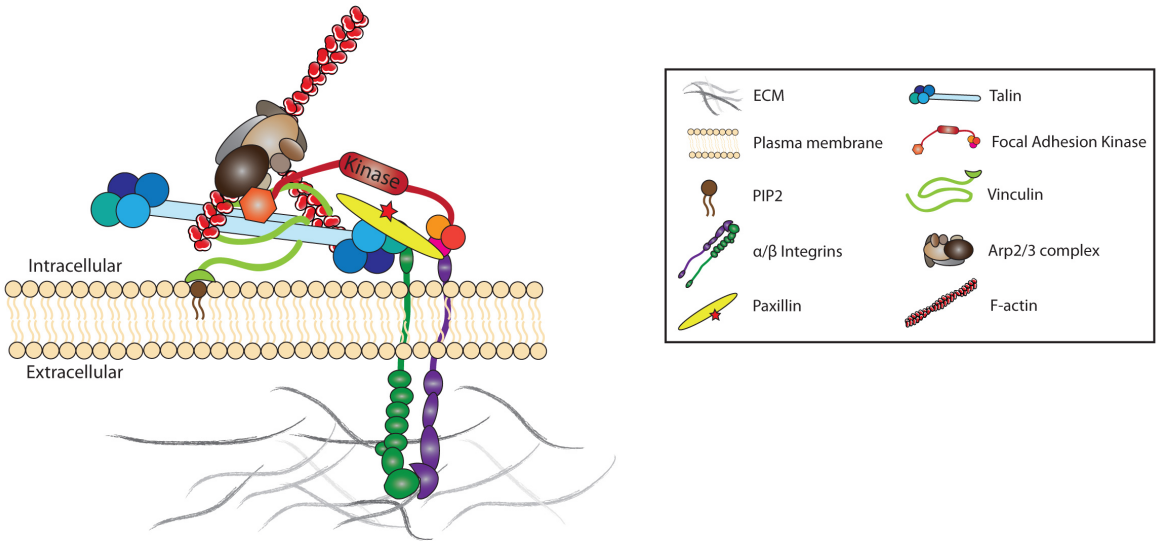

Figure 1-4: Schematic representation of an adhesion
Integrins are the molecular and signalling linkers between the extracellular matrix (ECM) and the cell. Once activated, proteins are recruited and transmit signals to the cell. Among the stimulated pathways, Arp2/3-dependent actin polymerisation allows a mechanical link with the cell body. Dynamic activation and regulation of this process leads to a coordination between cell protrusion and adhesion known as the clutch model (see **Figure 1.5**).

Adhesions are protein-rich structures but they are mostly organised around a core made by key ECM receptors, the integrin family. Upon activation and integrin clustering, Talin gets recruited in an actin-dependent way (Banno et al., 2012), followed by signalling and scaffolding molecules such as Src-family kinase, focal adhesion kinase (FAK), Paxillin, and Vinculin (Arias-Salgado et al., 2003; Brown et al., 1996; Humphries et al., 2007). Together, these proteins form a platform able to recruit the Arp2/3 complex (DeMali et al., 2002; Serrels et al., 2007). Those nascent adhesions are enriched underneath the lamellipodium area (Nobes and Hall, 1995) where they mature to focal adhesion (FA) and are mediators for force transmission. It is thought that transition to a maturation step is dependent and correlated to the matrix stiffness (Walcott et al., 2011). Moreover, actomyosin contractility (Choi et al., 2008) and Rac1 signalling (Nayal et al., 2006), and more generally RhoGTPases, are important factors for FA formation, maturation and dynamics. FA disassembly is mostly mediated by clathrin dependent and independent recycling of integrins, which are either degraded or sent back to the plasma membrane (Bridgewater et al.). Interestingly, integrins are still signalling even while being recycled by the endosomal compartment (Alanko et al., 2015). Together, those events lead to constant renewal of FAs and follow a clutch model synchronised with the cell protrusions (**Figure 1-5**) and this coordination is crucial during force transmission.

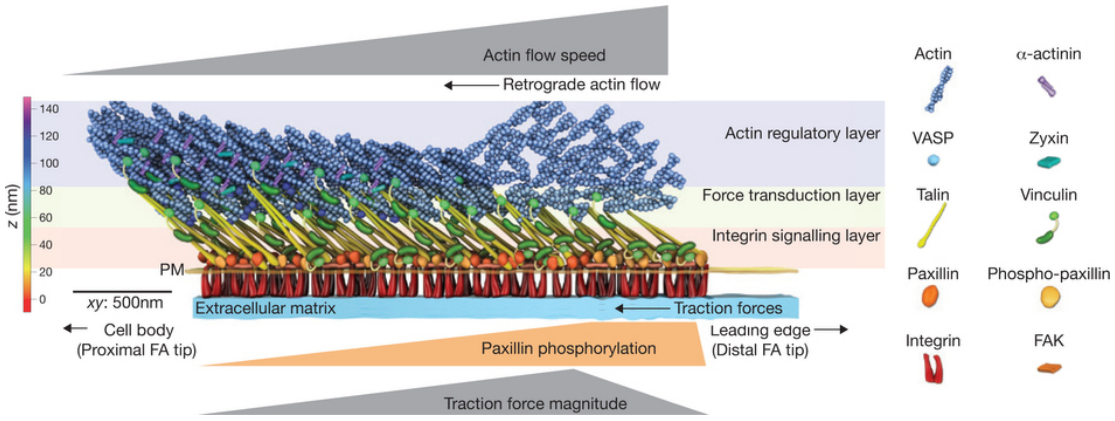

Figure 1-5: The molecular clutch model
The model is based on the coordination at 3 molecularly distinct levels signalling to each other. The integrin signalling layer involves the focal adhesion kinase (FAK) and Paxillin, which are in close relation with the integrins. Talin and Vinculin form an intermediate zone that connects the integrin layer and the actin cytoskeleton. The nature of interactions within this layer and its organisation suggest a role of force transduction. The more distal layer is rich in actin and actin-regulatory proteins that stimulate actin polymerisation and structure the actin network. Mechanistically, when integrins are not engaged as part of the clutch, actin polymerisation follows a rapid retrograde flow and does not promote any traction force. However, upon engagement, forces resulting from actin polymerisation are directly transmitted to the ECM and as a consequence, slow down the actin retrograde flow, while active polymerisation at the + end drives membrane protrusion. Reprinted with permission from Nature Publishing Group: [Nat. Cell Biol], (Case and Waterman, 2015), copyright (2015).

1.2.2.4 Relevance of cell protrusion in 3D and alternative structures

A cancer cell making its way out from the primary tumour to reach the closest capillary has to remodel a complex surrounding matrix. In line with this observation and in order to mimic more closely physiological conditions, assays have been designed where cells are forced to migrate through an ECM plug. In this condition, the typical polarisation of a cell is altered with a less well-defined front/rear axis. Notably, the lamellipodium is absent and the presence of stable focal adhesions has been questioned (Doyle and Yamada, 2016; Fraley et al., 2010). In order to illustrate this principle, Lammermann *et al* knocked out all integrin heterodimers in murine leukocytes and showed that 3D migration is not affected (Lammermann et al., 2008). However, it is now generally accepted that cells form adhesions, which are smaller and more transient in most 3D models. Cells also extend transient protrusions called pseudopods but filopodia, actin spikes, and invadopodia-like structures have also been described during 3D migration (Jacquemet et al., 2015). Together, they represent an interface between cell-matrix and play an important role for mechanosensing and force transduction. The rear of the cell is still the place of contraction forces, helping the cell to pull its body forward. In parallel, active secretion of proteases help the cell body to make its way through the tight lattices.

In spatially confined conditions such as 3D ECM, a new structure working independently of protease activity can be observed. Blebbing or amoeboid migration represents a high-dynamic type of migration, independent from protease activity and is seen as a more primitive process. Membrane blebs are bulky membrane extensions characterised by their fast turnover. Unlike others, their formation is actin polymerisation-independent (Cunningham, 1995) and mostly based on different intrinsic and extrinsic properties, such as cortical tension and matrix stiffness (Tinevez et al., 2009). Their formation is driven by the increase of intracellular pressure, dependent on the tension of the acto-myosin network, combined with a disruption of cortical actin (Keller and Eggli, 1998; Paluch et al., 2005). This generates a hydrostatic flux, pushing the membrane apart from the underlying cytoskeleton until an equilibrium between intra and extracellular pressures is reached. At this point, bleb retraction requires both Actin and Myosin-II (Blaser et al., 2006), although the mechanisms mediating actin polymerisation in a bleb are unclear: Indeed, neither Arp2/3 complex nor formins have been found localising at the retractile blebs, whereas contractile proteins (myosin and regulators) were recruited during the last step and localised at tiny clusters below the blebbing membrane (Charras et al., 2006).

In order to translate membrane blebbing to a proper movement, cells need: 1) To undergo cycles of bleb expansion/retraction. 2) To polarise membrane blebbing to one side of the cell body. Mechanisms allowing bleb polarisation are barely known but contractile molecules were shown to localise at the rear of migrating blebbling cells (Pinner and Sahai, 2008), suggesting that forces could directly come from one end and lead to increasing pressure at the other end. Together, both mechanisms lead to translocation of forces to the environment, and reduced cell-matrix attachment (Blaser et al., 2005; Grebecki et al., 2001), allowing the cell body to pull itself forward.

To conclude, although cell protrusions show differences between 2D and 3D, they also share some common features and both promote cell migration. Depending on the environment, cells can rely on one type of protrusion over the others and this cross talk can also be considered as a potential target for therapeutic approaches
In order to go more deeply into the regulation of these protrusions and understand how the actin network is formed, we will now describe the molecular mechanisms of actin polymerisation.

1.2.3 Actin & actin polymerisation

Actin is a 42 kDa protein encoded by 6 different genes (in birds and mammals). Isoforms can be classified in 3 main categories: Alpha-actin is predominantly found in muscle cells (skeletal, smooth and cardiac) that are specialised to be primarily a contractile machine, while beta and gamma-actin are not restricted to any cell types.
At the protein level, actin isoforms are extremely well conserved with greater than 93% between the isoforms. Furthermore, as one of the most conserved proteins throughout evolution, actin displays around 85% amino acid identity even between distant organisms, from mammals to yeasts and divergent single celled organisms. The crystal structure of the monomeric form reveals a globular shape composed of 2 domains (large and small), each of which is subdivided into 2 subdomains and organised around a nucleotide-binding cleft (**Figure 1.6)** (Kabsch et al., 1990; Otterbein et al., 2001). Each domain contains a five-stranded β sheet, with a β meander region and a right-handed βαβ motif. A flexible region links the large and small domains, resulting in an open/closed conformation. (Kabsch et al., 1990; Otterbein et al., 2001).

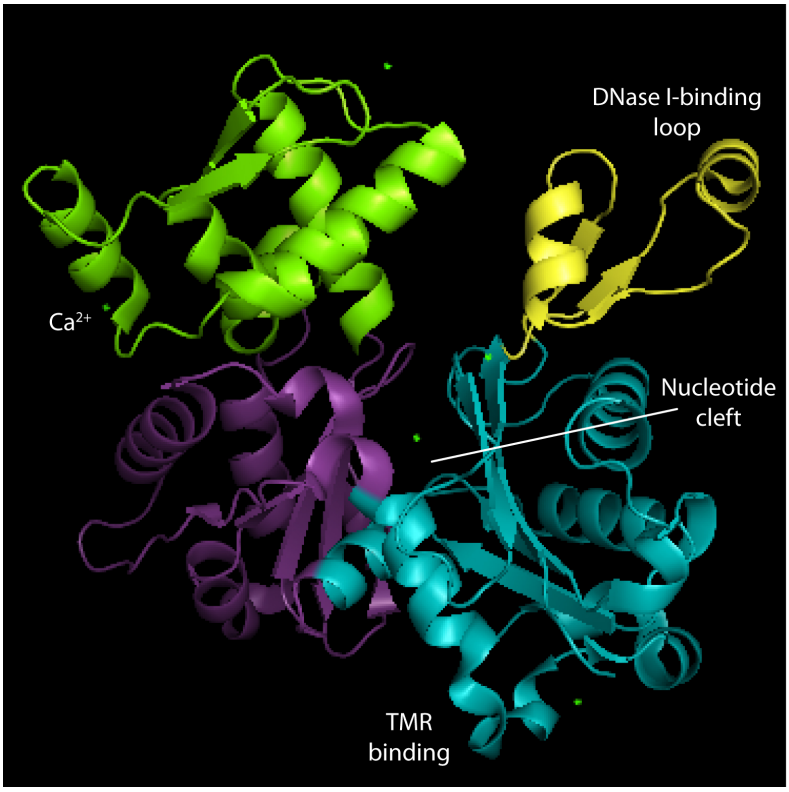

Figure 1-6: Structure of an actin monomer in the ADP-bound state
Ribbon structure of uncomplexed ADP-bound G-actin corresponding to the PDB entry 1J6Z (Otterbein et al., 2001). Structure was generated using PyMOL (v.1.7.4.5) and subdomains are shown using different colours: Sub-domain 1 (turquoise), sub-domain 2 (yellow), sub-domain 3 (purple) and sub-domain 4 (green). ADP is not represented in the cleft. Green balls represent calcium ions.

Previous structures were missing some parts of the sub-domain 2 because of its tight binding to DNase-I that was used for stabilisation purpose. The presented structure was obtained by using a molecule (TMR) covalently bound to a cysteine from sub-domain 1.

ATP sits in this pocket formed by subdomains 2 and 4 and can further be hydrolysed. The nature of the nucleotide affects the conformation of the actin structure.

Actin polymerisation is an ATP-Mg^{2+}-dependent process, although other cations have been shown to function *in vitro* (Kang et al., 2012; Strzelecka-Golaszewska et al., 1978). Polymerisation follows different steps: 1) the nucleation requires the formation of an actin nucleus composed by a trimer of G-actin. Thermodynamically, this step is highly unfavourable due to the instability of the dimer (K_d=4.6M) and therefore represents the rate-limiting factor (Sept and McCammon, 2001). Recently, it was however suggested that this nucleus grows in an unstable way until forming a pentameric seed, which was proposed as a more stable structure to induce actin polymerisation (Oda et al., 2016). However, a lot of biochemical evidence suggests that a trimer would be enough to initiate actin polymerisation. 2) Once the initiation step is overcome, polymerisation occurs very quickly and the elongation rate is proportional to the concentration of ATP-G-actin, although not totally linear (Weber et al., 1987). Polymerisation of ATP/Mg^{2+} bound-G-actin can occur at both ends but is thermodynamically more favourable at the barbed end (K_d=0.12µM versus K_d=0.6 µM) whereas depolymerisation preferentially occurs at the slow growing pointed end. At the steady state, rate of growth and shrinkage are equal and this is referred to as treadmilling.

Moreover, the chemical property is not homogenous throughout the filament and a molecule of G-actin at one end of the filament is different from a molecule released at the other end. Indeed, just after its introduction into the growing filament, ATP/Mg^{2+} bound-G-actin gets quickly hydrolysed to ADP+Pi/Mg^{2+} bound-G-actin (half-life ~2sec). This is followed by the release of the inorganic phosphate (Pi) with a half-life 6 min. This results in the existence of an ATP gradient along the filament itself (Carlier et al., 1984). However, in an *in vitro* set up, presence and hydrolysis of ATP is not essential for actin polymerisation *per se* (Cooke, 1975; Kinosian et al., 2004) and just stabilises the molecule of actin within the filament (Isambert et al., 1995). Similarly, De La Cruz *et al* demonstrate that nucleotide-free actin is able to polymerise in high-sucrose concentration forming stable filaments in these conditions. However, F-actin slowly disassembles in low sucrose concentration. Electron microscopy showed similar organisation of these filaments, although 3D-reconstruction revealed a difference in the density between the 2 strands forming the filaments, possibly reflecting a slight difference in the filament twist. Together, authors concluded that hydrolysis and Pi dissociation are required to create this differential energy at the two ends of the filament, resulting in distinct critical concentrations. (De La Cruz et al., 2000).

Moreover, actin dissociation can be accelerated by cofilin, an actin-binding protein that was shown to associate with ADP-bound G-actin (Didry et al., 1998). *In cellulo*, the complex cofilin-ADP-bound G-actin can move away from the F-actin-rich compartment where it can interacts with other proteins such as the LIMK1 and the cyclase associated protein, both acting in parallel for the release of ADP-bound actin (Moriyama and Yahara, 2002). Finally, nucleotide exchange is mainly dependent on the concentration difference between cytoplasmic ATP and ADP-actins, and allows the pool of ATP-bound G-actin to regenerate (**Figure 1.7**).

1.2.3.1 Arp2/3 complex

As mentioned previously, initiation of actin polymerisation is very slow on its own and would not be efficient enough to allow an adequate cellular response. However, once this kinetic barrier is overcome, the efficiency of the elongation process is really high and must be regulated in order to avoid uncontrolled events. This requires a tight balance between the main activators and inhibitors of the actin machinery, both in space and time.
Cells have developed a way to catalyse actin nucleation and concomitantly, allow a spatio-temporal control of the polymerisation. Although different actin nucleators have been described, among them the formin family (Goode and Eck, 2007), I will mainly focus here on the Arp2/3 complex.

The Arp2/3 complex was initially recovered from *Acanthanoeba* lysate in a screen aiming to find new profilin interactors (Machesky et al., 1994; Mullins et al., 1997). The complex is organised around 2 actin-related proteins (Arp), Arp2 and Arp3 and 5 other subunits (ArpC1-5). Protein purification followed by size exclusion chromatography directly confirmed that at least 5 subunits (Arp2, Arp3, p40-Arc and p35-Arc, p14-Arc, equivalent to human Arp2, Arp3, ArpC1, ArpC2, and ArpC5) display a 1:1:1:1:1 stoichiometry distribution. Despite a lower stoichiometry value explained by difference during the gel staining process, p18 and p19 (human homologue of ArpC3 and ArpC4 respectively) have also been considered as being distributed in equimolar proportions (Machesky et al., 1994; Welch et al., 1997) (Kelleher et al., 1995;) and this was confirmed later (Mullins et al., 1997).
Complex members are highly conserved across evolution and both Arp2 and Arp3 sequences and structures show a good similarity to G-actin (~30-50%) (Kelleher et al., 1995; Machesky et al., 1994; Mullins et al., 1997).

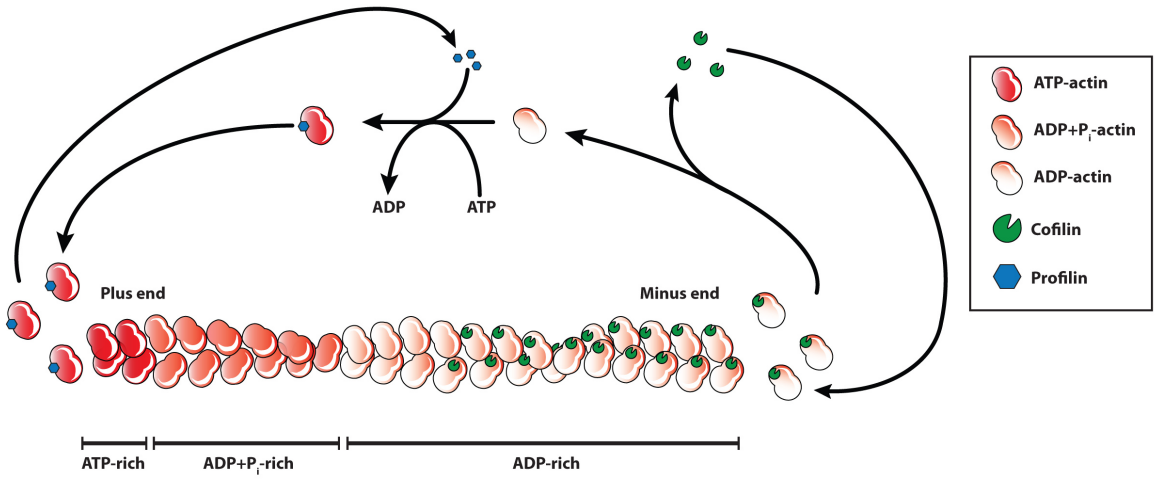

Figure 1-7: Actin polymerisation and treadmilling
Actin filament is not a homogeneous molecule. ATP-bound actin gets incorporated at the barbed (+) end, promoting filament growth. Quickly, ATP is hydrolysed to ADP-bound actin followed by a slow released of inorganic phosphate (P_i). Accumulation of ADP-bound actin destabilises the pointed (-) end, in parallel with its association with Cofilin. ADP-actin-Cofilin complex shuttles away from the actin-rich zone and upon phosphorylation by various proteins, such as LIMK and CAP proteins, ADP-actin is released and passively re-loaded with ATP. However, this reaction can be stimulated by profilin. Image inspired by (Moriyama and Yahara, 2002).

An initial structural study characterised the complex as a horseshoe shape able to bind actin filaments sideways (Mullins et al., 1997). They also proposed a rough organisation of the subunits relative to each other based on different crosslinking experiments before the 3D X-ray crystal structure was then released following the crystallisation of what is thought to be the inactive conformation of the complex (Robinson et al., 2001).

All these studies brought new insights about actin polymerisation regulation and allowed the community to have a broader mechanistic view. Arp2 and Arp3 sit next to each other within the complex and because of their actin-like structure, they serve as an initial seed, mimicking an actin dimer, therefore significantly lowering the kinetic barrier required to initiate the nucleation step. *In vitro* experiments showed that Arp2/3-mediated nucleation starts by the addition of a molecule of ATP/Mg^{2+} G-actin to the pre-formed Arp2-Arp3 dimer in order to complete the trimeric shape required for the initiation step. In parallel, ArpC2 and ArpC4 form a structural platform, which the remaining subunits can bind. Indeed, both major subunits create an interface with the actin filament and are crucial for nucleation, branching and stability of the complex itself but also for stability of the newly formed branch (Goley et al., 2010).

Together, the subunits sit on the side of a pre-existing mother filament with a 70 degree angle and the current model suggests that this preferentially occurs near the barbed end (rich in ATP-loaded actin) (Amann and Pollard, 2001). Upon ATP hydrolysis during filament aging, the interaction between the filament and the complex becomes weaker leading to the dissociation of the complex and its recycling for a new cycle.

1.2.3.2 Functions of Arp2/3 complex

As previously mentioned, the Arp2/3 complex stimulates the formation of branched-actin networks by bringing a template for the formation of a trimeric actin seed. Functions of the Arp2/3 complex have been extensively studied *in vitro*. Since genetic knockout mouse models were reported as lethal (Schwob and Martin, 1992; Yae et al., 2006), characterisation of the complex's function *in vivo* has been delayed. However, many groups have now directly studied Arp2/3 requirement in different *in cellulo* and *in vivo* systems.

Overall, loss of Arp2/3 complex leads to the absence of lamellipodia correlating with a spiky phenotype. Cell spreading is also greatly affected (Suraneni et al., 2012; Wu et al., 2012) but requirement during cell migration is still contradictory. While ArpC3 knockout cells have impaired chemotaxis toward EGF, knockdown of ArpC2 or chemical inhibition of the Arp2/3 complex doesn't affect migration along PDGF gradient (Wu et al., 2012).

Experimental design and technical features might be enough to explain this surprising result (Wu et al., 2013). Interestingly, ArpC2 knockout cells have a strong defect in haptotaxis and in focal adhesion morphology and dynamics (Wu et al., 2012). Authors linked this observation to a defect in the ability to align focal adhesions properly, suggesting a new role of the lamelipodium for sensing molecules bound to the ECM and rearranging spatial organisation of the focal adhesions. The Arp2/3 complex is also involved in a wide range of intracellular mechanisms. For example, a homologue of ArpC1 has been shown to be required for phagocytosis in *E. histolytica* (Babuta et al., 2015). In mammalian macrophages, Arp2/3 is recruited at phagosomes and required for engulfment (May et al., 2000). A potential mechanism in which the Arp2/3 complex brings opposite membranes close to each other, by excluding E-cadherin molecules, and therefore favouring membrane fusion has recently been proposed (Sumida and Yamada, 2015).

Among other functions, we can mention the requirement of the Arp2/3 complex during endosome fission using forces generated by the actin network and microtubules (Derivery et al., 2009b; Duleh and Welch, 2010).

Arp2/3 was also involved in monolayer integrity maintenance. Indeed, authors give some evidence of its requirement for proper localisation of the VE-cadherin at cell-cell junction allowing tissue remodelling (Abu Taha et al., 2014). Moreover, cortactin was shown to recruit WAVE2 and Arp2/3 at the zonula adherens, and together, maintains the cell-cell tension (Han et al., 2014; Verma et al., 2012).

Finally, Arp2/3 can be hijacked by pathogens to locally polymerise branched actin filaments. This can promote internalisation from the microenvironment of bacterial pathogens such as *Salmonella*, large parasitic pathogens like *Toxoplasma gondii* and even viruses. Once inside the cell, Arp2/3 can assist in intracellular movement and spreading of pathogens such as *Listeria*. This is dependent on bacterial virulence proteins directly injected or secreted into the host cell that mimic NPF functions by recruiting and stimulating Arp2/3-mediated actin nucleation, creating actin comet tails. (Bugalhao et al., 2015).

1.2.3.3 Regulation of the Arp2/3 complex

It is now well accepted that purified Arp2/3 complex is functionally inactive (Mullins et al., 1998; Welch et al., 1998). This observation reflects different thoughts: 1) Arp2/3 activation is crucial for a cell and has to be controlled. 2) Complex activation is dependent on other factors.

1.2.3.3.1 Intrinsic organisation of the Arp2/3 complex

For a long time, the existence of different subunit isoforms has been under-investigated from the mechanical and functional points of view. However, recent studies suggest a more complex intrinsic regulation directly linked to the ability of the complex to nucleate actin. Recently, Abella and colleagues (Abella et al., 2016) showed the existence of different Arp2/3 complexes composed by the combination of specific ArpC isoforms, resulting in functionally different complex. Indeed, in mammals, gene duplication has led to the evolution of 2 distinct ArpC1 (termed ArpC1A and ArpC1B) and ArpC5 (ArpC5 and ArpC5L) proteins. Surprisingly, *in vitro* and cell-based experiments showed that the association of ArpC1B/ArpC5L within the complex promotes much stronger actin polymerisation compared to a complex including the two other isoforms. In parallel, ArpC1B or ArpC5L-induced faster filament shrinkage because of the involvement of specific actin regulators. (Abella et al., 2016)

In addition, some partial Arp2/3 complexes were retrieved from mass spectrometry experiments looking at the composition of focal adhesions (Chorev et al., 2014). The authors proposed a model involving a core complex composed by Arp2, Arp3, ArpC2 and ArpC3. This would be able to either form a fully functional Arp2/3 complex or be directed to the focal adhesions after binding to vinculin/alpha-actinin. Mechanisms regulating this switch are still unknown but the thought of having a site-specific functional Arp2/3 complex can open new hypotheses and help to decipher new mechanisms controlling local polymerisation.

1.2.3.3.2 Role of ATP during Arp2/3 regulation

Like actin, Arp2 and Arp3 have a nucleotide-binding cleft where ATP is able to fit in (Dayel et al., 2001; Le Clainche et al., 2001). ATP binding is crucial for the complex activity and once coupled to nucleation promoting factor (NPF) binding (see section 1.2.3.2.4), actin polymerisation is initiated. Both events allow conformational changes of the complex and are critical for the activity of the complex (Rodal et al., 2005). Recently, the conserved C-terminal tail of Arp3 was identified as an ATP-dependent molecular switch, regulating actin nucleation (Rodnick-Smith et al., 2016). Although ATP hydrolysis has been reported for Arp2 in specific experimental conditions, the same event has not been confirmed for Arp3 (Goley et al., 2004). However, it is still unclear whether ATP-hydrolysis of Arp2 and potentially Arp3 is mandatory for stimulating actin assembly (Martin et al., 2005). Indeed, the current model points toward a link between ATP hydrolysis on Arp2 and complex dissociation *in vitro* and during endocytic event in *S. cerevisae* (Martin et al., 2006).

1.2.3.3.3 Role of phosphorylation during Arp2/3 regulation

Post-translational modifications such as phosphorylations, are reversible events and can positively and negatively modulate protein activity within a few seconds. This is also true for the Arp2/3 complex and phosphorylation of Arp2 has been reported in rat adenocarcinoma cells. LeClaire *et al* (LeClaire et al., 2008) show that phosphorylations of the conserved Tyr202 and Thr237/238 are required for actin polymerisation and lamellipodia formation. This event is tightly regulated by the cell upon epidermal growth factor (EGF) stimulation and reached a peak after 3min before going back to its basal state. A model was proposed in which Arp2 was maintained in an inactive conformation by a network of salt-bridges, the latter being disrupted upon Arp2 phosphorylation and allowing the switch to an active conformation (Narayanan et al., 2011). However, phosphorylation events are not sufficient to induce actin polymerisation in the absence of NPFs, which remain key activators of the Arp2/3 complex (LeClaire et al., 2008).

1.2.3.3.4 Nucleation Promoting Factors (NPFs)

Most of the aforementioned events act in synergy with NPFs, and together, fine-tune the complex activity. They are classified in 2 categories based on the organisation of their C-terminus end and the presence (Class I) /absence (Class II) of a VCA domain (Verpolin-Central-Acidic domain) (Rotty et al., 2013). It represents a very conserved combination of amino acids with common features and is composed by 3 motifs with distinct functions: 1) V-motif also known as WH2-domain binds G-actin and brings an actin monomer in close vicinity to the Arp2-Arp3 dimer. 2) C-motif also known as Central domain and 3) A- or Acidic motif acts in parallel to mediate interactions with the Arp2/3 complex (Kelly et al., 2006). Binding and activation of the complex were shown to be dependent on a conserved tryptophan residue in the A-motif (Ti et al., 2011). It has now been widely shown *in vitro* that VCA domain on its own is sufficient for the complex activation and can greatly accelerate filament formation (Higgs and Pollard, 1999; Machesky et al., 1999).

Class I

Members of the class I family include WASP, N-WASP, Scar/WAVE1-3, WASH, WHAMM, and JMY, and am commonly known as the WASP family. They are all characterised by a conserved VCA domain and a more diverse N terminal part leading to different regulating and binding partners. WASP and N-WASP are characterised by the presence of a Cdc42 Rac1 Interacting Binding domain, responsible for interaction with these GTPases (Rohatgi et al., 2000). Regulation of this family is thought to be similar, although still unclear for some members. For example, basic region of N-WASP interacts

with the A-motif while the autoinhibitory domain folds over the regulatory C-terminal domain, leading to the inhibition of the protein. Upon activation by Cdc42 and lipid binding, the protein opens up and releases its VCA tail, making it free to interact with the Arp2/3 complex (Rohatgi et al., 2000). In contrast, Scar/WAVE is part of a stable pentameric complex known as the WAVE Regulatory Complex (WRC) (see section 1.4), responsible for both localisation and regulation of the Arp2/3 complex. A similar mechanism is proposed to have evolved in parallel for the regulation of the WASH protein, which belongs to a homologous complex (WASH complex) and plays a role during Arp2/3-mediated endosomal trafficking (Jia et al., 2010).

Biological functions of each member are reported in Table 1 and we will highlight the roles and the regulation of the Scar/WAVE proteins in more details in section 1.4.2.5.

Class II

Cortactin is the typical Class II NPF and similar to members from the Class I, it contains an acidic region mediating the binding to Arp2/3. The absence of a G-actin binding motif is overcome by an F-actin binding motif composed by a central tandem repeat motif. Cortactin-mediated Arp2/3 activation is much less efficient compared with Class I NPFs (Uruno et al., 2001; Weaver et al., 2001) and the mechanism is still not entirely clear. A FRET study suggests that cortactin is not able to promote the conformational change of the Arp2/3 structure required for its activation (Goley et al., 2004), which could explain the weaker effect observed. The actual view proposes a role of cortactin in the stabilisation of the Arp2/3 complex branching and strengthening the Arp2/3 association with F-actin (Weaver et al., 2001), by contacting Arp2, ArpC2, ArpC4 and ArpC5 (Weaver et al., 2002).

However, cortactin can act in parallel and synergise the activity of a Class I NPF. This was shown *in vitro* using smTIRF and by mathematical modelling based on the ability of cortactin to displace purified VCA within a N-WASP-stimulated Arp2/3 complex and speed up nucleation at the side of a forming branch (Helgeson and Nolen, 2013).

Other NPFs.

Deeper understanding of actin nucleation led to the discovery of new regulators. Among them, Dip1, a member of the WISH/DIP/SPIN90 family has been reported to stimulate Arp2/3-actin polymerisation during endocytosis using a distinct mechanism (Wagner et al., 2013). Indeed, this family stands out because of the 3 major features: 1) Members do not bind to G-actin. 2) They do not require mother filaments to stimulate actin polymerisation.

3) Binding to Arp2/3 is different from the canonical model proposed for the WASP-family. Full understanding of how these proteins work awaits further research.

Protein	Localisation/Function	Reference
WASP/N-WASP	Phagocytic structures	Tsuboi et al., J. Biol. Chem. 2007
	Endocytic structures	Benesh et al., J. Cell Sci. 2005
	Lamellipodia	Lorenz et al., Curr. Biol. 2004
	Filopodia	Miki et al., Nature 1998
	Invadopodia	Lorenz et al., Curr. Biol. 2004
	Golgi	Bhattacharya et al, Sci. Rep. 2016
WAVE proteins/WRC	Phagocytic structures	Hymphreys er al., Cell Rep. 2016
	Lamellipodia	Hahne et al., FEBS Lett. 2001
	Cell junctions	Yamazaki et al., J. Cell Sci. 2007
WASH	Endocytic structures	Derivery et al., Dev. Cell 2009
WHAMM	Golgi	Campellone et al., 2008
JMY	Nucleus, Lamellipodia & Ruffles	Zuchero et al, Nat. Cell Biol. 2009

Table 1-1: Localisation of NPFs in mammalian cells
Table summarising the localisation of the Class I NPFs and their importance for the formation and organisation of different cellular structures.

1.2.3.3.5 Branching inhibitors

Actin polymerisation regulation is a double-edged process where the stimulating factors have to be counterbalanced. Here I will briefly discuss the emergence of negative regulators affecting actin branching.

The first idea of actin branching inhibitor came based on the composition of the actin filament itself. Indeed, in a cell, actin filaments are not naked and can be covered by different molecules. Blanchoin *et al* (Blanchoin et al., 2001) showed that tropomyosin, a protein involved in acto-myosin contraction, has a negative effect on actin branching, probably due to a steric effect. Indeed, tropomyosin runs along each side of the filament, which impaired Arp2/3 binding to the existing filament playing a crucial role as a second signal to initiate actin polymerisation. This greatly delays the initiation of the branching and affects the number of branching events.

PICK1 protein (Protein interacting with C kinase 1) was also shown to inhibit Arp2/3-dependent endocytosis via a direct binding to both F-actin and Arp2/3 (Rocca et al., 2008). Although the mechanism by which the inhibition occurs has not been deeply investigated, residues involved were mapped and point mutants were not able to rescue the knockdown phenotype anymore. However, the function of PICK1 as a regulator of the Arp2/3 complex is still controversial (Madasu et al., 2015).

GMF (Glial Maturation Factor) is a member of the ADF/cofilin superfamily and was described as a debranching protein, dynamically colocalising with cortical actin patches in *S. cerevisae* (Gandhi et al., 2010). Mass spectrometry and biochemical pulldown showed a direct interaction between GMF and Arp2/3, inhibiting actin nucleation. TIRF imaging shows that addition of GMF leads to the severing of the newly formed branches resulting in a more linear actin network. GMF function *in vivo* was confirmed using RNA interference (RNAi) in *D. melanogaster* as it affects actin rearrangement and drives collective migration of border cells during development (Poukkula et al., 2014).

Since actin nucleation is not only restricted to the region adjacent to the plasma membrane, but also has an important role in intracellular vesicle trafficking, specific regulators have been described to spatially regulate Arp2/3 activity. Gadkin (Gamma-A1-Adaptin and Kinesin Interactor) is one of them and acts at the endomembrane level, specifically at the trans-Golgi compartment (Maritzen et al., 2010). Gadkin binds to the complex via a tryptophan residue located in its acidic motif and co-localises with endosomal ArpC2. Depletion of Gadkin redistributes Arp2/3 complex at the membrane and results in an

increase of cell spreading (Maritzen et al., 2012). Also, Gadkin is important for *in vitro* 2D and 3D migration of primary dentritic cells, although this effect is not reflected *in vivo* (Schachtner et al., 2015).

Finally, Arpin (Actin-related protein inhibitor) is the most recent Arp2/3 regulator that came out from sequence alignments aiming to find new NPFs (Dang et al., 2013). Arpin binds to ArpC2 in an active Rac1-dependent manner and colocalises with the WRC. Together, this leads to negatively regulate protrusion dynamics and balance the activity of the WRC. Recent structural analyses suggest that the acidic motif of Arpin competes with and blocks the VCA-Arp2/3 interaction. Indeed, 2 Arpin-binding sites were mapped close to Arp2 subunit, and binding to Arp2/3 was shown to further induce a conformation modification of the complex (Fetics et al., 2016; Sokolova et al., 2017). Consistently with its inhibitory effect towards the Arp2/3 complex, Arpin is down-regulated in different breast cancer cell lines and mRNA level from patient samples has been anti-correlated with the tumour aggressiveness. Surprisingly, Nap1 and Arpin show co-exclusivity in the analysed samples (Lomakina et al., 2016). At the protein level, authors claimed that invasive carcinoma cells show a lower IHC signal for Arpin compared with adjacent fibroblast cells or to normal epithelial ducts, although further analysis and thorough quantification are still required to support their data. For example, independent cBioPortal analysis showed that Arpin is in fact upregulated in most cancer types.

1.3 The RhoGTPases family

1.3.1 Introduction to the RhoGTPases family

The Ras superfamily contains evolutionary conserved proteins, subdivided into 5 categories: The Ras, Rho, Ran, Rab, Arf families. Together, it accounts for over 150 structurally related proteins with similar domains and functions. They are characterised by a common G-domain, which is responsible for the binding of GTP and most of them contain a carboxyl-terminal CaaX box, allowing lipid modification and membrane tethering. Extensive reviews of the different subfamilies are available (Rojas et al., 2012; Wennerberg et al., 2005) and I will discuss the Rho family in further detail as Rho proteins are implicated as master controllers of actin cytoskeleton.

There are 20 members of the Rho family in mammals, divided into 5 classical (Rho, Rac, Cdc42, RhoF and RhoD) and 5 atypical (RhoBTB, Rnd, RhoU, RhoV and RhoH)

subfamilies, which signal to cytoskeleton, vesicular trafficking, and cell cycle progression (Etienne-Manneville and Hall, 2002) (**Figure 1-8**).

Among these, Rac1, RhoA and Cdc42 have been the most characterised so far and their role during actin dynamics and migration are extensively studied.

1.3.2 Structural features of the RhoGTPases

Like other Ras-related family members, the structure of RhoGTPase encompasses a G-domain, characterised by 5 G-motifs (G1-G5) and an insert region that determines the specificity of binding to effector proteins. G1, also known as the P-loop, connects the β-Phosphate of the nucleotide with a Mg^{2+} ion, and is required for the nucleotide stability. Together, they form a globular structure made of 6-stranded β sheets and 5 α-helixes, complemented by an additional α-helix coming from the Rho-family specific insert region. This structure has high affinity for guanine nucleotide and is relatively stable, except across 2 regions named switch I and switch II (Milburn et al., 1990; Vetter and Wittinghofer, 2001). Because of their dynamic association with guanine nucleotide and their ability to hydrolyse GTP, RhoGTPases are seen as major signalling molecules. They have been widely pictured as molecular switches, oscillating between an active (GTP-bound) and inactive (GDP-bound) state. This difference in the nature of the nucleotide is also reflected by a conformational change, mediated by the two flexible switches (Milburn et al., 1990). Indeed, oxygen from the γ phosphate of GTP creates 2 hydrogen bonds with 2 residues on switch I and switch II. Upon GTP hydrolysis, this physical constraint is lost, resulting in a relaxation of the structure (called disorder-to-order transition) (Vetter and Wittinghofer, 2001). Together, nucleotide specificity and conformation changes mediate the binding to distinct downstream effectors.

The carboxyl-terminal domain contains a motif of high sequence variability encompassing a common CaaX box (Cysteine, 2 aliphatic amino acids and any amino acid that will dictate the enzyme specificity) (Clarke, 1992). This motif is a signal for lipid modifications which allows proper localisation at the plasma membrane. A wide variety of lipids (geranylgeranylation, farnesylation, palmitoylation) have been identified as important for RhoGTPases functions and localisation. As an example, it has been reported that palmitoylation (Navarro-Lerida et al., 2012) and prenylation of Rac1 (Gorzalczany et al., 2000) were crucial for its activity, specifically the ability to stimulate phosphorylation-primed WRC (Lebensohn and Kirschner, 2009).

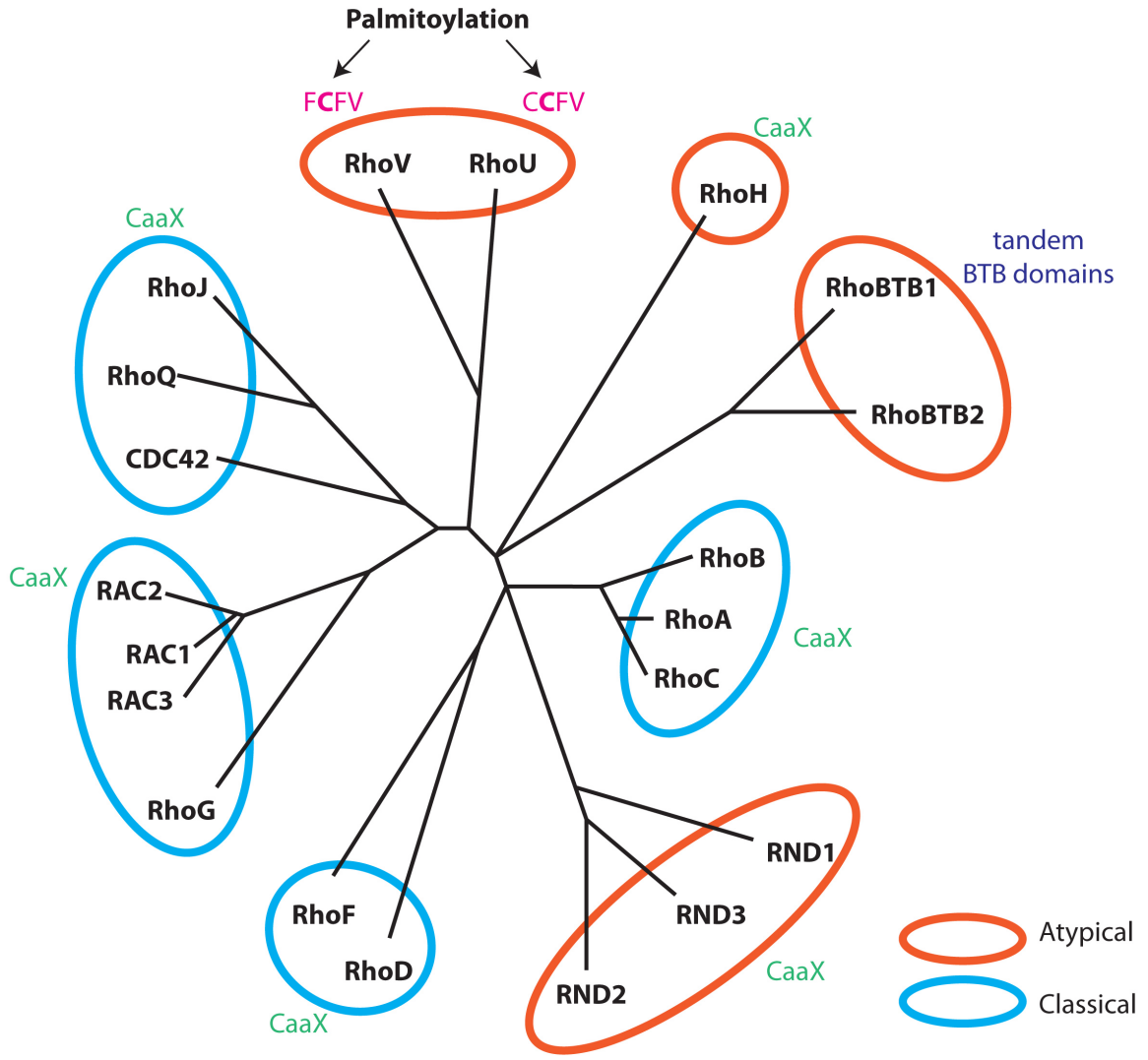

Figure 1-8: Evolution of the RhoGTPase family
Graphical representation of the phylogenetic tree of the RhoGTPase family. Analysis was based on the similarity of amino acids between each member. Classical (blue circled) and atypical (orange circled) RhoGTPases are highlighted. Atypical RhoGTPases are preferentially GTP-bound and their function is independent of the activity of GAPs/GEFs. Their regulation is mostly based at the transcriptional level and their inactivation depends on proteasomal degradation, although protein-protein interaction might also be involved.

Most of RhoGTPases contain a CaaX sequence, regulating their localisation at the membrane following S-acylation. RhoBTB1/2 don't contain a CaaX domain but instead two BTB domains. RhoV and RhoU are also devoid in CaaX sequence and have the antepenultimate cysteine palmitoylated (Kardash et al., 2010).

Evolutionary distance is not proportional to the branch length.

Adapted from (Roberts et al., 2008) and (Heasman and Ridley, 2008)

1.3.3 Regulation of RhoGTPases activity

1.3.3.1 The guanine nucleotide exchange factors (GEFs)

Stability of the GDP in the nucleotide binding pocket is high (nano to picomolar range), resulting in a very slow cycling between GTP and GDP-bound state. In order to speed up this process, RhoGTPases are activated at the plasma membrane by guanine nucleotide exchange factors (GEFs), which stimulate the exchange of GDP to GTP by several orders of magnitude (Bos et al., 2007). Indeed, GEF proteins will bind to the RhoGTPases in order to destabilise the switch regions and the P-loop, resulting in weakening of the phosphate binding first and then the base gets expelled. A ternary complex between GEF, GTPase and nucleotide can exist, but because of its transient state, it has been problematic to purify to date. Finally, the reloading of GTP is a passive event based on the excess of cytosolic GTP compared to GDP. Spatial localisation of the GEFs at the plasma membrane has been shown to be partially dependent of their pleckstrin homology domain (Ferguson et al., 1995). However, the low affinity and the lack of specifity of this binding (Snyder et al., 2001) require other protein domains for an efficient membrane targeting (Stam et al., 1997). The mechanisms leading to the nucleotide exchange are highly dependent of the nature of the GTPase/GEF pairing, so it is difficult to give a specific example that could be generalised. In order to illustrate this part, I will focus on the published interaction between Rac1 and one of its GEFs, Tiam1 (Worthylake et al., 2000). Most of the GEFs are characterised by an invariable Dbl-homology domain followed by the Pleckstrin-homology domain in C-terminus (DH and PH domains) (Bos et al., 2007). These two domains are dependent on each other in order to mediate the protein's functions. Worthylake and co-workers used a truncated Tiam1 construct encompassing the DH-PH domains to crystallise and solve the dimer structure at 1.52Å. Despite some disordered portions in the Tiam1 crystal, they reported that Tiam considerably modified the organisation of Switch I and II regions of Rac1. Following binding, Switch I moved up to ~3Å, resulting in the loss of interaction between Cys18 and the oxygen group from the α-phosphate of the nucleotide. Moreover, this shift led to a mis-orientation of Phe28 that usually stabilises the nucleotide inside the pocket. The major disruption in Switch II comes from the insertion of the Ala59 inside the cation-binding site impeding the formation of a robust interaction with the Mg^{2+}, which is fundamental for the high-affinity nucleotide binding. This structure also highlights the lack of direct interaction between Tiam and the active site of Rac1, which is now commonly accepted for most of the GEF/GTPases interactions (Worthylake et al., 2000).

To note, the aforementioned description is related to the main GEF family (Dbl-family), containing a DH-PH domain. However, another family of GEFs lacking this usual structure and referred to as the DOCK-family have been described. Instead, they are characterised by two conserved sequences (DOCK-homology region 1 and 2 – DHR1/2). DHR1 links the protein to PIP3 wherease DHR2 encompasses the GEF activity toward Rac1 and Cdc42 (Cote and Vuori, 2002).

GTPase activating proteins (GAPs)

Despite their names, intrinsic GTPase activity of the Rho family is actually very slow and can be enhanced by GTPase activating protein (GAPs). The diversity of mechanisms driving GAP activity reflects the high number of GTPase-GAP interactions but some common features can be highlighted to draw an overall picture. Briefly, the hydrolysis is based on an in-line nucleophilic attack coming from a molecule of water, stabilized by a conserved glutamine from the Rho protein. Meanwhile, a highly conserved arginine finger supplied by the GAP itself stabilises a transient interaction with the γ-phosphate and this conformation is crucial for GTP hydrolysis (Nassar et al., 1998). Together, this weakens the liaison between β and γ phosphates and results in the formation of a molecule of GDP + Pi and a proton. This interaction drastically moves the reaction equilibrium and increases nucleotide cleavage by several orders of magnitude (Bos et al., 2007; Vetter and Wittinghofer, 2001).

However, with regard to the diversity of GTPases involved and the multitude of GAPs and GEFs already identified, some mechanisms can be slightly different but have been reviewed extensively (Bos et al., 2007; Vetter and Wittinghofer, 2001).

1.3.3.2 RhoGDIs

Finally, RhoGDIs (Rho guanine nucleotide dissociation inhibitor) are not as well characterised regulators but are seen as essential inhibitors of RhoGTPase cycle. Indeed they bind to inactive GDP-loaded protein and inhibit their translocation to the membrane, allowing the maintenance of a cytosolic pool of dimer RhoGTPase-RhoGDI (Cherfils and Zeghouf, 2013). However, binding to the GTP-loaded form of the RhoGTPase has also been reported (Hancock and Hall, 1993). This pool of inactive RhoGTPases acts as a reservoir of easily activated proteins and allows a quick response of the cell.

The main challenge for the RhoGDI is to keep RhoGTPases soluble. Indeed, prenylation of RhoGTPase is essential for their localisation and functions but incompatible with a cytosolic localisation of the protein due to its hydrophobicity. Once bound to a RhoGDI,

the isoprenyl moiety is shielded within a hydrophobic pocket of the protein, which then acts as a chaperone until a stimulus (protein-protein interaction, specific lipid composition, phosphorylation) releases this interaction and allows the interaction to the membrane. This switch is a highly regulated process and is seen as an essential step to maintain Rho activity at a basal level (Dovas and Couchman, 2005).

1.3.3.3 Post-translational modifications (PTM)

Post-translational modifications were also shown as potent regulators or RhoGTPases. While the carboxyl-terminal polybasic region helps for the GTPase targeting at the membrane, prenylation of the cysteine residue of the CaaX box is the most frequent PTM (Michaelson et al., 2001). Interestingly, only 16 out of 20 RhoGTPase contains this sequence, suggesting other membrane-targeting signals for Wrch-1 (RhoU), Chp/Wrch-2 (RhoV), RhoBTB1 and RhoB2/DB2 (RhoBTB2) (Roberts et al., 2008) (**Figure 1.8**). Post-translational modifications of the RhoGTPase family involve initial recognition and lipidation of the CaaX sequence by a farnesyltransferase or a geranylgeranyltransferase, followed by the cleavage of the 3 last residues (aaX) by an endoprotease. The last step involved a specific methylation process of the terminal cysteine. These successive modifications increase the hydrophobicity of the protein and assure its correct localisation at the membranes. Genetic disruption or chemical targeting of the CaaX domain leads to the cytosolic localisation and the inactivation the RhoGTPase and has been addressed as a potential therapeutic strategy (Winter-Vann and Casey, 2005).

Once anchored at the membrane, additional signals, such as sumoylations, ubiquitinations, phosphorylations fine-tune the activity of the RhoGTPases (Olson, 2016).

In addition, an extra level of regulation is assured by the post-translational modification of the GEFs and GAPs themselves (Hodge and Ridley, 2016).

1.3.4 Coordination between RhoGTPases activation and cell protrusion

Regulators finely coordinate RhoGTPases activity at specific locations and allow a fast cycle of activation/inhibition following stimulation. Over the last 15 years, the classical view of GTPase activity was restricted to a role of Rac1 and Cdc42 as regulators of membrane protrusions at the leading edge, whereas RhoA mostly regulates cell rear contractility. However, new imaging tools have been challenging this dogma and it is now accepted that this model is much more flexible according to the environment and the structures involved (Fritz and Pertz, 2016).

Indeed, the three main RhoGTPases were shown to be activated at the leading edge of migrating cells (Kraynov et al., 2000; Nalbant et al., 2004; Pertz et al., 2006) and much of Alan Hall's work has focused on the crosstalk between Rac1, RhoA and Cdc42 (Nobes and Hall, 1995; Rottner et al., 1999), making the understanding of the mechanism even more complex. However the coordination of Rho, Rac and Cdc42 during membrane protrusion was unclear and this has greatly been addressed by the use of FRET markers during membrane extension/retraction (Machacek et al., 2009). These authors were able to show that a narrow pattern of RhoA activation at the leading edge occurs concomitantly to the protrusion formation and co-exclusively with Rac1 activation, which has been proposed to sustain protrusion stability with Cdc42. In line with this sequential activation, Cdc42 and Rac1 activation is delayed by around 40 seconds compared with RhoA activation. In different settings however (microfluidic device rather than cell in a dish), this Rac1/RhoA antagonism is less clear and might be context-dependent, such as experimental design, cell types (Martin et al., 2016).

A tight coordination of RhoGTPases is then a crucial event for healthy cells to achieve their functions. On the other hand, deregulation of RhoGTPase signalling is a common features in cancers, and targets either the RhoGTPase directly (i.e. Rac^{P29S} frequently found in melanoma) or pathways involved throughout the GTPase cycle (Porter et al., 2016). For example, Rac1 GEF P-Rex1 is overexpressed in different cancers and was linked to metastasis in prostate cancer (Marei and Malliri, 2017; Qin et al., 2009).

1.3.5 Introduction to Rac family members

Rac1 (Ras-related C3 botulinum toxin substrate 1) was discovered as a substrate for ADP ribosylation by Botulinum toxin C3 ADP-ribosyltransferase in HL-60 cDNA screen and showed similarity to Ras protein, especially in the guanine nucleotide-binding site (Didsbury et al., 1989). In mammals, Rac2 (Didsbury et al., 1989) and Rac3 (Haataja et al., 1997) and RhoG (Vincent et al., 1992) complete the Rac family proteins (**Figure 1-8**) and play important roles in actin dynamics and lamellipodium regulation. Despite their high sequence conservation (human Rac1 is identical at ~95% with Rac2 and 3 and 72% with RhoG), expression pattern of the family members is quite different: Unlike Rac1 and RhoG that are ubiquitously expressed, Rac2 is hematopoietic-specific (Gu et al., 2002b) while Rac3 is enriched in the brain (Haataja et al., 1997).

Interestingly, the human *RAC1* gene encodes for two splice variants, Rac1a (hereafter referred as Rac1) and Rac1b (Jordan et al., 1999), which is extended by 19 amino acids following the switch II region. In overall, structures of Rac1 and Rac1b are highly similar,

with the exception of the switch regions, which are key parts to mediate alternative responses between an active versus inactive state of the protein. Indeed, both switches are suggested to be highly flexible (Fiegen et al., 2004). Intrinsic Rac1b GTPase activity was reduced but it can still respond to GAP activity (Fiegen et al., 2004; Matos et al., 2003). Unlike Rac1, Rac1b doesn't induce lamellipodia formation (Nimnual et al., 2010; Singh et al., 2004) but it was shown to be over expressed in various solid cancers and has been linked to poor prognosis (Jordan et al., 1999; Schnelzer et al., 2000; Zhou et al., 2013). This surprising data can be explained by the cellular transformation potency of Rac1b (Singh et al., 2004) and also by the tumorigenic effect of this splice variant. Finally, in a colon-cancer model, Rac1b was specifically overexpressed over Rac1a and this triggered reactive oxygen species production, leading to hyperproliferation of intestinal stem cells and tumourigenesis (Myant et al., 2013). So together, studies characterised Rac1b as a constitutively active GTPase, although exhibiting some specificity concerning downstream effectors (Matos et al., 2003; Singh et al., 2004).

1.3.6 Rac1, master regulator of cell protrusions

Given its wide expression, we will mostly focus on Rac1 and its function in actin-based cytoskeleton remodelling. Initially, active Rac1 was described as the main regulator of actin reorganisation, membrane ruffling and macropinocytosis in fibroblasts (Ridley et al., 1992). However, broader functions were later described and its roles in gene transcription (Matos and Jordan, 2006), proliferation (Hofbauer et al., 2014) and apoptosis (Zhang et al., 2015) are now well accepted.

Lamellipodia formation by Rac1 results from a balance between several signalling pathways, involving the Arp2/3 complex through Scar/WAVE complex and also the Rac1-mediated actin turnover through the LIMK/Cofilin pathway (Yang et al., 1998). Involvement of Rac1 during lamellipodia extension has been widened to different systems, including T cells (Faroudi et al., 2010), epithelial cells (Keely et al., 1997) and neurons (Chen et al., 2007) and is thought to affect their motility. A surprising result comes from Rac1-null macrophages: Despite their spindly shape and their defect in membrane ruffling, they were still able to chemotax and migrate as efficiently as their wild type counterparts, suggesting a lamellipodial-independent mechanism driving cell migration. (Wells et al., 2004). However, those observations contrast with more recent data obtained with Rac1 knockout fibroblasts, which are defective in random migration and chemogradient sensing, although spreading and adhesion are largely unaffected (Steffen et al., 2013).

In vivo models confirmed previous *in vitro* results about Rac1 as a key player in actin dynamics and have also brought new insights into the role of this RhoGTPase. In neuronal cells, Rac1 loss or deletion has shown different roles in different systems. In transgenic mice, expression of constitutively active Rac1 in Purkinje cells increases dendritic trunks branching (Luo et al., 1996) while dominant negative and constitutively active Rac mutants indistinguishably cause embryonic lethality in *Drosophila* and affect axonal growth but not dendrite morphology (Luo et al., 1994). Also using *Drosophila* as a model, expression of a functionally dead version of Rac1 in egg chambers affected membrane protrusions and collective migration of border cells (Bianco et al., 2007; Duchek et al., 2001). Similarly, actin-protrusion formation as well as cell polarity were also affected upon inhibition of Rac activity in zebrafish, resulting in a defect in germ cell migration (Kardash et al., 2010).
In a mouse model, constitutive whole-body depletion of Rac1 is lethal at mid-gastrulation (E9.5) (Sugihara et al., 1998). However, development of tissue-specific CRE-driven expression allows a precise study during development and in adult mice. For example, specific depletion of Rac1 during melanoblast migration (precursors of pigmented skin cells), profoundly affected adult colour coat with a striking white belly phenotype, white paws and tail (Li et al., 2011). This results from a migration defect of those cells during embryogenesis. Indeed *Rac1*-knockout cells displayed only short stubby protrusions that are Rac1-independent, compared with the normally long pseudopods extending from the cell body. Similar phenotypes were also obtained with the specific deletion of a RacGEF (P-Rex1) in the melanoblats (Lindsay et al., 2011) and the double null-mutant embryo (Lindsay et al., 2015), suggesting that active Rac1 is functionally important for driving melanoblast migration.

1.3.7 Rac1, regulator of cell polarity

Epithelial cells are characterised by apical and basolateral domains, which correspond to distinct cellular compartments with different protein content, mediating specific functions. Establishment of cell polarity is a crucial event for the fate of the future cell and requires interconnected signalling pathways involving the conserved Par protein family, Crumbs/Scribble/Coracle complexes, RhoGTPases and phospholipids (Rodriguez-Boulan and Macara, 2014). Maintenance of cell polarity is tightly connected to cell-cell adhesion (Desai et al., 2009), vesicle trafficking (Polgar and Fogelgren, 2017), cell division (Panbianco and Gotta, 2011) and is emerging as an important feature to regulate cell fate, normal cell-based functions and proper localisation of potentially harmful molecules. This

self-organisation is based on intracellular signals and RhoGTPases, especially Rac1 has been involved as a regulator of cell polarity (Mack and Georgiou, 2014).

During the establishment of apico-basal polarity, Rac1 signalling allows proper lumen formation (O'Brien et al., 2001). Interestingly, Rac1 activity is not homogeneous along the apico-basal axis (High activity at basolateral – Low activity at apical). Creation of this gradient is based on differential activity of the RacGEF Tiam1, which gets baso-laterally activated by β2-syntrophin while the GEF activity is inhibited by the apical junctional complex and Par3 (Mack et al., 2012). Mis-activation of Rac1 using an apical-targeted Tiam1 in a 3D cyst system, results in the accumulation of cells within the cyst lumen and loss of tight junctions (Yagi et al., 2012b). So this differential expression has directly been linked to the ability of 3D cultured cysts to polarise a lumen (Mack et al., 2012; Yagi et al., 2012b). This gradient has directly been visualised using FRET probes and was shown to be crucial for cyst structure, epithelial cell shape and monolayer integrity (Couto et al., 2017; Yagi et al., 2012b). However a Rac1 gradient does not seem to be present during early cystogenesis event (Yagi et al., 2012b), suggesting that it might be dispensable during early cyst formation but important for its maintenance and may send signals to specific downstream effectors.

1.4 The Scar/WAVE complex and its regulators

1.4.1 The Scar/WAVE complex

WRC (WAVE regulatory complex) is a heteropentameric complex of ~400kDa and organised around 5 proteins Nap1, Cyfip1, Abi2, Hspc300 and Wave1 proteins (Eden et al., 2002; Gautreau et al., 2004).

The crystal structure completely changed the understanding of the complex organisation, which at the time was mostly based on biochemical experiments (Chen et al., 2010) (**Figure 1.9**). The current model includes a dimeric platform created by Nap1 and Cyfip1 forming a cradle, acting to recruit a trimer formed by Hspc300, Abi2 and WAVE1 where the VCA interacts at the surface of Cyfip1. In this state, *in vitro* assays show that WRC doesn't have an activity toward the Arp2/3 complex, suggesting an autoinhibitory conformation (Derivery et al., 2009a; Ismail et al., 2009). However, addition of Rac loaded with a GTP analogue but not GDP, is able to activate the WRC (Eden et al., 2002; Ismail et al., 2009). It is worth mentioning that the crystals obtained by Chen *et al* are a modified version of the actual WRC and thus might prevent elucidating the fine details of some of the interaction of the subunits. Indeed, the C-terminal proline rich region and the SH3

domain of Abi2 were deleted, and the proline-rich region of WAVE1 was replaced with a 18-mer linker (Chen et al., 2010). Intact structural characterisation still awaits other methods such as Cryo-EM, which might supplement this crystal structure with more details.

Regulation of the WRC will be discussed in further detail but together these observations plus the fact that WAVE proteins do not contain a GTPase binding domain, support the idea of different mechanisms mediating WRC-dependent Arp2/3 activity. In order to get a global picture of this process, it is therefore important to reveal some features of each of the subunits of the complex.

1.4.2 Characterisation of the WRC subunits

1.4.2.1 CYFIP1/2 (Sra1 and PIR121 respectively)

CYFIP1 (cytoplasmic FMR-interacting protein) was isolated from bovine brain extracts as a specific Rac1 interactor. CYFIP also goes by the names: Sra1 standing for Specifically Rac1-associated protein and PIR121 (p53-inducible RNA). Truncated mutants of the protein suggested interaction of RAC1 near the N-terminal region and showed that this interaction promoted colocalisation of both proteins at cell ruffles (Kobayashi et al., 1998).

CYFIP1/2 are large proteins of ~145kDa with 88% identity and are highly conserved. Both isoforms have a Fragile X interacting protein domain at their C-terminus, mediating interactions with Fragile X-related proteins and have been involved in mental retardation anomalies (Pathania et al., 2014). Consistent with this neurological effect, CYFIP1 and CYFIP2 are expressed during brain development, although showing different patterns (Bonaccorso et al., 2015). Moreover, CYFIP1 has been involved in protein anabolism via its interaction with eIF4E (Napoli et al., 2008) and also as a regulator of the mTOR pathway in neuronal progenitors (Oguro-Ando et al., 2015). CYFIP1/2 are also characterised by a DUF1394 domain (Domain of unknown function), running across the first 300 amino acids. This domain is highly conserved and Pfam alignments suggest that is only shared with another protein family named FAM49 proteins (see section 1.5).

In addition to their functions in the nervous system, CYFIP proteins are key players in actin dynamics due to their central role in the WRC. Indeed, CYFIP1 depletion leads to the disruption of the complex, probably suggesting a structural function for the complex integrity (Tang et al., 2013). Interestingly, depletion of CYFIP2 doesn't affect the complex formation, possibly reflecting a distinct function of this isoform, at least in the cell types

tested thus far (Tang et al., 2013). Alternatively, it can also be claimed that CYFIP2 is only a minor component, while CYFIP1 is the most abundant form and is responsible for the WRC function. The WRC structure suggested a mechanism for the activation of the complex involving CYFIP1 playing a major role. It was proposed that active Rac1 could bind to CYFIP1 and causes a conformational change that displaced the VCA motif of WAVE1, which was previously hidden within the inactive complex (Chen et al., 2010).

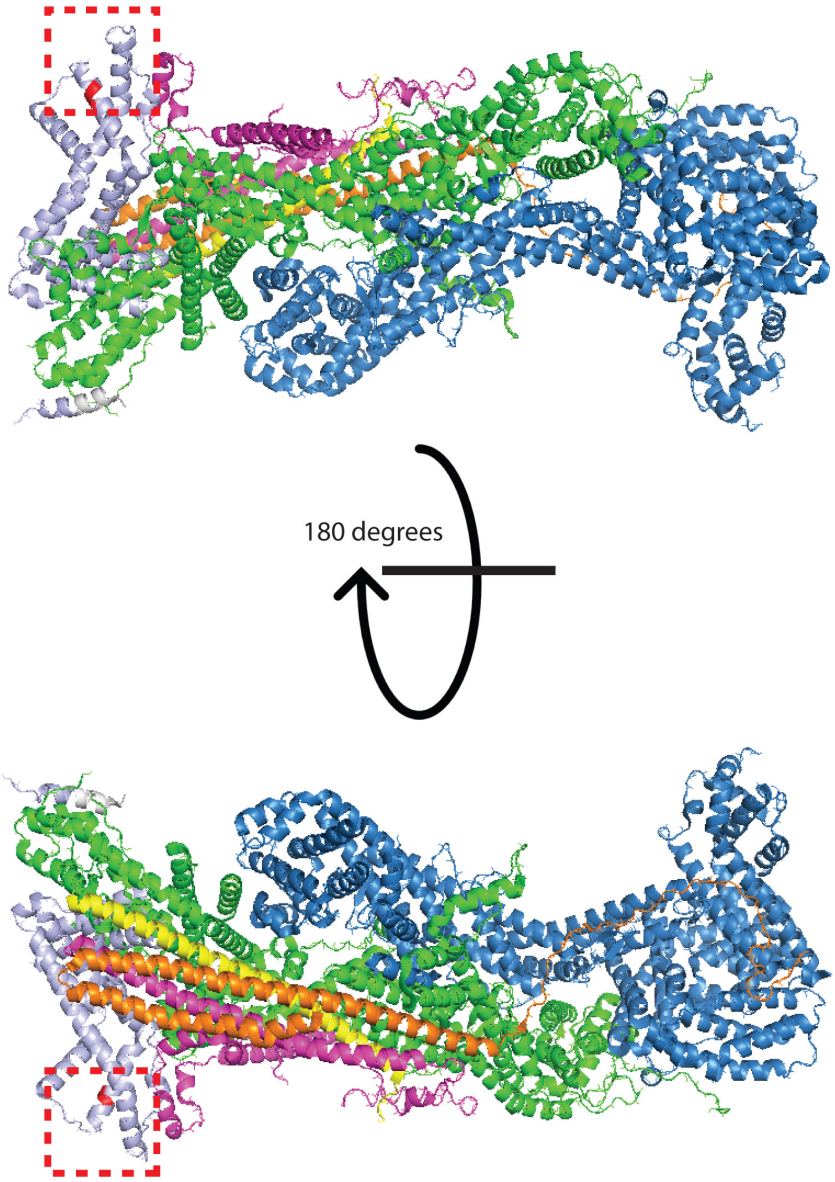

Figure 1-9: Structure of the Scar/WAVE complex
Ribbon structure of the Scar/WAVE complex represented as a front (top) and back (bottom) view. Figure was obtained from the published structure of the Scar/WAVE complex (PDB 3P8C) (Chen et al., 2010) using PyMol. Each subunit was assigned a specific colour: NAP1 (blue), CYFIP1 (green and lilac), Scar/WAVE (Pink), HSPC300 (yellow), ABI (orange). DUF1394 domain of CYFIP is highlighted in lilac. Red dotted square represents the region of CYFIP involved in Rac1 binding.

Point mutations along CYFIP1 sequence identified at least 5 critical residues required for Rac1 binding. Spatially, those residues form a tight pocket at the surface of an exposed part of the complex, where Rac1 could easily fit in (Chen et al., 2010) (**Figure 1.9**).

In cells, CYFIP1 localises at the cell edge with other WRC members, consistent with a role in membrane protrusions (Steffen et al., 2004) and also drives force translocation during *D. melanogaster* egg chamber rotation (Cetera et al., 2014; Squarr et al., 2016). The interpretation of data on the role of WRC in cancer cell invasion is however less clear than its established role in migration. Silva *et al* (Silva et al., 2009) reported CYFIP1 as a putative negative regulator of invasion. Looking at human cancer tissues, the authors anti-correlated CYFIP1 expression to tumour progression. This was confirmed with subcutaneous injection of *cyfip1*-knockdown transformed cells. However, the cooperation between CYFIP1, WAVE3 and Nap1 was recently shown to promote breast and prostate cancer invasion making unclear the exact involvement of CYFIP proteins during invasion (Teng et al., 2016a; Teng et al., 2016b). These differences may reflect other functions of CYFIP1/2 independently of its role in the WRC or can also be tissue-dependent.

1.4.2.2 NAP1

As its name suggests, NAP1 (Nck-associated protein 1) was identified as a binding partner of Nck (Kitamura et al., 1996) and in collaboration with CYFIP1, forms a structural base for the recruitment of the remaining WRC subunits.

NAP1 also localises at the cell edge in mammal cells and is required to sustain lamellipodia formation (Steffen et al., 2004). NAP1 plays a role in motility and cell adhesion in *D. discoideum* partially mediated by the Scar/WAVE complex itself (Ibarra et al., 2006). An *in vivo* study in mice shows that constitutive deletion of NAP1, correlates with a loss of other WRC member and leads to midgestation lethality with failure in the organisation of the main embryonic tissues (Rakeman and Anderson, 2006). This is supposed to be directly linked to a defect in cell migration during embryonic development.

However, NAP1 does not always seem to promote cell migration and the level of expression has to be tightly regulated. Indeed, ectopic expression of NAP1 stops cells from migrating and induces differentiation (Yokota et al., 2007). This might reflect a broader function of NAP1 in WRC-independent processes. Alternatively, too much NAP1 might disrupt the equilibrium of the complex as a whole and could be destabilised. We can also not exclude the fact that NAP1 on its own could aberrantly sequester a binding partner of

the WRC and thus act as a dominant negative. Those are just hypothetical mechanisms that could explain their result.

1.4.2.3 ABI1/2/3

ABI proteins (ABL interactor) were found as binding partners of the ABL tyrosine kinase in murine leukaemia cells (Shi et al., 1995) and play roles as scaffolding proteins. They are organised around an SH3 domain mediating the interaction with ABL and several proline-rich domains interspersed with tyrosine residues, which can be phosphorylated and regulate protein activity.
Given this direct interaction, ABI proteins play an important role in leukaemia (Chorzalska et al., 2014; Dai et al., 1998; Li et al., 2007; Yu et al., 2008). Indeed, leukaemia arises from the translocation between 2 regions from chromosome 9 and chromosome 22 (respectively encompassing the *abl1* and *bcr* genes), resulting in a fusion gene called Bcr-Abl, or Philadelphia chromosome. This leads to the uncontrolled expression of the tyrosine kinase pathway, activating downstream proliferation-related signalling. Moreover, ABI1 has also been linked to other cancer types. For example, it has been shown to induce invadopodia formation during breast cancer progression (Sun et al., 2009).

Although the role of ABI proteins is crucial in Bcr-Abl-driven leukaemia by diverse mechanisms, it exists in a strong collaboration with the WRC. Indeed, ABI proteins have a pivotal role and can either be found free, as a subunit of WRC or in complex with ABL. This is partially regulated by another adapter protein called CRK. CRK competes with ABI1 for the binding to ABL, and a high level of CRK displaces the equilibrium toward CRK-ABL complexes, leaving more ABI1 available to be integrated into the WRC. In light of this dual function, deregulation of either protein can affect actin polymerisation and cell motility. CRK expression is affected in various cancer types (Miller et al., 2003; Sriram and Birge, 2010; Wang et al., 2007) but these studies focused on the ABL-dependent role of CRK and did not make a connection with the WRC. Involvement of ABI as a fully functional member of the WRC comes from mass spectrometry data and *in vitro* binding assay combined with *in cellulo* experiments (Innocenti et al., 2004).

Finally, homozygote *Abi1*-null embryos stop developing after E11.5 and display abnormal neural tube and heart development (Dubielecka et al., 2011). Conditional *Abi1*-knockout MEFs affects ability of these cells to form dorsal ruffles and slightly decreases wound closure. This weak effect on cell migration is quite surprising as the WRC integrity is

compromised upon Abi1 loss. However, ABI2 and WAVE3 expression significantly increase and may offer partial compensation, although upregulation of both isoforms is not sufficient to reconstitute the complex (Dubielecka et al., 2011).

1.4.2.4 HSPC300/BRICK1

HSPC300 (Haematopoietic stem/progenitor cell protein 300) is the smallest member of the Scar/WAVE complex but plays important roles for the complex formation and its activity. Initial studies showed the role of plant homologue of HSPC300, BRICK1, as a regulator of epidermal cell shapes in maize (Frank and Smith, 2002) and in *A. thaliana* (Djakovic et al., 2006). This phenotype is dependent on the activity of the Arp2/3 complex, SCAR1 and SCAR2 (Djakovic et al., 2006; Le et al., 2006).

The central domain of HSPC300 forms an alpha helix, overlapping at the C-terminus with a coiled-coil region. The latter was shown as an important motif to promote the formation of a free homotrimer, initiating the formation of the WAVE complex (Derivery et al., 2008). Supporting this observation, structure of the full complex shows that 3 helixes coming from HSPC300, WAVE and ABI form a stable core (Chen et al., 2010). This would suggest that the trimeric form of HSPC300 might recruit WAVE2 and ABI step by step, forming a structure stable enough to further recruit NAP1 and CYFIP1. However, there exists a dynamic equilibrium between the trimeric and the monomeric form (Linkner et al., 2011) but how this switch is regulated remains speculative although posttranslational modifications have been suggested as putative regulators (Derivery et al., 2008).

HSPC300 functions in actin regulation driven by the WRC are conserved in *D. discoideum*, *D. melanogaster* and in mammal cells (Derivery et al., 2008; Kunda et al., 2003; Pollitt and Insall, 2009). Unlike CYFIP1, which was surprisingly proposed as a tumour suppressor (Silva et al., 2009), loss of HSPC300 decreases cell proliferation and migration. Invasion and metastasis formation in a tail vein assay are also impaired. In parallel, *hspc300*-null embryos are undersized compared to their wild type counterpart and show early lethality, correlating with actin disorganisation, loss of cell compaction and increased apoptosis (Escobar et al., 2010).

1.4.2.5 Scar/WAVE proteins

Scar/WAVE proteins are the major NPFs stimulating Arp2/3 and mediating lamellipodia formation and extension. WAVE1 was discovered at the same time by 2 independent

groups aiming to find new WASP-like proteins (Machesky and Insall, 1998; Miki et al., 1998). WAVE1 has been linked to membrane ruffling in a Rac1-dependent manner (Miki et al., 1998) whereas Machesky and colleague made a strong link between Scar/WAVE1 and its ability to bind to G-actin and the Arp2/3 complex (Machesky and Insall, 1998). Together, they drew a good picture of the important actors regulating WAVE-dependent processes (see section 1.4.4).
Scar/WAVE proteins are similarly organised with a conserved WAVE-homology domain mediating the binding to other WRC subunits, a basic domain ($PI(4,5)P_2$ and other phospholipids binding) followed by a proline-rich domain and the VCA motif (Kim et al., 2000). Unlike WASP proteins, they are not autoinhibited and follow a trans-regulation as part of the WRC.

WAVE proteins are very well conserved (Kurisu and Takenawa, 2009). WAVE1 and 3 show specificity to the brain and hematopoietic cells respectively whereas WAVE2 seems ubiquitously expressed. Interestingly, plants have an additional SCAR member (SCAR4) that reflects a divergent evolution of the Scar gene following successive gene duplications (Zhang et al., 2008a). Moreover, in this study, activity of the VCA motif was drastically different compared to the other Scar proteins used in the pyrene actin assay. This could suggest the need of different actin polymerisation efficiency in specific compartment. However in mammals, it is believed that all isoforms of Scar/WAVE are part of a functionally similar complex (Stovold et al., 2005) but functions of each isoform have not been deeply studied. For example, WAVE3 was linked to lamellipodia stability and persistence of cell migration (Spence et al., 2012). WAVE3 knockdown cells showed a reduced speed of migration but had no effect on invasion, which tends to reaffirm a potential role of tumour suppressor of the WRC.

As previously mentioned, WAVE1 becomes restricted to the central nervous system during development. Disruption of the WAVE1 gene in mice is not embryonic lethal but severely compromises the lifespan (Dahl et al., 2003). Indeed, WAVE1 knockout (KO) mice die within 3 weeks after birth, correlating with loss of weight and cortex hypotrophy, which usually show high WAVE1 expression in normal individuals. However, primary neuronal cultures from wild-type or *Wave1* KO embryos don't show any striking differences in their ability to grow, polarise or form neurites, which emphasises the difficulties to equate findings made *in vitro* to *in vivo* (Kim et al., 2006). On the other hand, WAVE1 plays only a partial role during oligodendrocyte morphology and myelinisation of specific regions of the brain, affecting ion channel clustering (Kim et al., 2006).

Similarly to the Arp2/3 isoforms affecting actin nucleation in different ways, future studies should aim to link Scar/WAVE protein isoforms within the complex and their specificity in regulating actin polymerisation.

1.4.3 Other function of Scar/WAVE complex

Additional to its role in Arp2/3 activation that has already been emphasised, Scar/WAVE complex activity may also regulate actin cytoskeleton by a less direct way than via Arp2/3 activation. Indeed, WRC can bind to a specific sequence present in a large family of membrane-associated/transmembrane proteins (WIRS standing for WRC interacting receptor sequence). Among the WIRS-containing proteins, protocadherins 10 and 19 are transmembrane proteins involved in cell-cell adhesion and have been previously confirmed to interact with the WRC (Nakao et al., 2008). Chen *et al* gave evidence that the interaction between WIRS-containing proteins and the WRC is mediated by Sra and Abi and structural analysis shows that it does not displace the VCA tail of WAVE1. In line with this observation, WIRS-containing peptides are not sufficient for WRC/Arp2/3 activation, although, addition of Rac1 shows a partial effect, suggesting that WIRS binding might prime the WRC for activation. Disruption of this interaction affected actin organisation and normal oogenesis in flies (Chen et al., 2014a) and other functions are still waiting for further characterisation.

The mechanisms of activation of the complex have to be solved. On one hand Scar/WAVE proteins are not autoinhibited but on the other hand, the WRC complex itself is inactive, meaning that other signals are required to release the VCA C-terminal tail of the Scar/WAVE proteins, responsible of the stimulation of the Arp2/3.

1.4.4 Regulation of the Scar/WAVE complex

1.4.4.1 Rac1

Prior to the understanding of the relation between the WRC and the mechanisms of actin polymerisation, a member of the complex was already linked to Rac1. Indeed, almost 20 years ago, Kobayashi *et al* (Kobayashi et al., 1998) showed a direct interaction between the first 300 amino acids of Sra1/CYFIP and GST-Rac1 loaded with GTPγS but not with GDP. This shows a specificity of binding to the active Rac1, which was previously shown to induce membrane ruffles (Ridley et al., 1992). At this time though, the connection with the Scar/WAVE complex was not made.

In the most recent structure of the complex, active Rac1 interaction with the Scar/WAVE complex was estimated to be low affinity (~8 μM) (Chen et al., 2010). Moreover, cutting off the VCA from the complex improves the binding to 1 μM, suggesting that Rac1 and the VCA might compete with each other. Although we are still missing a structure of the active WRC, it is hypothesised that binding of Rac to CYFIP1 destabilises the interaction between the VCA and the surface of CYFIP1, exposing the VCA out from the complex and making it free to interact with the Arp2/3 complex (Chen et al., 2010; Davidson and Insall, 2011).

However, a binding affinity of few micromolar is not considered as very high and other factors cooperating with Rac1 have been examined. For example, Arf GTPases collaborate with Rac1 to activate purified WRC in a lipid-coated beads assay (Koronakis et al., 2011). This finding might also have a bigger impact in the current view of the spatial activity of the WRC. Indeed, Arf signalling predominantly regulates Golgi morphology and trafficking (Gaynor et al., 1998), suggesting that WRC might also be important to mediate Arp2/3-dependent actin polymerisation away from the plasma membrane.

Another link between Rac1 and the WRC was initially proposed to be IRSp53 (insulin receptor substrate protein of 53kDa). It was shown that IRSp53 binds concomitantly to Rac1 at its N-terminus and to WAVE via a C-terminal SH3 domain (Miki et al., 2000). This model was challenged by another study showing that the complex, which co-eluted with other components (including IRSp53) was totally inactive regarding Arp2/3 complex (Lebensohn and Kirschner, 2009).

1.4.4.2 Phospholipids

WRC acts just below the plasma membrane, which contains a full repertoire of lipids, mostly phosphatidylcholine. Among them, phosphatidylinositols have been extensively studied for their role as second messengers, able to interact with cytosolic proteins. They can be phosphorylated at different locations, resulting in a full combination of molecules that can activate different pathways, including the cytoskeleton. Their role as partner for the activation of the WRC has been studied in different *in vitro* systems, involving beads coated with different concentration/composition of lipids mixed with crude cell extract. *In vitro*, Rac1/WAVE pathways were shown to be important for PI(3,4,5)P_3-dependent actin comet motility assay (Koronakis et al., 2011). Indeed, WAVE2 can bind to PIP_3 via its N-terminal domain, which is sufficient to localise the protein at the membrane. Conversely, a WAVE2 mutant defective in PIP_3-binding is unable to induce lamellipodium formation

after Rac1 activation (Oikawa et al., 2004), emphasizing the direct role of PIP_3 for the WRC activation.

PIP_3 can also directly bind to IRSp53, and plays an important role in the co-activation of the WRC with Rac1. However, PIP_3-mediated activation of the WRC complex is independent of the formation of the complex (Suetsugu et al., 2006). Also, independently of their direct role as activator of the WRC, PIP_3 is also required downstream from tyrosine kinase receptors, for the GEF-mediatied activation of Rac1, resulting in more active Rac1 and the creation of a positive feedback loop (Innocenti et al., 2003; Welch et al., 2003). This can directly feed the activation of the WRC. However, the exact role of the PIP pathway in migration is still matter of debate. *D. discoideum* lacking all enzymes required for PIP_3 generation still chemotax toward cAMP, although mean velocity was slightly affected (Hoeller and Kay, 2007). This mutant could polymerise actin as efficiently as the wildtype strain. So together, active Rac1 and PIP_3 might play important functions for the complex activation in higher eukaryote but mechanisms involving PIP signalling remain unclear.

Finally, physical properties of the plasma membrane lipid bilayer may also have a role for the organisation of the complex below the plasma membrane. Indeed, in the actual model based on Chen's structure (Chen et al., 2010) it was proposed a distribution of basic charges all along the surface of CYFIP1 and NAP1, which can interact with the negatively charged PIP_3 and orientate the complex in a way that makes the VCA accessible. However, it is still unclear whether the small amount of PIP_3 compared to other phosphorylated forms, is enough for explaining the regulation of the complex activation in a structural point of view. Indeed, PIP3 represents roughly ~2% of the plasma membrane composition and this raises the question whether PIP3 patches *in cellulo* might be used by the cell to trigger PIP3-dependent WRC activation.

1.4.4.3 Lamellipodin

Lamellipodin was found from a screen aiming to find new regulators of the Ena/VASP family containing proline rich domains. It harbours a Ras-association motif and a PH-domain that could mediate the binding to the plasma membrane. In addition, putative SH3 domains and profilin binding sites were described. Microscopy analysis showed that lamellipodin expression correlates with lamellipodium dynamics. Knockdown cells have a defect in lamellipodium formation and F-actin content, although total actin was not

affected. This suggests a role of Lamellipodin in regulation of actin polymerisation at the lamellipodia (Krause et al., 2004).

Mechanistically, three C-terminal regions interact with the SH3 domain of ABI1, in an active Rac1-dependent fashion, confirming that lamellipodin is a new partner of the Scar/WAVE complex. Further *in vivo* characterisation shows that Lamellipodin-KO mice are viable, although most of the homozygote mice either die within 6 weeks or are infertile. In either case, animals show a 20% reduction of their body weight (Law et al., 2013). Lamellipodin also affects melanoblast migration in mouse embryos resulting in a pigmentation defect of the adult animal. Lamellipodin functions as regulator of the Scar/WAVE complex activity, which is also conserved in *Xenopus* and *Drosophila* (Law et al., 2013).

Finally, Lamellipodin expression correlates both with metastatic potential and breast cancer survival (Carmona et al., 2016). Distinct signalling pathways from ABL and SRC kinases lead to differential regulation of lamellipodin and together with Scar/WAVE and Ena/VASP, promotes invadopodia precursors formation and/or maturation/stabilization, leading to increase invasion *in vitro* (Carmona et al., 2016).

1.4.4.4 Nance-Horan syndrome (NHS)

NHS proteins (Nance-Horan syndrome) have been linked to cataract and dental defects, dysphormism, which are characteristic abnormalities of this syndrome (Toutain et al., 1997). These defects are directly linked to mutations within the NHS gene that result in a frame shift and a truncated protein (Coccia et al., 2009; Tian et al., 2017). The wild-type gene produces different isoforms of the NHS proteins, although functions of each isoform have yet to be fully studied. NHS proteins localise to cell-cell junction, at focal adhesions, and translocate to the lamellipodium upon EGF stimulation. They contain a Wave-Homology domain (similar to WAVE proteins) able to recruit the other members of the Scar/WAVE complex. In addition, depletion of NHS leads to increase spreading correlating with an accumulation of Scar/WAVE complex members at the leading edge (Brooks et al., 2010). Therefore, NHS proteins also regulate actin-based protrusions via the WRC.

1.4.4.5 Post-translational modifications of the WRC

Phosphorylation events of WRC members affecting actin polymerisation were described far before understanding the global mechanism. WAVE2 is the principal modified protein and phosphorylation is able to optimise the activity of the WRC. Interaction between ABI1

and WAVE2 promotes their localisation to the plasma membrane, followed by recruitment of the Abl kinase, which in turn phosphorylates Tyr150 of WAVE2 (Tyr151 of WAVE1). Moreover, Abl kinase is able to further stimulate the ability of WRC to activate Arp2/3 (Leng et al., 2005). Based on Chen et al's model (Chen et al., 2010), Tyr151 is proposed to hold the meander region in close contact to CYFIP1. Phosphorylation would destabilise this interaction, leading to the expulsion of the VCA from the core of the complex. Indeed, the phospho-mimetic WAVE2 mutant increased lamellipodia formation and Arp2/3-dependent actin-polymerisation. Other residues of WAVE proteins can be phosphorylated by different kinases and work in common to affect actin dynamics by regulating Arp2/3 interaction (Ardern et al., 2006; Krause and Gautreau, 2014; Miyamoto et al., 2008). Independently, these signals don't dramatically affect the activity of the WRC. However, together, they co-amplify and fine-tune the activity of the complex (Lebensohn and Kirschner, 2009).

However, to date, direct negative regulation of the Scar/WAVE complex has barely been addressed and the only way for a cell to turn the complex off, is to directly modify Rac1 activity (via GEF, GAP, or GDI signalling) or to target the complex to the proteasome pathway. Here, we thus sought to find new regulators of the Scar/WAVE complex.

1.5 FAM49 family: Characterisation & functions

1.5.1 Discovery and organisation

FAM49 (Family of unknown function 49) was retrieved from a pulldown experiment in *Dictyostelium discoideum (D.d)*, aiming to characterise new Scar/WAVE complex interactors that could be considered as putative regulators (Fort et al, in revision) (**Figure 1-10**). GFP-transfected wild-type cells or GFP-NAP1 rescued *napA* knockout cells were lysed and cross-linked, followed by GFP-pulldown and mass spectrometry analysis. Reversible crosslinking allowed stabilisation of weak and transiently associated proteins, increasing the sensitivity of the screen to identify novel interacting candidates. Unsurprisingly, the 4 members of the Scar/WAVE complex co-precipitated with GFP-NapA and represented the most enriched hits (SRA1, ABI1, WAVE2 and HSPC300). Among the other significantly enriched candidates, VASP came down and was previously shown to interact with ABI1 (Chen et al., 2014c), giving us more confidence about the experimental design. Although not massively enriched, FAM49 was consistently pulled-down in the 4 independent biological replicates. The absence of information about this

protein was seen as a challenge and Batista and co-workers decided to focus on FAM49. We joined in as collaborators to characterise the role of mammalian FAM49B, which is the main topic of my PhD thesis.

FAM49 is a small protein of ~37 kDa with no previously described functions, domains or structure at the time of this screen. However, initial sequence alignments showed a very high conservation across evolution, especially in the metazoan phylum, highlighting an underestimated importance of FAM49. In vertebrates, 2 different genes encode for 2 specific isoforms (FAM49A and FAM49B), sharing 80% identity and 90% similarity. Pfam searches (Finn et al., 2014) revealed that FAM49 proteins contain a unique domain named DUF1394 (domain of unknown function 1394). Interestingly, this domain is commonly shared with CYFIP proteins and overlaps with some portions of the Rac1-binding site as described by Chen et al (Chen et al., 2010) (**Figure 1-11**). Multi sequence alignment pinpointed a 30 residues stretch with high conservation between FAM49 homologues and also between DUF1394 domains of FAM49 and CYFIP proteins. Interestingly a Y-Y/F-RR motif stands out from the alignments. The second arginine is involved in Rac1-binding in CYFIP1 and required for WRC activation (Chen et al., 2010). Moreover, the structure of FAM49 has not been solved yet but a prediction tool based on multi-alignment and available protein structures database (i-TASSER) (Roy et al., 2010) considered CYFIP1 as the best template for FAM49 (**Figure 1-11**). Interestingly, a portion of FAM49B perfectly maps onto the pocket formed by Cyfip1 at the surface of the Scar/WAVE complex (PDB 3P8C) (Chen et al., 2010), where Rac1 fits. FAM49 putative structure suggests a fairly compact core made by successive alpha helixes. This contrasts with the N-terminal part of the protein that forms a short alpha helix followed by an unfolded region, which would stand out from the overall structure by its apparent flexibility.

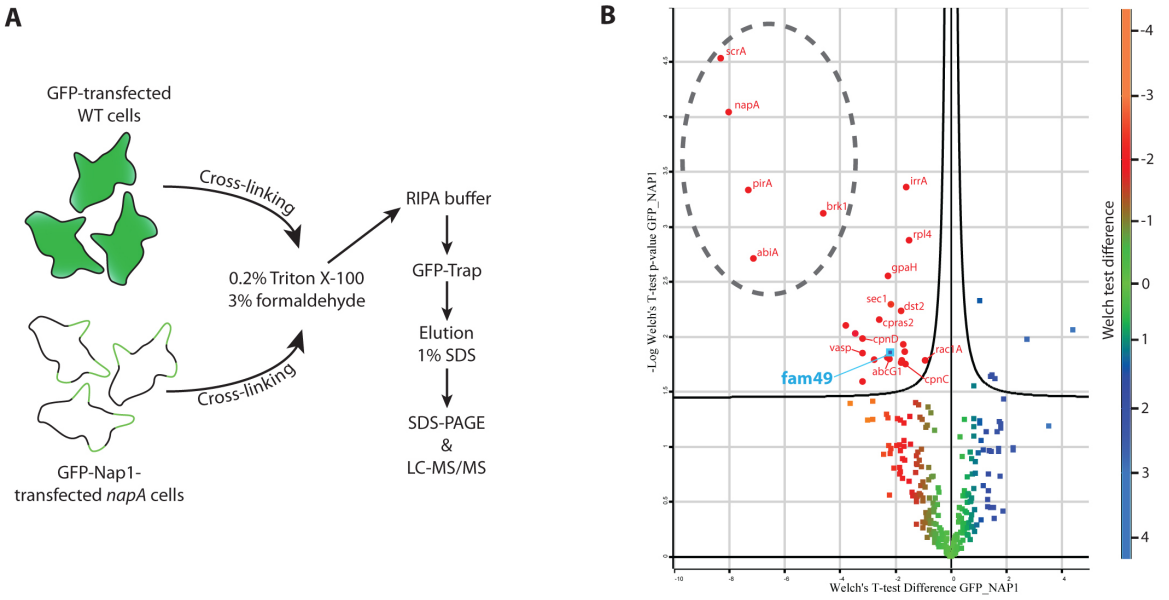

Figure 1-10: Discovery of FAM49 in *D. discoideum*
A – Schematic of the experimental design of the crosslinked GFP-Pulldown. Wild-type or *napA* knockout Ax3 cells were transfected with GFP or GFP-NAP1 respectively. Cells were lysed using a low concentration of detergent buffer complemented with 3% formaldehyde for the reversible crosslinking. GFP-tagged proteins were immunoprecipitated, resolved by SDS-PAGE and gels analysed by LC-MS/MS.

B – Volcano plot from pooled replicates of the mass spectrometry experiment. Significant hits lay above the 5% false-discovery rate curve (black curve) and are represented with red dots. Gene name is reported for some candidates. Scar/WAVE complex members represent the top hits and are highlighted with a dotted circle. FAM49 is represented in blue. Colour scale is based on the Welch's test difference.

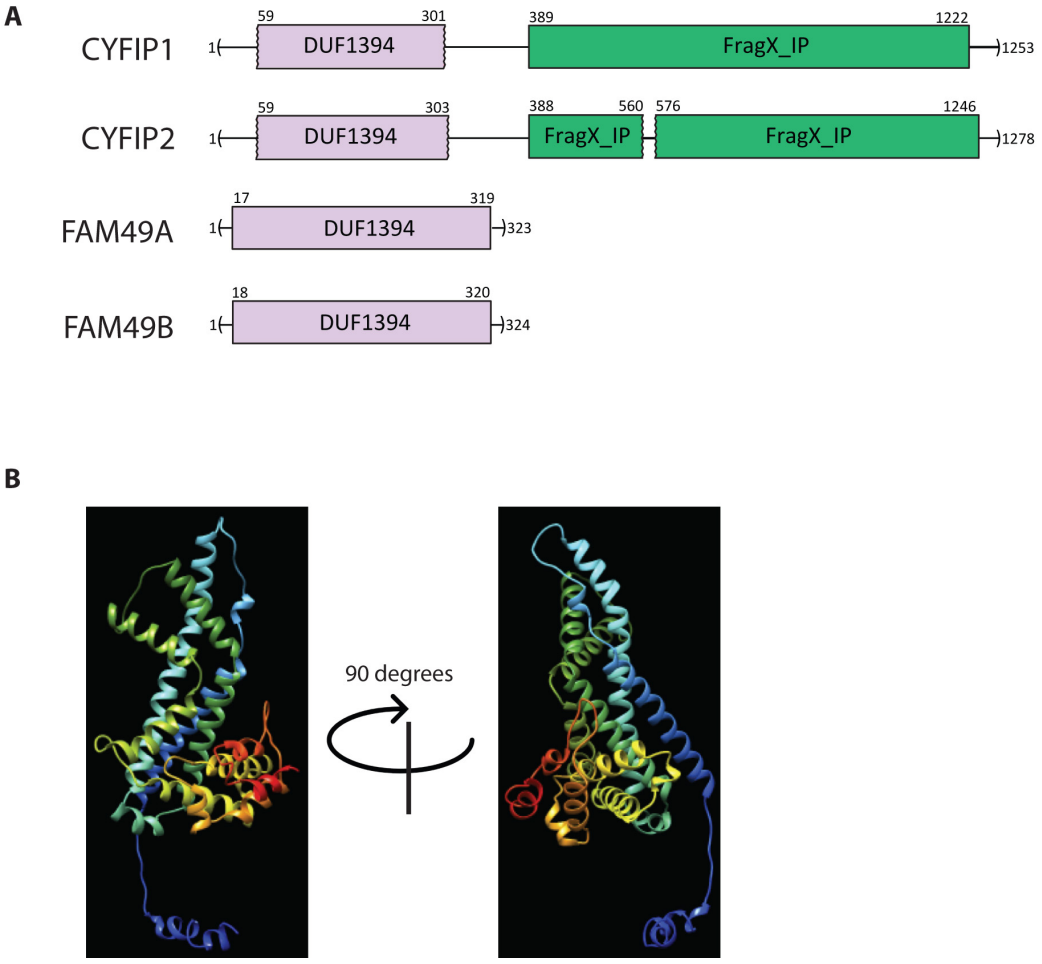

Figure 1-11: Organisation and structure of FAM49 proteins
A – Side by side comparison of the organisation of CYFIP1/2 and FAM49A/B. DUF1394 domain (Pfam PF07159) is shared between CYFIP and FAM49 proteins and is represented in lilac. Fragile X mental FMR1-interacting domain (FragX_IP, Pfam PF05994) is unique to CYFIP proteins and shown in green. Numbers represent position of the amino acid across the protein sequence based on Pfam.

B - i-TASSER prediction structural model for human FAM49B. Two views are displayed, corresponding to a rotation of 90 degrees. The best template for this structure corresponds to the PDB entry 3P8CA (CYFIP1) with a TM-score (template modelling score) of 0.873. TM-score is a read out for the structural similarity between two proteins. It ranges from 0-1 with high value corresponding to better similarity. It is widely accepted that a TM-score above 0.5 corresponds to protein with a similar structure (Roy et al., 2010)

The model is colour coded from blue (N terminus) to red (C terminus).

1.5.2 FAM49A

FAM49A is localised on chromosome 2 and just one study has been published describing its function so far. FAM49ab (homologue of human FAM49A) was recently described as a negative regulator of PTEN (Phosphatase and Tensin homologue) signalling during zebrafish development (Li et al., 2016). PTEN is a major tumour suppressor by promoting differentiation and inhibiting proliferation in collaboration with PI3K. PTEN is frequently lost in lymphoid cancers but its roles during lymphopoiesis were unknown. Authors found that N-myc downstream-regulated gene 1b (Ndrg1b) could rescue PTEN loss during thymocyte development (Li et al., 2016). Database searches orientated toward *Danio rerio* FAM49ab as a conserved interactor of Ndrg genes, in *zebrafish* and *C. elegans*. *In situ* hybridisation revealed that FAM49ab is expressed at early developmental stage in the somites, eyes and neural crest before being expressed in the ventral aorta. Later, the transcript is found in the thymus and was confirmed by isolation of thymocytes and lymphoid precursors followed by qRT-PCR. Overexpression of FAM49ab affects differentiation of thymic precursors and blocks T-cells differentiation, mimicking the loss of PTEN. Interestingly, co-overexpression of FAM49ab and Ndrg genes or inhibition of PI3K signalling rescues this phenotype. Finally, over expression of FAM49ab synergises with the effect of Ndrg1b knockdown on T cell differentiation.

Together, their model suggests that FAM49ab interrupts PTEN signalling by inhibiting Ndrg1b (Li et al., 2016) (**Figure 1-12**). However, involvement of FAM49A in cancer is still waiting for further investigation but analysis of FAM49A gene alteration in humans doesn't seem to be hugely affected across different solid and blood cancers (cBioPortal).

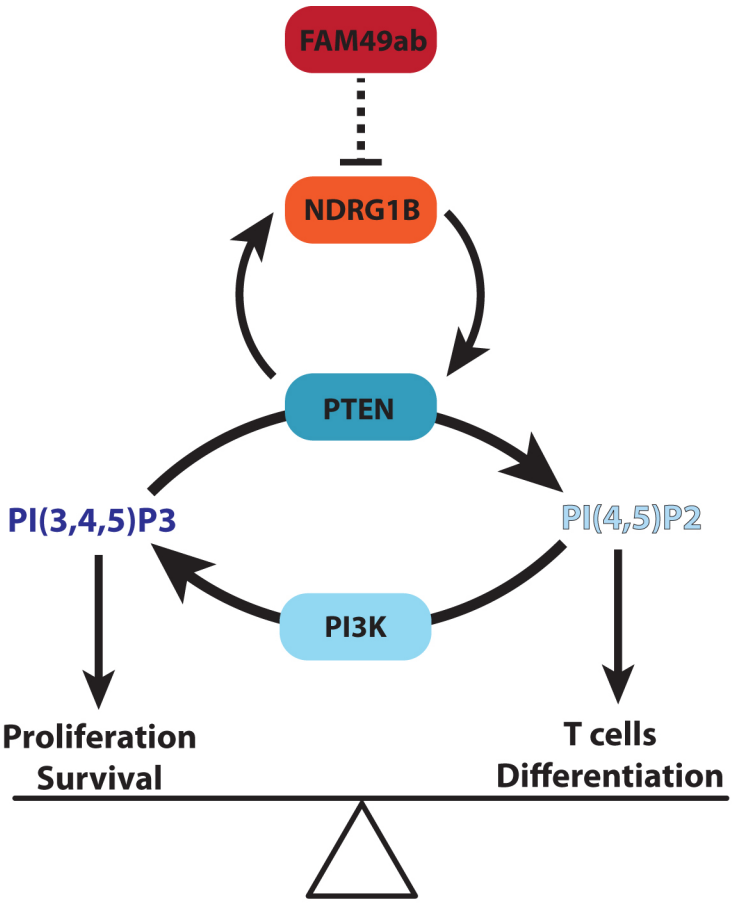

Figure 1-12: Model of regulation of T cell differentiation by *D. rerio* FAM49A

FAM49ab (*D. rerio* FAM49A) was shown to be a negative regulator of PTEN signalling in zebrafish. Based on genetic evidence, model depicts FAM49ab upstream of N-myc downstream-regulated gene 1B (NDRG1B), together regulating lymphoid differentiation. Figure inspired by (Li et al., 2016)

1.5.3 FAM49B in the literature

FAM49B is localised on chromosome 8 and interestingly is amplified in a large subset of cancers (cBioPortal). For example, 50 % of the breast cancer samples available on the database display an amplification of the gene. Although this might be meaningful, one could also hypothesise that this amplification reflects the close proximity of FAM49B gene with the widely amplified oncogene Myc, as both genes are situated next to each other on chromosome 8, resulting in a passive amplification of the *fam49b* gene. To support this hypothesis, cBioPortal analysis reveals a strong and significant correlation of co-alteration between both genes. Nevertheless, one cannot rule out that amplification of FAM49B is associated with cancer progression and may have a functional role.

FAM49B was also mentioned in various proteomic studies: For example, it has recently been proposed as a biomarker for oral cancer, as it has been found significantly enriched in the saliva of cancer patients. However, it cannot be used as a predictive marker associated with a risk of developing oral squamous cell carcinoma (Kawahara et al., 2016).

Additionally, FAM49B was found, among other proteins, as downregulated in omental fat from women with endometriosis (Williams et al., 2015). Unfortunately, this study doesn't bring more information about the mechanism or the biological relevance of their findings.

FAM49B mRNA also was detected as enriched in multiple-sclerosis women before and after pregnancy, whereas levels go back to similar ratio throughout the pregnancy. However, this difference was not reflected at the protein level (Gilli et al., 2010) and suggests a minor contribution of FAM49B in this system.

Finally, FAM49B has also been linked to immunosurveillance. Indeed, in normal cells, self-antigens are usually loaded onto a specific MHC-class I whereas FAM49B peptides are cleaved by the endoplasmic-reticulum specific endopeptidase ERAAP. However, ERAAP-deficient cells (cancers, auto-immune disorders to only cite some examples) cannot trim these self-antigens so a 9-amino acid peptide from FAM49B gets loaded onto the specific MHC-I and traffics to the cell surface where it mediates strong $CD8^+$ T cell response and cytotoxicity (Nagarajan et al., 2012). This mechanism, mediated by a region of FAM49B, allows monitoring the functionality of an intracellular enzyme, leading to a targeted death if the cell is deficient in ERAAP signalling. However, function related to the full-length protein has not been reported yet.

1.5.4 Biological functions of FAM49 in *D. discoideum*

Here I'm reporting the main unpublished findings of Jose Batista and co-workers regarding the study of *D.d* FAM49 in the Ax3 cell line (internal communication).

Initial characterisation of *D.d* FAM49 were realised using GFP-tagged constructs and genetic knockout of the gene. Despite a cytosolic background, spinning-disc and TIRF (Total internal reflection fluorescence) microscopy clearly revealed a polarised localisation of GFP-FAM49 at the leading pseudopod of cells migrating in a chemotaxis under agarose assay. This enrichment is maintained during the extension of the pseudopod and the signal tends to disappear just before retraction, suggesting a very dynamic and controlled localisation of FAM49. Further imaging revealed that FAM49 is highly co-enriched with the active Rac reporter Pak-CRIB but only showed a weak co-localisation with Scar. These movies suggest that FAM49 accumulation is spatially similar to Rac1 but dynamically closer to Scar. It is worth noting that *napA* knockout cells still present a specific enrichment at the pseudopods, highlighting that the Scar/WAVE complex is dispensable for the localisation of FAM49.

Finally, doxycycline-induction of active Rac1 drives the recruitment of GFP-FAM49 at the ruffling edge of the cell. Interestingly, the majority of the population shows homogenous localisation of active Rac1 reporter around the cell edge whereas FAM49 is more polarised. Unfortunately, in this experiment, correlation between localisation of FAM49 and cell movement or protrusion formation has not been investigated.

Disruption of the endogenous gene was performed by introduction of a blasticidin resistance cassette using homologous recombination technique, followed by clonal selection and PCR validation. Selected clones have a severe cell growth defect both in suspension or when plated on a bacterial lawn. Moreover FAM49 knockout cells become larger over time. Together these observations suggest a defect during cytokinesis and/or phagocytosis, which is the main strategy used by the amebae to uptake nutrients.

Chemotactic development into fruiting bodies and cell adhesion were not affected upon genetic deletion of FAM49. Similarly, active Rac, Scar/WAVE, Arp2/3 and WASP localisation was similar between wild-type and knockout cells. Together, these results point toward a collaborative role between FAM49, Scar/WAVE complex and Rac for membrane dynamics and cell division, without affecting normal morphogenesis.

Because FAM49 localises at protrusive ends, Batista and co-workers were interested by the behaviour of the knockout mutants and also the rescue clone in an under agarose chemotaxis assay. Interestingly, knockout cells showed a much rounder and smooth-edged phenotype, with a decrease in membrane protrusion rate leading in overall to a slower

motility. *fam49b*-knockout cells expressing GFP-FAM49 showed a full rescue of the phenotype whereas rescue using an untagged version of FAM49 made the wild-type phenotype even worse. Indeed, untagged rescued cells commonly exhibited split and narrow pseudopods. This may suggest an effect of the tagging strategy on the protein activity, and might provide some hints about a potential internal regulation of the protein.

In conclusion, this work strongly suggests an important role of FAM49 in the protruding behavior of *D. discoideum*, with possible cross talk with Rac signalling. The fact that FAM49 homologues are highly conserved convinced us to investigate deeper into the functions of FAM49 in mammals, especially as FAM49B antibodies were available at the beginning of the project.

1.6 Aim of the thesis

Cell protrusion is at the base of all cell motility events and is required throughout the normal lifetime of an organism but can also be altered during cancer. Indeed, a very tight balance and coordination of signals has to be processed within a range of seconds to achieve an appropriate response.

Understanding the mechanisms regulating pseudopod formation, splitting and dynamics has been an exciting challenge over the last decade and a precise vision of the main pathways has already been pictured. However, until recently negative signals involved in this process have unwisely been under estimated. Strong and elegant data from *D. discoideum* revealed FAM49 as an important partner in the loop between Rac1-Scar/WAVE complex and protrusion dynamics. Despite its extraordinary sequence conservation, FAM49B has barely been studied and so far, no function has been assigned to the full-length protein. By using different genetic approaches, biochemical strategies, imaging and 3D culture, I will attempt to address this question by deciphering the molecular mechanism(s) driving FAM49B functions.

Aims in summary:

Aim 1: Evolutionnary study of FAM49
Aim 2: Mechanistic and functional analysis of FAM49B
Aim 3: Relevance of FAM49B in 3D models and *in vivo*

In addition, Fascin is associated with cancer dissemination and invasion. As a side project, I will discuss the data obtained after Fascin overexpression in a slow pancreatic cancer mouse model and the potential involvement of Fascin during pre-malignant lesion formation.

Aim 4: Importance of Fascin 1 during early pancreatic cancereous lesion formation

2 Materials and methods

2.1 Material and reagents

2.1.1 Cell lines and bacterial strains

Table 2-1: Cell lines and bacterial strains

Name	Description & Application	Source
Mammalian cell lines		
CHL1	Human melanoma cell line	ATCC
B16F1	Mouse melanoma cell line	Prof. K. Anderson
COS-7	Monkey kidney cell line	ATCC
HEK293T	Human embryonic cell line	Prof. L. M. Machesky
MDCK	Dog kidney cell line	Dr. D. M. Bryant
Chemically competent cells		
E. Coli DH5alpha	Cloning and subcloning	Homemade
E. Coli BL21 CodonPlus (DE3)-RIL	Expression of GST-tagged proteins	Agilent #230245
E. Coli BL21 (DE3) pLysS	Expression of His-tagged proteins and inclusion body	Promega #L1195

2.1.2 Reagents and solutions

Table 2-2: Reagents and solutions

Name	Description, Composition & Application	Source
Cell culture		
DMEM		Gibco #21969-035
MEM, high glucose, high sodium bicarbonate		Gibco #A1451801
L-Glutamine		Gibco #25030-032
FBS		Gibco #10270-106
FBS TetON	Approved tetracycline-free FBS	ClonTech #631106
PBS	3.3mM KCl, 137mM NaCl, 8mM Na_2HPO_4 and 1.5mm KH_2PO_4, pH7.3	Beatson central services
2.5% Trypsin, no phenol red	Serine protease	Gibco #15090046
PE buffer	0.037% (w/v) EDTA in PBS	Beatson central services
CASYton buffer	Cell counter diluent	OLS OMNI Life Science #5651808
DMSO		Fisher Chemical #D/4121/PB08
Doxycyclin		Sigma #D9891
Hexadimethrine bromide		Sigma #H9268

Puromycin		Gibco #A11138-03
Matrix		
Fibronectin from bovine plasma		Sigma #F1141
Rat tail Collagen-I		Corning #10224442
Laminin from Engelbreth-Holm-Swarm murine sarcoma basemement membrane		Sigma #L2020
Matrigel basement membrane matrix		BD Bioscience #354234
Gelatin from pig skin, Oregon-green 488nm		Molecular Probes #G13186
Protein lysate, SDS-PAGE and Western blotting		
RIPA buffer	150mM NaCl, 10mM Tris-HCl pH7.5, 1mM EDTA, 1% Triton X-100, 0.1% SDS	Homemade
NuPAGE Protein Sample buffer 4X		Invitrogen #NP0007
NuPAGE Reducing Reagent 10X		Invitrogen #NP0004
4-12% NuPAGE Bis-Tris gels		Invitrogen #NP0321
MOPS Running Buffer 20X		Novex #NP0001
MES Running Buffer 20X		Novex #NP0002
PageRuler pre-stained protein ladder		Thermo Scientific #26616
Nitrocellulose blotting membrane	Protran 0.45µm	GE Healthcare #10600002
Transfer buffer	20% Methanol, 10% 10X SDS-blotting buffer diluted in water	Homemade
10X SDS-blotting buffer	1% SDS, 250mM TRIS and 1.92M Glycin	Beatson central services
TBS-T	150mM NaCl, 10mM Tris-HCl pH7.4, 2.7mM KCl, 0.1% Tween20	Beatson central services
Molecular biology and subcloning		
2X PrimeStar Master Mix		Takara #R045
High molecular biology grade agarose	0.8-2% final concentration	Melford #MB1200
50X TAE buffer	2M Tris, 50mM EDTA, 1M Glacial acetic acid, pH~8.3	Beatson central services
Midori green		Nippon Genetics #MG04
6X DNA loading buffer	12% glycerol, 60mM Na_2EDTA, 0.6% SDS, 0.003% bromphenol blue, 0.003% xylene cyanol, H_2O	Homemade

O'GeneRuler 1kb		ThermoScientific #SM1163
100pb DNA ladder		NEB #N3231L
L-Broth		Beatson central services
SOC medium	2% w/v trypton, 0.5% w/v yeast extract, 10mM NaCl, 2.5mM KCl, 10mM $MgCl_2$, 20mM glucose	Homemade
LB-agar plate	15g agar/L of L-Broth	Beatson central services
Ampicillin	Working concentration 50µg/mL	Sigma #A9518
Kanamycin	Working concentration 50µg/mL	Sigma #K4000
Chloramphenicol	Working concentration 50µg/mL	Sigma #C0378
Protein purification		
IPTG		Sigma #I6758
Lysis buffer	200mM NaCl, 30mM Tris-HCl pH7.5, 3mM β-ME, Protease inhibitors (Roche)	Homemade
GST buffer	200mM NaCl, 30mM Tris-HCl pH7.5, 3mM β-ME	Homemade
GSTrap HP column		GE Healthcare #17-5282-01
GSH buffer	20mM GSH in GST buffer, pH7.5	Homemade
Thrombin	Serine protease	Sigma #T4648
His buffer A	300mM NaCl, 25mM Tris-HCl pH7.5, 2mM β-ME	Homemade
His buffer B	300mM Imidazol in His buffer B, pH 7.5	Homemade
HisTrap HP column		GE Healthcare # 17-5248-01
Gel filtration buffer	150mM NaCl, 25nM Tris-HCl pH7.5, 2mM β-ME	Homemade
HiLoad 16/600 Superdrex 75pg		GE Healtcare #28989333
HiLoad 16/600 Superdrex 200pg		GE Healtcare #28989335
Amicon Ultra-4 centrifugal Filter unit		Amicon #UFC801024
Amicon Ultra-15 centrifugal Filter unit		Amicon #UFC901008
MicroAmp Fast Optical 96-well plate		Applied Biosystems #4346906
Surface Plasmon Resonnance		
CM5 chip		GE Healtcare #BR100012
NTA chip		GE Healtcare #BR100034
Biacore T200		
Biacore Buffer	150mM NaCl, 25nM Tris-HCl pH7.5, 2mM β-ME, 10% P-20	
Surfactant P-20		GE Healtcare #BR100054
Cell biology technics		

GST Pulldown		
Buffer A	GST pulldown - 50mM NaCl, 50mM Tris-HCl pH7.5, 5mM $MgCl_2$, 3mM DTT	Homemade
Glutathione sepharose 4B beads		GE Healthcare #17075601
Lysis buffer	100mM NaCl, 25mM Tris-HCl pH7.5, 5mM $MgCl_2$, 1x Protease and Phosphatase inhibitor, 0.5% NP-40	Homemade
Washing buffer	100mM NaCl, 25mM Tris-HCl pH7.5, 5mM $MgCl_2$	Homemade
GFP-Trap		
Lysis buffer	25mM Tris HCl, pH7.5, 100mM NaCl, 5mM $MgCl_2$, 0.5% NP-40, Protease and phosphtase inhibitors	Homemade
GFP_Trap_A beads		ChromoTek #gta_200
Immunofluorescence & Immunohistochemistry		
16% paraformaldehyde		Electro Microscopy Sciences #15710
Permeabilisation buffer	20mM Glycine, 0.05% Triton-X100	Homemade
ProLong Gold antifade mounting media		Molecular Probes #P36934
Glutaraldehyde		
Citrate buffer pH6.0	Antigen retrieval solution	Dako #S2031
Peroxydase blocking solution		Dako #S2023
Dako Antibody diluent solution		Dako #S3022
Anti Mouse/Rabbit peroxidase labeled polymer		Dako #K401011 or #K400611
CLICK reaction		
Fatty-acid free BSA		Sigma #A7030
Palmitic acid-azide		Gift from Jennifer Greaves (Strathclyde university)
Myristic acid-azide		Gift from Jennifer Greaves (Strathclyde university)
Tris[(1-benzyl-1H-1,2,3-triazol-4- yl)methyl]amine		Sigma #678937
L-Ascorbic acid		Alfa Aesar #A15613
Copper II Sulphate		Sigma #451657
GFP-Trap		
Lysis buffer	100mM NaCl, 10mM Tris-HCl pH7.5, 5mM $MgCl_2$, 0.5% NP-40, Protease Inhibitor Cocktail,	Homemade

	Phosphatase Inhibitor Cocktail	
Washing buffer	100mM NaCl, 10mM Tris-HCl pH7.5, 5mM $MgCl_2$	Homemade
GFP-Trap_A beads		ChromoTeK #gta_10
3D MDCK cysts		
PFS	0.7% (w/v) fish skin gelatin in 0.025% Saponin-PBS	Homemade
Sodium azide		Sigma #S2002

2.1.3 Cell culture plastic ware and consumables

Table 2-3: Cell culture plactic ware and consumables

Dishes, plates and tissue culture material		
Name	**Description & Application**	**Source**
∅10cm plastic plate		Corning #430147
6-well plastic plate		Falcon #353046
24-well plastic plate		Falcon #353047
96-well plastic plate		Falcon #353072
∅35mm glass-bottom dish		MatTek #35G-1.5 20-C
∅35mm glass-bottom dish	For circular invasion assay	Ibidi #81158
Silicon stopper	For circular invasion assay	Ibidi #80209
6-well glass-bottom plate		MatTek #06G-1.5 20-F
24-well plate with transwell		Corning #3422
E-Plate 16	xCELLigence assay	Acea #05469830001
∅13mm glass coverslips		VWR #631-0151
8-well glass bottom chamber	For MDCK cysts	MatTek #Lab-TekII 155409
Precellys CK14 lysing tubes	Tube for tissue lysate	Precellys #03961-1-003
Tissue culture centrifuge	Rotor A-4-44	Eppendorf C5804R
2mL Cryovial		Greiner bio-one #126263

2.1.4 Inhibitors

Table 2-4: Inhibitors

Inhibitors		
Name	**Description & Application**	**Source**
Proteases inhibitor cocktail	For cell lysate - WB	ThermoFisher #1861279
Phosphatases inhibitor cocktail	For cell lysate - WB	ThermoFisher #78427
cOmplete™, EDTA-free Protease Inhibitor Cocktail	For protein lysate – Protein purification	Roche #11873580001
PMSF	For tissue lysate - WB	Sigma #93482
Aprotinin	For tissue lysate - WB	Sigma #A6279

NaF	For tissue lysate - WB	Sigma #S7920
Na_3VO_4	For tissue lysate - WB	Sigma #450243
EHT 1864	Rac family GTPase inhibitor	Tocris #3872
NSC 23766	Selective inhibitor of Rac1-GEF interaction	Tocris #2161

2.1.5 Kits

Table 2-5: Kits

Kits	
Name	**Source**
Lipofectamine 2000	Invitrogen #11668019
Lullaby	OzBiosciences #FLL73000
Calcium phosphate transfection kit	Invitrogen #K2780-01
Prescission Red advanced assay	Cytoskeleton Inc. #ADV02
Zymoclean DNA gel recovery kit	ZymoResearch D4008
Zero Blunt TOPO PCR Cloning Kit	Invitrogen #K2800
Rapid DNA ligation kit	Thermo Scientific #10775841
Q5-site directed mutagenesis kit	NEB BioLabs #E0554
µMACS GFP isolation kit	MACS Miltenyl Biotec #130-091
Thermal shift assay	Applied Biosystem #4461146

2.1.6 Antibodies and dyes

Table 2-6: Antibodies and dyes

Antibodies and dyes		
Antibody	**Source**	**Working concentration & Dilution**
Rabbit anti FAM49B	Sigma #HPA009076	WB 1:500
Rabbit anti FAM49B	ProteinTech #20127-1-AP	WB 1:1000
Mouse anti GFP (4B10)	Cell Signaling #2955	WB 1:1000
Rabbit anti GFP	Abcam #ab290	WB 1:2000
Chicken anti GFP	Abcam #ab13970	IF 1:500
Mouse anti GST	Abcam #ab18183	WB 1:1000
Rabbit anti GST	Cell Signaling #2622	WB 1:1000
Rabbit anti Phospho-Paxillin (Y118)	Cell Signaling #2541	IF 1:200
Mouse anti Vinculin	Sigma #V9131	IF 1:400
Rabbit anti WAVE2 (H-110)	SantaCruz #sc-33548	IF 1:50
Rabbit anti Ki67	Abcam #ab15580	IF 1:200

Rat anti Tubulin (YL1/2)	Abcam #ab6160	IF 1:200
Mouse anti Podocalyxin	Gift from Dr. David Bryant	IF 1:100
Mouse anti Cortactin (4F11)	Millipore #05-180	IF 1:200
Rabbit anti p34-Arc/ARPC2	Millipore #07-227	IF 1:200
Rabbit anti N-WASP (30D10)	Cell signaling #4848	IF 1:100
Mouse anti Fascin (55K-2)	Dako #M3567	IF 1:200 WB 1:1000 IHC 1:500
Mouse anti BrdU	BD Bioscience #347580	IHC 1:200
Rabbit anti Ki67	Thermo #RM9106	IHC 1:200
Rabbit anti Cleaved Caspase 3 (Asp175)	Cell Signaling #9661	IHC 1:300
Rat anti NIMP (NIMP-R14)	Abcam #ab2557	IHC 1:200
Rat anti F4/80 (CI:A3-1)	Abcam #ab6640	IHC 10 µg/mL
Rabbit anti Rac1/2/3	Cell Signaling #2465	WB 1:500
Rabbit anti GAPDH	Cell Signaling #2118	WB 1:1000
Mouse anti Tubulin (DM1A)	In house	WB 1:3000
Donkey anti Rabbit-HPR	GE Healtcare #LNA934V	WB 1:2000
Goat anti Rabbit 800nm	Thermo Scientific #SA5-35571	WB 1:10000
Goat anti Mouse 800nm	Thermo Scientific #SA5-35521	WB 1:10000
Donkey anti Rabbit 680nm	Invitrogen #A21206	WB 1:10000
Donkey anti Mouse 680nm	Invitrogen #A10038	WB 1:10000
Donkey anti Rabbit 594nm	Invitrogen #A21207	IF 1:200
Donkey anti Mouse 594nm	Invitrogen #A31203	IF 1:200
Goat anti Rat	Invitrogen #A11077	IF 1:200
Goat anti Rabbit 488nm	Invitrogen #A11008	IF 1:200
Goat anti Mouse 488nm	Invitrogen #A11001	IF 1:200
Donkey anti Chicken 488nm	Invitrogen #A11039	IF 1:200
Phalloidin 488nm	Molecular Probe #A12379	IF 1:200
Phalloidin 594nm	Molecular Probe #A12382	IF 1:200
Phalloidin 647nm	Molecular Probe #A22287	IF 1:200
Hoechst 33342	Thermo Scientific #62249	IF 1:50000
Calcein AM	Life Technologies #C1430	4µM
800CW Alkyne Infrared dye	LICOR Biosciences Ltd #929-60002	5µM

2.1.7 DNA constructs

Table 2-7: DNA constructs

cDNA and DNA constructs		
Name	**Backbone**	**Source**
Human FAM49B	pOTB7	GE Healthcare - Clone ID: 3501828

Mouse FAM49B	pCMV-SPORT6	GE Healthcare – Clone ID 4012217
GST-2x8His-FAM49B	pBDDP-SPR4	Homemade (backbone: Gift from Dr.Chris Gray)
GFP-30-236 FAM49B	pEGFP-N1	Homemade
R160D GFP-30-236 FAM49B	pEGFP-N1	Homemade
R161D GFP-30-236 FAM49B	pEGFP-N1	Homemade
R160/161D GFP-30-236 FAM49B	pEGFP-N1	Homemade
eCFP-PBD-Pak	pECFP-N1	Prof. L. M. Machesky
GST	pGEX4T2	Gift from Dr. Jan Ohotski
GST-wt Rac1	pGEX2T	Prof. L. M. Machesky
GST-Q61L Rac1	pGEX2T	Prof. L. M. Machesky
GST-Q61L Cdc42	pGEX2T	Prof. L. M. Machesky
GST-Q63L RhoA	pGEX2T	Prof. L. M. Machesky
GFP-rGBD	pCS2+	Addgene #26732
mTq-sREACh Raichu Rac probe	pKan-Rac-Raichu	Gift from Dr. Kirsty Martin
mTurquoise2-C1		Gift from Dr. Kirsty Martin
FAM49B-GST	pProExHT6	Homemade (Backbone: Gift from Dr. Shehab Ismail)
G2A FAM49B-GFP	pEGFP-C1	Homemade
C10A FAM49B-GFP	pEGFP-C1	Homemade
C223A FAM49B-GFP	pEGFP-C1	Homemade
C231A FAM49B-GFP	pEGFP-C1	Homemade
C253A FAM49B-GFP	pEGFP-C1	Homemade
C284A FAM49B-GFP	pEGFP-C1	Homemade
pLIX401-mVenus-FAM49B	pLIX401-mVenus_New MCS	Homemade (backbone: Gift from Dr. David Bryant)
pLIX401-mVenus-R160D-FAM49B	pLIX401-mVenus_New MCS	Homemade (backbone: Gift from Dr. David Bryant)
pLIX401-mVenus-R161D-FAM49B	pLIX401-mVenus_New MCS	Homemade (backbone: Gift from Dr. David Bryant)
pLIX401-mVenus-R160/161D-FAM49B	pLIX401-mVenus_New MCS	Homemade (backbone: Gift from Dr. David Bryant)
6His-wt Rac1	pRSET	Homemade
6His-Q61L Rac1	pRSET	Homemade
GST-Pak-CRIB	pGEX2T	In-house
GST-30-236 FAM49B	pGEX4T2	Homemade
R161D GST-30-236 FAM49B	pGEX4T2	Homemade
GFP-Fascin	pEGFP-N1	Gift from Dr. Josephine Adams
GFP-Paxillin	pEGFP-N1	In-house

FAM49B-FLAG	pcDNA3.1	Homemade

2.1.8 siRNA, shRNA and sgRNA sequences

Table 2-8: siRNA, shRNA and sgRNA sequences

Silencing RNA and guide RNA			
Target gene	**Type**	**Sequence (5'-3')**	**Source**
Human FAM49B – Exon 3	CrispR	CACCGGGTGCAGTCGTGCCACTAGT	LifeTech
Human FAM49B – Exon 4	CrispR	CACCGCGAGTATGGCGTACTAGTCA	LifeTech
Mouse FAM49B Seq1	siRNA	CAGGCTCTCGCTAAACAGTTT	Qiagen #SI04452035
Mouse FAM49B Seq4	siRNA	TCAGGTGAATGTAGTGTTAAA	Qiagen #SI00782341
Human FAM49B Seq6	siRNA	AGGGTAATGGTGGGTGTCATA	Qiagen #SI04278890
Human FAM49B Seq7	siRNA	ATAGAAGAACATTGAGTCGTA	Qiagen #SI04359369
AllStar Negative siRNA	siRNA		Qiagen #SI03650318
Dog FAM49B #577	shRNA	GATGAGACTACCTCCAAGCAA	Sigma #TRCN0000172577
Dog FAM49B #901	shRNA	ACTGCCTATTCTGCTATTTAA	Sigma #TRCN0000430901

2.1.9 Softwares and websites

Table 2-9: Softwares and Websites

Softwares & Websites		
Name	**Provider**	**Version**
ImageStudioLite	LICOR Biosciences Ltd	v 5.2.5
NEBaseChanger	NewEngland Biolabs	v 1.2.6
ApE	M. Wayne Davis	v 2.0.47
7500Fast Real-Time PCR system	Applied Biosystems	v 2.06
Fiji	National Health Institute, USA	v 1.48t
Prism	GraphPad	v 5.0c
Digital Image Hub	Leica Biosystems	v 4.0.6
CrispR Design	Zhang lab	2015
MaxPlant	Max Planck Institute	V 1.5.5.1
DAVID	NIAID, NIH	v.6.7
i-TASSER	Zhang lab	v. 5.1
Skylign	Jody Clements, Travis Wheeler & Robert Finn	v.3.0
PyMol	Schrödinger	v. 1.7.4.5

2.2 Methods

2.2.1 Cell culture

2.2.1.1 Cell lines and growth conditions

CHL1, B16F1, HEK293T and COS7 cells were maintained in 10% FBS and 2mM L-Glutamine supplemented Dulbecco's Modified Eagle's Medium. MDCK cells were kindly provided by Dr. David Bryant (University of Glasgow and Beatson Associate). Cells were cultured in MEM, high glucose, high sodium bicarbonate, 5% FBS and 2mM L-Glutamine. Cells transfected with a TetON plasmid were grown in their respective medium complemented with approved Tetracycline-free FBS. All cell lines used in this study were maintained in ∅10cm plastic dishes at 37 °C and perfused with 5% CO_2.

2.2.1.2 Subculture and counting

The following protocol applies for all cell types used during this work. Subconfluent cells were washed once with 1X phosphate buffer saline. Cells were detached using an appropriate volume of trypsin diluted at 0.25% in PE buffer and incubated at 37 °C. Cell detachment was checked regularly under a phase transmitted light microscope. Once fully detached, cells were resuspended in fully complemented medium, therefore inhibiting trypsin activity. Cell suspension was carefully resuspended and 400uL were taken up and diluted in 20mL of CASYton buffer. Cell counting was proceeded using CASY cell counter (Roche). Cell concentration was automatically calculated after averaging 3 counting cycles and adjusted by the aggregation coefficient. In order to start off a fresh culture, cells were typically passaged at 1 in 5 (CHL1 and MDCK) and 1 in 10 (HEK293T and B16F1). Passages were recorded and fresh cells were taken out from the liquid nitrogen once reaching passage 20.

2.2.1.3 Cryopreservation and cell recovery

The following procedure applies for all cell types used during this work and has been optimised for a confluent 10 cm dish. Cells were collected as described above. Cell suspensions were centrifuged for 5min at 1000 rpm and pellets were resuspended in 3mL of freezing medium (50% fully complemented DMEM, 40% FBS, 10% DMSO). 1mL of cells was then aliquoted into 2mL cryovial tubes and immediately frozen at -80°C before being transferred to the liquid nitrogen tank.

To recover cells from the liquid nitrogen, cryovials were quickly transferred into a 37°C waterbath. Cells were gently resuspended in pre-warmed fully complemented medium and centrifuged as previously described in order to remove any trace of DMSO. Cell pellets were resuspended in fresh medium and plated onto 10cm dishes. Fresh media was added to the adherent cultures the day after thawing and cells were allowed to recover for at least one week before using them for any experiment.

2.2.1.4 Transient transfection - Plasmids

All cells lines were transfected in suspension, except when mentioned otherwise. Basically, cells were collected and counted as previously described. $1x10^6$ cells were seeded into 6-well plate. For CHL1, cells were plated at 70% confluence the day before processing. Meanwhile, Lipofectamine 2000 transfection mix was prepared accordingly to the manufacturers instructions. Briefly, 2.5-5µg of plasmid was diluted in 100µL final of SFM and 7µL of Lipofectamine 2000 was diluted in 93µL of SFM. Plasmid mix was then added to the Lipofectamine mix and incubated 5min at RT before adding onto cells. Cells were typically used 24-48h after transfection. Transfection of cells plated onto 15cm dishes requires scaling up to 20 µg of plasmid and 35µL of Lipofectamine 2000.

2.2.1.5 Transient transfection - siRNA

$3x10^5$ cells were used for each reaction according to the manufacturers protocol. Oligos were used at a final concentration ranging from 10-100nM. Briefly, 1.5-15 µL of 20µM stock oligos was diluted in 100µL final of SFM, whereas 7-14µL of Lullaby was diluted in 100uL SFM in another eppendorf. Tubes were mixed together and kept 5min at RT before adding onto the cells. The same procedure was repeated 48h after the first treatment and cells were typically used 24-48h following the second shot.

2.2.1.6 Lentiviral infection and stable cell line selection

Knockout cell lines were produced using the CrispR-Cas9 editing genome technique as published by Ran *et al* (Ran et al., 2013). Basically, HEK293T cells were seeded at 1.5 x 10^6 cells/10cm dish and transfected the day after using the calcium phosphate transfection kit. 10µg of lentiCrispR (empty vector or containing the CrispR targeting sequence), 7.5µg of pSPAX2 and 4µg of pVSVG were diluted in a final volume of 440µL of tissue culture water, mixed with 500µL 2X HBS and 60µL of 2M $CaCl_2$ and left 30min at 37°C. Transfection mix was added overnight onto HEK293T cells. Medium was then removed

and replaced by 6mL of 20% FBS complemented DMEM, allowing virus production. Meanwhile, recipient cells were plated at 1 x 10^6 cells/10cm dish, in order to be at 40-50% confluence.

The day after, medium-containing viruses was filtered through a ∅0.45µm pore membrane and mixed with 2.5µL of hexadimethrine bromide at 10mg/mL before infecting recipient cells. The same procedure was repeated the following day and puromycin selection was carried out after two shots of infection. Puromycin sensitivity was tested beforehand by treating untransfected recipient cells with a range of drug dose (usually up to 5µg/mL) and the appropriate concentration (leading to 100% cell death within 48h) was chosen for stable cell line establishment. Generally, most cell lines were sensitive to 1µg/mL but puromycin concentration had to be increased up to 5µg/mL for the MDCK cells.

2.2.2 SDS-PAGE, coomassie staining and western blotting

2.2.2.1 Protein lysate preparation from cell lines

Culture medium was aspirated and cells were washed three times in ice cold PBS. Plates were then transferred onto ice and ice-cold RIPA buffer containing proteases and phosphatase inhibitors were added onto the cells, leading to direct cell lysis. Cells were scraped out from the dish, collected into a clean chilled eppendorf tube and kept on ice for about 5min. Tubes were centrifuged at 13000rpm for 10min at 4 °C and soluble proteins were transferred into a clean eppendorf for either direct analysis or frozen down.

2.2.2.2 Protein lysate preparation from tissues

Tissues were collected from humanely sacrificed mice, snap freezed on dry ice and kept in a pre-chilled eppendorf. Samples were thawed on wet ice and tissues were transferred into Precellys CK14 lysing tubes. 300µL of Ripa buffer containing 0.5% deoxycholate and protease inhibitors (1.25mM PMSF, 1µg/mL of Aprotinin, 0.5mM NaF, 1.25mM Na_3VO_4) was added and lysis was performed after 1 cycle of shaking using a pre-cold Precellys homogenizer (3 blasts of 30 sec with 90 sec gap between each blast). Tubes were kept on ice 1h to allow sedimentation of debris and supernatants were centrifuged at 13000rpm for 15min at 4 °C. If the lysates were not clear, another spin was performed.

2.2.2.3 Protein quantification

Protein concentration is routinely tested using Prescission Red advanced protein assay. Briefly 5µL of cell lysate was mixed with 995µL of reagent and incubate for 30sec. Protein concentration is proportional to the absorbance at OD_{600nm} and typically 15-40µg of proteins was resolved on a SDS-PAGE gel.

2.2.2.4 Protein separation using SDS-PAGE

Appropriate protein concentration was mixed with NuPAGE LDS sample buffer and NuPAGE reducing agent to a final concentration of 1X. Samples were boiled 5min at 100 °C and quickly centrifuged prior to loading. Samples were resolved using pre cast Novex 4-12% Bis-Tris acrylamide gels and NuPAGE MOPS SDS running buffer, along side to 6µL of PageRuler pre-stained protein ladder. When looking at Rac1, NuPAGE MES SDS buffer was used in order to increase the resolution of low molecular weight proteins. Gels were usually run at 180V until the front of the sample buffer reaches the bottom of the gel.

2.2.2.5 Coomassie staining

Gels were gently transferred into a clean plastic tray and stained overnight with InstantBlue. Stained gels were scanned using laser 700nm from the Li-Cor Odyssey CLx scanner.

2.2.2.6 Western blotting

Wet electrotransfer allows proteins to be exposed at the surface of a solid matrix. To do so, SDS-PAGE size-separated proteins were transferred onto a 0.45µm nitrocellulose blotting membrane for 60min at 110mA using a BioRad tank, filled with transfer buffer and an ice block. Membranes were blocked for at least 30min at room temperature using either 5% (w/v) non-fat dry milk/TBS-T or 5%BSA/TBS-T then incubated overnight at 4°C with primary antibody (see Table 2.6). In order to remove background caused by the excess of antibody, the membrane was washed 3 times for 5min in TBS-T at room temperature. Alexa-Fluor conjugated secondary antibody was diluted 1:10000 in 5% (w/v) non-fat dry milk/TBS-T and membrane was incubated 1h at room temperature. Excess antibody was washed out twice in TBS-T and finally once in water. All incubation steps were realised with gentle agitation.

2.2.2.7 Western blot scanning and quantification

Membranes were scanned using the automatic setting intensity mode of the Li-Cor Odyssey CLx scanner. Images were processed as grey scale picture and signal intensity was calculated using the Li-Cor ImageStudioLite v.5.2.5 software.

2.2.3 Molecular biology and subcloning

2.2.3.1 PCR reaction

Each reaction was set up with with 10ng of DNA template, 100ng of forward and reverse primers, 25µL of 2X PrimeStar Max Premix to a final volume of 50µL. PCR reaction was performed accordingly to Takara's Taq polymerase requirements using a T100 Thermal Cycler (BioRad). Basically, program was set up as follows:

1) 5min @ 98°C
2) 10sec @ 98°C
3) 15sec @ Tm (specific for each primer set)
4) 1min/kb @ 72°C
5) Repeat steps 2-4 for 30 cycles
6) 15min @ 72°C
7) ∞ @ 4°C

2.2.3.2 Agarose gel electrophoresis and gel purification

DNA gels were made up using high-grade agarose (from 0.8 up to 2% depending of DNA fragment size) diluted in TAE buffer. Agarose was boiled until completely dissolved and 1% of Midori green added before casting the gel. DNA was diluted in 6X loading buffer and loaded into each well along with 8µL of O'GeneRuler 1kb or 8µL of 100pb DNA ladder for smaller fragments. Gels were typically run at 100V for 35min in TAE buffer. DNA fragments were quickly excised under UV lamp and DNA was purified using Zymoclean DNA gel recovery kit accordingly to manufacturer's protocol. Basically, agarose fragments were weighed and heated at 50°C with 3 volumes of ADB buffer until completety dissolved. The mix was then loaded onto the spin column and centrifuged for 30 sec at 10000rcf. Filters were washed twice with 200µL of washing buffer and DNA was eluted using 15µL of pre-heated nuclease-free water.

2.2.3.3 Zero Blunt Topo cloning

Eluted DNA was subcloned into a shuttle Topo vector accordingly to manufacturer's protocol. Briefly, 4µL of PCR product was mixed with 1µL of salt solution and 1µL of

PCR-II-Blunt-Topo and kept for 5min at room temperature. 3µL of the Topo reaction was transformed into chemically competent *E. Coli* DH5alpha cells as described below.

2.2.3.4 Transformation of chemically competent cells

Most of cells used in this study were *E. Coli* DH5alpha, *E. Coli* BL21 CodonPlus (DE3)-RIL or *E. Coli* BL21 (DE3) pLysS. Plasmids were gently mixed with competent cells and kept for 30min on ice. 45sec heat-shock at 42°C allows a transient permeabilisation of the plasma membrane and incorporation of the DNA into the cells. Cells were then allowed to recover on ice during 2min and a further hour at 37°C with 500µL of SOC medium before spreading a fifth of culture on pre-warmed LB-agar plates containing the correct antibiotic (50µg/mL). Plates were transferred overnight into a 37°C incubator.

2.2.3.5 Restriction digestion

All restriction enzymes and buffer used were purchased from New England Biolabs. Reaction were basically set up using 0.5-2µg of DNA, 2µL of appropriate NEB buffer and 5-10 units of each enzyme and left overnight in a 37°C waterbath. Incubation time was cut down to 0.5-1h for FastDigest enzymes. Reactions were gel purified as previously described before any further applications.

2.2.3.6 Ligation

DNA concentrations were quantified using NanoDrop2000C (Thermo Scientific). Ratio vector:insert of 1:5 were mixed together in 2µL of rapid ligation buffer and 1µL of T4 DNA ligase to a final volume of 20µL. Reactions were left at room temperature for 5 min and 5µL were transformed into *E. Coli* DH5alpha competent cells.

2.2.3.7 Mutagenesis

Primers were designed using the NEBaseChanger website (v1.2.6) and point mutations were created within the cDNA of interest using the Q5-site directed mutagenesis kit. Basically, PCR reactions were set up using 10ng of parental backbone, 0.5µM of each primer and 1X of Q5 Hot start high-fidelity master mix and following manufacturer's instructions:

1) 30sec @ 98°C
2) 10sec @ 98°C
3) 15sec @ Tm (specific for each primer set)
4) 30sec/kb @ 72°C

5) Repeat steps 2-4 for 25 cycles
6) 2min @ 72°C
7) ∞ @ 4°C

1µL of the PCR reactions was then used for circularization and template removal based on the digestion of the parental methylated DNA for 5min at room temperature using the KLD mix. 5µL of the reactions were then transformed into chemically competent *E Coli* DH5alpha cells as previously described.

2.2.3.8 Miniprep, screening of transformants, sequencing and maxiprep.

Individual colonies were delicately touched with a sterile tip and used to inoculate 5mL of LB containing appropriate antibiotic(s). Cultures were grown overnight at 37°C with energetic shaking (200 rpm). Plasmids were purified using the QIAprep Spin Miniprep kit and 5µL were used for a quick screen by restriction digest. Clones containing the insert were sent for sequencing performed by the Beatson research services. Correct DNA sequences were confirmed by sequence alignment to the plasmid map (ApE Mavericks v2.0.47) and DNA was transformed into new *E. Coli* DH5alpha competent cells. 250mL culture was used for the Maxiprep purification performed by the Beatson research service. Plasmids were eluted in nuclease-free water.

2.2.4 Protein purification and Biacore analysis

2.2.5 Culture and induction conditions

Basic protein preparations were set up in 2.5L flasks containing 1L of LB. Depending on the application, between 5-20 flasks were prepared. Pre-culture were grown overnight in LB containing appropriate antibiotics. For each culture, 10mL was used to inoculate 1L of pre-warmed LB containing antibiotics and kept at 37°C, 200rpm until culture reached OD_{600nm} 0.4. At this stage, 0.2mM IPTG was added to the culture and temperature was decreased to 20°C for 17h.

2.2.5.1 Cell lysis

Overnight cultures were centrifuged for 15min at 4000rpm and pellets were re-suspended in filtered lysis buffer containing protease inhibitor. Lysates were passed twice through a 20000psi-pressurised microfluidizer and collected in a clean beakers. Soluble and insoluble proteins were separated out by centrifugation at 20000rpm for 50min at 4°C and supernatant was filtered through ∅5µm pore membranes.

2.2.5.2 Purification of GST-tagged proteins

AKTA machine was cleaned with water and equilibrated with fresh GST buffer. GSTrap HP column was washed with 5 column volumes of water and equilibrated with at least 10 column volumes of buffer and until UV curve becomes stable. Lysate was loaded from the P960 pump onto the column and flow-through was collected in a clean bottle. At this step, UV curve typically picks up at 3500 units. The column was then extensively cleaned with GST buffer until UV went back to the baseline.

At this step, the protein was either directly eluted in its tagged form by stripping the column with 10mL of elution buffer, or the tag was directly cleaved on the column. To do so, a loop was created between the column and a Falcon tube and 8mL of GST buffer supplemented with 100 units of thrombin was circulated overnight at 0.5mL/mL, 12°C. Efficient cleavage was monitored on the screen and resulted in a wave-like pattern of the UV curve, reaching ~150-300 units. 3-4 column volumes of GST buffer were used to collect the untagged protein.

2.2.5.3 Purification of histidine-tagged proteins

For purification of histidine-tagged protein, a similar protocol was used for the cleaning, equilibration and loading steps but buffer A and HisTrap HP column were used to specifically retain histidine-tagged protein. Proteins were directly eluted using a gradient of imidazole at 1mL/min. Basically, buffer A was pumped through lane A and buffer B through lane B. A gradient from 0-100% of buffer B was created with 1% step increase over 120mL and 1.5mL fractions were collected.

2.2.5.4 Size exclusion chromatography

Proteins were all gel purified in order to increase purity but also to facilitate storage in the standard GF buffer. The appropriate columns (HiLoad 16/600 Superdrex 75pg or HiLoad 16/600 Superdrex 200pg) were equilibrated using GF buffer flowing at 1mL/min for at least 1hour. Proteins were injected into a 10mL loop and GF buffer was pumped at 1mL/min into the loop, pushing the protein down the column. 1.2mL fractions were collected and few microliters of each fraction matching to a UV peak was loaded on a 4-12% Bis-Tris acylamide gel for Coomassie staining.

2.2.5.5 Protein Concentration and protein storage

Proteins were concentrated was performed using Amicon Ultra-4 or Ultra-15 centrifuge filter units with a 10kDa cut-off. Basically, samples were loaded and the tubes were centrifuged at 3000rcf, 4°C for at least 15min. Successive spins allowed concentratation of the protein to an appropriate volume. 200µL aliquots of proteins were snap frozen in liquid nitrogen and transferred at -80°C for long-term storage.

2.2.5.6 Thermal shift assay

Protein folding was tested by thermal shift assay. Basically, 5µM of protein was mixed with 1X dye diluted in buffer. Both GF buffer and kit melt buffer were tested and enough mix was prepared to have four technical replicates. 20µL of mix was pipetted into a MicroAmp Fast Optical 96-well plate and reaction run on the 7500Fast Real-Time PCR system using the 7500 software v2.06. The melt screen went from 25 to 95 °C with 1% increments.

2.2.5.7 SPR – Biacore

SPR analysis was performed using Biacore T200 (GE Heathlcare). Using GF buffer complemented with 5mM $MgCl_2$ and 0.5% of surfactant P20 as running buffer, GST-tagged proteins were immobilised at 22°C onto CM5 sensor chip and reached ~320 RU. Same procedure was used for His-tagged protein onto NTA sensor chip and reached 650 RU. All immobilisation step were done at a flow rate of 10µL/min. Serial dilution of each analyte was injected across a reference flow cell and the flow cell containing the ligand at a flow rate of 30µL/min. Data were solvent corrected, reference subtracted, quality controlled and evaluated using the Biacore T200 evaluation software. Affinity was determined by curve fitting a 1:1 binding model.

2.2.6 Cell biology technics

2.2.6.1 GST pull down

100mL preculture of *E. Coli* BL21 CodonPlus (DE3)-RIL were grown overnight. Cells were diluted 1:100 and induced at OD_{600nm} 0.4 for 4h with 0.2mM IPTG. Lysates were obtained by resuspending cell pellets in ice-cold buffer A and 8x10sec blasts of sonication, followed by a 30min spin at 20000rpm (Beckman JA17). GST tagged proteins were

immobilized on glutathione-sepharose beads 30min at 4°C with gentle agitation whereas unbound proteins were washed out 3 times in ice-cold buffer A.
CHL1 cells were transfected transfected as previously described and collected in ice-cold lysis buffer. 2mg of lysates were mixed with pre-equilibrated beads and binding was allowed for 2h at 4°C with gentle agitation. Beads were then washed 3 times in washing buffer and proteins eluted with sample buffer, prior to loading and blotting as described.

2.2.6.2 Coating

Coatings were done at a final concentration of 20µL/mL of protein diluted in PBS. Plates were kept overnight at 4°C. The next day, coatings were washed out 3 times in PBS and kept in PBS.

2.2.6.3 Immunofluorescence

Immunofluorescence was performed using ∅13mm glass coverslips. Cells were seeded at low concentration (3-5x10^4cells/coverslip) and allowed to adhere overnight (uncoated) or 4h (coated coverslips). Media was aspirated from coverslips and cells were fixed in 4% paraformaldehyde for 10min, permeabilised for another 10min and blocked for 30min in 5% BSA-PBS. For fascin staining, cells were fixed 10min with -20°C methanol, washed with PBS and directly blocked in 5% BSA-PBS. Primary and secondary antibodies, phalloidin and nuclear dye were diluted in blocking buffer and incubated for 1h in a dark and humidified chamber. Coverslips were washed twice in PBS and once in water before being mounted on glass slides using ProLong Gold antifade reagent. Coverslips were allowed to settle down on a glass slide overnight at room temperature, protected from light. Images were taken using an inverted Olympus FV1000 confocal microscope using a Plan Apochromat N 63x/1.40 oil SC or a Uplan FL N 40x/1.30 oil objective.

2.2.6.4 Peptide array

Overlapping 25-mer peptides of FAM49B were spotted on a cellulose membrane by Fmoc (9-fluorenylmethoxycarbonyl) chemistry (Frank, 2002) using an AutoSpot-Robot ASS222 (Intavis Bioanalytical Instruments). Membranes were then mounted on a glass slide. Slides were first wet in TBS-T and blocked in 5% BSA-TBS-T for 1h at room temperature. Slides were rinsed with TBS-T and incubated overnight at 4°C with 0.9µM of recombinant untagged protein diluted in 0.5% BSA-TBS-T, with gentle agitation. After 3 washes in TBS-T, primary Rac1/2/3 antibody was added overnight at 4°C with gentle agitation.

Slides were washed 3 times with TBS-T and incubated with the horseradish peroxidase conjugated anti-Rabbit antibody. ECL pico system was used according to the manufacturer's protocol and pictures taken using MyECL Imager chemoluminescent mode.

2.2.6.5 Two-hybrid

Two-hybrid screen was outsourced but below is a short description of the method used by Hybrigenics SA.

The coding sequence for the constitutively active full-length Rac1 (NM_006908.4 ; mutations G12V, C189S) was PCR-amplified and cloned into pB27 as a C-terminal fusion to LexA (LexA-Rac1). All libraries that were used to screen are domain libraries cloned into the prey vector pP6. pB27 and pP6 derive from the original pBTM116 (Vojtek and Hollenberg, 1995) and pGADGH (Bartel et al., 1993) plasmids, respectively. The bait was screened against the different libraries using a mating approach with YHGX13 (Y187 ade2-101::loxP-kanMX-loxP, mat alpha) and L40deltaGal4 (mata) yeast strains as previously described (Fromont-Racine et al., 1997). Positive colonies were selected on a medium lacking tryptophan, leucine and histidine, and supplemented with 3-aminotriazole whenever necessary to reduce the total number of clones. The prey fragments of the positive clones were amplified by PCR and sequenced at their 5' and 3' junctions. The resulting sequences were used to identify the corresponding interacting proteins in the GenBank database (NCBI) using a fully automated procedure. A confidence score (PBS, for Predicted Biological Score) was attributed to each interaction as previously described (Formstecher et al., 2005).

2.2.6.6 Inverted invasion assay

This method is a modified version of the previously published assay from Hennigan *et al* (Hennigan et al., 1994). Matrigel was diluted 1:1 in ice cold PBS and 100µL was allowed to polymerise for 30min at 37°C in each transwell. Meanwhile, cells were collected in fully complemented DMEM and $4x10^4$ cells were plated onto the underside of the filter in order to cover the entire filter. Transwells were then carefully covered with the base of the 24-well plate such that it contacted the droplets of cell suspension and was left for 2h in the incubator, allowing cell attachment to the bottom side of the filter. Transwells were finally washed into 3 x 1mL of serum free medium. Chemotactic gradients were created by filling the upper chambers with fully complemented medium, and the bottom chambers were kept in SFM. Cells were then allowed to migrate for 3 ½ days and stained for 1h at 37 °C with

4µM of calcein AM. Serial optical sections of 15µm interval were obtained with an Olympus FV1000 confocal microscope, UplanSApo 20x/0.74 objective. Images were analysed using Fiji software (ImageJ v1.48t)

2.2.6.7 Fluorescent gelatin degradation assay – Invadopodia assay

Sterile ∅13 mm coverslips were coated with 1mg/mL Oregon green 488nm gelatin and kept for 30min in the dark at room temperature. Coating was fixed for 40min using 0.5% of gluteraldehyde in PBS, then washed 3 times in PBS and sterilized with 70% ethanol for 15min, before extensive washes. $3x10^4$ cells were then seeded, fixed after 4h and immunofluorescence was performed as previously described. Images were taken using an inverted Olympus FV1000 confocal microscope, equipped with a Plan Apochromat N 63x/1.40 oil SC objective.

2.2.6.8 Random migration assay and spider plots

$1x10^5$ cells were plated onto glass bottom 6 well plates and kept 4h (coated) or overnight (uncoated) at 37°C. Timelapse movies (1frame/10min – 17h) from randomly migrating cells were acquired using a Nikon TE2000 microscope, PlanFluor 10x/0.30 objective and equipped with a heated CO_2 chamber. Cells were individually tracked using the MTrackJ plugin from Fiji. The chemotaxis tool from Fiji was used to plot individual x-y points from each track and to generate spider plot.

2.2.6.9 3D Spheroid invasion assay

1.5% agarose was diluted in PBS and microwaved until completely dissolved. 100µL were then pipetted into 96-well plate and kept at room temperature until totally set. Cells were collected as previously described and diluted at $2x10^4$cells/mL. 100µL of cell suspension were added on the top of the agarose plug and cells were grown for 6 days until tightly packed.

At this stage, the spheroid was gently transferred into a new 96-well plate and sandwiched between 2 layers of polymerised matrigel. Normal complemented medium was then added on the top and pictures taken every 24h using an inverted Olympus CKX41 micrcoscope equipped with a CAch N 10X/0.25PhP objective Invasion through the matrigel was calculated as below:

$$Invasion\ index = \frac{Spheroid\ Area_{D6} - Core\ Area_{D6}}{Spheroid\ Area_{D6}} x100$$

2.2.6.10 Circular invasion assay

∅35mm glass bottom dishes were specifically used for this assay. A square-shaped silicon stopper was added at the center of the dish, creating a space devoid of cell. $1x10^6$ cells were collected and seeded as a confluent layer. Once attached, medium was aspirated from the dish, the insert was removed and 250µL of Matrigel diluted 1:1 in ice-cold PBS (final concentration of 4.5mg/mL) was overlaid onto the cells. The dish was transferred back to the incubator for 1h allowing matrigel polymerisation prior to adding fully complemented DMEM on the top of the matrigel layer. Timelapse movies (1frame/15min – 24h) were recorded using a Nikon TE2000 microscope, PlanFluor 10x/0.30 objective and equipped with a heated CO_2 chamber. Invasion was quantified by measuring the invasion of cell within the cell free area created by the silicon insert. Basically, invasion was calculated as follows:

$$Invasion\ index = \frac{Cell\ Area_{\ tn} - Cell\ Area_{\ t1}}{Cell\ \ Area_{\ t1}} x100$$

2.2.6.11 XCelligence spreading assay

E-Plates 16 were coated as previously described with collagen I and equilibrated with fully complemented medium for 30min at 37°C. $5x10^3$ cells were seeded on each well in quadruplicate and the plate was immediately set up into the Acea RTCA DP xCELLigence device. Cell index was measured every 5min for 8h and readings were averaged for each condition.

$$Cell\ index_t = \frac{Rce_t - Rb}{15}$$

Rce_t corresponds to the cell-electrode impedance at time point t and Rb to the background impedance. The nominal impedance value of 15 is constant for this device.

2.2.6.12 Immunohistochemistry staining

Tissues were dissected out from humanly sacrificed mice and fixed overnight in a large volume of 10% formalin. Tissues were embedded into a paraffin block and 2.5µm sections were cut and placed on a glass slide. Sections were dried in a 60°C oven for at least an hour. Most of the stainings were performed using the DAKO autostainer by the histology research service. Otherwise, tissues were manually rehydrated by successive baths in xylene (5min), 100% ethanol (2x1min), 70% ethanol (1min) and finally in tap water. Antigene retrieval was performed using the pressure cooker system by pre-warming a basket containing citrate buffer pH6.0 placed in 600mL of water. Slides were microwaved

for 13min using the full power setting and cooled down on ice for 15min. Slides were quickly washed with TBS-T and incubated 5min with the peroxidase blocking solution. Tissues were washed 3 times in TBS-T and overlaid with the primary antibody diluted at the appropriate concentration in the diluent solution for 2h at room temperature in a humidified chamber. After 3 washes in TBS-T, peroxidase labeled polymer was applied for 30min at room temperature. Sections were washed and 1 drop of the substrate-chromogen DAB was diluted in 1mL of buffer and applied on the tissue until a light brown precipitate was detected. At this stage, slides were washed in TBS-T, dehydrated by passing through an ethanol gradient, counterstained with hematoxylin, and mounted between a rectangular coverslip. Slides were archived using the Leica SNF400F scanner and analysed using the Leica Biosystems software version 4.0.6.

2.2.6.13 Cell labeling with fatty acid and alkyne probes

HEK 293T cells were seeded onto 27-well poly-D-lysine coated plates and transfected using Lipofectamine 2000 reagent. 24h post transfection, cells were serum-starved in DMEM containing 1% fatty-acid free BSA for 30min at 37°C and then incubated with DMEM/1% fatty-acid free BSA containing 100µM azido-palmitate or azido-myristate (synthesised by Prof. Nicholas C. O. Tomkinson and Dr. Kevin R. Munro) for 3hours at 37°C

2.2.6.14 CLICK chemistry, GFP-IP step and detection of S-acylated proteins

Cells were washed twice in ice-cold PBS and lysed with 100µL of 50mM Tris pH8.0 supplemented with 0.5% SDS and protease inhibitors. 80µL of CLICK reaction mix (5µM alkyne dye, 2mM $CuSO_4$, 0.2mM Tris[(1-benzyl-1H-1,2,3-triazol-4- yl)methyl]amine, 4mM ascorbic acid) were added to the cell lysate and incubated 1h at room temperature with end-over-end rotation. GFP-tagged proteins were isolated using the µMACS GFP isolation kit following manufacturer's protocol and resolved by SDS-PAGE as previously described. Protein acylation was quantified by expressing the intensity of the CLICK signal relative to the protein signal.

2.2.6.15 GFP-Trap pulldown and mass spectrometry analysis

Transiently transfected COS7 cells expressing GFP, GFP-FAM49B, FAM49B-GFP or GFP-30-236 were washed twice with PBS on ice and scraped out with 400 µL of lysis buffer. Lysates were kept on ice 30min and thoroughly mixed every 10min. Soluble

proteins were collected after a 10min centrifugation step at 15000rpm and protein concentrations were measured as previously described. 1.5mg of protein were mixed with 25µL of pre-equilibrated GFP-Trap_A beads and incubated 2h at 4°C with gentle agitation. Beads were then washed 3 times with 500 µL of washing buffer.

Purified proteins from biological triplicates were digested with Lys-C (Alpha Laboratories) and trypsin (Promega) on beads as previously described (Hubner et al, 2010). Tryptic peptides were separated by nanoscale C_{18} reverse-phase liquid chromatography using an EASY-nLC 1200 (Thermo Fisher Scientific) coupled online to an Orbitrap Q-Exactive HF mass spectrometer (Thermo Fisher Scientific) via nanoelectrospray ion source (Thermo Fisher scientific). Peptides were separated on a 20 cm fused silica emitter (New Objective) packed in house with reverse phase Reprosil Pur Basic 1.9 µm (Dr. Maisch GmbH). For the full scan a resolution of 60,000 at 250 Th was used. The top ten most intense ions in the full MS were isolated for fragmentation with a target of 50,000 ions at a resolution of 15,000 at 250 Th. MS data were acquired using the XCalibur software (Thermo Fisher Scientific).

The MS Raw files were processed with MaxQuant software version 1.5.5.1 (Cox and Mann, 2008) and searched with Andromeda search engine (Cox et al., 2011), querying both UniProt (UniProt, 2010) *Chlorocebus sabaeus* (13/03/2017; 19,228 entries) and *Homo sapiens* (09/07/2016; 92,939 entries) plus an in-house database containing common proteomic contaminants and the sequence of all GFP-FAM49 constructs used in the experiment. Combined databases were searched requiring specificity for trypsin cleavage and allowing maximum two missed cleavages. Methionine oxidation and N-terminal acetylation were specified as variable modifications, and Cysteine carbamidomethylation as fixed modification. The peptide, protein and site false discovery rate (FDR) was set to 1 %. The common reverse and contaminant hits (as defined in MaxQuant output) were removed. Only protein groups identified with at least one uniquely assigned peptide were used for the analysis. For label-free quantification, proteins were quantified according to the label-free quantification algorithm available in MaxQuant (Cox et al., 2014). Significantly enriched proteins were selected using a t-test analysis with a 5% FDR (Welch's test).

Hits from the mass spectrometry data were submitted for gene ontology analysis to the DAVID database

2.2.6.16 FLIM imaging

Level of active Rac1 was measured by FLIM, based on the emission lifetime of the mTurquoise2 fluorophore. The probe used in this study is a modified version of the initial Raichu Rac1 probe (Martin et al, PloS One in revision). Basically the initial acceptor was switched with the sREACh dark acceptor (super resonance energy-accepting chromoprotein), designed to improve the signal-to-noise ratio (Murakoshi et al., 2008). Probe and control mTurquoise alone were transfected transiently into cells using Lipofectamine 2000 as previously described. $4x10^5$ cells were plated on laminin coated glass-bottom dishes and imaged 4h later. Widefield pictures were acquired using a Nikon FLIM/TIRF system Z6014 equipped with a Plan Apochromat 63x/1.45 oil objective and a 465nm LED. Dishes were fit in a 37°C heated chamber perfused with 5% CO2. Fluorescein was used for the microscope calibration in order to optimise the microscope parameters. Once calibrated, MCP was kept at the same voltage for all readings. For each repeat, lifetime from at least 15 cells was measured. FRET efficiency was calculated by standardising the probe lifetime (σ_{Probe}) to the average lifetime of the donor alone (σ_{mTq}) as follows:

$$FRET\ efficiency\ (\%) = \frac{\sigma_{mTq} - \sigma_{Probe}}{\sigma_{mTq}} x100$$

2.2.6.17 3D MDCK cyst - Culture

MDCK cells were split 1:10 the day before, in puromycin-free medium in order to ensure cells are in proliferation mode. High growth factor Matrigel was thawed in an ice-water slurry for 30min while a 8-well glass bottom chamber was cooled down on ice inside a sterile dish. Chambers were coated by spreading 5µL of undiluted Matrigel over the well and transferred to 37°C incubator for at least 10min. MDCK cells were collected as described before and diluted to $4x10^4$ cells/mL in puromycin-free medium. Suspension was thoroughly mixed by pipetting in order to break down any aggregates that would affect normal cyst formation. Matrigel was then diluted to 4% in normal medium and mixed with the similar volume of cell diluted at $1.5x10^4$ cells/mL, bringing the final Matrigel concentration down to 2%. 300µL of the cells-Matrigel mix was added to each well and the chamber was placed for 5 days at the back of the incubator. In order to reduce the evaporation, a humidified environment was created by placing the Mat-Tek chamber in a ∅10cm dish filled with a small amount of sterile water.

2.2.6.18 3D MDCK cyst – Immunofluorescence and imaging

Medium was aspirated and wells were quickly washed twice with PBS. Cysts were fixed using 4% PFA for 10min, washed, and permeabilised for 10min at room temperature using 0.5% Triton X100 diluted in PBS. PFS was used as blocking solution for 30min at room temperature with gentle shaking. Primary antibodies were diluted in PFS and incubated overnight at 4°C with gentle shaking. The day after, cysts were washed 3 times in PFS at room temperature. Secondary antibodies, nuclear dye and phalloidin were diluted at 1:200 in PFS and incubated for an hour at room temperature before further washes. Chambers were then kept sealed in 0.02% NaN_3-PBS at 4°C until analysis. Cysts were imaged using the Nikon A1R Z6005 confocal microscope using either a Plan Apochromat 20x/0.75 DIC N2 or a Plan Fluor 10x/0.30 DIC L/N1 objective. In order to sharpen up images, factor line averaging was set up at 4. Z-stacks images were acquired with a 4µm increment step from the bottom to the top of the cyst. 3D-reconstruction using the Fiji plugin was used for a better visualisation.

2.2.6.19 *Ex vivo* skin explant preparation and imaging

This protocol is adapted from a previously published method (Mort et al., 2010). Skin from a E15.5 mouse embryo was delicately peeled off and flattened between a nucleopore membrane and a gas permeable 24-well Greiner Lumox plate. In this set up, the epidermis is facing the Lumox membrane, the dermis is in contact with the nucleopore membrane and covered by a fine layer of 100% Matrigel. Plate was incubated 15min at 37°C and 500µL of 10% FBS Phenol-free DMEM was added to each well. Timelapse movies (1frame/5min over 4h) were acquired using a Nikon A1R Z6005 confocal microscope at 37°C/5%CO_2, with a Plan Fluor 10x/0.30 DIC L/N1 objective. Tracking and quantification of cell speed were obtained using the MTrackJ plugin from Fiji.

2.2.6.20 Adhesion and FAAS server

During the 2nd shots of siRNA, B16F1 cells were co-transfected with 5µg of GFP-Paxillin. 24h post transfection, cells were re-plated on laminin-coated glass-bottom dishes and imaged 4h later. Short timelapse movies (1frame/30sec over 30min) were acquired using a Zeiss 880 LSM with AiryScan Z6028 at 37°C/5%CO_2, with a Plan-Apochromat 63x/1.4 oil DIC M27 objective. Movies were processed using the Zeiss software ZEN, version 2.1 SP1 and submitted to the Focal Adhesion Analysis Server (http://faas.bme.unc.edu/).

Threshold of 3.5 units was set up and any GFP-Paxillin positive structures above 15 pixels^2 lasting for at least 5 successive frames were quantified as being a focal adhesion.

2.2.7 Fly work

2.2.8 Maintenance and mating conditions

D. Melanogaster strains bearing a transposable element targeting CG32066 (*D.m.*. FAM49B gene) were obtained from the Vienna Drosophila Resource Center (KK107318 and GD44825). Mattings were set up using virgins with a tubulin-Gal4 driver and males from either a w1118 background (control flies) or the RNAi lines (knockdown flies). Crosses were kept at 25°C with a 12-12h dark-light cycle and flies were flipped into a fresh tube every 2 days.

2.2.9 Hemocyte extraction

L3 stage larvae were collected and quickly washed in PBS and placed in a drop of PBS in order to isolate circulating hemocytes. Basically, the larval posterior part was pulled apart from the rest of the body using 2 forceps. A round forceps was placed at the level of the anterior part and pushed inward into the body so that the inner part is facing outside. Hemolymph was pipetted and adjusted to 200µL with PBS. Cells were then plated in a glass-bottom 24-well plate and processed for immunofluorescence microscopy as described previously.

2.2.10 Mouse work

2.2.10.1 Mouse maintenance, breeding and genotyping

Mice were maintained by the animal house service staff according to the UK home office regulations. Breedings were set up between 1 male and 2 females with the appropriate genotype in order to respect the 3R's. Ear punch was used for genotyping puropose and sent to TransnetYX®.

2.2.10.2 Fascin mouse

Fascin mouse was created by Douglas Strathdee's group and details can be found in appendix.

2.2.10.3 FAM49 mouse

Flox FAM49B mouse was obtained by IVF of frozen sperm (Tm1c variant) obtained from the Canadian Mouse Mutant Repository. C57BL/6 mice were used for the rederivation and maintained as described above.

2.2.10.4 Quantification of PanIN

Quantification were realised on haematoxylin/eosin staining. Area of PanIN, PDAC and cyst were independently measured and a ratio of lesion area over the total area of the pancreas was calculated. Classification of PanIN was based on http://pathology.jhu.edu/pancreas/professionals/DuctLesions.php

2.2.11 Statistical analysis

Datasets were analysed using Graph Pad Prism5 v5.0c. Normality of the distribution was tested using the Agostino and Pearson function. If the dataset failed to pass the test, an arcsine transformation was applied and the normality tested again. Non-parametric tests were only used when dataset failed to pass both tests. Description of the test performed for each experiment can be found in the corresponding figure legends. If not stated otherwise, all experiments were performed at least 3 times corresponding to independent biological replicates. Error bars represent S.E.M (ns: $p > 0.05$, *: $p \leq 0.05$, **: $p \leq 0.01$, ***: $p \leq 0.001$).

3 Evolution and characterisation of FAM49B sequence

3.1 Introduction

Starting a project with no background has been the most challenging part of this study. Indeed, FAM49B has been defined as a protein of unknown function, with a unique uncharacterised DUF1394 domain encompassing the whole protein, except the first 18 N-terminal amino acids and the last 4 amino acids. However FAM49 was shown to have important functions in actin-driven protrusions formation in *D. discoideum* (Jose's thesis) but its function in mammals has not been addressed yet.

We then decided to focus on the only information available that we could trust: the protein sequence. Jose's preliminary work was based on sequence alignment across evolutionarily distant organisms. The overall picture showed a good conservation in the eukaryotic phylum meaning a putative conserved function. However a more thorough and unbiased analysis has not been done.

The aim of this chapter is to look precisely at FAM49 sequences and distinguish residues or domains with high conservation or with similarities to already published motifs. Indeed, we hypothesised that 1) given its putative role in actin dynamics, FAM49 must have co-evolved with main actin regulators. 2) important functional motifs must have been positively selected over time.

3.2 Results

3.2.1 FAM49B is conserved and seems to have co-evolved with Arp2/3 and WASP proteins

In order to get a picture of the diversity of FAM49 sequences that have emerged from evolution, selected candidates from Uniprot were aligned using the Clustal multi-alignment tool (**Appendix 1**). Alignment of FAM49 sequences from evolutionary distant organisms showed an extremely good conservation of the protein and confirmed Jose's previous alignments. For example, *H. sapiens* and *D.discodeum* FAM49 have just below 50% identity. The fact that the level of conservation had not been noticed before convinced us of the importance to follow up this project and extend the study to FAM49B in mammals.
Together, Jose's data and the sequence homology suggest that FAM49 is highly conserved and may have a role in actin dynamics. We therefore compared the evolution of FAM49B with the Arp2/3 complex and the WASP family proteins, keeping in mind that if FAM49 plays an important role for actin dynamics, it would have been co-selected with the main components driving this process. A study published a few years ago about the evolution of WASP family proteins (Veltman and Insall, 2010) was used as a template. Authors concluded their paper with a phylogenetic tree reflecting the co-evolution of Arp2/3 complex subunits and WASP proteins. Basically, the organisms mentioned in this paper were used for a BLASTP search for the presence of FAM49 sequence (**Appendix 2**). We noticed the absence of FAM49 in chromalveolates and plants whereas both Arp2/3 and WASP proteins were conserved in the second half of the plant phylum. The only plant with a putative FAM49 is *A. amincola* and it might be interesting to look at this candidate for further study and characterisation. Conversely, we noticed a parallel evolution between FAM49, Arp2/3 and WASP proteins in the other phyla. Together, we can then say that presence of FAM49 seems to be specific of the excavates and the unikonts phyla. It also appears that FAM49 has co-evolved with key actin dynamics players suggesting that they might belong to and regulate the same pathway.

3.2.2 Notable features of FAM49B sequence

Looking at the good overall sequence conservation, we went on and looked precisely at the sequence of FAM49B. We started our analysis by the common DUF1394 domain that runs across most of the protein sequence. We took the advantage of the hidden Markov models (HMM) logos online tool (Wheeler et al., 2014). HMM logos are a useful tool to summarise and represent complex alignments in an unbiased way. The output is a

graphical alignment, displaying a stack of letters according to their distribution and conservation at a specific position across the entire dataset. The height of the stack reflects the relative entropy at one position, whereas the height of one letter represents the letter frequency. This visual representation allowed us to look over various DUF1394 domains coming from a seed or a full Pfam dataset. The seed dataset contains an alignment of 38 sequences from which the family is built using Pfam reference proteomes. The full dataset represents over 900 sequences from the entire Pfam database and can be found in appendix 3. However, DUF1394 domains from CYFIP versus FAM49 proteins cannot be distinguished. From the HMM logo, regions with a minimum of 5 consecutive residues with the highest letters were considered as highly conserved motifs. Eight portions were retrieved as fully conserved in the seed dataset (**Figure 3-1**).

Among those, 4 motifs are present in all the DUF1394 sequences (occupancy=1), whereas the low occupancy value from the others suggests they show up only in a small subset of sequences (occupancy=0.03) and therefore, are unlikely to be conserved. However, only one of these motifs is retrieved from the HMM logos generated using the full Pfam dataset (Q-N-D-F-S-Y-Y-R/K-R). Although not present across every single sequence, it has the highest occupancy value of the dataset, peaking at 0.91 (**Figure 3.1 - inset**). Together analysis of the HMM logo suggests a positive selection of a highly conserved 9-amino acid sequence that is found in most of the DUF1394 domains present in the Pfam database. This sequence stretches from residue 153-161 in *H. sapiens* FAM49A/B and unsurprisingly, multi-alignment confirmed its wide conservation across divergent organisms (**Appendix 1**). The 2 last arginine residues stand out from the alignment with 100% identity in FAM49 proteins and 100% similarity between FAM49B and CYFIP proteins and kept our attention. Indeed Arg161 is fully conserved whereas Arg160 is replaced by a lysine in CYFIP, although both are positively charged, so with similar chemical properties.

Moreover, using our CLUSTAL alignments and some of Jose's previous work, we also noticed that the second glycine is highly conserved (**Figure 3.2 - A**). Presence of a glycine as the second residue of the protein is commonly seen as signal for protein myristoylation (Chamberlain and Shipston, 2015). Myristoylation is an irreversible process where a myristate group (C14:0 lipid) is added by a N-myristoyl-transferase (NMT) and mediates a weak interaction to the plasma membrane. However, stable interaction with the plasma membrane requires an additional signal.

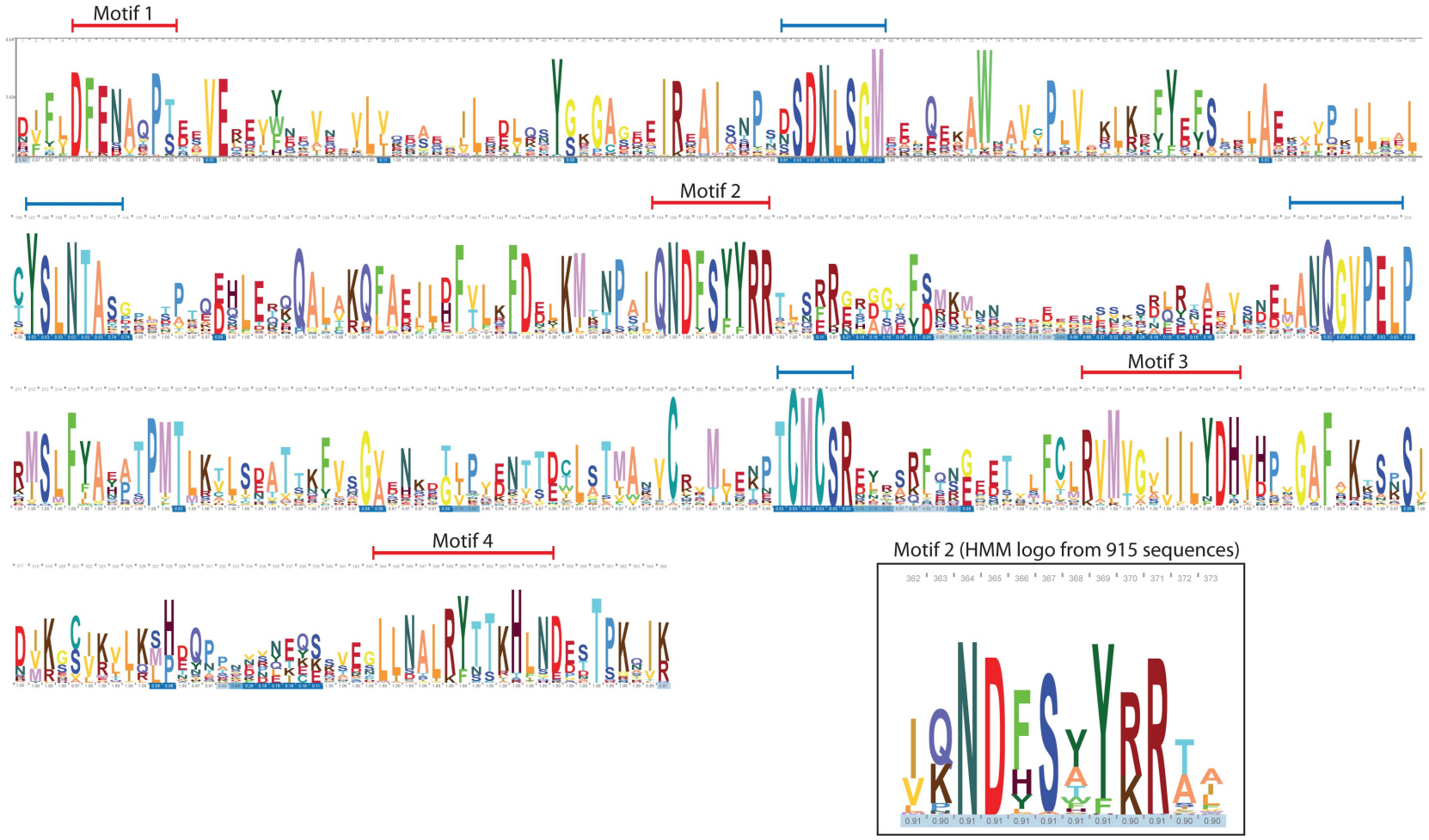
Motif 1
Motif 2
Motif 3
Motif 4
Motif 2 (HMM logo from 915 sequences)

Figure 3-1: HMM logo of the DUF1394 domain
HMM logo was generated by feeding a 38-sequence seed dataset of the DUF1394 domain to Skylign. Letter stack represents the conservation of the residue at this position across the dataset. Occupancy score is also mentioned below each letter and is a readout of the presence of a letter across the dataset, ranging from 0 (no present) to 1 (present). Highly conserved motifs have been highlighted in blue (low occupancy) and red (high occupancy). Among all the red motifs, motif 2 was the only portion with high conservation/high occupancy. Motif 2 alignment of the full dataset (915 sequences) is represented on the side.

This can either be a hydrophobic patch near the putative myristoylation site or the addition of another lipid that stabilises the myristoylated protein at the membrane. In the latter case, palmitoylation (addition of a C16:0 lipid) is a common second signal. We then sought for potential lipidation events across FAM49B sequence using CLICK chemistry. This technique allows to metabolically label proteins using azide-analogues (azide-myristate or azide-palmitate). Typically, the lipid is added onto each modified protein with the free azide able to react with a labelled metabolite. Immunoprecipitation of the protein of interest followed by western blot allowed us to investigate the post-translational modifications occurring across FAM49B sequence. FAM49B-GFP was used over the N-terminal tagged protein because of the close proximity between the Gly2 and the GFP tag. Indeed, depending on the folding of the fusion protein and because of the steric hindrance, NMT might not be able to access to and modify the Glycine.

Following GFP-pull down, we were not able to distinguish any signal coming from control GFP-transfected cells incubated with either azide-C14:0 or azide-C16:0. However, a strong signal was detected for the fusion protein, indicating that FAM49B gets both myristoylated and palmitoylated (**Figure 3-2 - B**). The next step was to determine what residues were modified. This question was addressed by performing point mutation along the protein sequence. As mentioned earlier, myristoylation only occurs on N-terminal glycine residue therefore, a point mutation mediating the transition Gly->Ala (G2A mutant) was introduced. Interestingly, expression of this construct in cell resulted to a shifted migration on a SDS-PAGE gel (**Figure 3-2 - C**). It is quite commonly accepted that post-translational modifications affect protein migration, especially because of differential charges present on the modified versus unmodified protein. This differential running pattern was also observed using an alternative *in vitro* approach (**Figure 3-2 - D**). Bacterially expressed FAM49B-$GST_{\Delta Met1}$ was purified so that the glycine is the 1st N-terminal residue. This is a trick to pass over the methionine cleavage happening *in cellulo* to allow PTMs. C-terminal tagging strategy was also preferred for a similar reason as mentioned above for the GFP construct. Incubation of the purified protein with NMT and in the presence or not of Myristoyl-CoA shows a similar differential running pattern. In this case, the protein mixed with the myristoyl-CoA migrated slightly faster compared to the un-myristoylated protein. In order to fully confirm that this shift was a consequence of the myristoylation, these samples were sent for further analysis but mass spectrometry was unable to detect any myristoylation event, even on the positive control (Lck protein incubated with Myristoyl-CoA and NMT). We suspected a technical issue with the column used for the analysis that might retain hydrophobic proteins. This analysis might require a different mass spectrometry strategy in order to ascertain the modification of the protein (i.e. SILAC).

Based on these observations, I directly asked whether FAM49B was modified and performed the CLICK reaction with both WT and mutants FAM49B (**Figure 3-2 - E**). Incorporation of C14:0 analogue was quantified in our different constructs. CLICK signal level from the G2A mutant was close to the background level, meaning that myristoylation of the protein is specific to the Gly2 and mutation of this residue abrogates the protein myristoylation. Once again, a shift of the G2A mutant compared with the other constructs was observed. Studying palmitoylation was not as straightforward and this is mainly due to the diverse range of putative residues present. Palmitoylation is a dynamic and reversible event, preferentially occurring on cysteine but glycine palmitoylation has also been described (Kleuss and Krause, 2003). FAM49B contains 5 cysteine residues at position 10, 223, 231, 253, 284 (**Figure 3-2 - A**). Despite its lack of conservation Cys10 was initially a good candidate as we thought it would have been close enough from the Gly2 to strengthen the interaction of the protein at the membrane. It is also one of the predicted palmitoylated residues in FAM49B when using a palmitoylation prediction tool (www.swisspalm.epfl.ch). However, C10A mutant was still showing a strong CLICK signal in the preliminary experiment already performed **(Figure 3.2 - F**). Interestingly, palmitoylation of the G2A mutant was abrogated, suggesting that myristoylation is crucial for further modification and confirms the 2-step model for protein acylation. In order to map the palmitoylation site, individual point mutants of each cysteine were created. Among them, Cys231 is extremely well conserved whereas Cys223, Cys253 and Cys284 show a fairly good conservation, although not as good as the previous one (**Figure 3.2 and 3.2 - A**). Results from the CLICK assays didn't show any significant reduction of the CLICK signal (**Figure 3.3**), bringing to the hypothesis that more than one cysteine must be modified. A FAM49B-GFP$_{Cys->Ala}$ mutant was designed but despite many different conditions and cell lines tested, none of them were able to express this construct. This was really unfortunate for our purpose but also not totally surprising as cysteines are important residues for protein folding by participating to the formation of disulphide bridges. So mutations to any other amino acid might affect protein stability and lead to the degradation of the construct.

Together, our data show that FAM49B is myristoylated and palmitoylated. We mapped the myristoylation site on the conserved glycine 2. At this point however, we cannot conclude concerning the residue(s) involved in palmitoylation and we are currently working on this specific question. We hypothesised that several cysteines are involved and double/triple mutant will next be investigated.

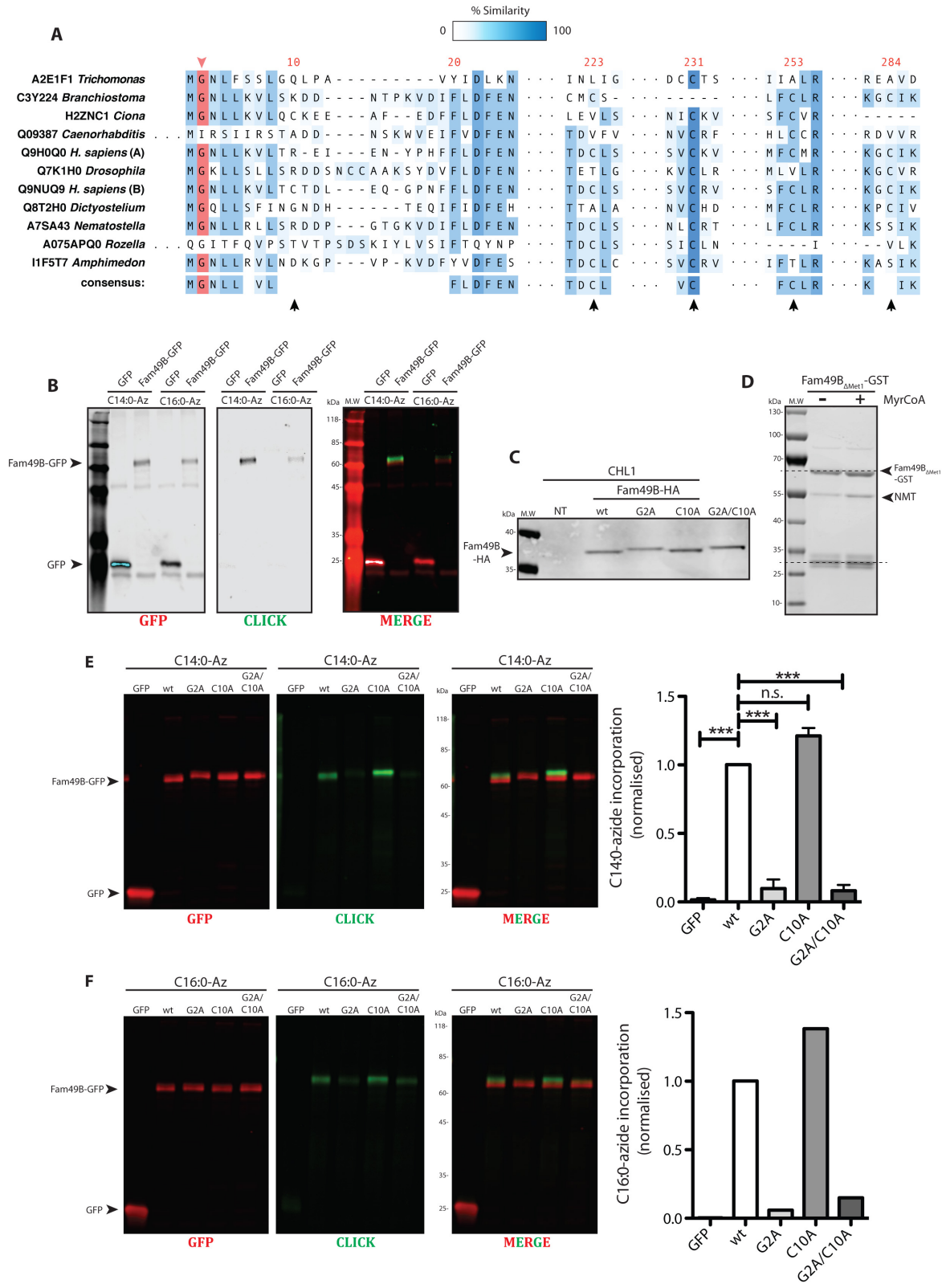

Figure 3-2: Post-translational modifications of FAM49B

A – Selected fragments from the protein alignments of FAM49 homologues from different organisms. UniProt accession number is mentioned for each protein. The full alignment is presented in **appendix 1**. In order to facilitate the nomenclature, red numbering above the alignment is based on the human FAM49B sequence. Conserved glycine 2 is highlighted in red and corresponds to a putative myristoylation site. Cysteine residues are pointed with a black arrowhead.

B – Western blot membrane from a CLICK experiment. HEK293T cells were transfected with GFP or FAM49B-GFP and incubated either with C14:0-Azide (myristate analogue) or C16:0-Azide

(palmitate analogue) for 3h. GFP-tagged proteins were pulled down and CLICK reaction performed before resolving the samples on a SDS-PAGE gel. Membranes were blotted against GFP (red) or the CLICK (green). Picture of the merge channel is also presented with the corresponding molecular weights on the side.

C – Western blot analysis from the different FAM49B-HA mutants. Lysate from control CHL1 cells (NT) or transfected with wild type FAM49B-HA (wt), single G2A or C10A FAM49B-HA mutant or double G2A/C10A FAM49B-HA, were resolved by SDS-PAGE and blotted against HA-tag. Molecular weights are displayed on the side.

D – *In vitro* myristoylation assay. Purified FAM49-$GST_{\Delta Met1}$ was incubated overnight at RT with NMT in the presence (+) or absence (-) of MyrCoA. Samples were loaded on SDS-PAGE and Coomassie stained. Top black dotted line highlights the migration shift of the GST-tagged protein compared to a contaminant band (bottom black dotted line). Molecular weights are displayed on the side.

E - CLICK experiment looking at myristoylation of the different FAM49B-GFP constructs transfected into HEK293T cells and incubated with C14:0-Azide for 3h. Individual channel and merge picture are presented with the corresponding molecular weights on the side. Protein acylation was quantified from 3 independent experiments by comparing the CLICK signal relative to the protein signal, and normalised to the wild-type control. One-Way ANOVA with Tukey test was applied. (n.s. $p > 0.05$, *** $p < 0.001$).

F - CLICK experiment looking at palmitoylation of the different FAM49B-GFP constructs transfected into HEK293T cells and incubated with C16:0-Azide for 3h. Individual channel and merge pictures are presented with the corresponding molecular weights on the side. Protein acylation was quantified from only one experiment by comparing the CLICK signal relative to the protein signal, and normalised to the wild-type control.

Both palmitoylation and myristoylation suggest a partial localisation of FAM49B at the plasma membrane during the protein lifetime. It has however been impossible to localise the endogenous protein as none of the commercially available antibodies have shown specific staining. Indeed, cytosolic staining was obtained in both control and *fam49b* knockout cells under different antibody concentrations and fixation conditions. This problem is specifically addressed at the moment as we are currently in the process of purifying our own antibody. Meanwhile a tagging strategy was preferred, always keeping in mind that small tags might be more relevant for a localisation study, in order to not disrupt PTMs. FLAG tag was an initial good candidate for its fairly small tag (8 amino acids) and easy detectability by immunofluorescence. However, among the different cell lines tested (B16F1, B16F10, CHL1, MDCK), only COS-7 cells would tolerate more than twice the endogenous level (**Figure 3.4 - A and B**). FAM49B-FLAG-transfected COS-7 cells were plated on laminin and stained against the FLAG-tag. Population had two distinct localisation of the tagged-protein. Signal was either exclusively cytosolic or accumulation of membranous FLAG staining at cell protrusions was also noticed. In the latter case, staining seems to follow a gradient fading on each side of the protrusion and across the cell. Quantification of pixel intensity of the Phalloidin and FLAG-tag staining across different transfected cells clearly reflects this gradient, peaking at the tip of the protrusion (**Figure 3.4 - A and C**). Also, FAM49B colocalises with both F-actin and WAVE2

(**Figure 3.4 - A and D)**. The correlation between the FLAG positive areas and the protrusion is however worth noticing. Characterisation of the FAM49B^{G2A}-FLAG mutant, defective in myristoylation and palmitoylation, has not been investigated but loss/reduction of the membrane staining and colocalisation with WAVE2 would be expected and would reflect its lack of membrane targeting sequence.

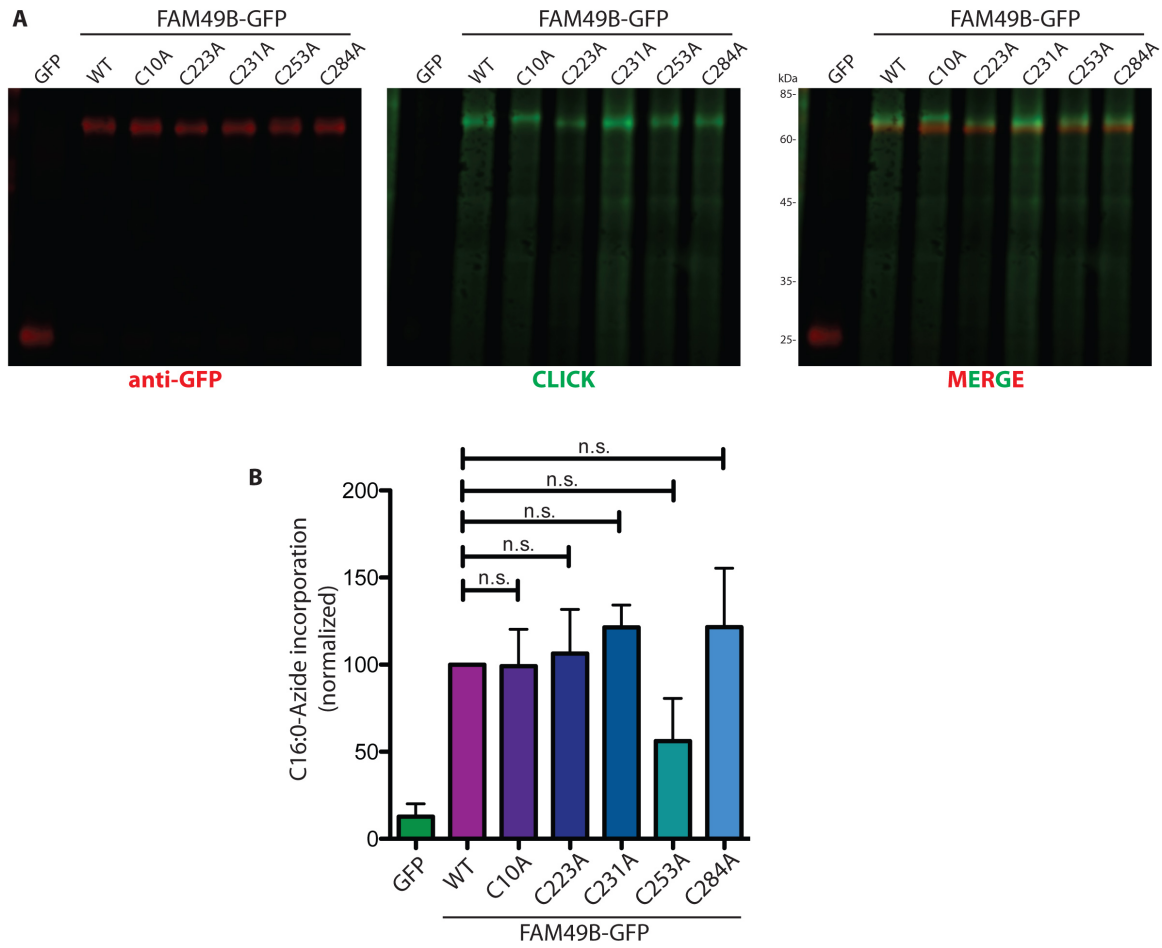

Figure 3-3: Palmitoylation events on FAM49B
A - Western blot membrane from a CLICK experiment. HEK293T cells were transfected with GFP or wild type FAM49B-GFP (WT) or C>A point mutant FAM49B-GFP and incubated with C16:0-Azide (palmitate analogue) for 3h. GFP-tagged proteins were pulled down and CLICK reaction performed before resolving the samples on a SDS-PAGE gel. Membranes were blotted against GFP (red) or the CLICK (green). Picture of the merge channel is also presented with the corresponding molecular weights on the side.

B - Protein acylation was quantified from 4 independent experiments by comparing the CLICK signal relative to the protein signal, and normalised to the wild-type control. One-Way ANOVA with Tukey test was applied. (n.s. $p > 0.05$)

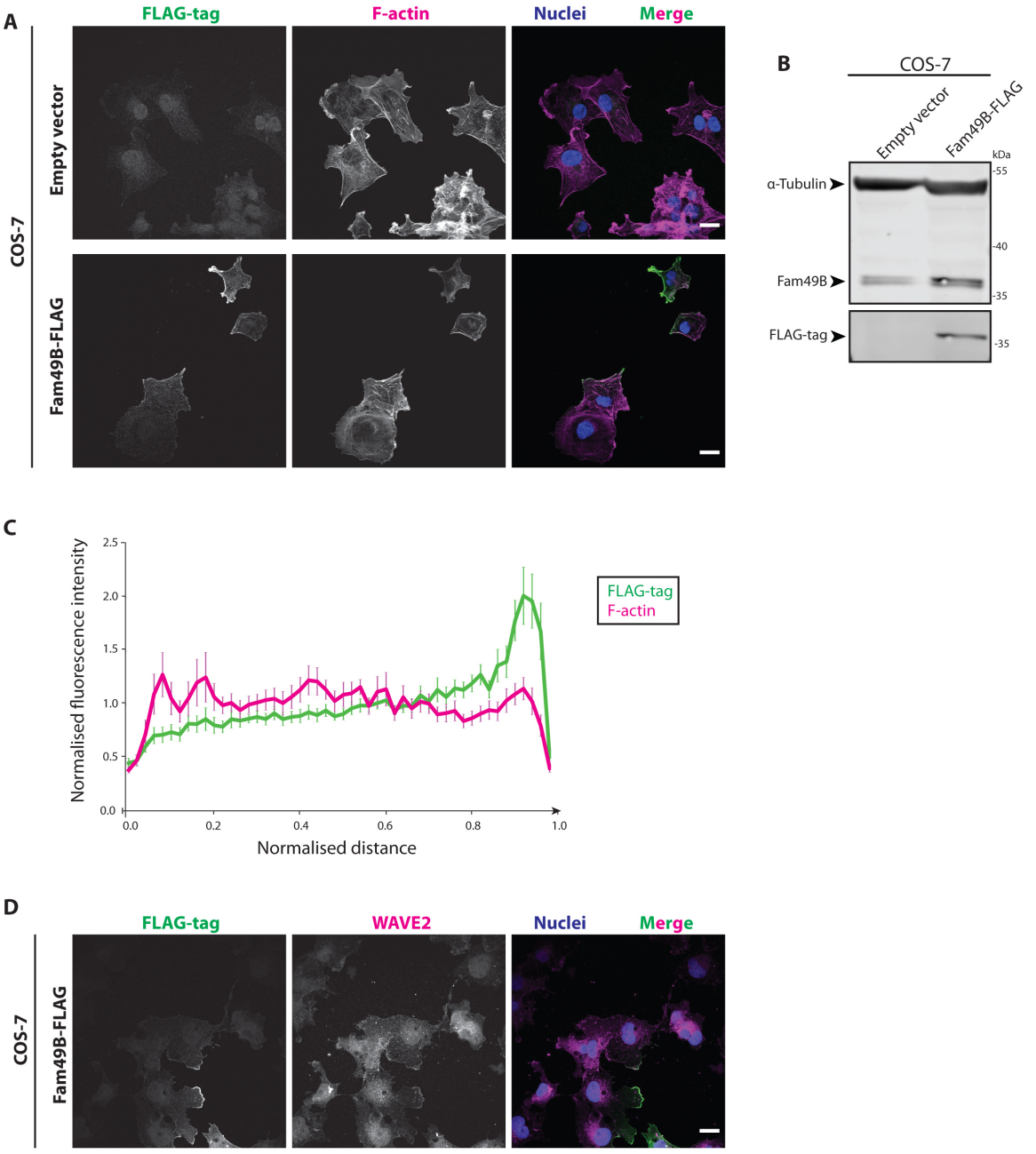

Figure 3-4: Localisation of FAM49B-FLAG

A – Immunofluorescence of COS7 cells transfected with empty vector (pcDNA3.1) or FAM49B-FLAG. Cells were plated on laminin for 4h, fixed and stained for FLAG-tag (green) and F-actin (magenta). Scale bar = 10 µm.

B – Western blot from COS7 cells, transfected with empty vector (pcDNA3.1) or FAM49B-FLAG. Lysates were resolved on a SDS-PAGE gel and membranes were blotted against FLAG-tag, FAM49B and α-Tubulin. Molecular weights are displayed on the side.

C – Fluorescence intensity quantification of FLAG-tag (green) and F-actin (magenta) staining, across 17 transfected cells (red arrow from panel B). Intensity is normalised for each channel with the average intensity along the red arrow. Protrusive end =1 and opposite end = 0. Error bar represent S.E.M.

D - Immunofluorescence of COS7 cells transfected with FAM49B-FLAG. Cells were plated on laminin for 4h, fixed and stained for FLAG-tag (green) and WAVE2 (H-110) (magenta). Scale bar = 10 µm

3.3 Discussion

In this chapter, we showed that FAM49B appears as a conserved protein that has co-evolved in parallel to the Scar/WAVE complex and the Arp2/3 complex in most of the eukaryote kingdom. *H. sapiens* FAM49B is myristoylated and palmitoylated allowing its localisation at the plasma membrane where actin polymerisation is initiated. Also, Jose Batista's work shows that the DUF1394 domain is only shared between the Scar/WAVE complex member CYFIP and FAM49 proteins. Looking at these alignments and some additional sequence analysis, we noticed a specific motif (Q-N-D-F-S-Y-Y-R/K-R) with a striking conservation across evolution.

Interestingly, the homologue of Arg161 in CYFIP (Arg190) is localised at the surface of an exposed loop of the Scar/WAVE complex and was involved in Rac1 binding (Chen et al., 2010). Mutation of this arginine to an acidic residue abrogates the interaction between the WRC and active Rac1 in a pulldown assay. This conserved motif does not show any kind of similarity with the well-characterised CRIB (Cdc42/Rac interactive binding) domain. CRIB domain consists of ~16 conserved amino acids corresponding to the following sequence: I-S-X-P-$(X)_{2-4}$-F-X-H-X-X-H-V-G (Burbelo et al., 1995) and is part of Rac/Cdc42 effectors. For example, PAK peptides containing this motif show affinity to $Rac1^{Q61L}$ starting from 50 nM up to a micromolar range, depending on the length of the peptide (Thompson et al., 1998). Therefore, CRIB domain binds with high affinity to the GTP-bound conformation of GTPase over the inactive GDP-loaded version. However, such a domain is absent from the DUF1394 domains. Alternatively, a conserved sequence containing 2 consecutive basic amino acids and mediating CYFIP1-mediated Rac1 binding is conserved in FAM49B. This can reflect a functional similarity between the 2 proteins.

It is now well accepted that the Scar/WAVE complex is acting at the plasma membrane upon recruitment/activation by Rac1 and together, mediate actin polymerisation. Indeed, although prenylation of the Scar/WAVE complex has not been described, Rac1 was shown to be geranyl-geranyl modified at Cys189 allowing its localisation at the membrane (Kinsella et al., 1991). Additional palmitoylation of Rac1 on Cys178 drives a full activation of the GTPase and its stabilisation at the membrane (Navarro-Lerida et al., 2012). This allows spatio-temporal regulation of the GTPase. Indeed, palmitoylation is a reversible event, allowing cycles of palmitoylation/depalmitoylation, thereby mediating different signalling cascades (Chamberlain and Shipston, 2015). Using immunofluorescence, we were able to confirm the localisation of FAM49B at the membrane, but only in a subset of the population due to the low transfection efficiency

(<5% of the total). In some cases, FLAG-staining was cytosolic and this different localisation might reflect different activation state during the protein lifespan (when the protein is not needed/inactive).

How FAM49B gets targeted to the membrane has been an exiting question throughout this PhD. Multiple proteomic studies looking at global post-translational modifications, have already found FAM49B as being myristoylatied/palmitoylated in their screen (Thinon et al., 2014; Wilson et al., 2011). Martin *et al* (Martin et al., 2011) designed a pulse-chase experiment combined with SILAC analysis to look at the dynamic palmitoylation signature of the proteome. Interestingly, this study characterises FAM49B as an outlier of their dataset and concludes that it might reflect an extremely high palmitoylation turnover of the protein. Here we suggest that upon activation of the protein, myristoylation of FAM49B irreversibly anchors the protein at the membrane and that cycles of palmitoylation further stabilise FAM49B and regulate its activity. Our data suggest that the protein is multi-palmitoylated as CLICK signal was not significantly decreased after mutating individual cysteine. Presuming that multiple cysteines would be modified, and given the large number of possible combinations that this would imply, this part is still being investigated. Also, we cannot rule out that FAM49B belongs to the subset of glycine-palmitoylated protein family. Together, these modifications may allow the protein to be spatially close from the Scar/WAVE complex and Rac1.

An althernative model would be that FAM49B gets modified while being synthesised and would be able to hide the myristoyl group within an internal hydrophobic pocket of the protein. This model is called myristoyl switch and enables a pool of inactive cytosolic protein that is ready to respond to a stimulus. The myristoyl group is most frequently released following interaction with another protein that leads to changing the conformation of the myristoylated protein. In order to test this hypothesis, Peter Thomason expressed full length or truncated version of the N-terminal region of FAM49B (residue 1-15 or 1-27) with a C-terminus GFP tag into wildtype *D. discoideum* cells. As previously observed, full length protein did not show any specific localisation whereas 1-15-GFP strongly localised to endomembranes in Ax3 cells. Interestingly, the longer truncation, 1-27-GFP showed a decrease of intensity at endomembranes, suggesting that this construct might already be able to hinder membrane localisation. It is interesting to note that a hydrophobic patch, mostly formed by leucine residues, lies between Gly2 and Cys10. This would be enough to stabilise the membrane interaction, along with a potential palmitoylation of the Cys10, supporting the 2-signal model for membrane targeting (Wright et al., 2010). Based on this model, the endomembrane localisation is consistent with a weak affinity of myristoylated-

only protein. Weak signals tend to target protein to abundant cellular membranes. A second signal - such as palmitoylation – will trap the protein by increasing its hydrophobicity. In the case of palmitoylation, this trapping occurs at the membrane where the palmitoylating enzymes reside. Since zDHHCs (S-acyltransferases) are mainly, but not exclusively, enriched to the endoplamic reticulum and Golgi membranes (Gorleku et al., 2011; Lemonidis et al., 2015), protein trapping in these compartments allows its modification and newly modified proteins can then continue their journey and traffic to the plasma membrane. The point mutant 1-27-GFP^{G2A} is exclusively cytosolic, suggesting that the Glycine 2 is sufficient to drive the membrane localisation of the construct. These data are still preliminary but it would be interesting to get similar constructs for mammalian expression. The mutated constructs will also be analysed by CLICK chemistry and compared with the full-length version. Finally, we will look at shorter truncations in order to restrict the minimum membrane-binding site before performing alanine scanning of the sequence.

Moreover, during the *in silico* analysis of *D.discoideum* FAM49, the sequence was submitted to an online structure homology prediction tool (Phyre2 - http://www.sbg.bio.ic.ac.uk). Similarly to i-TASSER, this software uses the available protein structures with an identified PDB to apply it to the query sequence and found the closest template that matches to the putative protein structure based on primary sequence and biochemical properties. We were intrigued to see that the second hit with the highest structural homology was the viral protein H7 of vaccina virus (PDB c4w5xA) that contains a phosphoinositide-binding fold. This also showed up in human FAM49B Phyre2 model but with a lower confident score. Together, we think than the N-terminus part of the protein mediates membrane tethering and we are currently investigating this.

Based on the protein sequence and similarity to CYFIP, we then hypothesised that the DUF1394 domain might be a new Rac1-binding domain and play a role in Rac1 signalling.

4 Investigating the cross-talk between FAM49B and the small RhoGTPase Rac1

4.1 Introduction

The previous observations motivated us to understand the functions of FAM49B and whether the conservation between the DUF1394 domains of FAM49B and CYFIP, especially in the Rac1 binding region of CYFIP is significant. The link with Rac1 was also emphasised by the initial mass spectrometry experiment. Indeed, GFP-NAP1 used as bait also pulled down Rac1 (falling just above the 5% FDR Welch's test) (**Figure 1-8**). This could come from either a direct interaction between the Scar/WAVE complex and Rac1, or a binding of Rac1 with any of the significantly enriched candidates.

Rac1 oscillates between an inactive GDP-bound and an active GTP-bound state. This dynamic activity is reflected by its ability to bind to different proteins, mostly effectors or GAPs/GEFs. Rac1 activation is downstream of the growth factor signalling pathway and occurs within 5-15 min depending of the cell type and the method used for the stimulation (Fujii et al., 2013; Kurokawa et al., 2004; Royal et al., 2000). Activation is mostly based on GEF proteins that allow rapid dissociation of GDP from the nucleotide pocket. Subtle re-arrangement of Rac conformation in key motifs (switch I and II) favours Rac1 binding to downstream effectors that contain some specific motifs, including the CRIB domain and rasGAP-related domain, which are unrelated to any conserved motif of the DUF1394 domain. Turning off Rac1 signalling is a much slower process and so far GAP proteins are thought to be the only major actors involved.

In this chapter, I used a combination of molecular biology, biochemistry and imaging to decipher the biological relevance of the putative Rac1 binding site of FAM49B *in vitro* and *in cellulo*.

4.2 Results

4.2.1 FAM49B binds active Rac1 mediated by a central domain containing the two conserved arginine residues

As part of Hybrigenics services for a two-hybrid screen, I gained access to their archived database entries in which FAM49B appeared as an interactor. Surprisingly, FAM49B had previously only been found in screens where full length $Rac1^{G12V,\ C189S}$ was used as bait (**Figure 4-1 - A**). Point mutation on the cysteine 189 abrogates Rac1 prenylation and so is more appropriate for a yeast 2-hybrid nuclear screen. This interaction was consistent in over 10 various cDNA libraries (human, mouse and rat), although not very strong according to the statistical analysis (**Figure 4-1 - B).**

This interaction was tested by pulldown assay using full length FAM49B but the binding was extremely weak, close from the background level and inconsistent (not shown). However, based on two-hybrid data, a minimum fragment sufficient for Rac1 binding was mapped between residues 20-204 or 39-223 of FAM49B (**Figure 4-1 – B & C**). Both fragments contain the conserved sequence of the DUF1394 domain. N and C terminal GFP-tagged constructs were designed and used in a GST-Rac1 pulldown assay but failed to bind to Rac1 (not shown). Looking more carefully at the predicted secondary structure of FAM49B, we noticed that the previous constructs started/finished in the middle of putative structurally folded regions of the protein (**Figure 4-1 – C**). We re-designed our GFP-tagged construct so that the first and last amino acids (Glu30 and Glu236) are respectively at the beginning and the end of a predicted alpha-helix (**Figure 4-1 – C & D**). We repeated our GST-pull down assay with this optimised Rac1 binding domain (termed RBD from now on). Bacterially expressed GST, GST-Rac^{WT} and GST-Rac^{Q61L} were purified and immobilised on sepharose beads. Lysates from CHL1 cells expressing GFP only, eCFP-CRIB-PBD (CRIB Pak Binding Domain), or GFP-RBD were incubated with a similar amount of GST-tagged proteins, pulled-down and resolved by SDS-PAGE. As expected, GFP does not bind to either GST-tagged proteins whereas the CRIB domain shows a weak interaction to Rac^{WT} and strongly interacts with Rac^{Q61L}. The FAM49B RBD shows a weak but consistent interaction specific to active Rac1 (**Figure 4-2 – A & B**).

A

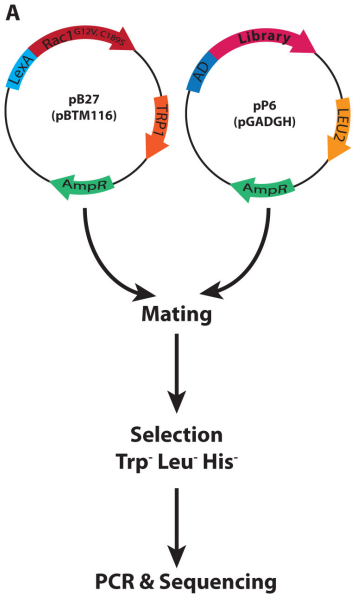

B

Library	Int. dom. (a.a)	Conf. score	# of fragments
Human bone marrow endothelial cells	2-324	D	3
Human breast tumour epithelial cells	7-210	D	1
Human fetal brain	37-246	D	1
Human embryonic stem cells	39-223	B	5
Human testis	21-206	D	1
Human reconstituted skin	39-324	D	2
Human leucocytes and act. mononuclear cells	9-324	D	2
Human fibroblasts	20-204	B	13
Human ventricle and embryo heart	19-217	D	7
Human normal lung	39-224	D	1
Human thymocytes	34-210	B	3
Mouse adult brain	39-223	D	1
Mouse pancreas	39-208	out-of-frame	2
Rat bloc posterior	24- ?	D	1

C

Human Fam49B

```
  CCHHHHHHCCCCCCCCCCEEEECCCCCCCHHHHHHHHHHHHHHHHHHHHHHHHHHHCCCCHHHHHHHHCCCCC
1 MGNLLKVLTCTDLEQGPNFFLDFENAQPTESEKEIYNQVNVVLKDAEGILEDLQSYRGAGHEIREAIQHPAD 72

 HHHHHHHHHHHHHHHHHHHHHHHHHHHHHHHHHHHHHHHHHHHCCCCCHHHHHHHHHHHHHHHHHHHHHHCC
73 EKLQEKAWGAVVPLVGKLKKFYEFSQRLEAALRGLLGALTSTPYSPTQHLEREQALAKQFAEILHFTLRFDE 144

 CCCCCCCCCCCCCHHHHHHHCCCCCCCCCCCCCCCCCHHHHCCHHHHHCCCCHHHHHHHHHHHHHCCCCCCC
145 LKMTNPAIQNDFSYYRRTLSRMRINNVPAEGENEVNNELANRMSLFYAEATPMLKTLSDATTKFVSENKNLP 216

 HHHHHHHHHHHHHHHHHHHCCHHHCCCCCHHHHHHHHEHHHHEEEEECCCCCCCCCECCCCCCCHHHHHEEH
217 IENTTDCLSTMASVCRVMLETPEYRSRFTNEETVSFCLRVMVGVIILYDHVHPVGAFAKTSKIDMKGCIKVL 288

 CCCCCHHHHHHHHHHHHHHHHCCCCCCCHHHHHHHCC
289 KDQPPNSVEGLLNALRYTTKHLNDETTSKQIKSMLQ 324
```

H = α-helix
E = Extended strand
C = Other

D

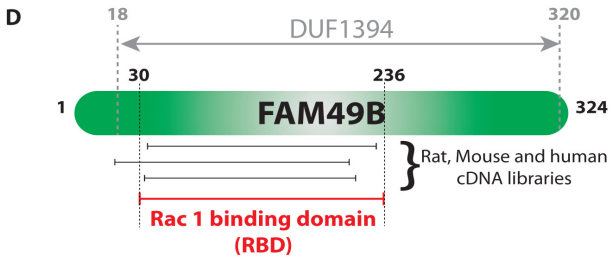

Figure 4-1: Two-hybrid strategy and screen analysis
A – Prey (pB27) and bait (pB6) vectors used for the two-hybrid screen (Hybrigenics Services). Vectors were incorporated using a mating strategy and cells selected in medium depleted in Tryptophane (Trp), Leucine (Leu) and Histidine (His).

B – Summary table of the two-hybrid screen presenting the library with a positive interaction between Rac1 $^{G12V, C189S}$ and FAM49B. Interacting domains were restricted by PCR and confidence score was assigned for each hit. High confidence hits are highlighted in red (see Materials and Methods).

C-D – Minimal interacting sequence found by two-hybrid was aligned with the putative secondary structure of human FAM49B (C) or on the graphical representation (D). Interacting fragment was adjust to start/finish at the beginning/end of a secondary structure. Rac-binding domain (RBD) used throughout this assay is highlighted in C with a grey background

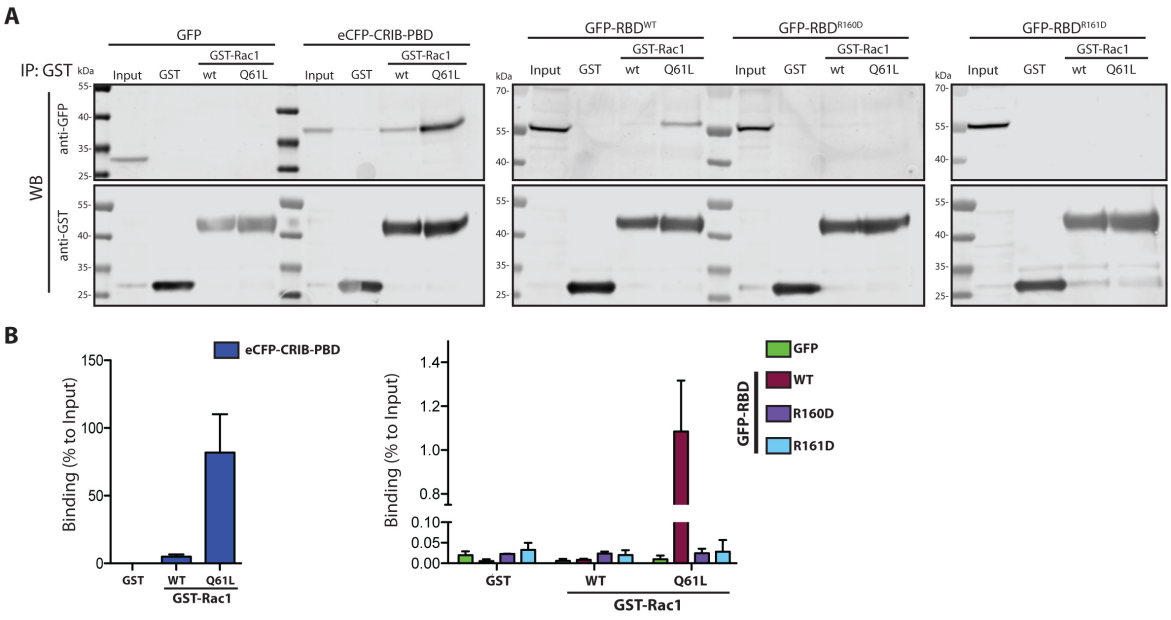

Figure 4-2: FAM49B interacts with active Rac1
A – B – GST pull down assay of immobilised GST, GST-Rac^{WT} and GST-Rac^{Q61L} mixed with lysate from CHL1 cells expressing GFP, eCFP-CRIB-PBD, GFP-RBD^{WT}, GFP-RBD^{R160D}, GFP-RBD^{R161D}. Membranes were blotted against GFP (cross-reacts with eCFP) and GST. Molecular weights are displayed on the side.

Three independent experiments were quantified based on densitometry reading and standardised to the input loading (B). Error bars represent S.E.M.

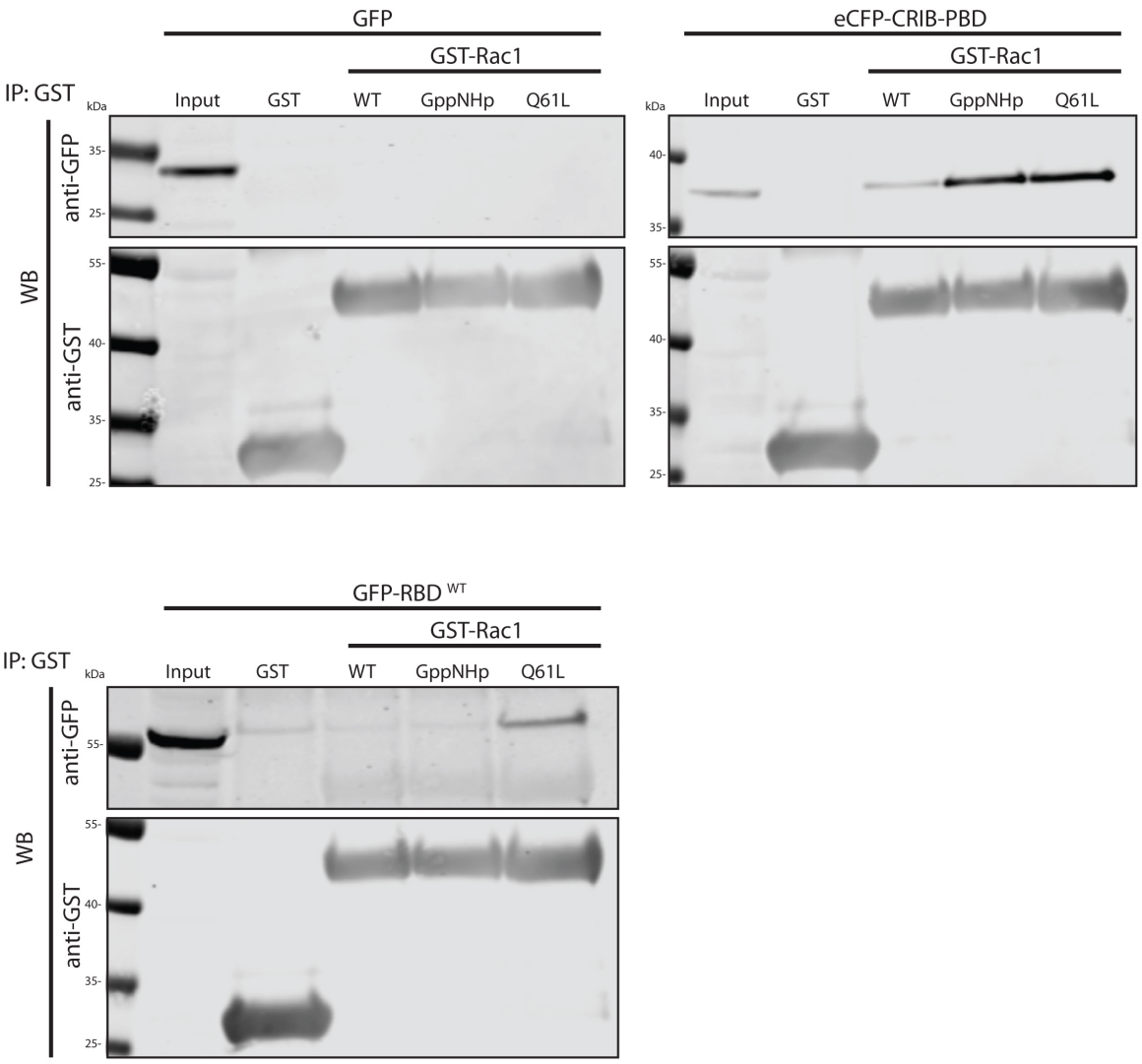

Figure 4-3: FAM49B binds to mutant Rac1 ^{Q61L} but not to GppNHp-loaded Rac1 ^{WT}
GST pull down assay of immobilised GST, GST-Rac^{WT}, GST-Rac^{WT} loaded with GppNHp and GST-Rac^{Q61L} mixed with lysate from CHL1 cells expressing GFP, eCFP-CRIB-PBD, GFP-RBD^{WT}. Membranes were blotted against GFP (cross-reacts with eCFP) and GST. Molecular weights are displayed on the side.

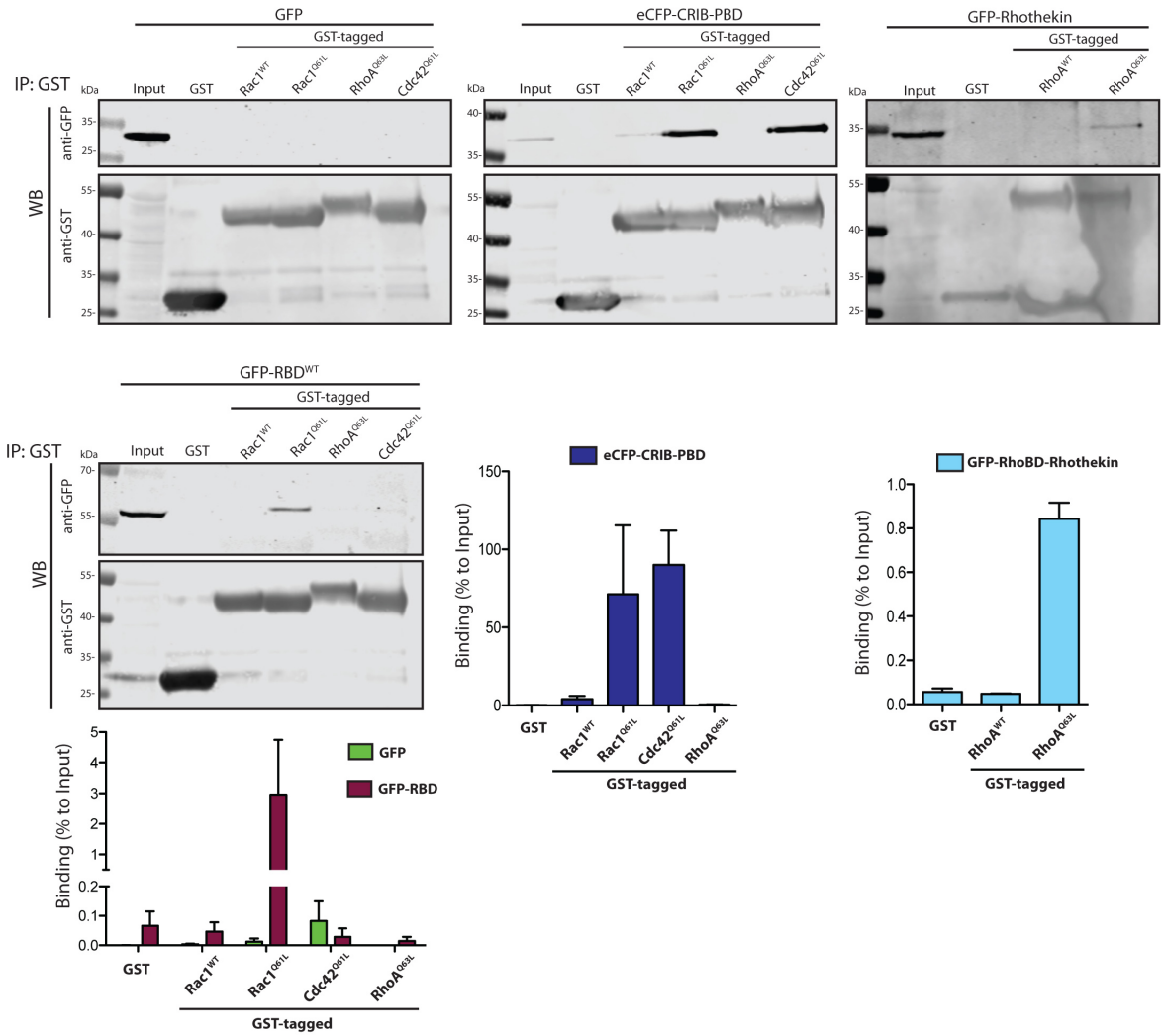

Figure 4-4: FAM49B binds specifically to active Rac1 over other active RhoGTPases
GST pull down assay of immobilised GST, GST-Rac^{WT} and GST-Rac^{Q61L}, GST-Cdc42^{Q61L}, GST-RhoA^{WT} and GST-RhoA^{Q63L} mixed with lysate from CHL1 cells expressing GFP, eCFP-CRIB-PBD, GFP-Rhothekin, and GFP-RBD ^{WT}. Membranes were blotted against GFP (cross-reacts with eCFP) and GST. Molecular weights are displayed on the side.

Three independent experiments were quantified based on densitometry reading and standardised to the input loading. Error bars represent S.E.M.

Next, we asked whether FAM49B binds to Rac1 in a similar way as CYFIP1. Given that the RBD encompasses the Rac binding domain of CYFIP (Jose's thesis), we point-mutated Arg161, which was previously implicated in Rac1-mediated binding of CYFIP (Chen et al., 2010). The adjacent Arg160 is fully conserved in FAM49 proteins but switched to a lysine in CYFIP proteins, thus was also a good candidate for mutagenesis. These constructs are referred to as RBD^{R160D}, RBD^{R161D} or the double mutant $RBD^{R160/161D}$ and were used for the same pull-down experiment.

Mutation of either or both arginines fully abrogates the binding of the RBD to Rac^{Q61L} suggesting that these residues mediate Rac1 interaction (**Figure 4-2**).
The pulldown experiments were repeated using the non-hydrolysable GTP analogue GppNHp, in which the oxygen between β and γ phosphates is replaced by an amine, making this compound non-hydrolysable. GST-$Rac1^{WT}$ was loaded with GDP or GppNHp and binding to GFP-RBD^{WT} was tested. Surprisingly, no binding was measured in this condition, although the CRIB-PBD bound with a similar efficiency between the GppNHp-loaded Rac^{WT} and the $Rac1^{Q61L}$ mutant condition (**Figure 4-3**).

To test the specificity of binding to active Rac1 among other GTPases, a pulldown using constitutively active mutants of the 3 main RhoGTPases was performed. GST-$Rac1^{Q61L}$, GST-$Cdc42^{Q61L}$, GST-$RhoA^{Q63L}$ were purified and loaded on beads. GST and GST-Rac^{WT} were also included as negative controls. In parallel, GFP, GFP-RBD^{WT}, eCFP-CRIB-PBD and GFP-Rhotekin-RBD were expressed into CHL1 cells. As mentioned previously, CRIB domains are Cdc42/Rac1-specific binding domains, so in order to assess Rho activity, Rhotekin-RBD was used as reporter. GFP alone didn't bind to any GST-tagged proteins. Pak-CRIB construct and Rhotekin-RBD showed a specific binding to their respective active RhoGTPase mutants over the wild-type forms (**Figure 4-4**). As expected from the previous pull down, GFP-RBD^{WT} binds only the Q61L mutant and not the $Rac1^{WT}$ construct. Moreover, this binding is specific to Rac1, as quantification doesn't show any specific interaction with the other RhoGTPases in their active state (**Figure 4-4**).

4.2.2 Biochemical characterisation of the binding between FAM49B and Rac1

In order to test whether this interaction was direct and to restrict a minimal interacting domain, we used a peptide array assay in collaboration with George Baillie's Lab (Glasgow University).

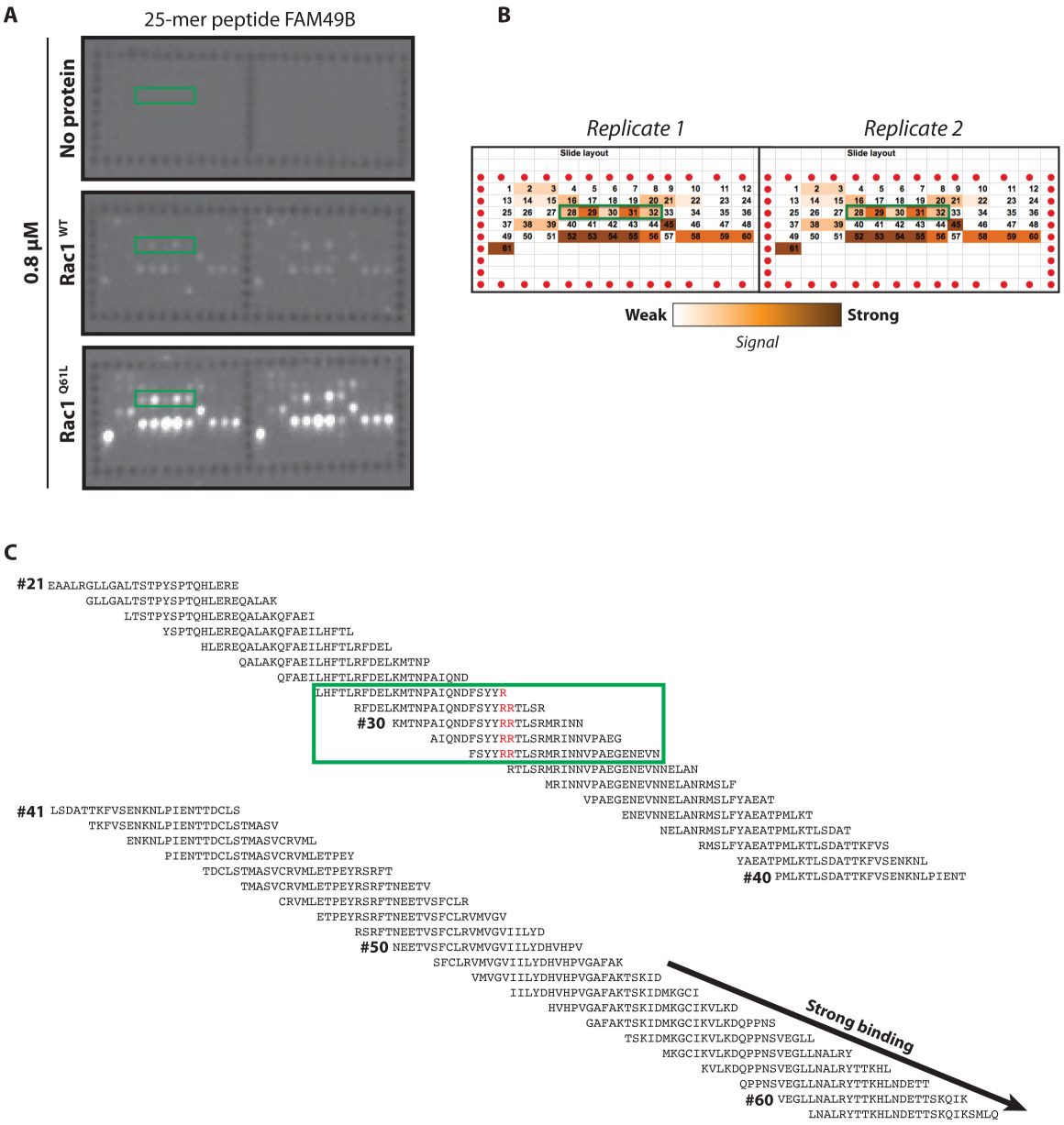

Figure 4-5: Active Rac1 binds to FAM49B fragments in a peptide assay
A – Chemilumiscence assay reveals Rac1 binding to different FAM49B peptides. 0.8 µM of purified untagged $Rac1^{WT}$ or $Rac1^{Q61L}$ was incubated on peptide slides and interaction was revealed using a Rac1/2/3 polyclonal antibody. Horseradish-Peroxydase-coupled antibody was used as a secondary antibody and incubated with ECL reagents. Green box highlights peptides containing the 2 conserved arginine residues involved in Rac1 binding.

B – Slide layout from the human FAM49B protein. Colour code represents the signal intensity. Green box highlights peptides containing the 2 conserved arginine residues involved in Rac1 binding.

C – Alignment of 25-mer peptide representing the sequence overlapping. Peptide number is mentioned accordingly to the slide layout. C-terminus part of FAM49B shows a strong binding to Rac1 and is indicated with a black arrow running over the corresponding peptides. Peptides containing the conserved arginine residues (red) are highlighted with a green box.

This method allows the creation of overlapping 25-mer peptides running across the entire protein length. 61 peptides corresponding to FAM49B sequence were synthetised onto a cellulose membrane and incubated with purified, untagged Rac^{WT} or Rac^{Q61L}. Interaction was revealed using a Rac1 antibody and the chemiluminescence assay (**Figure 4-5 - A**). Antibody background was null on the membrane. However, Rac^{Q61L}, but not Rac^{WT}, showed a strong binding to specific parts of the protein. Indeed, a medium interaction ranging from peptide 28-32 (136-180 FAM49B) and a strong binding from peptide 52-61 (266-324 FAM49B) were consistently found (**Figure 4-5 – A & B**). Unfortunately, GFP-fusion proteins of those peptides failed to bind to $Rac1^{Q61L}$ in a GST-pulldown assay. Although this assay is purely qualitative, it is however interesting to see that the first peptide showing a convincing binding (peptide 28) is the 1st fragment containing Arg160 and conversely, the binding is lost simultaneously to this same arginine (peptide 33).

Given the lack of quantitative data from the previous experiment and in order to confirm that this interaction between active Rac1 and the RBD was direct and not mediated by other components, surface plasmon resonance (SPR) assays were performed using a Biacore T200. This is a highly sensitive method that allows measurement of protein-protein interactions, kinetics and affinity. It is based on a detector sensor chip, linked to an attached binding partner (ligand). The method uses the phenomenon of SPR to detect the molecular interactions as they happened. SPR causes a reduction in the intensity of light reflected at a specific angle from the glass side of the sensor surface. As molecules (analytes) bind to the ligand, the refraction index at the surface changes, altering the angle of the minimum reflecting intensity. The change in SPR angle is proportional to the amount of molecules bound, so together it gives information about affinity and kinetics of the ligand/analyte pair.

Before running the SPR assay, these proteins were tested for folding using a thermal shift assay (**Appendix 4**). Indeed, unfolded or denatured proteins do not show any activity and are therefore useless. This assay is based on the ability of proteins to shield hydrophobic residues within the protein core, leaving hydrophilic residues at their surface. However, denatured proteins expose both hydrophobic/hydrophilic amino acids at their surface. In this assay, the protein is mixed with a dye that fluoresces when bound to hydrophobic residues. Temperature is then gradually increased to induce protein unfolding, resulting in an increase of fluorescence. This explains the absence of the full length FAM49B in the following SPR assay. Indeed, the protein didn't show any melting upon temperature

increase meaning that protein induction or purification steps led to a non-functional protein.

His-tagged $Rac1^{WT}$ or His-tagged $Rac1^{Q61L}$ (ligands) were immobilised on a nickel chip while purified untagged RBD (analyte) was flowed over a surface linked to either ligand or over a reference surface, in order to measure the unspecific binding. This value represents the background of the system and was subtracted from the final sensogram. Purified CRIB-PBD domain gave a K_d of 112 μM and 5 μM for $Rac1^{WT}$ and $Rac1^{Q61L}$ respectively (**Figure 4-6 – A & B**). This construct allowed us to be confident about the differential activity state of Rac1. Confirming our previous data, no binding was detected for $Rac1^{WT}$ whereas a K_d of 22 μM was determined between RBD and $Rac1^{Q61L}$ (**Figure 4-6 – C & D**). This interaction was confirmed by performing the reverse experiment with GST-RBD as a ligand on a CM5 chip and His-tagged $Rac1^{Q61L}$ used as the analyte. This sensogram showed a very similar affinity (K_d = 27 μM) to the converse set up (**Figure 4-6 – E**).

Using biochemical and biophysical approaches, we demonstrated that FAM49B is a new Rac1 interactor that shows specificity to the active form of the RhoGTPase. Binding seems to have some similarity with Rac1 and CYFIP1 binding, which suggested that FAM49B might play a role in the regulation of the Scar/WAVE complex by Rac1.

4.2.3 Modulation of FAM49B expression correlates with differential Rac1 activity

Together, the previous data suggest that FAM49B might be a Rac1 effector, so we addressed whether it affects Rac1 activity.. This hypothesis was directly tested using a Rac1 FRET biosensor. FRET technology is a useful tool to study protein/protein interaction using donor/acceptor proteins. It is based on the passage of energy to a fluorescent acceptor from a donor molecule when the two are in close proximity. In our case, fluorophores from the well-known Raichu Rac1 probe (Itoh et al., 2002) were modified to increase sensitivity and improve the signal-to-noise ratio (Martin et al, in revision). Instead of the commonly used CFP/YFP pair, this probe contains mTurquoise2 as a donor and the sREACh dark acceptor. sREACh was specifically designed by mutagenesis to enhance FRET signal while simultaneously reducing the detectable emission (Ganesan et al., 2006; Murakoshi et al., 2008). This is very convenient to reduce bleed-through between different imaging channels.

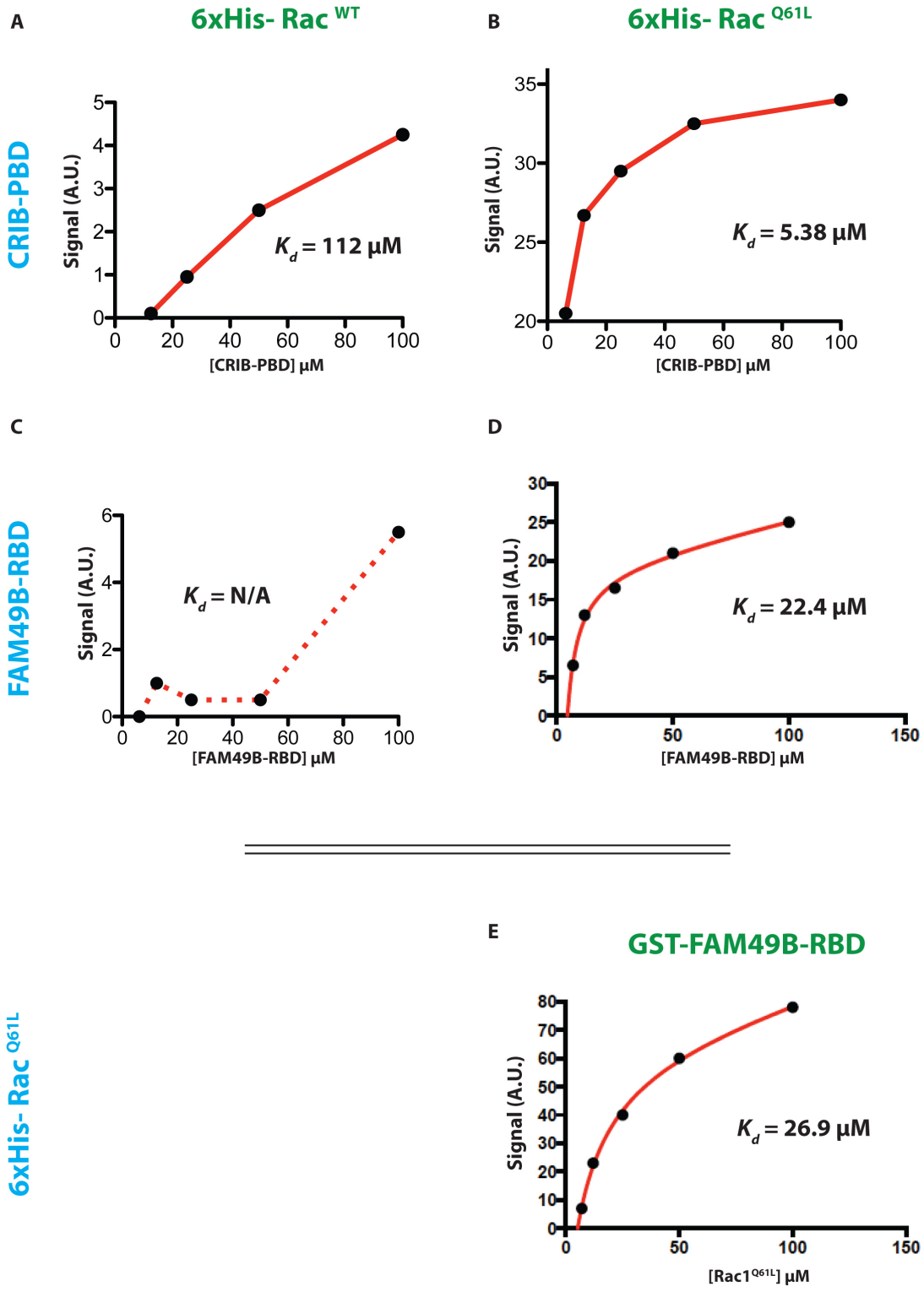

Figure 4-6: Surface plasmon resonance reveals a low affinity binding between active Rac1 and RBD

Sensogram from SPR experiment using purified CRIB-PBD over His-tagged Rac^{WT} (A) or Rac1^{Q61L} (B) bound to a NTA chip. Purified FAM49B-RBD was processed the same way onto the NTA chip (C-D). Reversed experiment (E) with immobilised GST-FAM49B-RBD on a CM5 chip gave a similar response to Rac1^{Q61L}. Affinity (K_d) is mentioned when appropriate. Ligands and analytes are represented in green and blue respectively.

Similarly to the Raichu probe, the construct contains Rac1 itself, the Pak-CRIB domain and a Ras-derived CaaX box that mediates its spatio-temporal regulation at the membrane (**Appendix 5**).

Upon activation, Rac1 binds to the Pak-CRIB domain, resulting in a modification of the probe conformation where the 2 fluorophores end up close enough to allow FRET. FLIM-based FRET imaging measures the shift in donor fluorescence lifetime that occurs when energy is transferred via FRET.

In the open (inactive) conformation, the donor lifetime is longer as all the energy is emitted as donor fluorescence, while in the closed (active) conformation a shorter lifetime is seen. This reflects the likelihood of the transfer of the longer components of the lifetime distribution to the acceptor (i.e. there are now two routes of decay instead of one). This value can then be processed in order to get a FRET efficiency that reflects the activity of the protein of interest and is independent from the intensity of the emitted light.

In order to select a cell line to study endogenous protein function, FAM49B expression was screened across various cancer cell types (**Figure 4-7 – A**). HT29 (human colorectal carcinoma) and CHL1 cells (human melanoma) highly express FAM49B but CHL1 cells were preferred because of the overexpression of FAM49B across various skin cancer types (ProteinAtlas). sgRNA oligos targeting 2 distinct regions of *fam49b* gene (Exon 3 and Exon 4) were designed and used in a Cas9-mediated CrispR strategy (hereafter named as Ex3 or Ex4.1). Efficiency of knockout was assessed by western blot showed a reduction of protein expression of ~90-95% compared with the control cell line (Empty vector or EV) (**Figure 4-7 – B**). To note, knockout cell lines don't show any growth or proliferation defect (**Figure 4-7 – C**) compared with the control and parental cells. Control and knockout cells were transfected with our homemade FRET probe, plated on collagen 24h post-transfection and lifetime was measured.

fam49b-knockout CHL1 cells showed an increase in FRET efficiency *(Mean ± S.E.M - Ex3=31.40 ± 0.43% and Ex4=31.94 ±0.38%)* compared with control *(Ctr=29.57±0.35%)*, reflecting a small but significant increase of signals able to activate Rac1 (**Figure 4-8**). This result was confirmed using siRNA-treated COS-7 as an alternative cell line. Protein expression was decreased by 70-90% after treatment (siRNA Seq6 and Seq7 respectively) (**Figure 4-9 - A**) and similar FRET data were obtained with an increase in FRET efficiency from 30.5 ± 0.65% (Ctr) to 34.07 ± 0.44% and 35.26 ± 0.5% using siRNA Seq6 and Seq7 respectively (*Mean ± S.E.M)* (**Figure 4-9 - B**).

We next hypothesised that FAM49B overexpression would have an opposite effect on Rac1 signalling. Most of the cell lines tested could not cope with high level of exogenous

FAM49B, except the COS-7 cells. In order to reduce cell toxicity, we opted for a Tet-ON inducible vector expressing in parallel a Venus reporter at the membrane. After 48h in presence of doxycycline, untagged FAM49B was greatly enriched compared to the empty vector-transfected (EV) or vehicle-treated cells (**Figure 4-10 - A**). In this case, FRET efficiency was reduced upon FAM49B overexpression and not modified in the other control conditions, leading to the conclusion that overexpressing cells have a lower ability to activate Rac1 (**Figure 4-11 - A**).

Together, genetic depletion and overexpression data directly correlates the expression level of FAM49B to its ability to bind to and modulate Rac1 activity at the membrane. Having previously characterised the arginine mutant as being defective for Rac1 binding, we aimed to see whether these constructs were still able to regulate Rac1 activity. Doxycycline-inducible FAM49B ^{WT}, FAM49B ^{R160D}, FAM49B ^{R161D} and FAM49B $^{R160/161D}$ were co-expressed into COS-7 cells along with the Rac1-FRET probe (**Figure 4-11 - B**). While overexpression of the WT protein caused a reduction in FRET efficiency as previously mentioned, R160D mutant showed a similar FRET efficiency. Similarly, R161D mutant was not statistically significantly different from the wild-type condition, although a trend toward an increased Rac1 signalling was observed. However, the double mutant was not able to modify Rac1 activity and showed no statistical difference compared with the control condition.

4.3 Discussion

Here we showed that despite the lack of CRIB domain, FAM49B is a novel interactor of Rac1, showing specificity to the active form of the GTPase.

We can map the binding domain to an internal portion of ~200 residues, containing a conserved sequence previously described in chapter 3. Mutation of either or both conserved arginine residues in this region totally abrogates this binding, suggesting that FAM49B binds to active Rac1 in a similar way to CYFIP (Chen et al., 2010). This observation allowed us to characterise the DUF1394 as a new Rac1-binding domain, although the minimum region sufficient for binding is still under investigation.

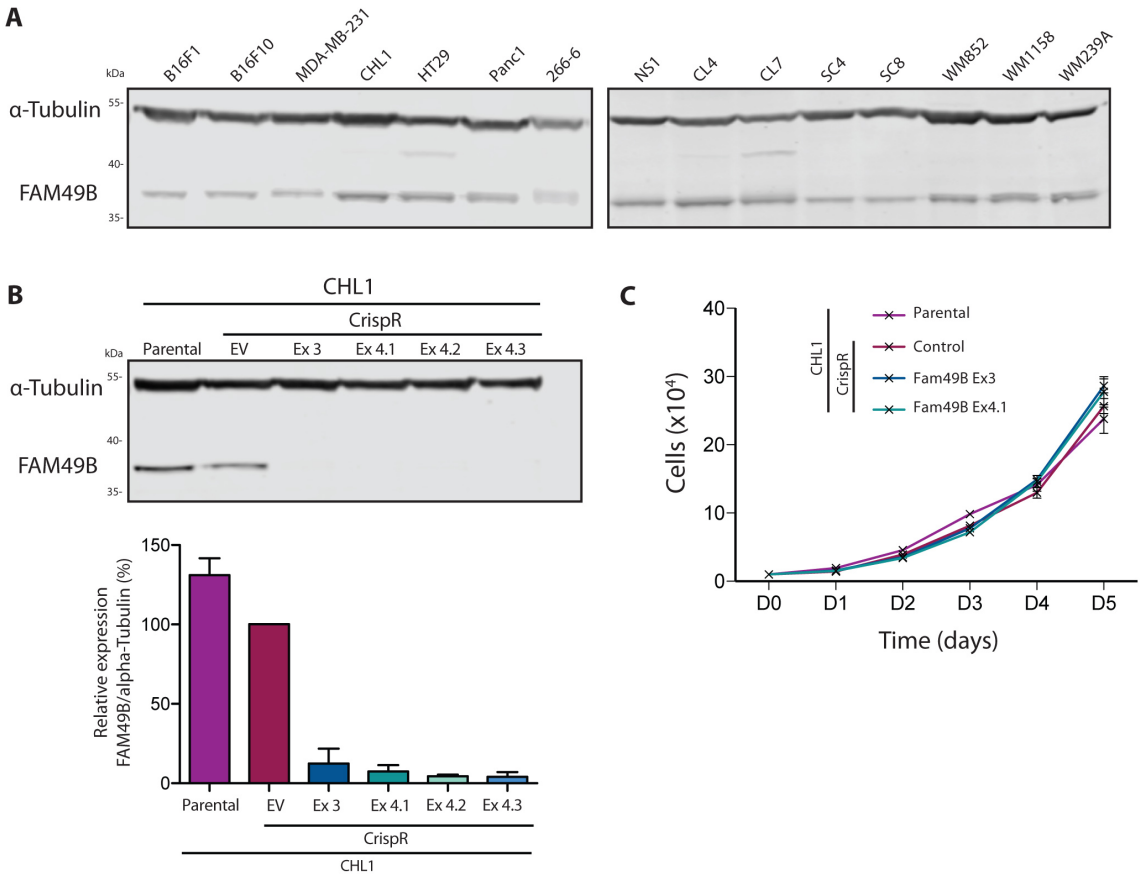

Figure 4-7: Establishment of stable *fam49b*-knockout cell lines by CrispR-Cas9 strategy
A – Western blot analysis of FAM49B expression level across different cancer cell lines. Membranes are blotted against FAM49B and α-Tubulin. B16F1: mouse melanoma cell lines, B16F10: metastatic mouse melanoma cell lines, MDA-MB-231: human breast triple negative adenocarcinoma cell line, CHL1: human melanoma cell line, HT29: human colorectal adenocarcinoma cell line, Panc1: human pancreatic carcinoma, 266-6: mouse pancreatic acinar tumour cell line, NSI, CL4 and CL7: human prostate cancer cells, SC4 and SC8: mouse prostate cancer cells, WM852, WM1158: human melanoma cell lines. Molecular weights are displayed on the side.

B – Western blot analysis and quantification by densitometry of *fam49b* CrispR knockout CHL1 cells after selection. Molecular weights are displayed on the side. Bar graph represents quantification of 3 independent experiments and S.E.M is displayed.

C – Growth curve of parental, CrispR control or *fam49b* CrispR knockout CHL1 cells over 5 days from 3 independent experiments.

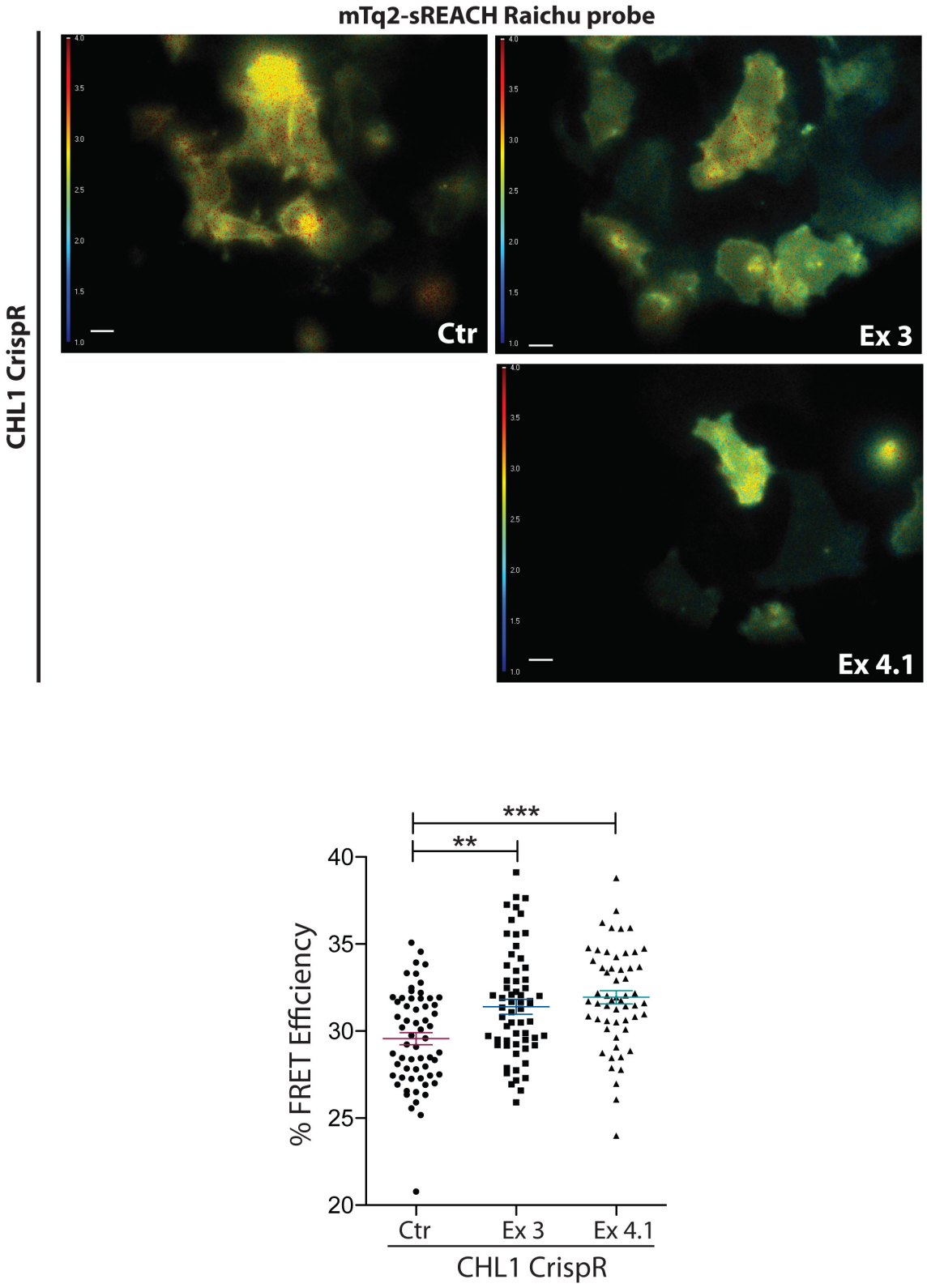

Figure 4-8: *fam49b*-knockout CHL1 cells have higher Rac1 activity
Representative pictures of FLIM-FRET experiment of CHL1 CrispR cells, transfected with the modified Raichu Rac1 probe and plated on Collagen I. Jet2 colour-code shows probe lifetime, ranging from 1ns (blue) to 4ns (red). Quantification of FRET efficiency is shown as a scatter plot with mean and S.E.M from 3 independent experiments. Scale bar = 10 µm. One-Way ANOVA with Dunn's post-test was applied. ** p<0.01, *** p<0.001

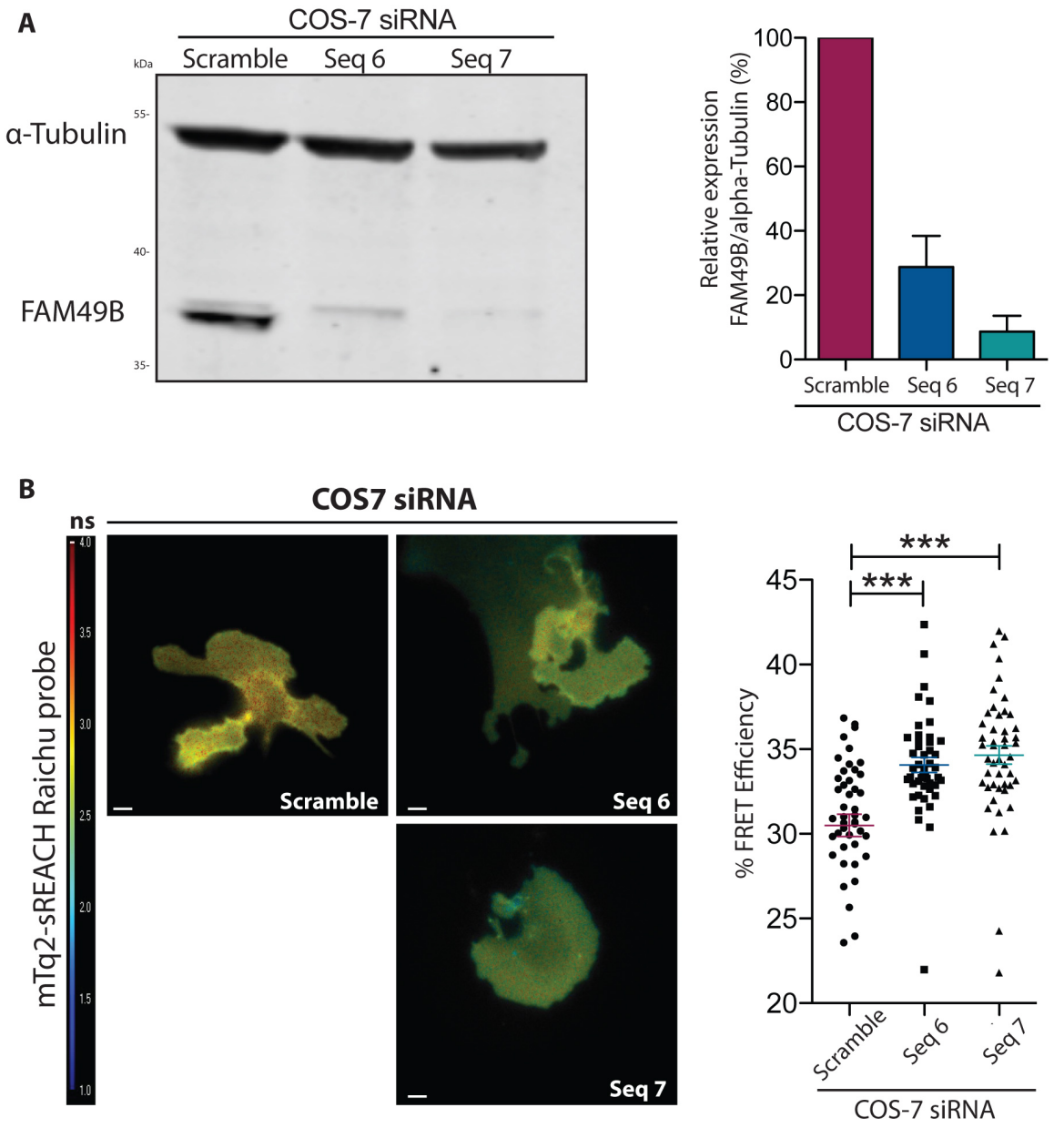

Figure 4-9: FLIM/FRET analysis of *fam49b*-knockdown COS-7 cells
A – Western blot analysis of siRNA-treated COS-7 cells (10 nM), probed for FAM49B and α-Tubulin. Molecular weights are displayed on the side. Bar graph represents quantification by densitometry of 3 independent experiments and S.E.M is displayed.

B - Representative pictures of FLIM-FRET experiment of COS-7 cells treated with 10 nM of siRNA, transfected with the modified Raichu Rac1 probe and plated on Laminin. Jet2 colour-code shows probe lifetime, ranging from 1ns (blue) to 4ns (red). Quantification of FRET efficiency is shown as a scatter plot with mean and S.E.M from 3 independent experiments. Scale bar = 10 μm. One-Way ANOVA with Dunn's post-test was applied. *** $p<0.001$

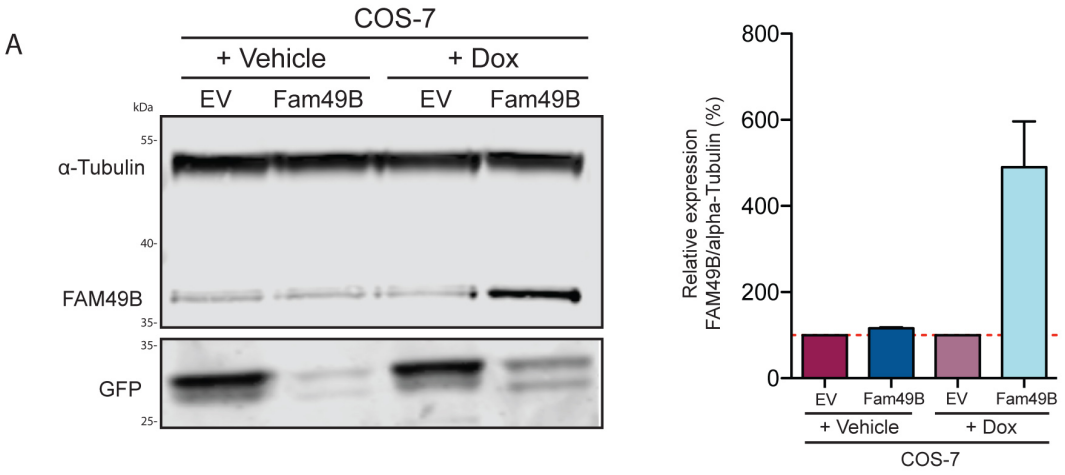

Figure 4-10: Establishment of a FAM49B-overexpressing COS-7 cell line
A – Western blot analysis of COS-7 cells transiently transfected with an inducible TetON empty vector (EV) or containing FAM49B cDNA. Cells were treated with vehicle or doxycycline for 48h and expression level was analysed by western blot against FAM49B, α-Tubulin, or mVenus as a reporter. GFP antibody cross-reacts with mVenus. Molecular weights are displayed on the side. Bar graph represents quantification by densitometry of 3 independent experiments and S.E.M is displayed. Red dotted line represents the level of expression standardised to the EV-transfected cells.

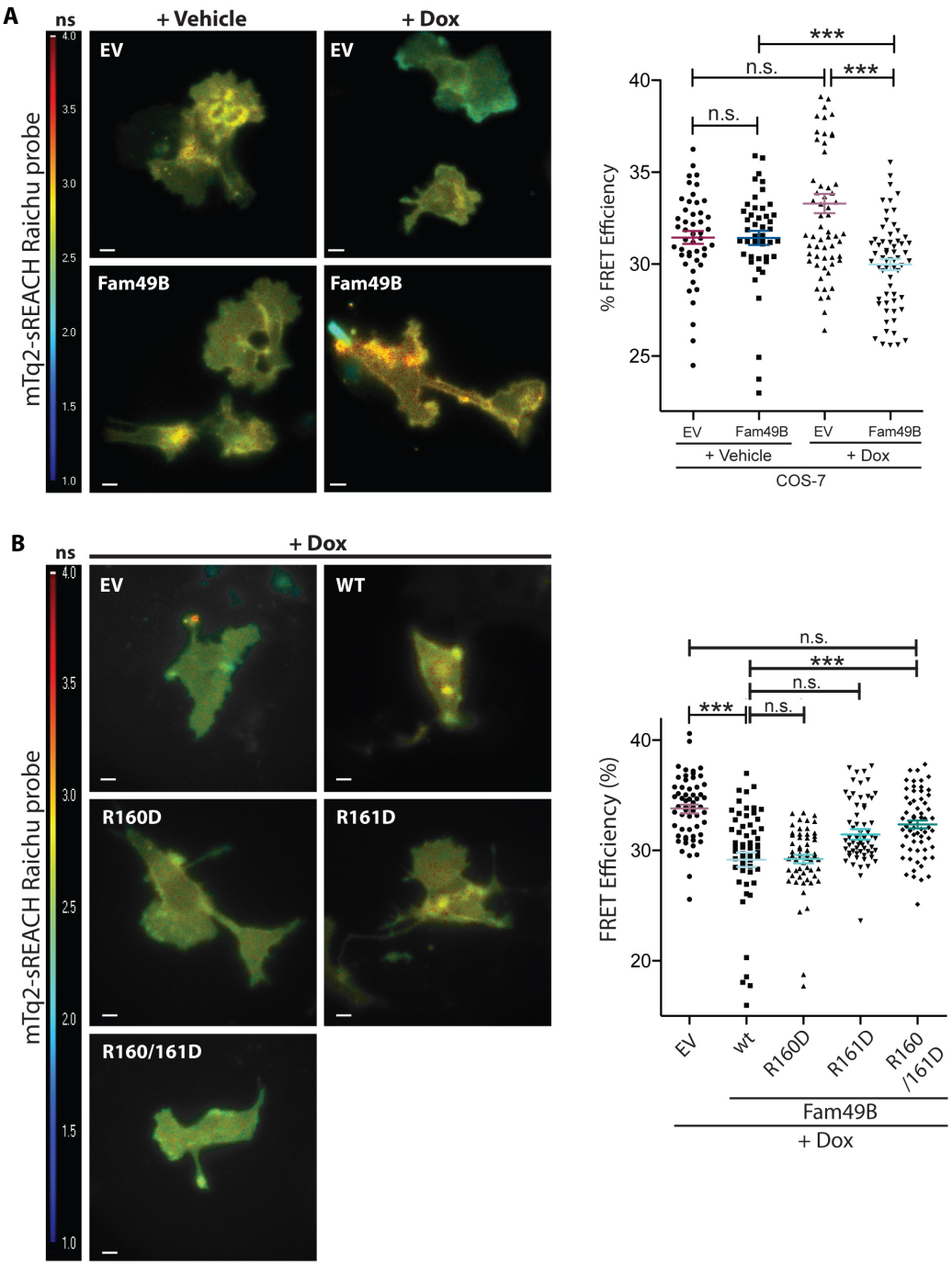

Figure 4-11: FLIM/FRET analysis of FAM49B-overexpressing COS-7 cells
A – Representative pictures of FLIM-FRET experiment of COS-7 cells co-transfected with the inducible TetON vector (EV or containing FAM49B) and the modified Raichu-Rac1 probe. Cells were treated with vehicle or doxycycline for 48h and plated on Laminin for imaging. Only mVenus-positive cells were part of this analysis. Jet2 colour-code shows probe lifetime, ranging from 1ns (blue) to 4ns (red). Quantification of FRET efficiency is shown as a scatter plot with mean and S.E.M from 4 independent experiment. Scale bar = 10 µm. Mann Whitney t-test was applied. n.s. p>0.05, *** p<0.001

B - Representative pictures of FLIM-FRET experiment of COS-7 cells co-transfected with the inducible TetON vector (EV or containing $FAM49B^{WT}$, $FAM49B^{R160D}$, $FAM49B^{R161D}$, $FAM49B^{R160/161D}$) and the modified Raichu-Rac1 probe. Cells were only treated with doxycycline for 48h and plated on laminin for imaging. Only mVenus-positive cells were part of this analysis. Jet2 colour-code shows probe lifetime, ranging from 1ns (blue) to 4ns (red). Quantification of FRET efficiency is shown as a scatter plot with mean and S.E.M from 3 independent experiments. Scale bar = 10 µm. One-Way ANOVA with Dunn's post-test was applied. n.s. p>0.05, *** p<0.001

Indeed, following up our peptide screen assay, the next step is to perform an alanine-mutant scan where every single amino acid is replaced by an alanine. This would also us to investigate what are the important residues sufficient for the interaction and together, to work out a minimal binding region.

Binding to active Rac1 causes a decrease in overall Rac1 activity, so we concluded that FAM49B buffers Rac1 activity at the membrane. The fact that mutation of only one arginine was able to disrupt the interaction but was not sufficient for modulating Rac1 activity might reflect a lack of sensitivity of the pull down assay. Indeed, FRET studies have been reported to have higher sensitivity and can reflect biologically relevant intermediate properties (Hieb et al., 2012). SPR analysis also revealed an affinity of ~25 μM between RBD and $Rac1^{Q61L}$. This low affinity is in agreement with the weak binding observed in our pull down assays but also with the hypothetical biological function of the protein. Indeed, we propose that FAM49B lowers Rac1 activity, which is a highly dynamic process. In regard with the dynamism of Rac1 activity and its ability to change within few minutes, the interaction between FAM49B and Rac1 requires a high turnover. This is more feasible with a low affinity interaction rather than a tight binding as reported for the CRIB domain (5 μM in our assay but the commonly accepted affinity ranges from 0.05-2 μM) (Thompson et al., 1998). This value of ~25 μM also agreed with the low affinity between the WRC and Rac1 (~10 μM) characterised by Chen et al, (Chen et al., 2010) and the need for a dynamic interaction at the leading edge.

The fact that GppNHp-loaded Rac1 did not pull-down the RBD still remains unexplained, although we can speculate on this observation. It would first be important to check that the analogue nucleotide has been properly loaded onto Rac1. Indeed, despite a similar interaction observed between loaded-Rac1 and the Q61L mutant, CRIB-PBD has a much higher affinity to active Rac1 than FAM49B. In the hypothesis where only 20% of $Rac1^{WT}$ is loaded with GppNHp, it will still be able to bind all the CRIB-PBD molecules. However, if the GTP analogue is only partially loaded, the effect will be high on FAM49B because of its initial low affinity. In order to specifically address this point, nucleotide exchange could be checked using high-performance liquid chromatography on GppNHp-loaded Rac1. This would allow us to quantify the percentage of loaded/unloaded Rac1 molecules and adjust our assay accordingly. Also, GppNHp mimics the conformation of Rac1 in its active state but is physically different from the Q61L mutant. Indeed, overall charges over the protein surface might be slightly different and might affect low-affinity binding. Indeed, despite sharing a similar mechanism, it has been suggested that GppNHp and GTP slightly affects H-Ras structure, especially around the β-γ bridging nitrogen group

(Scheidig et al., 1999). This could also be true for Rac1. Finally, it would be interesting to test other GTP analogues, such as GTPγS and see whether the binding still fails to happen.

The effects on Rac1 could also be explained if FAM49B was a GAP. However, the conserved RhoGAP domain, characterised by a 170 amino acids sufficient for GAP activity (Zheng et al., 1993), was absent from FAM49B sequence. We could however test the ability of FAM49B to hydrolyse GTP by performing a GAP assay using hot-labelled GTP or colorimetric readout. GTP can be loaded onto purified Rac1 inorganic phosphate release can be measured over time in the presence of absence of purified FAM49B. A GAP activity should increase the released of Pi. Although we generated all the controls required for this experiment, we have not had time to address this question yet.

Finally, it is interesting to point out that only a central domain of the protein interacts, whereas the full-length protein does not show any binding *in vitro*. However, our FRET experiment, with overexpression of the full-length wild type or mutant proteins shows an effect *in cellulo*. Based on the putative structure, we think that the first 30 residues, organised in an alpha-helix, have an auto-inhibitory function mediated in part by the post-translational modifications. In this model, the inactive protein would be folded with the N and C-termini covering the RBD and preventing binding to Rac1. Upon Rac1 activation, FAM49B would get myristoylated and palmitoylated resulting in a conformational change and making the RBD free to bind to and regulate Rac1 signalling. Once Rac1 stimulation is over, or once it has reached a balanced level able to mediate a regulated biological effect, FAM49B would be turned off by undergoing depalmitoylation and/or being degraded. However, it is still not clear whether myristoylation of FAM49B is a post or co-translational modification. Indeed, myristoylated-protein can shield the myristate group within a hydrophobic pocket and only expose it upon protein activation. A structure of the protein would be required to test this hypothesis as well as a precise analysis of the surface hydrophobicity. Crystal trials have been set up but so far, optimal conditions for crystallisation have not been identified. Full-length FAM49B as well as $FAM49B_{\Delta 1\text{-}30}$ missing the floppy N-terminus (**Figure 1-11 – B**) were tested in over 600 conditions with no success in either case.

In this model, we hypothesised that deregulation of FAM49B expression would affect cell shape and protrusion formation. Indeed, as previously mentioned, Rac1 is a major regulator of cytoskeleton and cell shape. In order to test our model, we looked at cell morphology and the Scar/WAVE complex as a downstream effector of Rac1 signalling.

5 FAM49B, master regulator of cell protrusion formation, spreading and migration

5.1 Introduction

Our data point toward a role of FAM49B as a new player regulating Rac1 activity via a direct interaction. The importance of Rac1 regulation is crucial such that it is a major regulator of the cytoskeleton dynamics such as lamellipodia formation, filopodia, endocytosis, cytokinesis, migration and invasion. For example, overexpression of the active form of Rac1 has been shown to produce pancake-like shaped cells in 2D and increase invasion downstream of a Brk/Paxillin loop in different skin and breast cancer cell lines model (Chen et al., 2004). Rac1 is also crucial for cell adhesion and focal adhesions (Guo et al., 2006), although whether it is a direct consequence from Rac1 activity or driven by the increase of the cell area is not clear.

Given the tight connection between Rac1 and FAM49B, we hypothesised that interfering with FAM49B functions would result in defects of cell morphology, adhesion and motility. The following results were generated using knockout cells, and confirmed by knockdown in different cell types. FAM49B overexpressing COS-7 cells were also used as proof of concept. Those cells were used in different assays to look at filopodia, cell shape, matrix degradation, 2D migration and invasion.

5.2 Results

5.2.1 FAM49B controls protrusion extension

In order to see whether FAM49B plays a role in Rac1-driven processes, FAM49B CrispR knockout CHL1 cells were plated on collagen and left to spread for 4h before PFA fixation. Unlike the parental or control CrispR cells, *fam49b*-KO cells adopt two distinct phenotypes (termed the fried-egg and C-shape phenotype), aside from the normal cell morphology (**Figure 5-1 - A**). Around 35 % of the *fam49b*-knockout cells assume a fried-egg phenotype and are characterised by a broad and circular lamellipodia extended all around the cell, whereas the C-shape cells (~15 % of the population) have a highly polarised lamellipodium dominating one side of the cell. Together, those 2 shapes arose in less than 10 % of the control cell lines (**Figure 5-1 - B**). This difference in cell shape is also reflected by an increase of cell area, as the *fam49b*-knockout cells are on average 25 % larger than their control counterparts (**Figure 5-1 – A & C**). In the four independent knockout cell lines we have looked at, an accumulation of Cortactin staining at the leading edge was observed (**Figure 5-1 - A**). Cortactin is a NPF that directly stimulates the Arp2/3 complex and we initially used it as a marker of lamellipodia extension where it colocalised with cortical F-actin. According to this definition and reflecting the cell shape phenotype, 70 % of the *fam49b*-knockout population have a lamellipodium compared with 15 % of the control CrispR cells (**Figure 5-1 - D**). Indeed, in control condition, Cortactin mainly localises at vesicle-like structures and only infrequently at the cell edge. Among the Cortactin-positive cells, the lamellipodium is much broader in the absence of FAM49B, covering on average 75 % of the total cell perimeter whereas only 20 % on the cell perimeter is dedicated to the lamellipodium in the presence of FAM49B (**Figure 5-1 - E**). Because the Cortactin staining is not a specific lamellipodial marker, immunofluorescence of WAVE2 was optimised and allowed us to confirm the previous results with similar proportion of WAVE2-positive cells and cell edge devoted to lamellipodium (**Figure 5-2 – A-C**). To note, control cells with a fried-egg shape were found in a few cases but interestingly these cells show a very weak and patchy WAVE2 staining that contrasts with the strong enrichment of the WRC at the cell edge of FAM49B-depleted cells (**Figure 5-2 - A**). This enrichment of WRC at the leading edge of knockout cells is followed by an accumulation of the WRC-downstream effector p34-ARC2, subunit of the Arp2/3 complex and by a recruitment of the WRC regulator Lamellipodin (**Figure 5-3**).

In order to back up these data and to show the generality of FAM49B function, various cell types (normal, cancer cell lines or mouse primary cells) in combination with different

genetic approaches (siRNA or Cre-driven floxed-gene deletion) were used. For example, mouse melanoma B16F1 cells treated with siRNA have a reduction of 80% of FAM49B level correlating with broader lamellipodia and larger cell area (**Figure 5-4**). Similarly, COS-7 cells depleted in FAM49B (**Figure 4-9 – A**) exhibit a beautiful fried-egg phenotype when plated on laminin **(Figure 5-5 - A**). WAVE2 is highly enriched at the protrusion edge and cells devote most, if not all the cell perimeter to the lamellipodium **(Figure 5-5 – A & B**). This striking phenotype is also reflected by an increase in cell circularity and cell area (**Figure 5-5 – C & D**).

Finally, because of the similarity between FAM49A and FAM49B and due to the absence of FAM49A antibody at the time of these experiments, we were worried about a potential off-target effect from our siRNA or CrispR strategies. Sperm from a conditional floxed FAM49B mouse was obtained and rederived into C57BL/6 mice. Immortalised mouse embryonic fibroblasts (MEFs) were isolated from different Cre-ER $^{+/0}$: *p16*$^{-/-}$ *fam49b*$^{fl/fl}$ embryos (C1 and D1) and deletion of *fam49b* gene was assessed after 5 days of OHT treatment by PCR of the genomic DNA and by western blot (**Figure 5-6 – A & B**). The DNA agarose-gel confirmed a switch from a ~1400 bp (corresponding to the expected size for a PCR product with no recombination) to a ~650 bp PCR product (representing the knockout allele). This disruption of *fam49b* gene was directly translated at the protein level by the absence of signal in the OHT-treated samples. The aim of this targeted strategy was to reassure us about the specificity of the observed phenotypes. MEFs were plated on laminin and stained for F-actin and the WRC. Representative pictures of either cell lines show an increase in cell area and WAVE2 localisation at the lamellipodium upon OHT treatment (**Figure 5-6 – C**).

In order to be sure that WRC enrichment is not due to an overall increase of the Scar/WAVE complex members expression, western blot of NAP1, CYFIP1 and WAVE2 was performed on *fam49b*-knockout CHL1 cells (**Figure 5-7**). Analysis showed that protein expression is unaffected between control CrispR and *fam49b*-knockout cells. Also, FAM49A antibody was optimised for western blot and confirmed the specificity of the sgRNA used for the CrispR knockout as expression level is similar between control and *fam49b*-knockout cells.

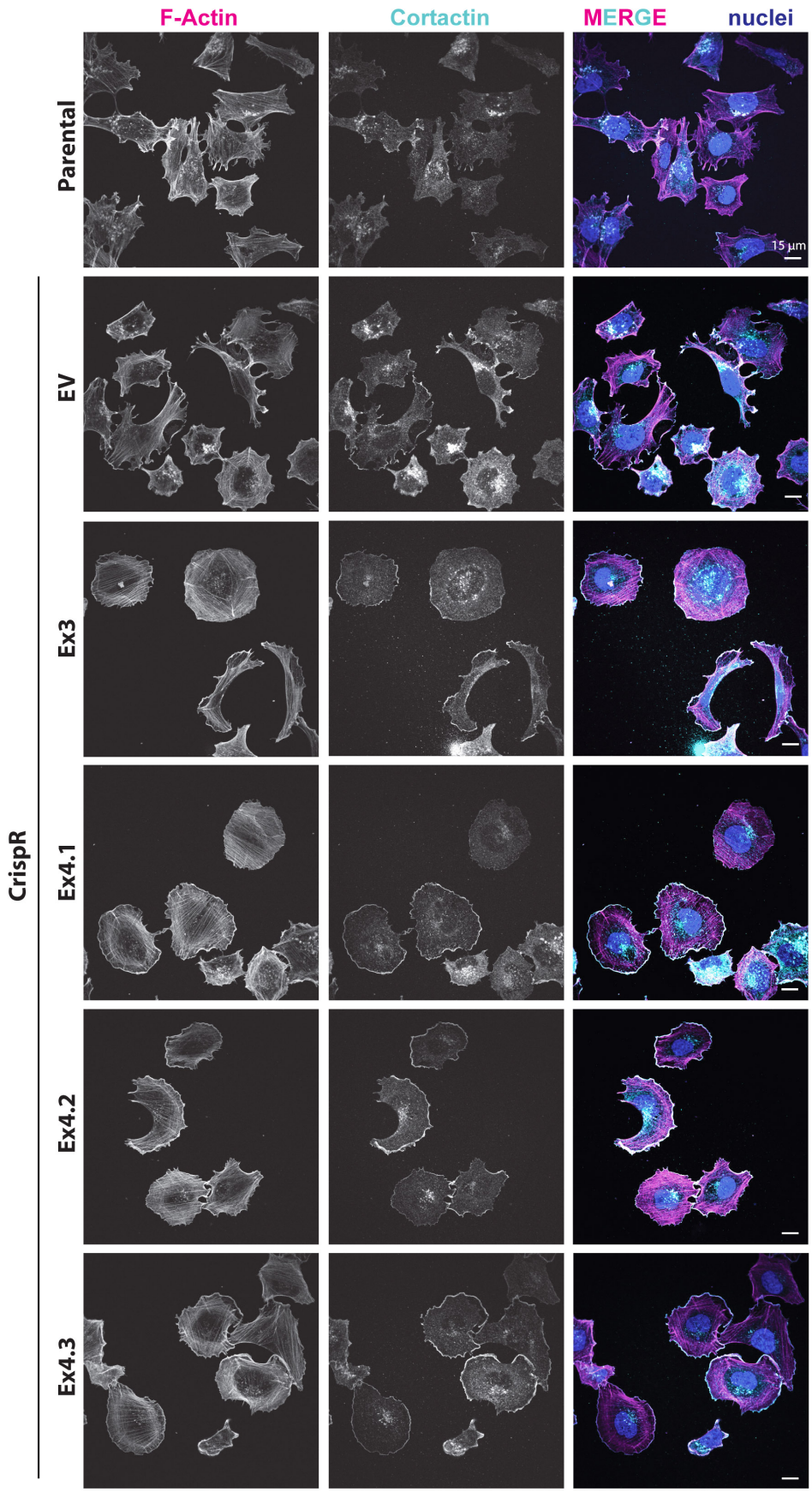

Figure 5-1: FAM49B regulates cell shape in CHL1 cells
Immunofluorescence of control (parental and EV) or *fam49b*-CrispR knockout (Ex3, Ex4.1, Ex4.2, Ex4.3) CHL1 cells plated on collagen-I and stained for F-actin (magenta), Cortactin (cyan) and nuclei (blue). Scale bar = 15 µm.

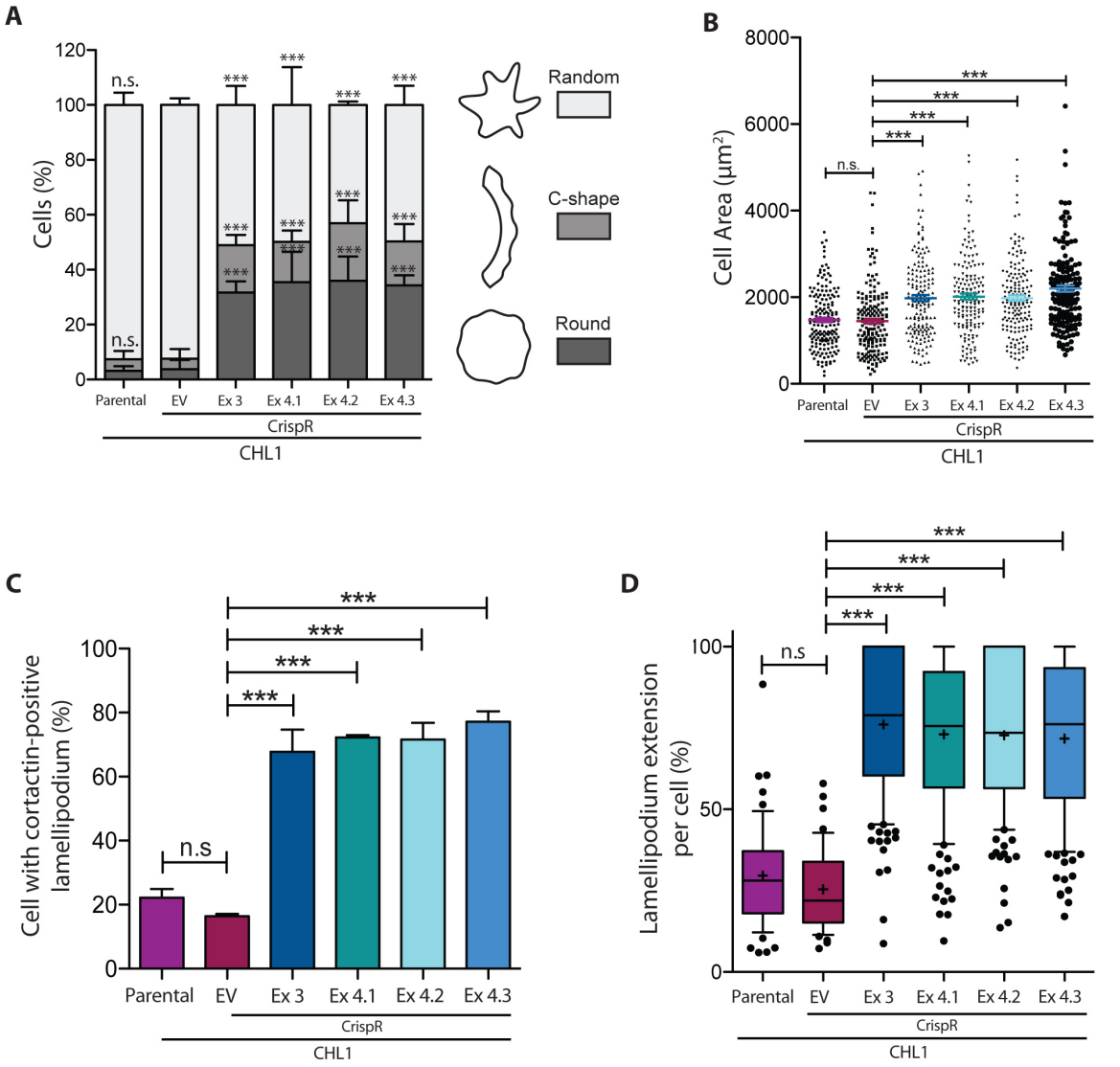

Figure 5-2: fam49b knockout CHL1 cells show an enlarged lamellipodium

A – Shape scoring of control or *fam49b*-knockout cells plated on collagen-I. F-actin staining was used to delimit the cell edge. Cells were classified as randomly shaped, C-shaped or round (fried-egg shaped). Quantification was performed from 4 independent experiments and two-tailed Chi-square test (95% confidence) was applied for each shape category compared with the EV control CrispR cells. n.s. $p>0.05$, *** $p<0.001$. Error bars represent S.E.M.

B – Quantification of cell area of control or *fam49b*-knockout cells plated on collagen-I. F-actin staining was used to delimit the cell edge. Scatter plots represent mean and S.E.M from 3 independent experiments. One-Way ANOVA with Tukey's post-test was applied. n.s. $p>0.05$, *** $p<0.001$.

C – Quantification of the number of Cortactin-positive cells based on the immunofluorescence staining. Bar plots represent quantification from 3 independent experiments and error bars represent S.E.M. One-Way ANOVA with Dunn's post-test was applied. n.s. $p>0.05$, *** $p<0.001$.

D – Quantification of the cell perimeter devoted to lamellipodia was measured based on the extension of the cortactin staining at the cell edge over the total cell perimeter. Whisker plots represent 10-90 percentile, mean (cross) and S.E.M. One-Way ANOVA with Dunn's post-test was applied. n.s. $p>0.05$, *** $p<0.001$.

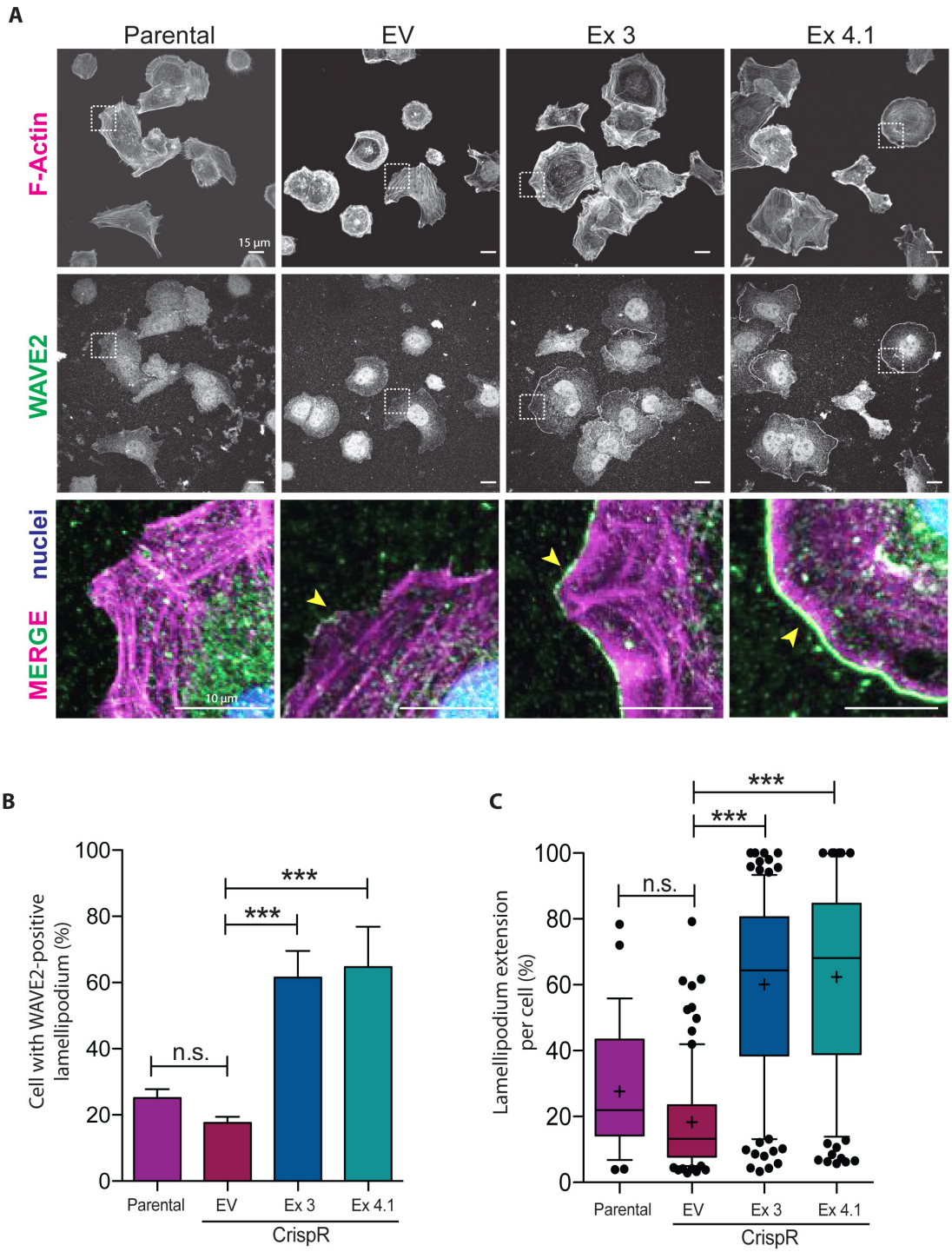

Figure 5-3: FAM49B-depleted cells have an enrichment of WAVE2 at the cell edge
A – Immunofluorescence of control (parental and EV) or *fam49b*-CrispR knockout (Ex3, Ex4.1) CHL1 cells plated on collagen-I and stained for F-actin (magenta), WAVE2 (green) and nuclei (blue). Magnified view of the white dotted area is shown on the bottom panel. Yellow arrowheads represent WAVE2-rich area. Scale bar top panels = 15 µm. Scale bar bottom panels = 10 µm

B - Quantification of the number of WAVE2-positive cells based on the immunofluorescence staining. Bar plots represent quantification from 3 independent experiments and error bars represent S.E.M. One-Way ANOVA with Dunn's post-test was applied. n.s. $p>0.05$, *** $p<0.001$.

C - Quantification of the cell perimeter devoted to lamellipodia was measured based on the extension of the WAVE2 staining at the cell edge over the total cell perimeter. Whisker plots represent 10-90 percentile, mean (cross) and S.E.M from 3 independent experiments. One-Way ANOVA with Dunn's post-test was applied. n.s. $p>0.05$, *** $p<0.001$.

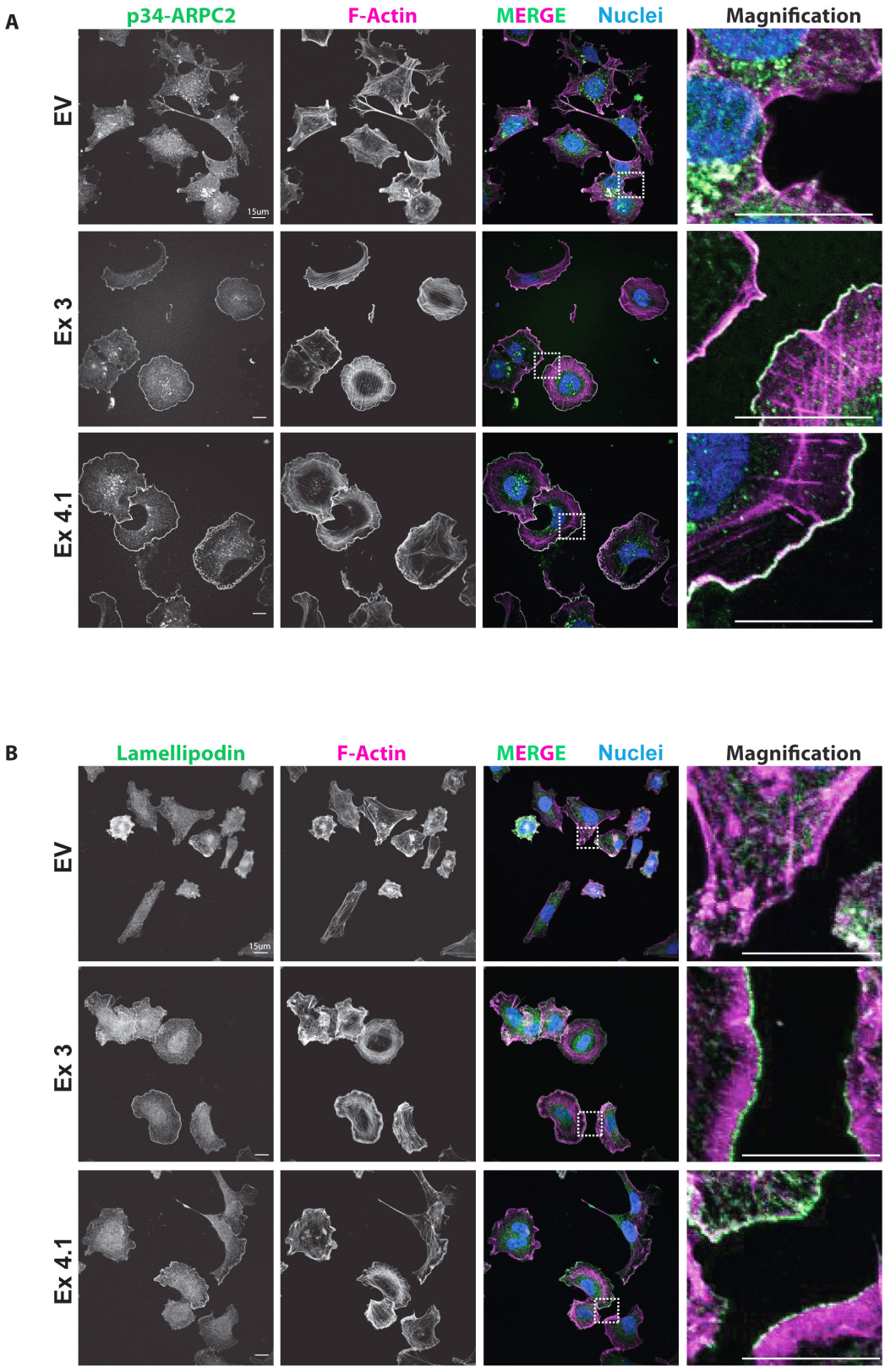

Figure 5-4: FAM49B-depleted cells show an enrichment of downstream WRC effectors at the cell edge

A - Immunofluorescence of control (EV) or *fam49b*-CrispR knockout (Ex3, Ex4.1) CHL1 cells plated on collagen-I and stained for F-actin (magenta), p34-ARPC2 (green) and nuclei (blue). Magnified view of the white dotted area is shown on the far right panel. Scale bar = 15 μm

B - Immunofluorescence of control (EV) or *fam49b*-CrispR knockout (Ex3, Ex4.1) CHL1 cells plated on collagen-I and stained for F-actin (magenta), Lamellipodin (green) and nuclei (blue). Magnified view of the white dotted area is shown on the far right panel. Scale bar = 15 μm.

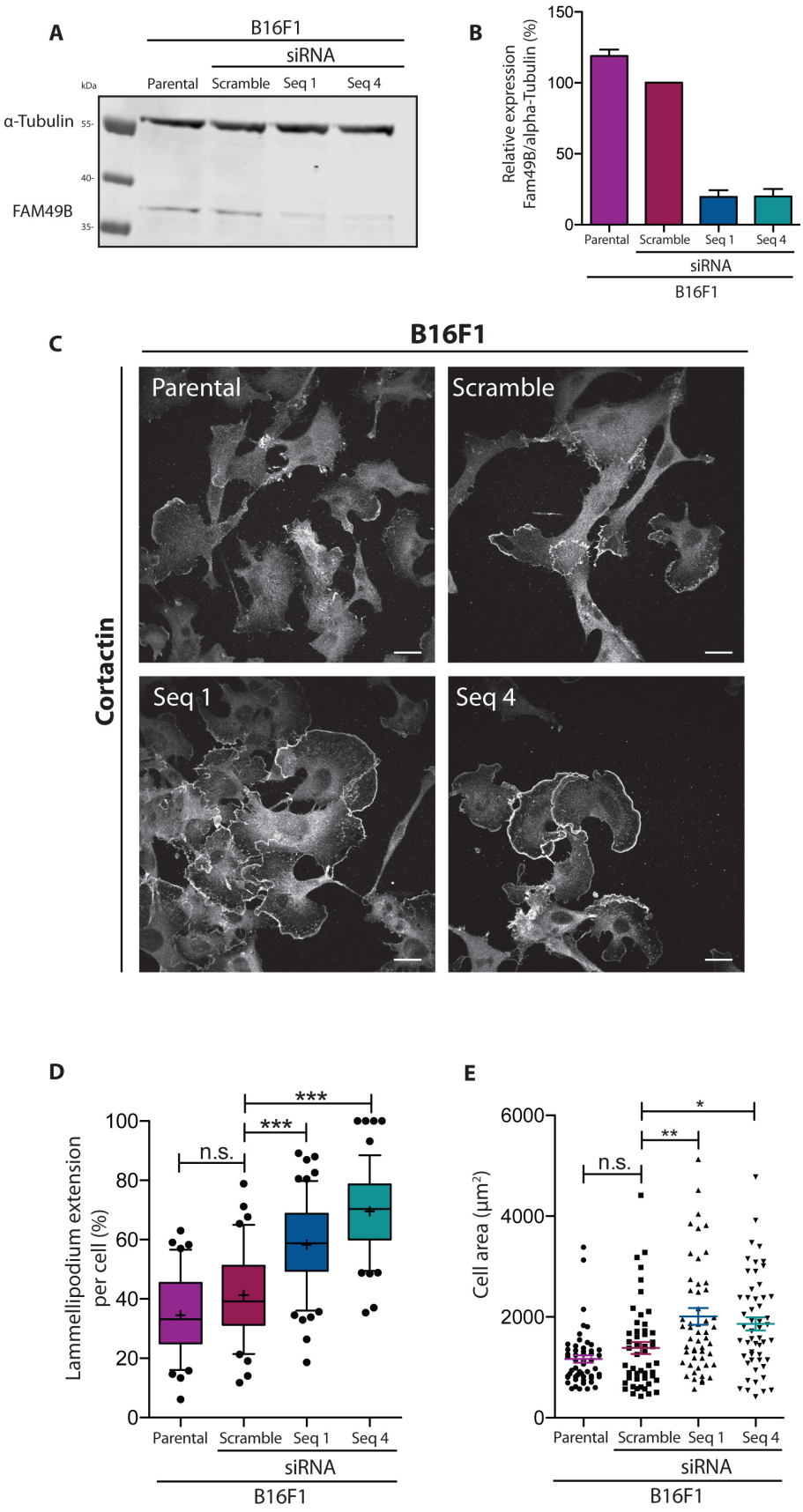

Figure 5-5: FAM49B function is conserved in B16F1 cells
A-B – Western blot analysis of parental B16F1 cells or treated with 100 nM of control (Scramble) or FAM49B siRNA (Seq1 and Seq4). Membrane was blotted against FAM49B and α-Tubulin. Molecular weights are displayed on the side. Bar graph (B) represents quantification of the relative protein expression level (normalised to EV) by densitometry of 3 independent experiments. S.E.M is displayed.

C-E – Immunofluorescence of parental B16F1 cells or treated with 100 nM of control (Scramble) or FAM49B siRNA (Seq1 and Seq4) and stained for Cortactin (C). Scale bar = 15 µm. Lamellipodia extension was measured using the length of Cortactin staining over the total cell perimeter (D). Whisker plots represent 10-90 percentile, mean (cross) and S.E.M from 3 independent experiments. One-Way ANOVA with Dunn's post-test was applied. n.s. $p>0.05$, *** $p<0.001$. Cell area was obtained from the F-actin staining (not shown) and displayed as a scatter plot in E, with mean and S.E.M represented from 3 independent experiments. One-Way ANOVA with Dunn's post-test was applied. n.s. $p>0.05$, * $p<0.05$, ** $p<0.01$.

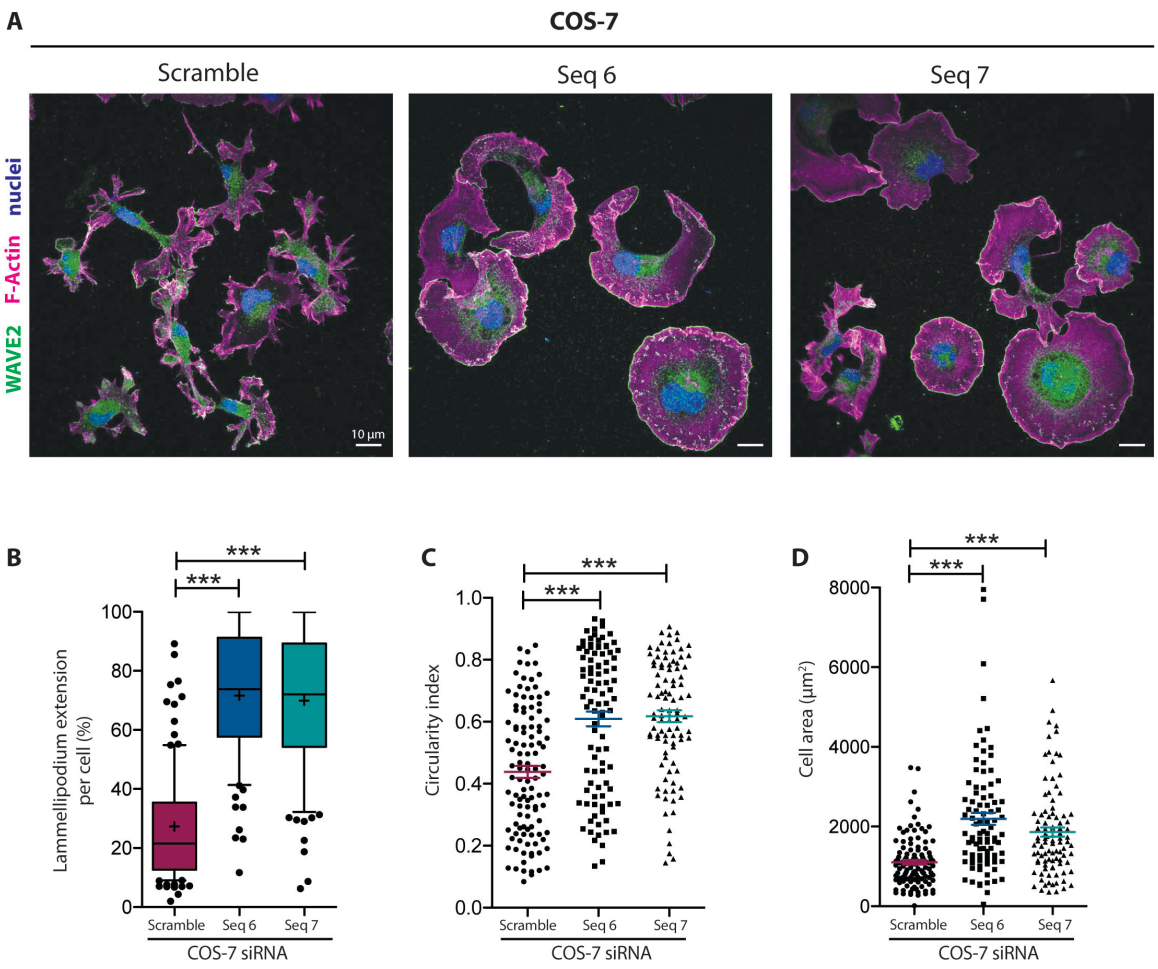

Figure 5-6: FAM49B function is conserved in COS-7 cells

A – Immunofluorescence of COS-7 cells treated with 25 nM of control (Scramble) or FAM49B siRNA (Seq6 and Seq7), plated on laminin and stained for WAVE2 (green), F-actin (magenta) and nuclei (blue). Scale bar = 10 µm.

B – Quantification of the cell perimeter devoted to lamellipodia was measured based on the extension of the WAVE2 staining at the cell edge over the total cell perimeter in control or siRNA-treated cells. Whisker plots represent 10-90 percentile, mean (cross) and S.E.M from 3 independent experiments. One-Way ANOVA with Dunn's post-test was applied. *** $p<0.001$.

C - Quantification of cell circularity of control or *fam49b*-knockdown COS-7 cells plated on laminin. F-actin staining was used to delimit the cell edge. Scatter plots represent mean and S.E.M from 3 independent experiments. One-Way ANOVA with Dunn's post-test was applied. *** $p<0.001$.

D- Quantification of cell area of control or *fam49b*-knockdown COS-7 cells plated on laminin. F-actin staining was used to delimit the cell edge. Scatter plots represent mean and S.E.M from 3 independent experiments. One-Way ANOVA with Dunn's post-test was applied. *** $p<0.001$.

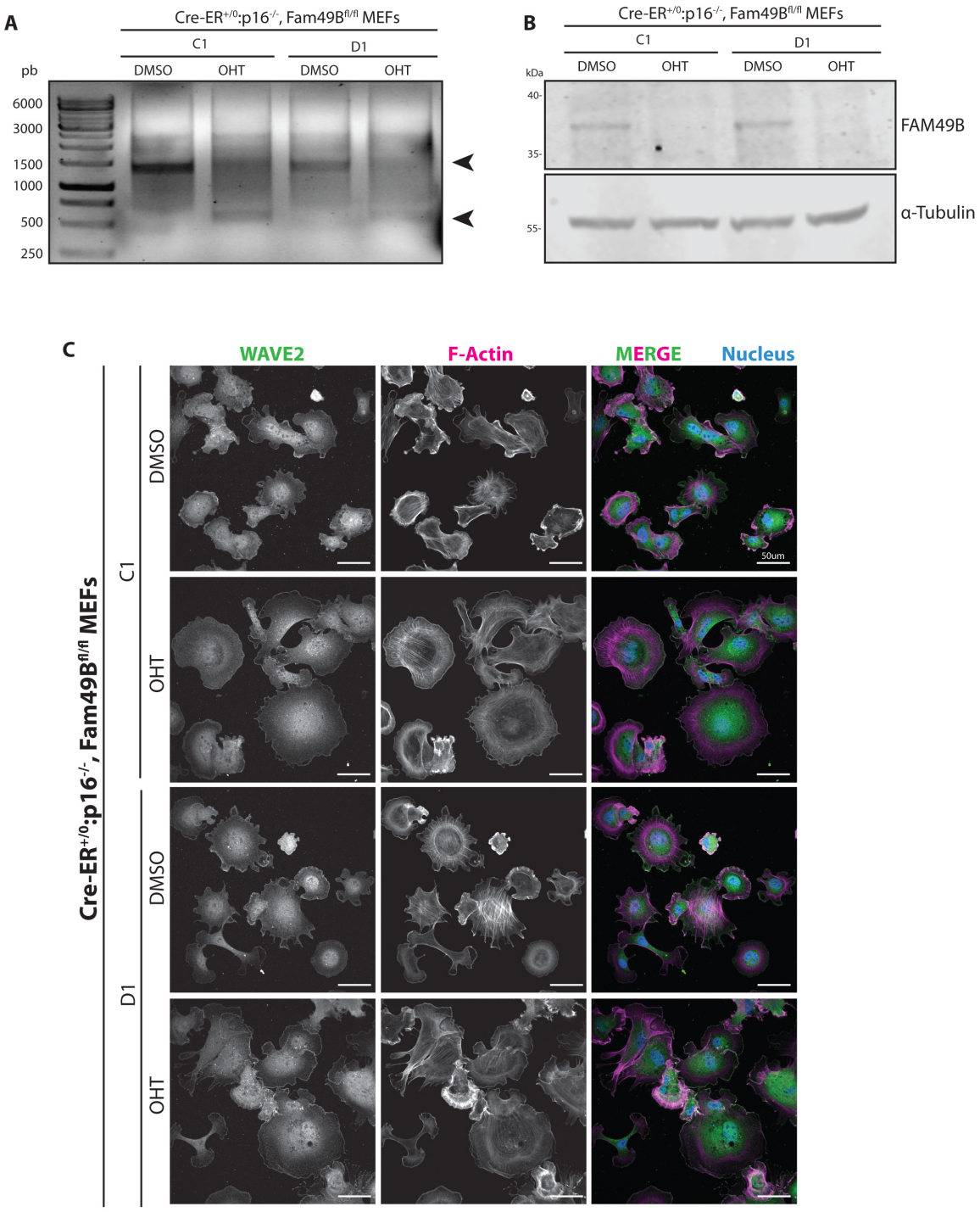

Figure 5-7: Increase of lamellipodia extension is also seen using a different knockout strategy

A – PCR-based analysis of the FAM49B recombination after 5 days of DMSO or OHT treatment. Genomic DNA from two distinct Cre-ER$^{+/0}$:*p16*$^{-/-}$, *fam49b*$^{fl/fl}$ MEF lines (C1 and D1) was isolated and floxed-FAM49B locus was amplified and analysed on a 1% agarose gel. Upper arrowhead represents the expected band size obtained from the PCR reaction of the un-recombined locus (~1400 bp). Lower arrowhead highlights the expected band size obtained after recombination (~650 bp). DNA ladder size is highlighted on the left side of the gel (in bp).

B – Western blot analysis of MEFs lines after 5 days of DMSO or OHT treatment. Membranes were blotted against FAM49B and α-Tubulin. Molecular weights are displayed on the side.

C – Immunofluorescence of DMSO or OHT-treated MEFs, plated on laminin and stained for WAVE2 (green), F-actin (magenta) and nuclei (blue). Representative pictures from 2 independent experiments. Scale bar = 50 µm.

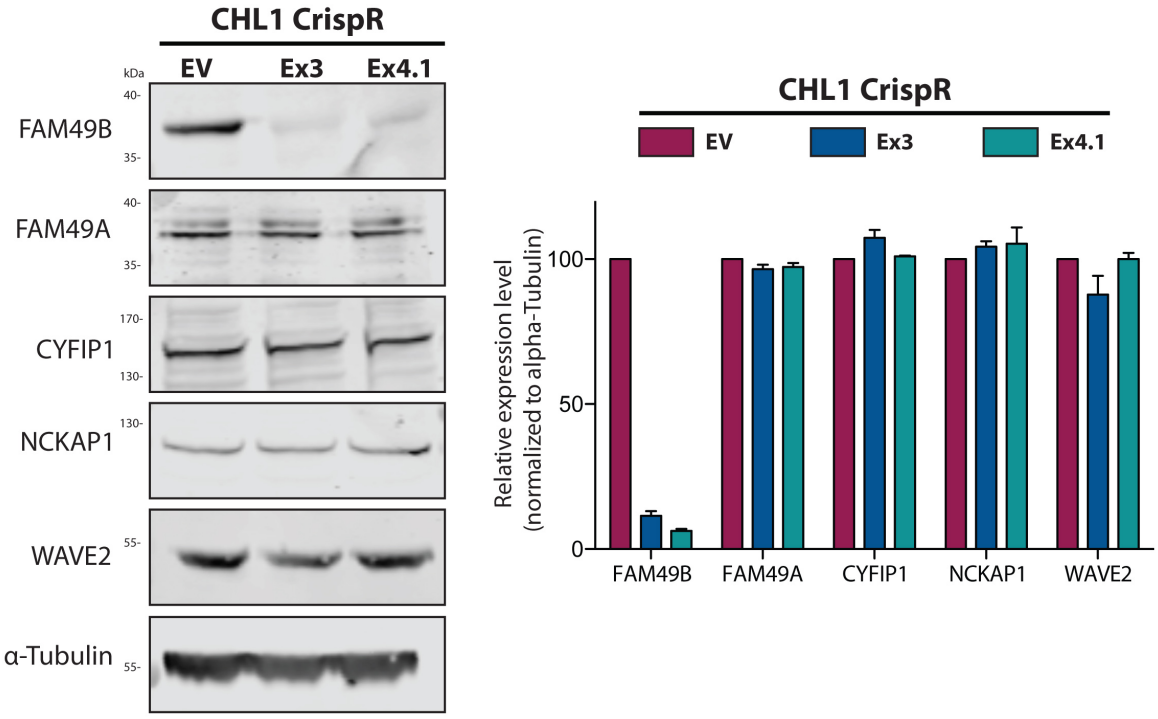

Figure 5-8: FAM49B-depletion does not affect WRC protein level or FAM49A expression
Western blot analysis of the protein expression of some WRC members (CYFIP1, NCKAP1, WAVE2) and FAM49A in control EV or *fam49b*-CrispR knockout CHL1 cells. Molecular weights are displayed on the side. Quantification of 2 independent experiments using densitometry are reported as a bar plot with error bar representing S.E.M. Protein expression was normalised to the α-Tubulin and standardised to the control cell line.

In light of these data, we hypothesised that FAM49B restricts the lamellipodium extension and thus, increased FAM49B level should affect cell protrusions. To test this, COS-7 cells transfected with the doxycycline-inducible plasmid (**Figure 4-10**) were plated on laminin and analysed by immunofluorescence. Only mVenus-positive cells were taken into account for further analysis. Green EV-transfected cells represent the proper control but non-transfected cells (mVenus negative) could also have been used as an additional internal control, although these have not been quantified. Vehicle treated transfected cells or doxycycline EV-transfected cells devoted on average 30 % of their perimeter for lamellipodia formation whereas this value goes down to 10 % for overexpressing cells (**Figure 5-8 – A & B**). These cells frequently exhibited a hyper-fragmented phenotype, as if they were unable to form and extend a lamellipodium (**Figure 5-8 – A**). This directly correlates with a reduction of the circularity index from 0.5 to 0.3 (**Figure 5-8 – D**). Moreover, half of the FAM49B overexpressing population did not spread at all and this results in a 50% decrease of the average cell area (**Figure 5-8– C**). Short time-lapse movies confirmed these immunofluorescence observations and also revealed that these fine protrusions are quite stable in 2D. However, protrusion rate of those has not been investigated further (**Figure 5-9**).

The observed increase of spreading in *fam49b*-knockout cells has been investigated throughout a timecourse experiment in which cells were plated at the same time on fibronectin and collagen-coated coverslips and fixed at different times (**Figure 5-10**). Cell area from over 400 control or *fam49b*-knockout CHL1 cells was measured for each time point and revealed that FAM49B-depleted cells spread faster, independently of the matrix used for the coating. This difference in spreading is significant as early as 30 min of spreading. This data was confirmed using xCELLigence as an alternative and unbiased approach. For this, cells are plated on electrodes that sense the electrical impedance of a current created by crawling/spreading cells. In order to limit the effect of cell migration and specifically focus on cell adhesion and spreading, the assay was restricted to the first few hours (**Figure 5-11 - A**). Parental and EV CrispR cells plated on collagen-I have a spreading halftime of 1h51 and 1h43 respectively that is slightly extended when compared to the 2 independent knockout cell lines (1h22 and 1h25 for Ex3 and Ex4.1 respectively) (**Figure 5-11 - B**). Together, these data reflect that cells depleted in FAM49B cannot restrict the extension of the lamellipodia so we conclude that FAM49B binds to Rac1 and buffers downstream Rac1 signalling allowing a regulation of Scar/WAVE complex.

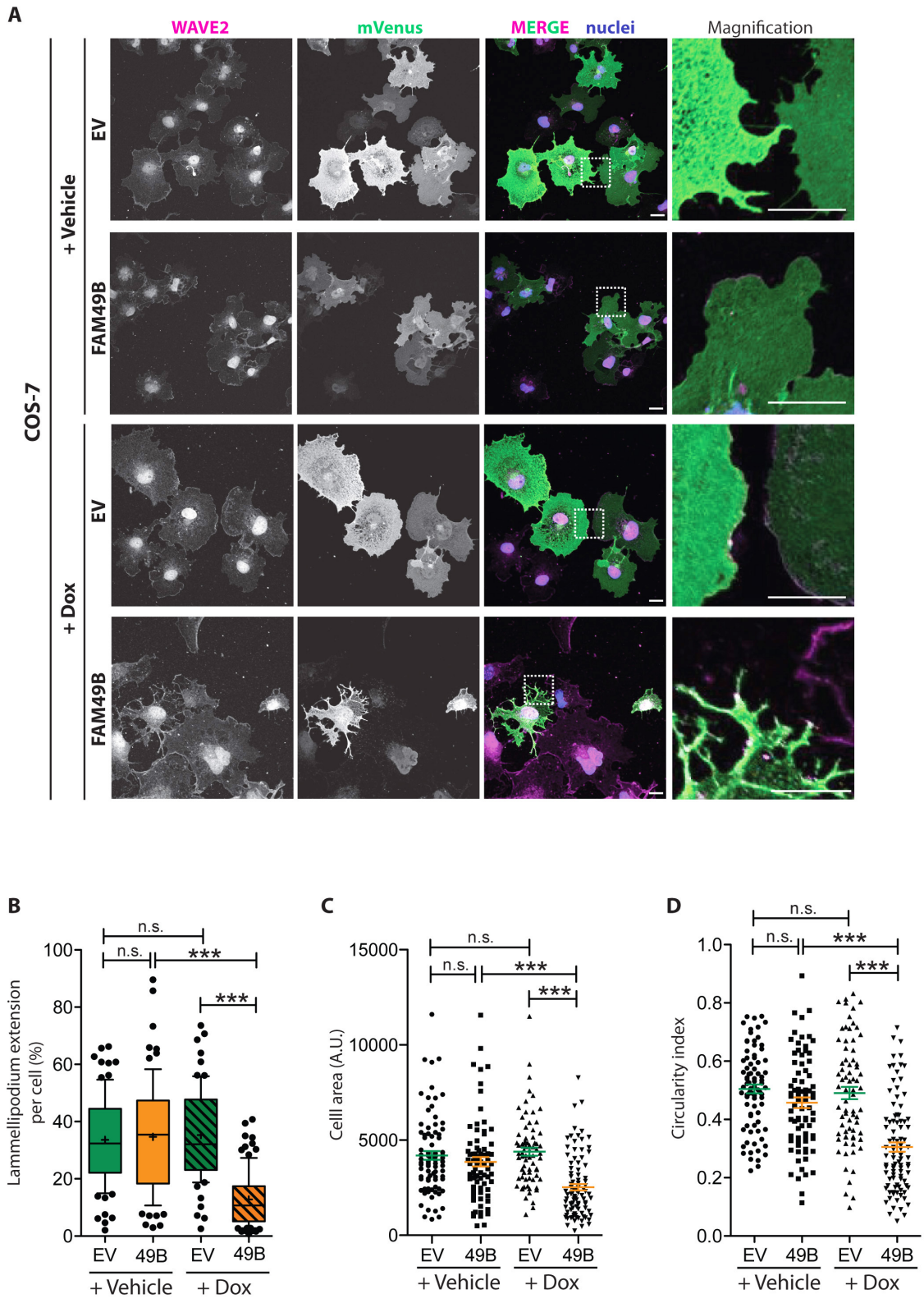

Figure 5-9: FAM49B overexpression leads to a fragmented lamellipodium

A - Immunofluorescence of COS-7 cells transiently transfected with an inducible TetON empty vector (EV) or containing FAM49B cDNA. Cells were treated with vehicle or doxycycline for 48h, plated on fibronectin and stained for WAVE2 (magenta) or mVenus (green - GFP antibody cross reacts with mVenus). Magnified view of the white dotted area is shown on the far right panel. Scale bar = 10 µm.

B - Quantification of the cell perimeter devoted to lamellipodia was measured based on the extension of the WAVE2 staining at the cell edge over the total cell perimeter. Whisker plots represent 10-90 percentile, mean (cross) and S.E.M from 4 independent experiments. Two tailed unpaired t tests were applied. n.s. $p>0.05$. *** $p<0.001$.

C - Quantification of the cell area was measured based on the F-actin staining. Scatter plots represent mean and S.E.M from 4 independent experiments. Two tailed unpaired t tests were applied. n.s. $p>0.05$. *** $p<0.001$.

D - Quantification of the circularity index was measured based on the F-actin staining. Scatter plots represent mean and S.E.M from 4 independent experiments. Two tailed unpaired t tests were applied. n.s. $p>0.05$. *** $p<0.001$.

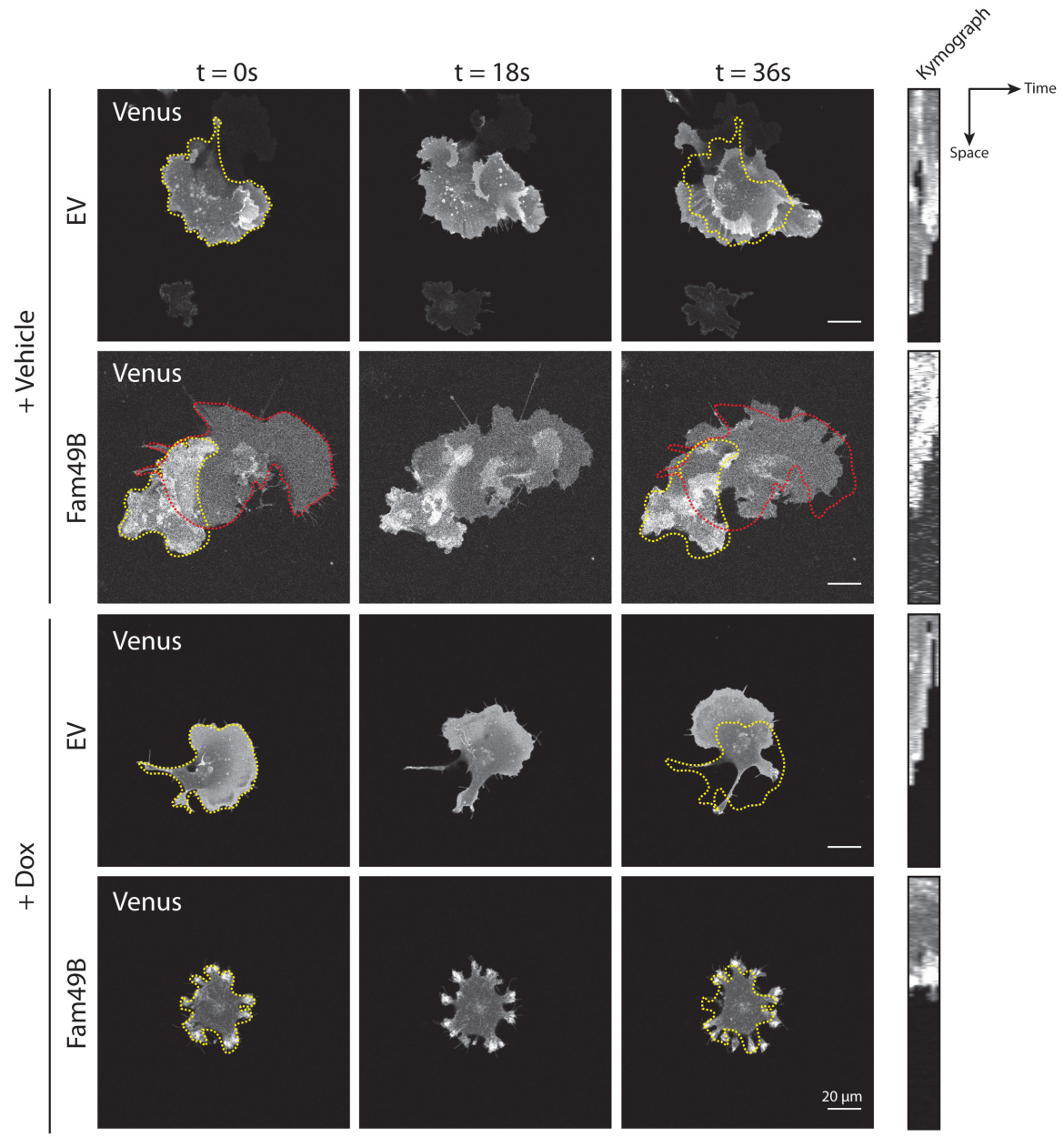

Figure 5-10: FAM49B overexpression leads to a less dynamic lamellipodium
Stills from time-lapse movies of COS-7 cells transiently transfected with an inducible TetON empty vector (EV) or containing Fam49B cDNA and co-expressing Venus as a reporter. Cells were treated with vehicle or doxycycline for 48h, plated on fibronectin and imaged every 3 seconds. Cell edge is highlighted in different colour at the beginning of each movie and reported at the end in order to appreciate how far a cell has moved. Kymographs are presented on the side of each condition with space and time shown on y and x-axis respectively. Scale bar = 20 µm

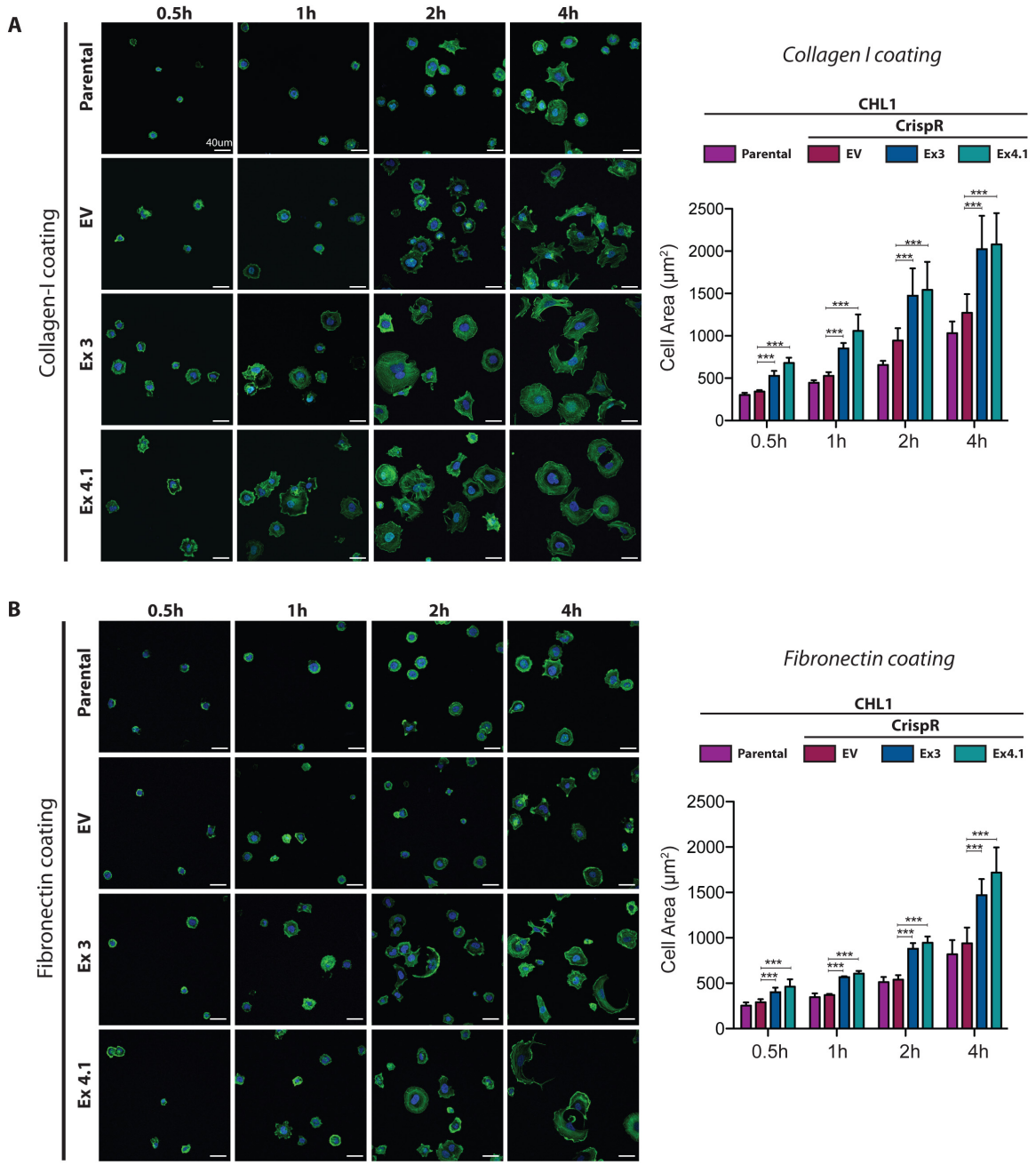

Figure 5-11: *fam49b*-knockout cells show an increase on cell spreading
A – Timecourse experiment of parental, control EV or *fam49b*-CrispR knockout cells plated on collagen-I and fixed after 30min, 1h, 2h, and 4h. Cells were stained for F-actin (green) and nuclei (blue). Scale bar = 40 µm. Quantification of cell area from 3 independent experiments is reported on the bar graph, with S.E.M represented. One-Way ANOVA with Tukey's post test was applied. *** $p<0.001$.

B – Timecourse experiment of parental, control EV or *fam49b*-CrispR knockout cells plated on fibronectin and fixed after 30min, 1h, 2h, and 4h. Cells were stained for F-actin (green) and nuclei (blue). Scale bar = 40 µm. Quantification of cell area from 3 independent experiments is reported on the bar graph, with S.E.M represented. One-Way ANOVA with Tukey's post test was applied. *** $p<0.001$.

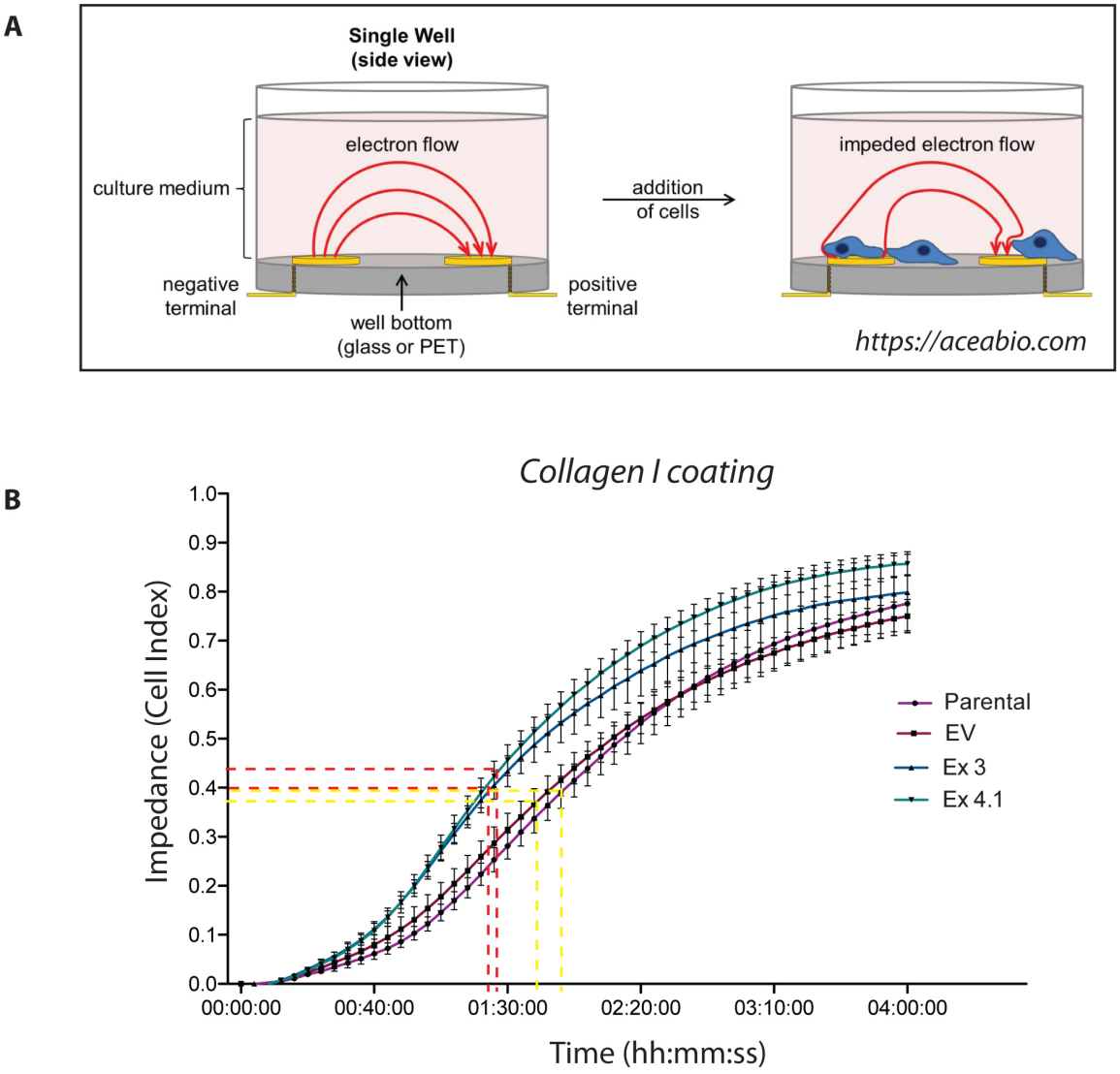

Figure 5-12: Real-time measurement of cell spreading using xCELLigence
A – Graphical representation of xCELLigence principle. Chips are covered by 2 electrodes able to sense the current. During cell adhesion and spreading, electron flow is affected and impedance can be measured.

B – Real-time measurement of adhesion and cell spreading over 4h of parental, control EV and *fam49b*-knockout CHL1 cells on collagen-I coated chip. Spreading halftime of control and *fam49b*-knockout cells is projected on the x-axis using respectively a yellow or red dotted line.

To be efficient and transmit forces, a lamellipodium has to be stabilised by focal adhesions. Based on the clutch model (Case and Waterman, 2015), focal adhesions follow a quick turnover dependent on the lamellipodia extension/retraction. In order to investigate whether the broad lamellipodia of *fam49b*-depeleted cells have any defect in focal adhesion organisation or dynamics, we used a combination of immunofluorescence, video-microscopy and image processing.

As a marker of active focal adhesion upon integrin engagement, phospho-Paxillin was an obvious staining to perform. Immunofluorescence analysis revealed more long and fine adhesions in the *fam49b*-knockout cells, running from the cell periphery toward the nuclei and sitting on transverse actin fibres (**Figure 5-12 – A**). This observation was even more obvious when looking at a global marker of focal adhesion, such as Vinculin. In this case, control cells showed a small and patchy staining whereas Vinculin staining was extended along the focal adhesion in the *fam49b*-knockout cells (**Figure 5-12 – B**).

However, CHL1 cells are not the best cell line to study focal adhesions because of their relative small size. So we switched to the B16F1 cells treated with siRNA against FAM49B and plated on laminin. The unusual shape of focal adhesions has been confirmed in this alternative cell line and gave an even more striking phenotype (**Figure 5-13 – A & B**). Using Fiji, we were able to threshold the vinculin staining and analyse different focal adhesion parameters. Quantification reveals that the number of adhesions was higher in knockdown cells, peaking at 30-35 focal adhesions (over 0.1 μm^2) per cell, compared to 19 focal adhesion/control cell (**Figure 5-13 – C**). Focal adhesions were also bigger, although the difference was not extremely different compared to the control cell line, which was a bit surprising based on the pictures (**Figure 5-13 – D**). Quite unsurprisingly, knockdown cells have more linear focal adhesions but once again, this quantification seems to underestimate the severity of the phenotype (**Figure 5-13 – E**). Indeed, the Fiji plugin seems to fragment the long focal adhesion, although they appeared as a homogeneous staining on the picture.

In order to be more confident, timelapse microscopy of GFP-Paxillin-transfected control and knockdown B16F1 cells, plated on laminin were obtained every minute. Still images from each movie were extracted and were attributed a specific colour corresponding to a specific time (**Figure 5-14**). Channels were merged and colocalisation of the colour means that the focal adhesion is stable. In our case, small focal adhesions were created at the extended lamellipodia of the control cells suggesting that these cells are able to form adhesion when a protrusion is created. However, at the rear, focal adhesions appeared relatively stable, as observed from the merge channel. This contrasts with the *fam49b*-knockdown cells that still form these elongated adhesions, which look more dynamic.

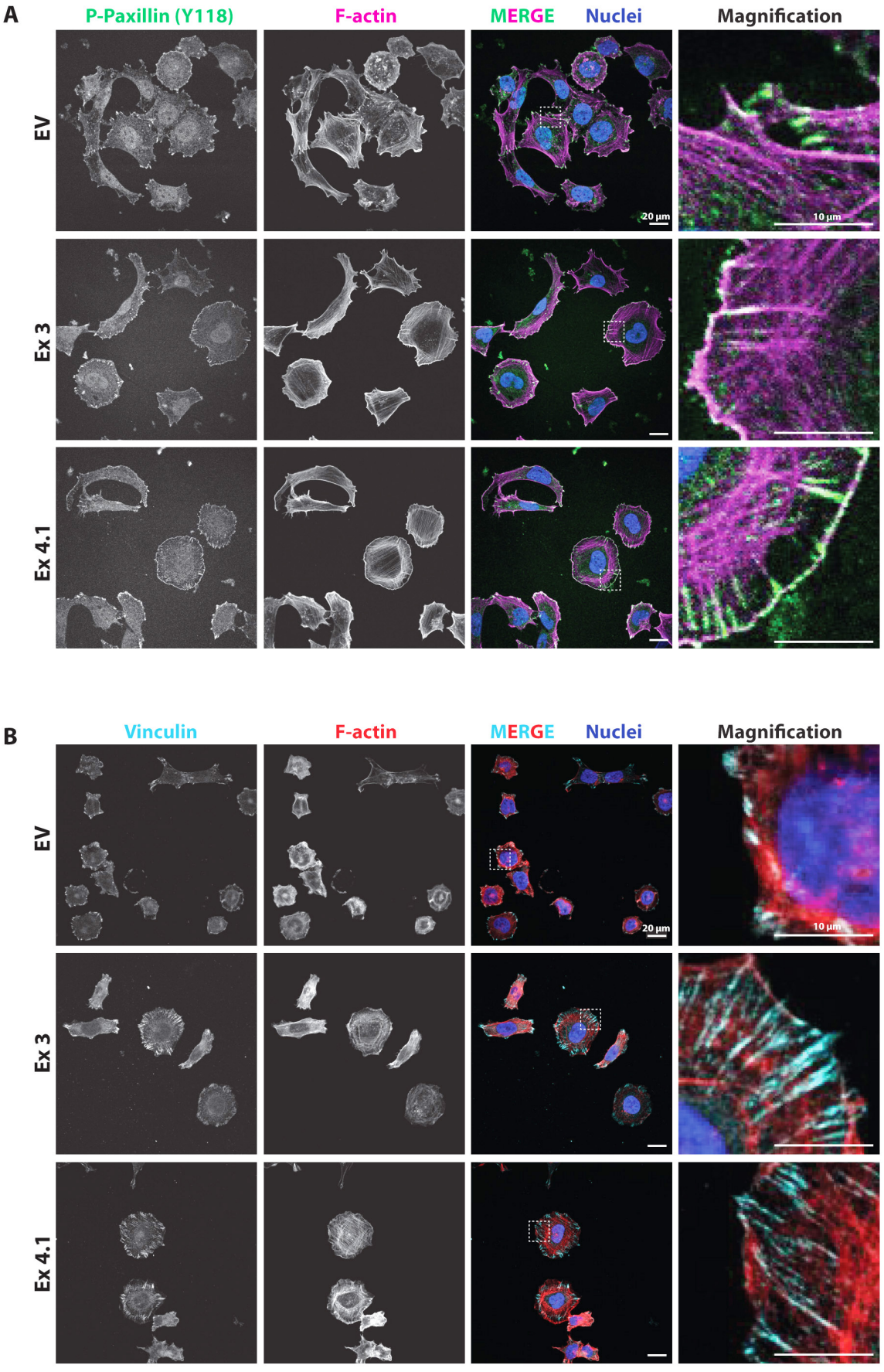

Figure 5-13: FAM49B affects focal adhesion morphology in CHL1 cells
Immunofluorescence of *fam49b*-CrispR knockout CHL1 cells plated on collagen-I and stained for different focal adhesion markers (pY118-Paxillin (A - green) or Vinculin (B - cyan)), F-actin (A – magenta or B - red) and nuclei (blue). Scale bar = 20 µm Magnified view of the white dotted area is shown on the far right panel. Scale bar = 10 µm.

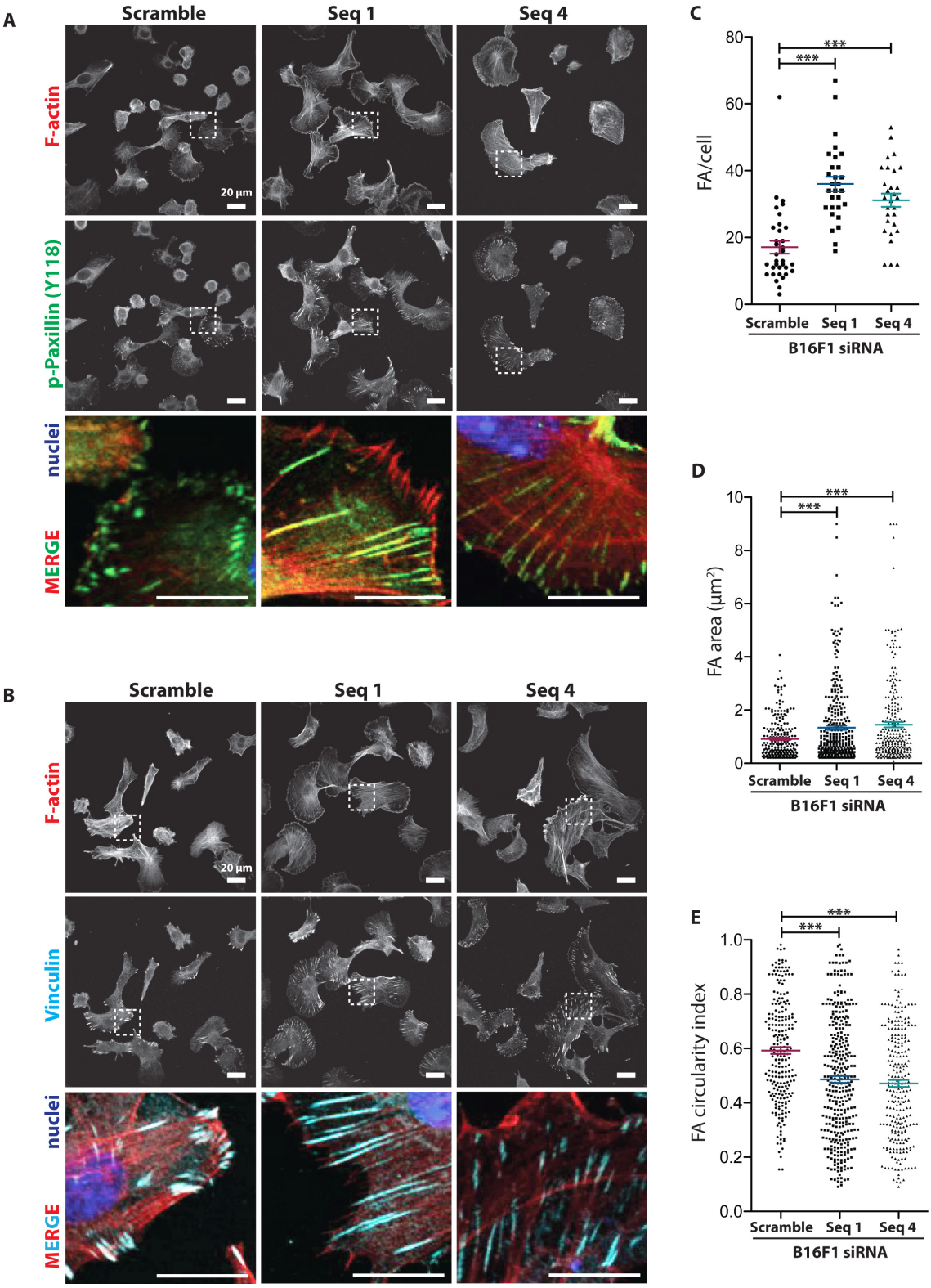

Figure 5-14: FAM49B regulates adhesions morphology and number in B16F1 cells
A-B - Immunofluorescence of *fam49b* knockdown B16F1 cells plated on laminin and stained for different focal adhesion markers (pY118-Paxillin (A - green) or Vinculin (B - cyan)), F-actin (red) and nuclei (blue). Magnified view of the white dotted area is shown below each panel. Scale bar = 20 µm.

C-E – Number of focal adhesion per cell (C), focal adhesion area (D) and focal adhesion circularity (E) were quantified based on vinculin staining from 3 independent experiments using Fiji plugin and presented as scatter plots with S.E.M displayed. One-Way ANOVA with Dunn's post-test was applied. *** p<0.001.

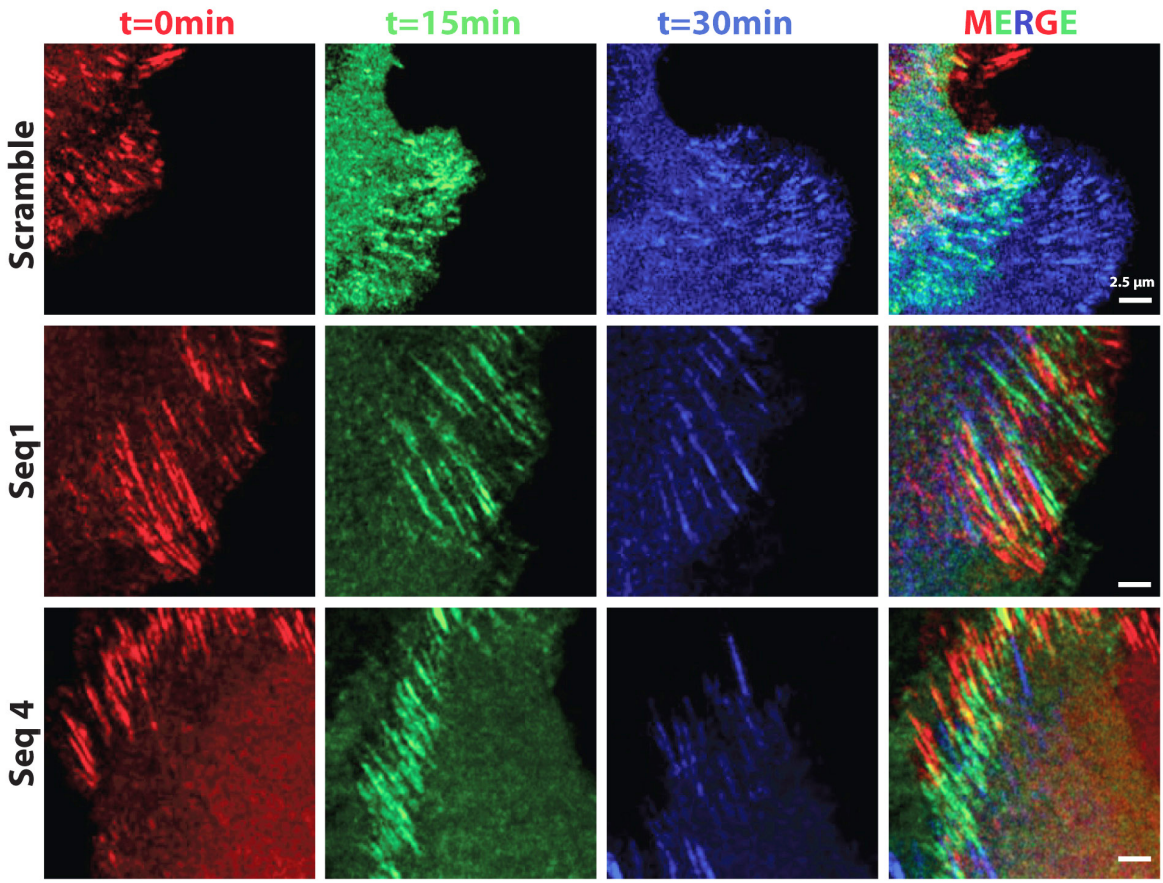

Figure 5-15: Timecourse of focal adhesion turnover in *fam49b*-knockdown B16F1 cells
Stills from a time-lapse experiment of control or *fam49b*-knockdown B16F1 cells transfected with GFP-Paxillin and plated on laminin. Pictures were taken every minute for 30 min and frame at 0, 15 and 30min was assigned a specific colour (red, green and blue respectively). Merge channel is also displayed. Scale bar = 2.5 µm

Another method to analyse focal adhesion dynamics in a quantitative way is to obtain fast-time frame movies (1 frame/20sec) and upload them to the Focal Adhesion Analysis Server (FAAS - http://faas.bme.unc.edu). Automatic tracking of each paxillin-positive area (bigger than 15px^2), lasting more than 5 frames, allowed us to analyse the directionality and the turnover of these adhesions. After analysis, the read out is a rainbow-colour map of each focal adhesion according to their turnover, ranging from cold-colour (fast turnover) to hot colour (slow turnover) (**Figure 5-15**). This server allowed the tracking of thousands of focal adhesions over a 30-minute movie and analyses their dynamics. Analysis of these preliminary experiments confirmed the previous observation. Indeed the algorithm picked longer focal adhesions for knockdown cells. Strikingly, the *fam49B*-knockdown cells have very stable focal adhesions at the cell edge whereas focal adhesion just below the cell body turned over more quickly.

Although the global characterisation of focal adhesions is important, their localisation within the cell and their organisation compared to the protrusion is even more critical for the potency of force transmission. The different staining techniques clearly suggest that knockout/down cells have more radially aligned adhesions relative to cell protrusions. We used the focal adhesion alignment index (FAAI) obtained from the FAAS. This index reflects the standard deviation (SD) from the dominant angle of the entire distribution of the population of focal adhesion and is defined by the following: FAAI=90-SD. The more alignment and homogeneous the distribution is, the lower the SD should be resulting in a high FAAI. The higher the index, the more aligned the adhesions are (Wu et al., 2012). In order to have a meaningful value that reflects a proper orientation of the adhesion, this index only analyses adhesions with a length/width ratio larger than 3. In our case, adhesion alignment of knockdown cells is much higher (in average 58 degrees) compared with control condition with an index of 47 degrees.

In summary, we showed using different genetic strategies and cell types that FAM49B-depleted cells have larger lamellipodia characterised by an increase of WRC at the cell edge. This broader protrusion displays numerous, bigger and more elongated focal adhesions. Also, these adhesions align in the same direction as the protrusion. Our hypothesis that FAM49B restricts lamellipodia extension by inhibition of Rac1 diffusion was backed-up by over expression of the protein that leads to pseudopod splitting, WRC restriction and lack of pseudopod dynamics.

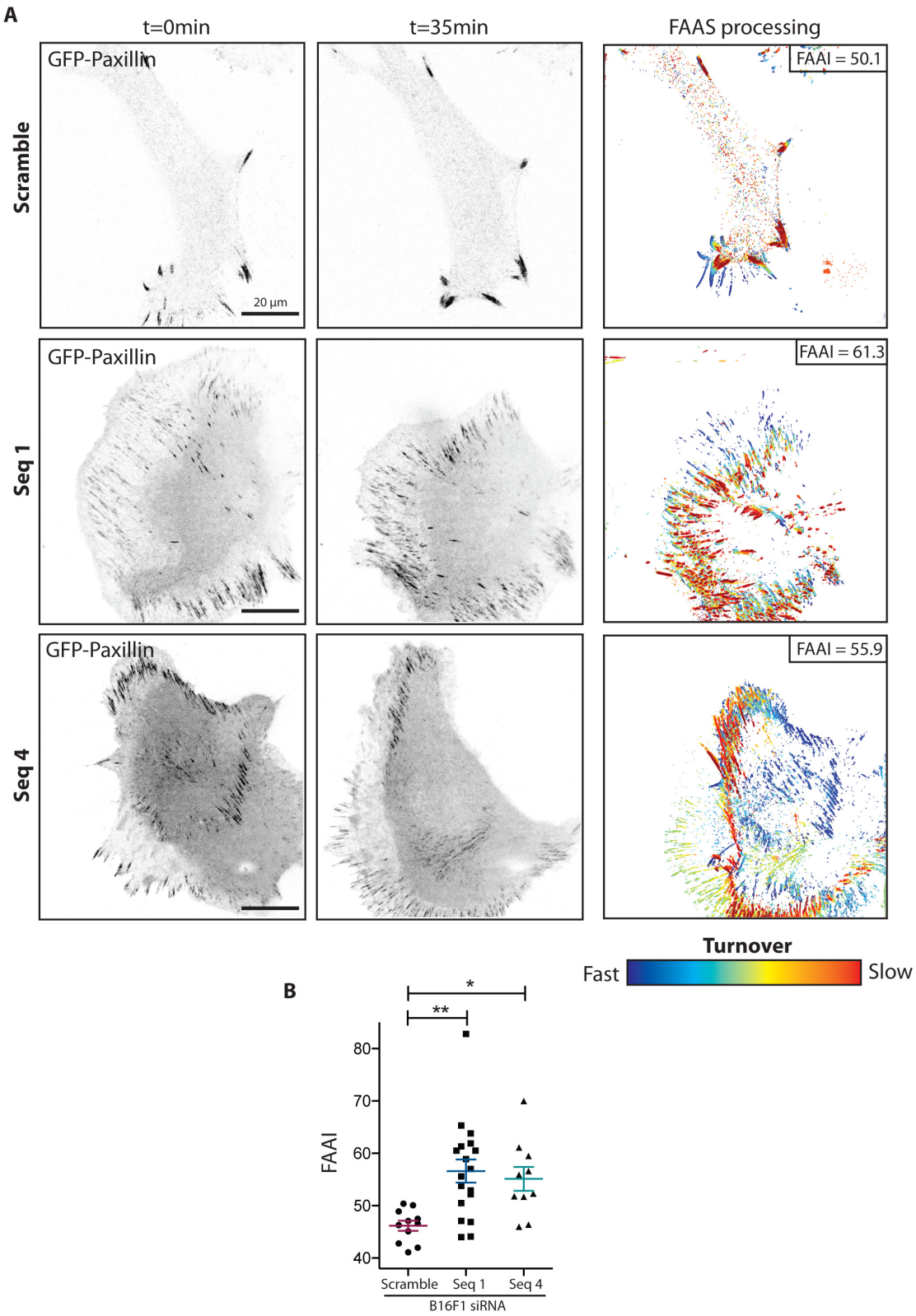

Figure 5-16: Dynamics of focal adhesion in control or *fam49b*-knockdown B16F1 cells
A – Stills from a timelapse movie of GFP-Paxillin transfected B16F1 cells, treated with control or FAM49B siRNA and plated on laminin. Movies were processed by the FAAS server and representative pictures from the focal adhesion turnover analysis are shown in a rainbow colour code, with the corresponding FAAI. Scale bar = 20 µm

B – Preliminary quantification of focal adhesion alignment using the FAAS server algorithm. Scatter plot represents quantification of 2 independent experiments and S.E.M is displayed. One-Way ANOVA with Dunn's post test was applied. * $p<0.05$, ** $p<0.01$.

5.2.2 Loss of FAM49B increases filopodia number using a CDC42-independent pathway

During the characterisation of our different knockdown/out cell lines, we came across an interesting phenotype linked to filopodia. Filopodia are motile and fine protrusions, arising from the lamellipodium and extending out of the cell body. Filopodia are formed by actin bundles, tightly linked together by various actin-binding protein (Chapter 1.2.2). The most predominant crosslinker is Fascin. Fascin staining has been previously optimised in our group and can be considered as a specific filopodium marker. B16F1 are well known for their ability to form dynamic and straight filopodia so they represent a good model. Cells were treated with siRNA against FAM49B, plated on glass coverslips overnight, ice-cold methanol fixed and stained for endogenous Fascin. Unfortunately in these conditions, phalloidin staining cannot be performed as methanol fixation affects actin structure (Whelan and Bell, 2015).

Surprisingly, scramble-siRNA treated cells showed an increase of cells exhibiting filopodia and also in number of filopodia per cell compared with parental cells (**Figure 5-16 – A & B**). This does not really affect our assay as scramble condition is always used as the control cell line but it was worth mentioning this effect in sake of transparency. Despite this effect, depletion of FAM49B increased the ability of cells to form filopodia and also increased the number of filopodia formed per cell by 75 % (*10 filopodia/cell for control versus 17 and 16 filopodia/cell for Seq1 and Seq4 respectively*) (**Figure 5-16 – A-C**). These filopodia are also on average much longer (3.5 µm versus 2 µm for control) and whereas only 15 % of the filopodia are longer than 3 µm in control conditions, this percentage increased to 60 % in the knockdown cell lines (**Figure 5-16 – D & E**).

In order to get more insight into the dynamics of these structures, control or *fam49b*-knockdown cells were transfected with GFP-Fascin and imaged by video-microscopy (**Figure 5-17**). Enrichment of GFP-Fascin-positive filopodium was confirmed and kymographs showed a very dynamic state of these structures. Indeed, usually 3-4 filopodia collide into each other and merge together in knockdown cells whereas this has never been seen in control cells. It is also interesting to note that these filopodia are embedded within an enlarged lamellipodium. Indeed, this phenotype seems highly dependent on the presence and the stability of the lamellipodium. For example, upon lamellipodium retraction, filopodia get more disorganised and thinner or disappeared (**Figure 5-17 - A** - see stills from Seq4).

To confirm this observation, CHL1 cells were treated with siRNA and protein expression was assessed by western blot. FAM49B level was reduced by 80 % using 4 independent siRNA oligos (**Figure 5-18**). Filopodia were manually analysed using fascin-stained parental, control or *fam49b*-knockdown CHL1 cells (**Figure 5-19**). Similar to B16F1 cells, CHL1 depleted of FAM49B formed more filopodia and filopodia-bearing cells compared to controls (**Figure 5-19 – A-C**). The length of the filopodia were also similarly affected in the same kind of range as B16F1 cells (**Figure 5-19 – D & E**). Despite its effects on filopodia, Seq5 appeared to be the least tolerated oligo. Treated cells rounded up quickly and extensive cell death was observed. This might suggest some off-target effects so phenotypes obtained with this oligo were not further investigated. Oligos number 6 and 7 were picked as they gave the most dramatic phenotype and could be tolerated by the cells. Timelapse microscopy of knockdown cells also confirmed the increased of filopodia number (**Figure 5-20**).

Finally, very similar results were obtained using CrispR knockout cell lines, which reassured us about the specificity of our siRNA treatment (**Figure 5-21**).

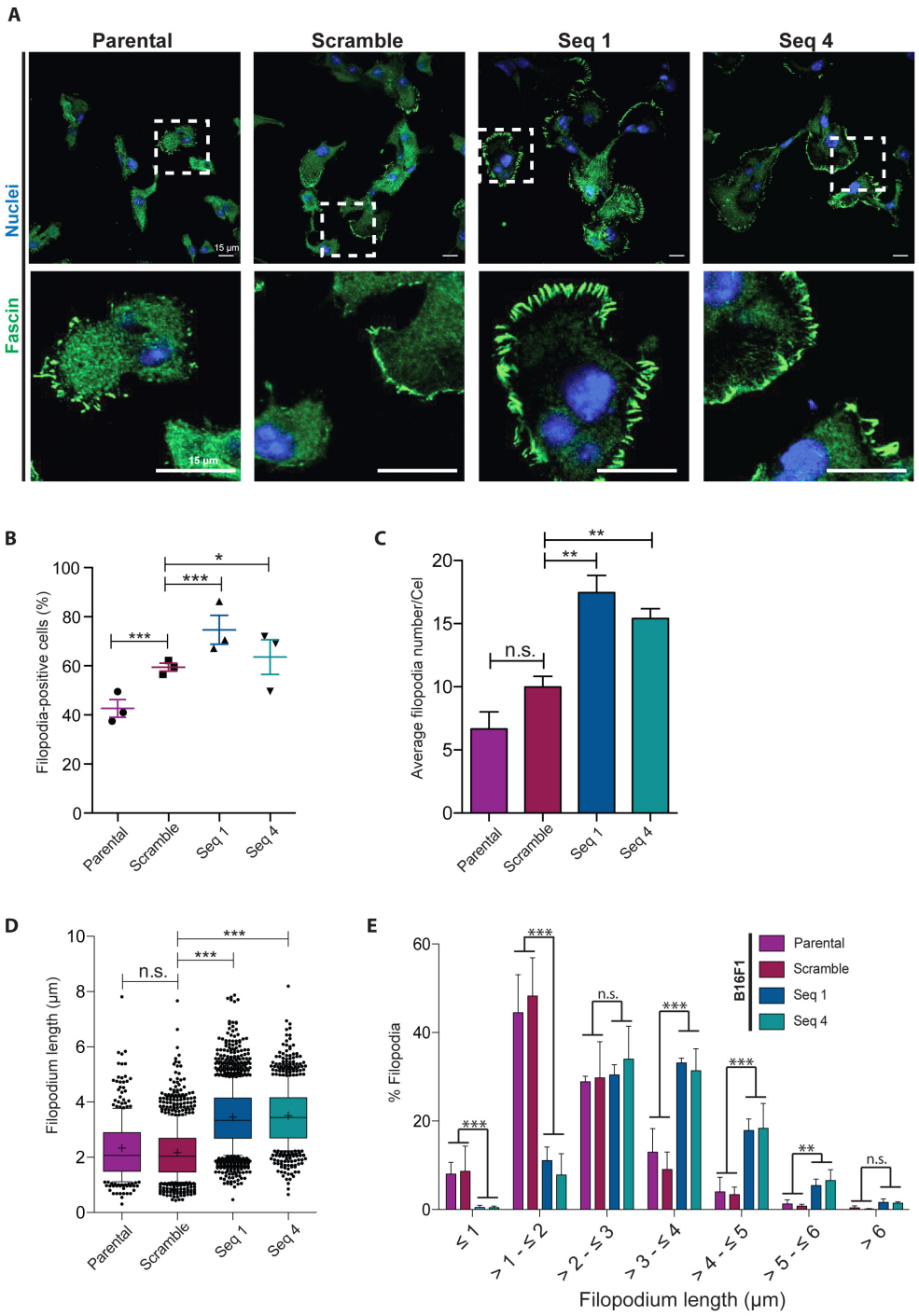

Figure 5-17: FAM49B-depletion increases filopodia formation and length in fixed B16F1 cells
A – Immunofluorescence of parental, Scramble-treated or *fam49b*-knockdown B16F1 cells, plated on glass coverslip, methanol-fixed and stained for Fascin (green) and nuclei (blue). Scale bar = 15 µm.

B – C – Quantification of the proportion of cells with filopodia (B) and the average number of filopodia per cell (C). Scatter and bar plots represent quantification from 3 independent experiment and S.E.M is displayed. Exact Cochran-Mantel-Haenszel test (B) and One-Way ANOVA with Dunn's post test (C) were performed. n.s. $p>0.05$, * $p<0.05$, ** $p<0.01$, *** $p<0.001$.

D – E – Quantification of filopodia length is shown as the total distribution (D) or ranked according to the percentage of filopodia with a designated length (E). Whisker plot and bar plot represent quantification of 3 independent experiments. 10-90 percentile, S.E.M and mean (cross) are displayed. One-Way ANOVA with Dunn's post-test (D) and two-Way ANOVA (E) were performed. n.s. $p>0.05$, ** $p<0.01$, *** $p<0.001$.

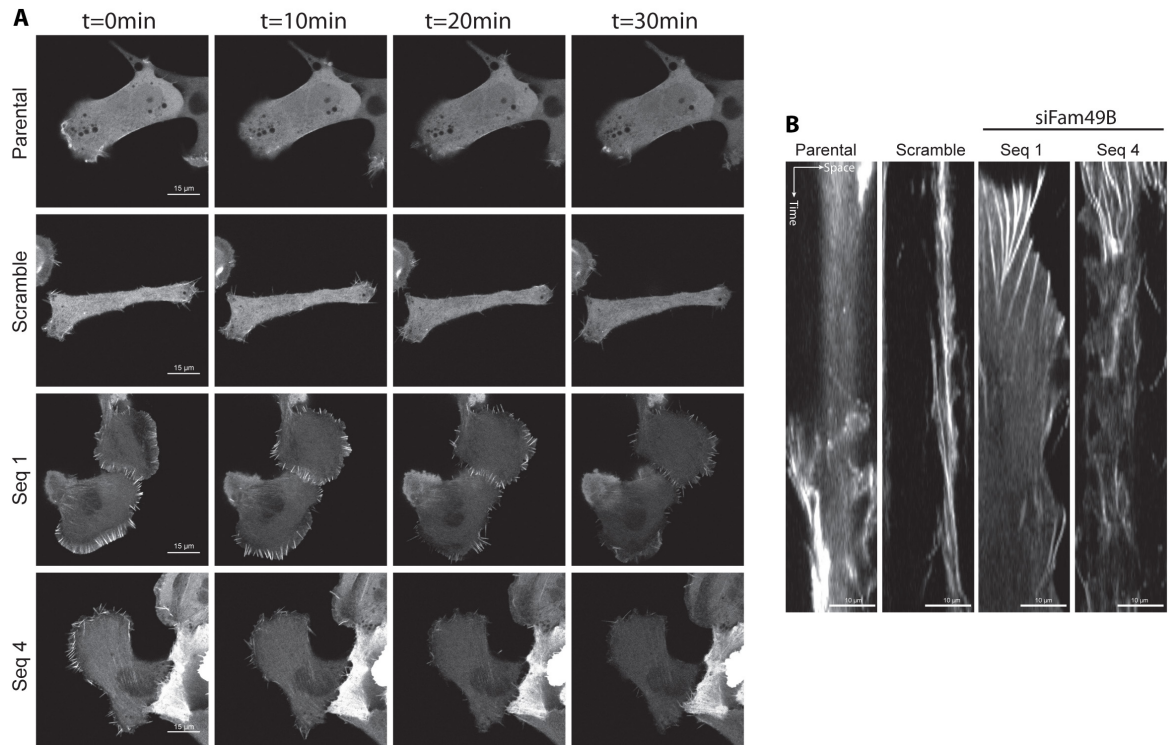

Figure 5-18: Live imaging of B16F1 cells upon FAM49B depletion confirmes an increase of filopodia number and length

A – Video-microscopy of parental, control or *fam49b*-knockdown B16F1 cells transfected with GFP-Fascin and imaged every minute. Representative still pictures are shown every 10min. Scale bar = 15 µm

B – Kymograph from representative movie showing filopodium dynamics in parental, control and *fam49b*-knocdown B16F1 cells. Scale bar = 10 µm

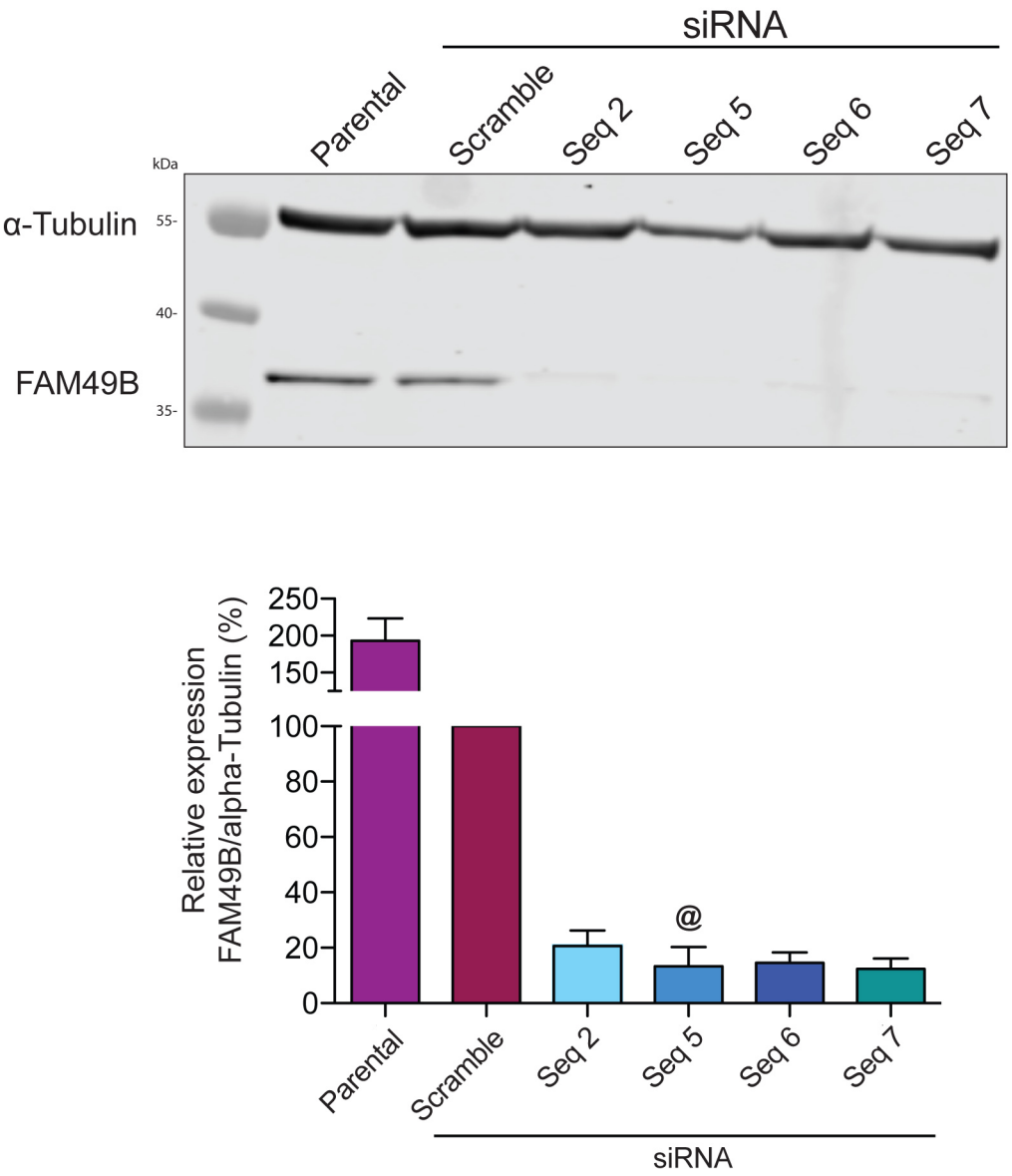

Figure 5-19: *fam49b*-knockdown in CHL1 cells
A – Western blot analysis of parental, control and *fam49b* knockdown in CHL1 cells using 4 independent siRNA. Membrane was blotted against FAM49B and α-Tubulin. Molecular weights are displayed on the side. Bar plot represents quantification of 3 independent experiments and S.E.M is displayed. (@ = only 2 repeats).

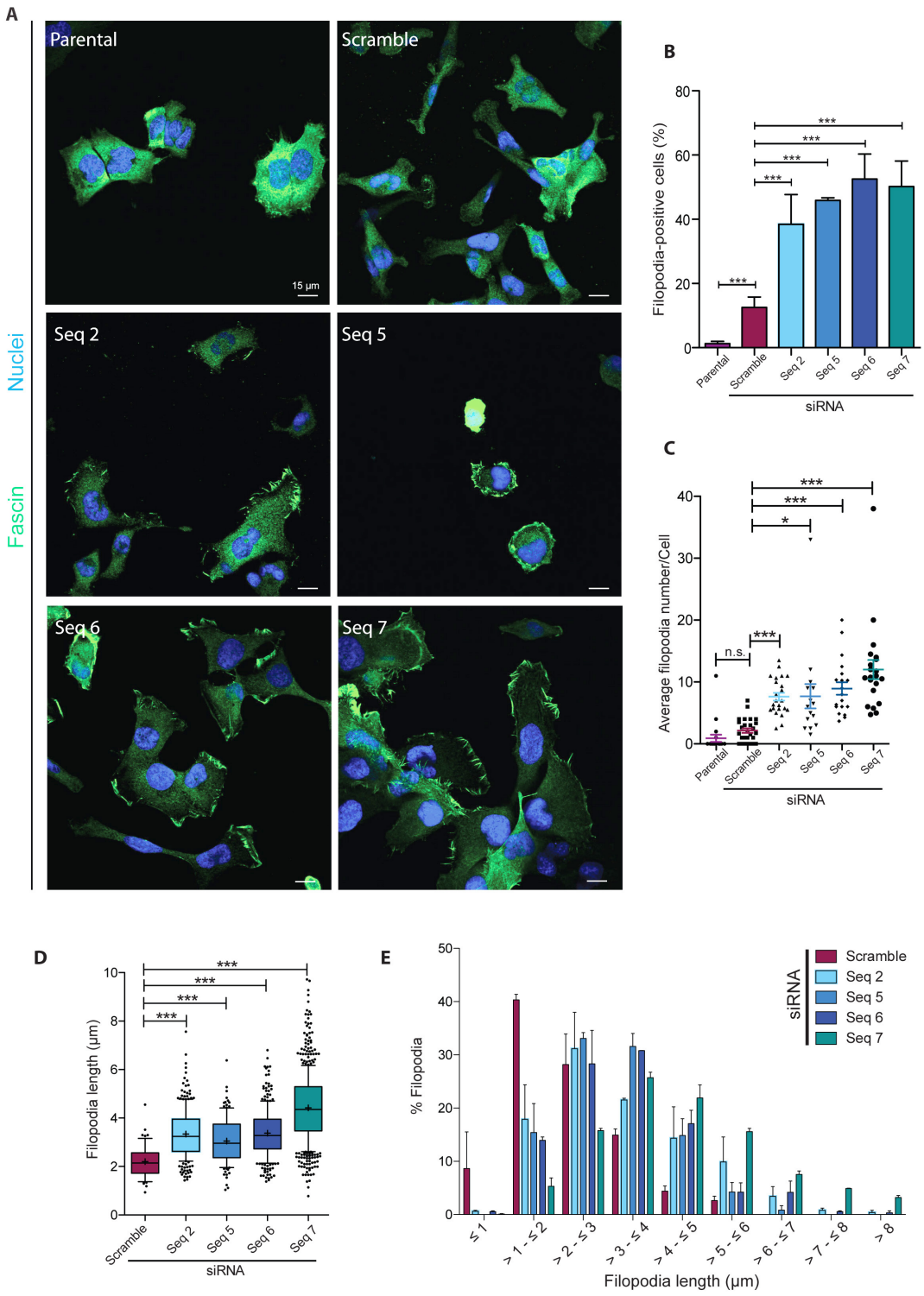

Figure 5-20: *fam49B*-knockdown CHL1 cells display more and longer filopodia
A - Immunofluorescence of parental, Scramble-treated or *fam49b*-knockdown CHL1 cells, plated on glass coverslip, methanol-fixed and stained for Fascin (green) and nuclei (blue). Scale bar = 15 µm.

B-C - Quantification of the proportion of cells with filopodia (B) and the average number of filopodia per cell (C). Scatter and bar plots represent quantification from 3 independent experiments and S.E.M is displayed. Exact Cochran-Mantel-Haenszel test (B) and One-Way ANOVA with Dunn's post test (C) were performed. n.s. $p>0.05$, * $p<0.05$, *** $p<0.001$.

D - E - Quantification of filopodia length is shown as the total distribution (D) or ranked according to the percentage of filopodia with a designated length (E). Whisker and bar plot represent quantification of 3 independent experiments. 10-90 percentile, S.E.M and mean (cross) are displayed. One-Way ANOVA with Dunn's post-test (D) was performed. *** $p<0.001$

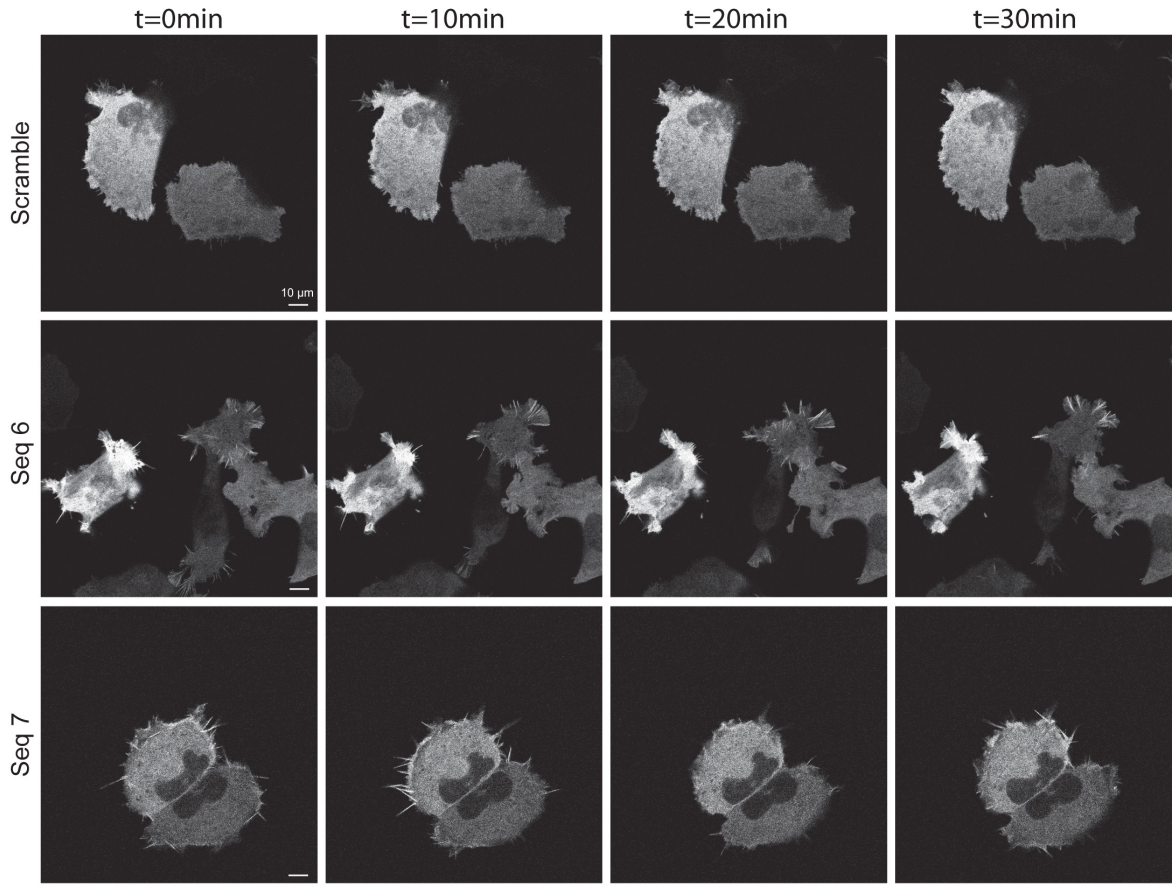

Figure 5-21: *fam49b*-knockdown increases filopodium formation and length in CHL1 cells
Video-microscopy of control or *fam49b*-knockdown CHL1 cells transfected with GFP-Fascin and imaged every minute. Representative still pictures are shown every 10min. Scale bar = 10 µm

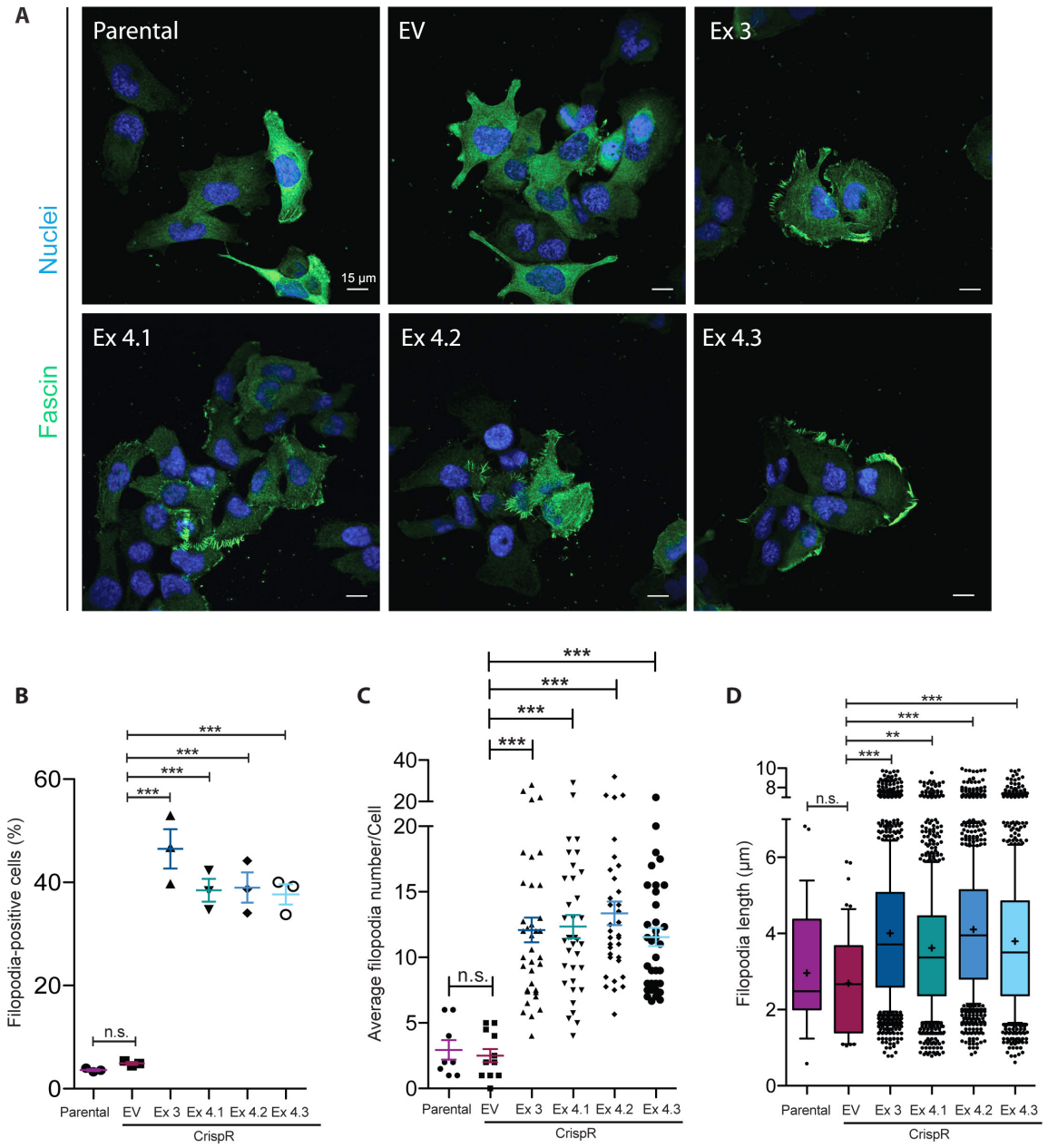

Figure 5-22: CrispR knockout of FAM49B increases filopodium formation and length in CHL1 cells

A - Immunofluorescence of parental, control (EV) or 4 independent *fam49b*-knockout CHL1 cell lines, plated on glass coverslip, methanol-fixed and stained for Fascin (green) and nuclei (blue). Scale bar = 15 µm

B-D - Quantification of the proportion of cells with filopodia (B), the average number of filopodia per cell (C) and filopodia length (D) in parental, control (EV) and *fam49b*-knockout CHL1 cells. Scatter and Whisker plots represent quantification from 2 independent experiments. 10-90 percentile, S.E.M and mean (cross) are displayed. Exact Cochran-Mantel-Haenszel test (B) and One-Way ANOVA with Dunn's post-test (C and D) were performed. n.s. $p>0.05$, ** $p<0.01$, *** $p<0.001$

CDC42 is commonly seen as the main regulator of filopodium formation (Krugmann et al., 2001). However, based on our pulldown assay, we have been unable to detect any direct interactions between FAM49B and CDC42, suggesting both proteins are unlikely to regulate each other's activity. In order to investigate whether this filopodium phenotype was driven by CDC42, B16F1 cells were co-transfected with siFAM49B (Seq1) and siCdc42. Western blot analysis confirmed the decrease of expression of both proteins (**Figure 5-22 – A**), so cells were stained for Fascin. Control cells treated with siCdc42 had a reduction of filopodia number and length, suggesting that B16F1 cells are dependent of CDC42 during filopodium formation. However, preliminary quantification suggests that *fam49b*-knockdown cells and FAM49B and CDC42 double knockdown cells had similar numbers of filopodia and similar average lengths, suggesting that filopodium formation due to FAM49B depletion is independent of CDC42 activity (**Figure 5-22 – B & D**). In parallel, chemical inhibition of CDC42 was also used in order to corroborate the genetic depletion. Control or *fam49b*-knockdown cells were treated overnight with the non-competitive allosteric CDC42 inhibitor ML141 at a concentration 5 times higher than the reported EC_{50}. Unlike Scramble-treated cells, *fam49b*-knockdown-induced filopodia were not affected by the inhibition of CDC42 (**Figure 5-22 – C & E**). In either case, inhibition of CDC42 did not affect lamellipodium extension and siCdc42 or ML141-treated *fam49b*-knockdown cells still maintained large and broad protrusions.

Taken together, this chapter has shown using a combination of cell lines and strategies that FAM49B depletion enhances lamellipodium extension and spreading, correlating with bigger focal adhesions. This enlarged lamellipodium is enriched with fast moving filopodia, which are regulated in a CDC42-independent pathway. Conversely, FAM49B overexpressing cells have a reduction in cell size and exhibit a fractal lamellipodium.

Together, this increase in actin-based protrusions in FAM49B-depleted cells should be directly correlated to a difference in motility.

5.2.3 Loss of FAM49B enhances 2D migration, matrix degradation and 3D invasion

Since *fam49b*-knockout/knockdown cells have an increase in focal adhesion, lamellipodium formation and filopodia, we asked how does this affect their migration. Migration of control or *fam49b*-knockout CHL1 cells was directly assessed using a random migration assay.

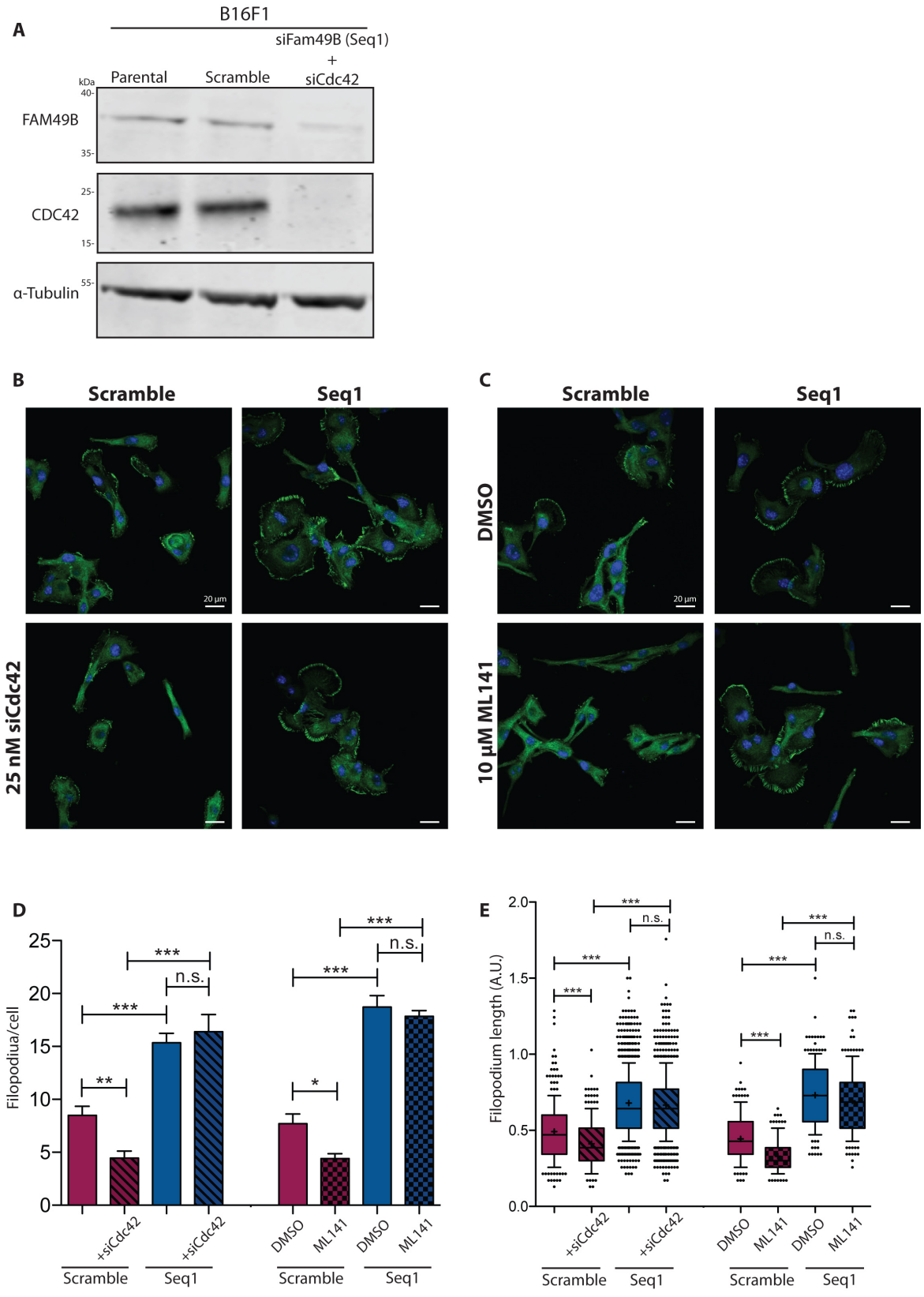

Figure 5-23: Increase in filopodia formation is independent of CDC42 activity
A – Western blot analysis of the double siRNA treatment against FAM49B (Seq1) and Cdc42 in B16F1 cells. Parental or Scramble-treated cell lysates were also analysed. Membrane was blotted against FAM49B, CDC42 and α-Tubulin. Molecular weights are displayed on the side.

B – Immunofluorescence of control or *fam49b* knockdown cells or co-transfected with siRNA against Cdc42. Cells were plated on glass coverslip, methanol-fixed and stained for endogenous Fascin. Scale bar = 20 µm

C - Immunofluorescence of control or *fam49b* knockdown cells treated overnight with DMSO or 10 µM of ML141. Cells were plated on glass coverslip, methanol-fixed and stained for endogenous Fascin. Scale bar = 20 µm

D-E – Preliminary quantification of number of filopodia/cell (D) and average filopodia length was measured (E). Whisker plot and bar plots represent quantification from 2 independent experiments. 10-90 percentile, S.E.M and mean (cross) are displayed. Mann Whitney tests were performed for each data set. n.s. $p>0.05$, * $p<0.05$, ** $p<0.01$, *** $p<0.001$

This assay allows to directly measure the speed of cell translocation in the absence of specific directional stimuli. In this setup, cells are sparsely seeded onto fibronectin-coated dish and imaged overnight every 10 min under normal culturing conditions.

Manual tracking of each cell allows the depiction of cell migration over the course of the experiment as a spider plot and informs us about average cell speed and travelled distance. Cell showing a travelled distance greater than 100 µm are depicted in black on the spider plots (**Figure 5-23 – A & B**).

Under these conditions, *fam49b*-knockout CrispR cells migrate slightly faster compared with controls. As previously mentioned, the C-shape phenotype is more frequently seen in *fam49b*-CrispR knockout cells (**Figure 5-1**). This was also observed in this assay and it was noticed that the increase in cell motility observed in the random migration assay was directly related to this C-shape phenotype (**Figure 5-23 – B-F**). Indeed, we correlated the percentage of time spent by a cell with this phenotype to the average speed over the 17 hours of movies. *fam49b*-knockout cells show a much better association between phenotype and speed compared with control cells, as expressed by the Pearson coefficient (**Figure 5-23 – C & D**). Interestingly, C-shape cells migrate faster than other randomly shaped cells. However, speed of control C-shape cell is much lower compared with *fam49b*-knockout C-shape cells *(Control = 0.25 µm/min, Ex3 = 0.5 µm/min, Ex4.1 = 0.4 µm/min)*(**Figure 5-23 – G**). From this analysis, we conclude that C-shape cells drive the increase of cell motility observed upon FAM49B loss. *fam49b*-knockout cells lacking a definite polarisation of their protrusions (random shape or fried-egg shaped cells in either control) migrated less than the C-shaped cells but when compared to their control counterparts, they still displayed a higher migration (**Figure 5-23 - G**).

In order to investigate the effect of FAM49B on matrix remodelling and invasion, B16F1 or CHL1 treated with control or Fam49B siRNA were plated on a fine layer of OregonGreen-gelatin. Cells were fixed after 4h, stained for F-actin and gelatin degradation was measured by pixel intensity threshold using Fiji. Independently to the cell lines used, transient depletion of FAM49B leads to an increase of matrix degradation (**Figure 5-24**).

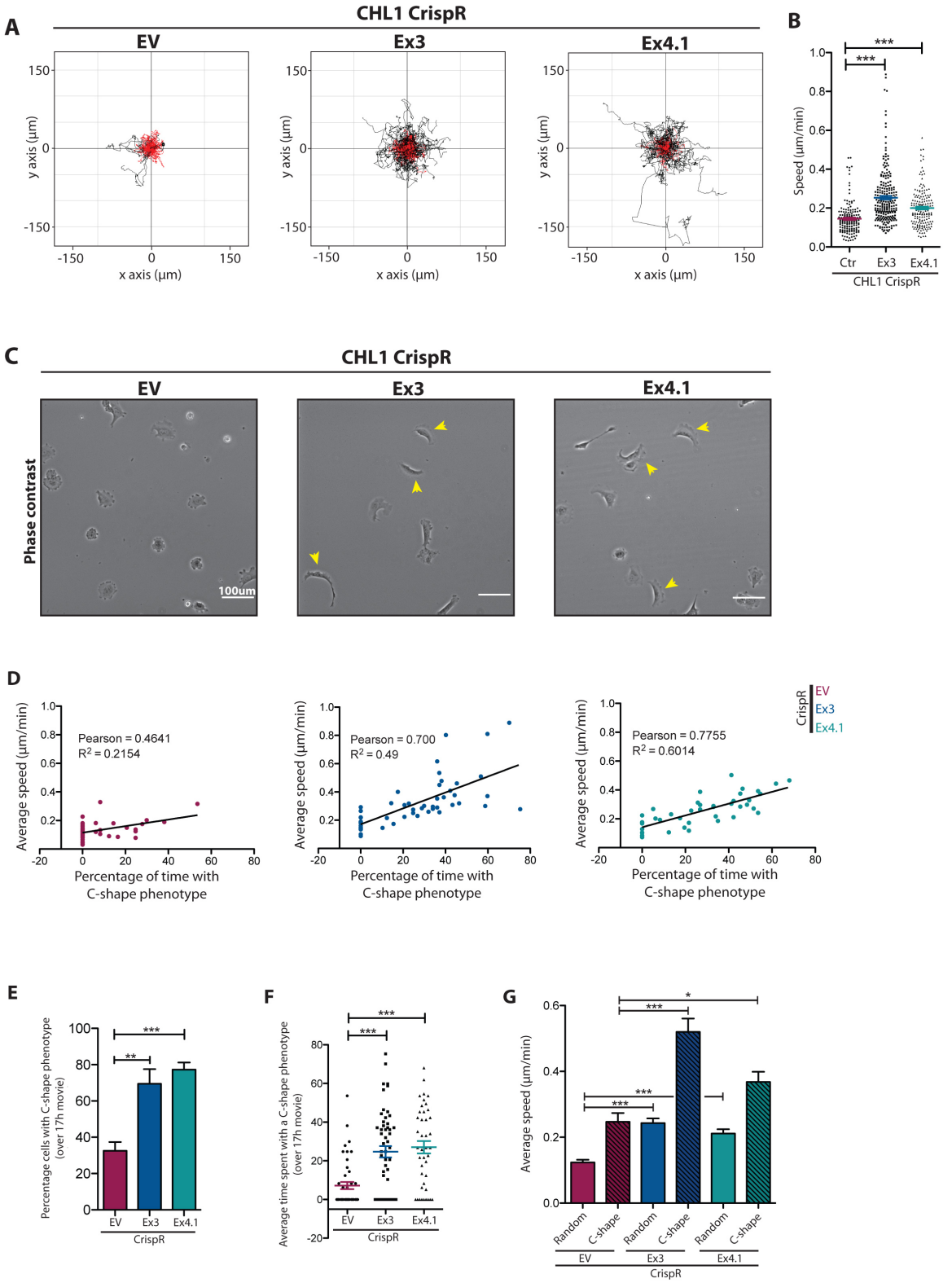

Figure 5-24: Regulation of membrane protrusion by FAM49B affects 2D-migration of CHL1 cells

A – Spider plots from 3 independent random migration assays of Control (EV) or *fam49b*-CrispR knockout cell plated on fibronectin. Displacement of each cell is reported on the x and y-axis and reflects the cell path over 17h of tracking (1 frame/10min). Black tracks represent cells with a travelled distance greater than 100 µm during 17h and red less than 100µm. Spider plot generated using the Chemotaxis tool from Fiji.

B – Average speed of each cell obtained from the random migration assay experiment. Scatter plot represents quantification from 3 independent experiments. Error bars represent S.E.M. One-way ANOVA with Dunn's test was performed. *** p≤0.001

C – Representative still phase contrast pictures from a random migration assay of control (EV) and *fam49b*-knockout CHL1 cells plated on fibronectin. C-shaped cells have been highlighted with a yellow arrowhead. Scale bar = 100 µm

D - Correlation between cell shape and average speed in control (Ctr) or *fam49b*-CrispR knockout CHL1 cells. Pearson coefficient and R^2 value are shown for each condition.

E-F - Random migration assay movies were analysed and percentage of cells presenting a C-shape and time spent with this phenotype were measured and plotted in E and F respectively. Scatter and bar plots represent quantification from 3 independent experiments, with S.E.M displayed. E - Cochran-Mantel-Haenszel test was applied ** p<0.001, *** p<0.0005. F - One-way ANOVA with Dunn's multiple comparison test was performed. *** p<0.001.

G) Speed of control (EV) or *fam49b*-CrispR knockout cells displaying a random or a C-shape. Bar plot represents quantification from 3 independent experiments and S.E.M is displayed. One-way ANOVA with Dunn's test was performed. * p<0.05, *** p≤0.001

This process is fully mediated by MMP-activity as incubation with a broad spectrum MMP inhibitor totally blocked matrix degradation (**Figure 5-24**). Gelatin-based zymography failed to show any increase in the secretion or activity of MMP-2 or MMP-9, the two main collagenases (not shown). Surprisingly, *fam49b*-CrispR knockout CHL1 cells do not show any increase of matrix degradation (not shown). This differential effect is not totally understood yet but might be due to an adaptation of the cell after knocking-out *fam49b* gene versus a rapid removal of the gene by siRNA..

Based on the previous data, CrispR knockout cells should not show any phenotype on different 3D-invasion assays. To test this hypothesis, cells were plated to confluence except in a middle area of the dish, protected by a silicon stopper. The stopper was then removed and cells covered with a fine layer of Matrigel and imaged using timelapse video-microscopy (**Figure 5-25 - A**). In this assay, cells are forced to invade through a Matrigel layer and the closure of the central area can be measured overnight. However, while cells are initially on a 2D surface, this experiment allows investigator to observe the transition from a 2D to a 3D environment. Surprisingly in these conditions, *fam49b*-CrispR knockout cells showed a slight but consistent increase in invasion, with a 1.5 and 1.3-fold increase of invasion (Ex3 and Ex4.1 respectively) compared with control cells (**Figure 5-25 - B**). Despite a statistical difference, these data were not strong enough to convince us about the relevance of FAM49B during invasion.

In order to validate the previous experiment, an alternative experiment classed as the inverted invasion assay, was optimised for these cells. Cells were plated at the bottom face of a ∅ 8µm filtered insert, filled with Matrigel and a chemotactic gradient was artificially created by filling the upper chamber in 10% FBS while the cells in the lower chamber were kept in serum-free medium (**Figure 5-26 - A**).

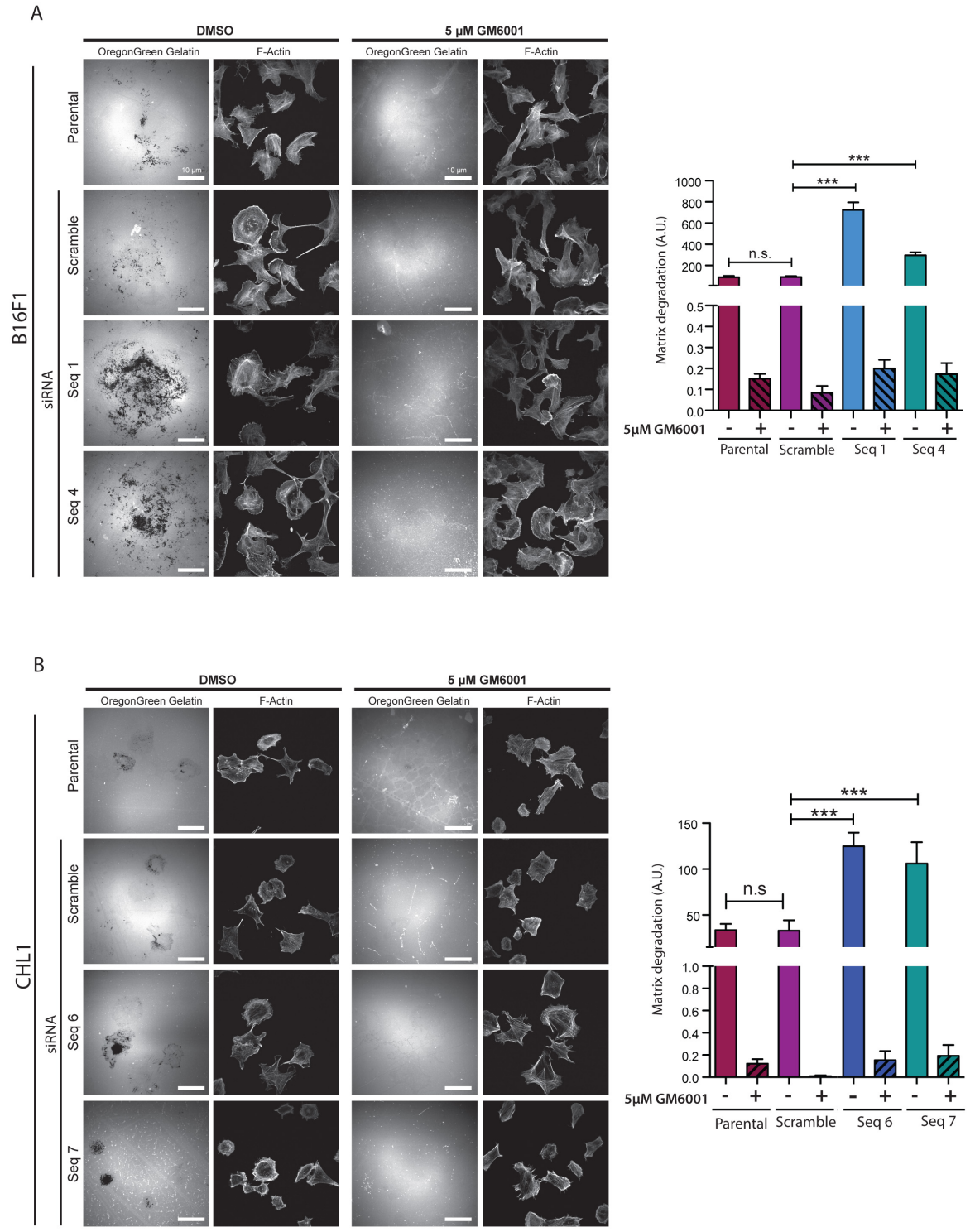

Figure 5-25: FAM49B affects matrix degradation in a MMP-dependent way
A-B – Immunofluorescence pictures from parental B16F1 (A) and CHL1 (B) cells or treated with control or FAM49B siRNA. Cells were plated on OregonGreen Gelatin and treated for 4h with DMSO or 5 µM of GM6001. F-actin was also stained using Phalloidin. Matrix degradation was quantified from 3 independent experiments and displayed as a bar plot with S.E.M displayed. One-way ANOVA with Dunn's test was performed. n.s. $p>0.05$, *** $p\leq0.001$. Scale bar = 10 µm.

Cells were allowed to invade up into the Matrigel plug for 3.5 days before performing a Calcein-live staining. Z-stacks of 15 µm were acquired throughout the plug and Fiji threshold was applied on the Calcein staining and used as readout for cell invasion. In this assay, cells are commonly considered as "invasive" once they migrate at least 45 µm above the filter (depicted by a yellow dotted line) (**Figure 5-26 - B**). In the time of the experiment, parental and control CrispR cells invaded up to 165 µm compared to the knockout cells that reached 225 µm. Also, more *fam49b*-knockout cells invaded to a given depth compared with controls. Statistical analysis performed by Dr. Matt Neilson show a difference between controls and knockout cells for depth equal and above 45 µm (**Figure 5-26 – C-D**).

Together, we can conclude that loss of FAM49B increases 2D cell motility and 3D invasion *in vitro*.

5.3 Discussion

In this chapter, I have shown that affecting FAM49B level or disruption of the interaction between FAM49B and active Rac1 had important consequences on Rac1's downstream processes, such as lamellipodia formation, focal adhesions and filopodia.

Cells lacking FAM49B exhibit large lamellipodia and frequently assume a fried-egg phenotype, which has previously been linked to Rac1 over-activation. Indeed, transfection of a dominant active Rac1 into cells leads to the formation of this fried-egg morphology (Gautier et al., 2011). This phenotype reflects a tight balance between GEF and GAP and their ability to regulate Rac1. Indeed, PDGF-stimulated cells show a similar fried-egg phenotype, which has been linked to the Rac1-GEF P-Rex1 (Barber et al., 2012).

It also appears that FAM49B effects are highly dependent on Rac1. Indeed, Heather Spence addressed this question by using immortalised mouse-tail fibroblasts floxed for Rac1 gene and treated with siRNA against FAM49B. She found that depletion of FAM49B was not able to rescue Rac1 knockout (Fort et al - in revision). Indeed, OHT-treated cells do not spread, become linear and bipolar as reflected by a circularity index of 0.3. This value was exactly the same when these cells were treated in parallel with 2 independent siRNA against FAM49B. In addition, recruitment of WAVE2 to the lamellipodia was not rescued upon co-depletion of Rac1 and FAM49B. This observation highlights the dependence of FAM49B on Rac1 activity in order to mediate lamellipodium extension.

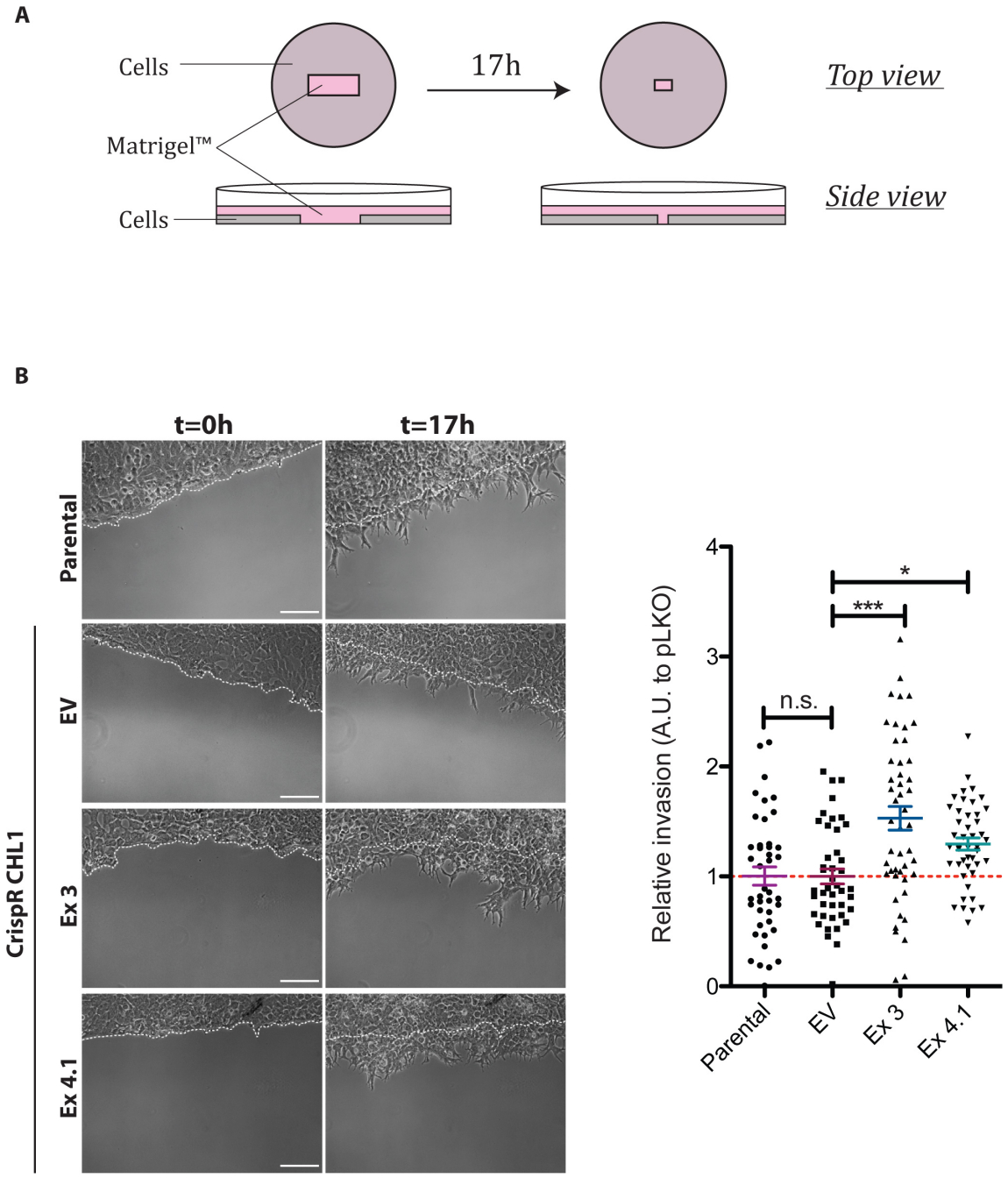

Figure 5-26: Depletion of FAM49B leads to a modest increase of invasion in a circular invasion assay

A – Schematic representation from the circular invasion assay setup.

B – Representative pictures from a circular invasion assay taken at the beginning and the end of the experiment. Invasion of parental, control (EV) and *fam49b*-CrispR knockout CHL1 cells relative to the cell front at t=0h (white dotted line) has been quantified from 4 independent experiments and represented as a scatter plot. Each value was standardised to the average invasion from the EV control (Red dotted line). Error bars represent S.E.M. One-way ANOVA with Tukey's test was performed. n.s. $p>0.05$, * $p<0.05$, *** $p\leq0.001$. Scale bar = 100 µm.

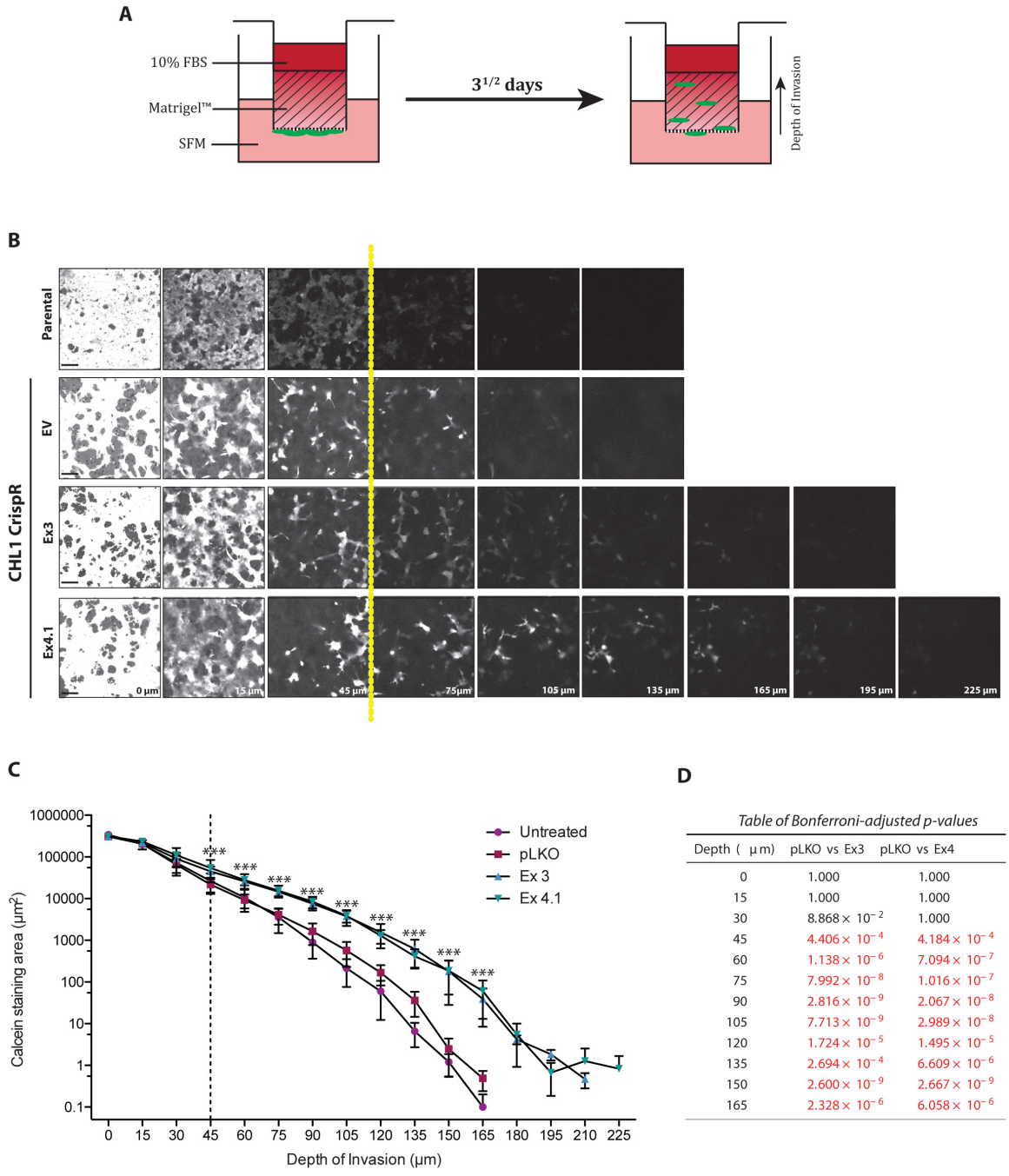

Table of Bonferroni-adjusted p-values

Depth (µm)	pLKO vs Ex3	pLKO vs Ex4
0	1.000	1.000
15	1.000	1.000
30	8.868×10^{-2}	1.000
45	4.406×10^{-4}	4.184×10^{-4}
60	1.138×10^{-6}	7.094×10^{-7}
75	7.992×10^{-8}	1.016×10^{-7}
90	2.816×10^{-9}	2.067×10^{-8}
105	7.713×10^{-9}	2.989×10^{-8}
120	1.724×10^{-5}	1.495×10^{-5}
135	2.694×10^{-4}	6.609×10^{-6}
150	2.600×10^{-9}	2.667×10^{-9}
165	2.328×10^{-6}	6.058×10^{-6}

Figure 5-27: FAM49B loss increases 3D-invasion in an inverted invasion assay
A – Schematic representation from the inverted invasion assay setup

B – Representative z-stack pictures of parental, control (EV) and *fam49b*-CrispR knockout CHL1 cells stained with Calcein after 3.5 days. Cells migrating above 45 µm (yellow dotted line) are considered as being invasive. Scale bar = 100 µm

C-D – Quantification of Calcein intensity area using the thresholding tool in Fiji. Intensity for each depth of invasion was quantified and reported as a line graph from 0 µm (filter) upwards. Graph represented quantification of 3 independent experiments and S.E.M is displayed. Table of Bonferroni-adjusted p-values corresponding to the likelihood ratio tests of negative binomial models is displayed in D. p-values that are less than 0.05 are highlighted in red.

This requirement of Rac1-driven lamellipodium formation has nicely been shown in Rac1-deficient MEFs rescued by expression of dominant active Rac1 (Steffen et al., 2013). This observation seems in slight contradiction with other findings from the same authors. Indeed, from 15 min onwards, $Rac1^{-/-}$ MEF spread more than $Rac1^{fl/fl}$ cells on laminin, fibronectin or gelatin (Steffen et al., 2013). This paper also contradicts another study that reported a strong defect in cell spreading upon genetic depletion of Rac1 using adenoviral-delivery of Cre-recombination in MEFs (Guo et al., 2006). Interestingly, this study also mentioned a spindle-like morphology for Rac1-depleted cells similar to what we observed with our Rac1-null fibroblasts (Guo et al., 2006).

Together, data from knockout and overexpression of FAM49B allowed us to investigate the function of FAM49B as part of a mathematical model. Cell migration is a complex event, involving thousands of different proteins required to fine-tune this process. However, the initial event leading to cell movement is based on a differential concentration of intracellular activators/inhibitors and this should be easily modelled. Initially, Meinhard was one of the first to conceive cell migration as a mathematical model. His work was based on a global activator responding to external cues and two types of inhibitors. The global inhibitor rapidly responds to the enhancement of activator and equilibrates over the cell by competition. The second inhibitor tends to act more locally and restricts peaks of activation by destabilisation (Meinhardt, 1999). In this crosstalk, destabilisation of the protrusion (peak of activator) leads to the retraction or splitting of the protrusion and the emergence of a new one.

Dr Matthew Neislon from the Beatson's bio-informatics facility modified Meinhard's model in order to visualise the profile of activation/inhibition over time (Neilson et al., 2010). A new pseudopod is formed following an increase of activator. This creates a feedback loop leading to the increase of the local inhibitor, which limits the diffusion of the activator. As a consequence, the local inhibitor directly restricts the spread of the pseudopod. Its progressive rise also causes a splitting of the pseudopod. In our model, Rac1 or Scar/WAVE is the activator and we here proposed that FAM49B fulfils all requirements to be seen as the local inhibitor (Fort et al - in revision). Indeed, its loss causes the pseudopod to spread as the activator is not restricted anymore whereas overexpressors are characterised by the hyper-splitting of their protrusions. We also expected FAM49B to diffuse faster than the Scar/WAVE complex as it is uncoupled to the actin network but this will have to await for a fluorescent reporter working in live cells. However, the main difference with Meinhard's model resides in the recruitment of the local inhibitor. In Meihard's model, the inhibitor gets synthesised upon activator

recruitment whereas in our case, we propose that FAM49B in its autoinhibitory state gets recruited to the plasma membrane following PTMs, where it can restrict Scar/WAVE activity by binding to active Rac1.

As mentioned in paragraph 1.5.4, FAM49-knockout *D. discoideum* or FAM49B-overexpressing cells show striking shape similarity to mammalian cells. Jose Batista and Peter Thomason were able to fully rescue the phenotype of knockout cells using untagged FAM49. Cell circularity, directness of migration, and pseudopod splitting returned to their wildtype condition. Interestingly, GFP-FAM49 only partially rescued this phenotype, suggesting that the protein is not fully active/functional (not shown). The tagging strategy seems to greatly affect FAM49 function and this provides a clear reason why we have not been able to create a fluorescent reporter so far. Similarly in a mammalian system, overexpression of untagged FAM49B commonly resulted in a hyper splitting of the lamellipodium.
Moreover, the relevance of the two conserved arginine residues in this phenotype was addressed in *D. Discoideum* (Arg155 and Arg156, homologues of human Arg160 and Arg161 respectively). Indeed, knockout cells stably expressing mutant FAM49$^{R155/156D}$ was totally unable to rescue the phenotype and cells show a very round morphology, characterised by a lack of pseudopod splitting, at a level similar to the knockout cells (Fort et al – in revision). These data strongly support and complement our previous observations and allowed us to claim that the function of FAM49 as a regulator of cell shape is totally dependent on these two conserved arginine residues in *D. discoideum*. We assume that this is also the case for mammalian cells although we don't have evidence regarding this part yet. Establishment of a rescue cell line, stably expressing FAM49B ^{WT} or FAM49B $^{R160/161D}$ is currently our priority. To do so, knockout MEFs will be transfected with our inducible lentiviral mVenus construct used for the FRET experiment and FACS sorted across different cell passages in order to positively select for integrated construct.

Chemotaxis assay performed with wildtype or *fam49*-knockout *D. discoideum* cells also revealed that a low proportion of cells failed to end cytokinesis properly upon removal of *fam49* gene and daughter cells stayed connected by a long mid-body (internal communication - J. Batista's thesis). During normal mitosis in HeLa cells, the Matsuda lab showed using FRET-biosensor that Rac1 gets inactivated at the cleavage furrow during anaphase and telophase (Yoshizaki et al., 2003). This exclusion has also been observed in *D. discoideum* using active Rac-reporter (GTPase-binding domain of PAK1 - GBD) that localises at the extremity of each daughter cell at the time of scission, whereas the Rac1-

sequesterer DGAP1, accumulates at the mid-body (Filic et al., 2012). Moreover, overexpression of Rac1 ^{Q61L} in HeLa cells increases by 5 fold the number of bi-nucleated cells compared with Rac1 ^{WT} (Bastos et al., 2012). This effect is dependent on the activity of the Rac1-GAP CYK7 and is mediated by ARFGEF7 and PAK protein downstream of Rac1. This clearly reflects the need to locally down-regulate Rac1 signalling upon cell division.

As previously shown, FAM49B-depleted cell have higher Rac1 activity so we hypothesised that loss of the polarisation of Rac1 activity would interfere with the downstream signalling pathways and cells would fail to divide properly. Moreover, we also noticed than despite their normal proliferation rate, ~5% of *fam49b*-knockout CHL1 cells are multinucleated, although this phenotype has not been properly quantified. This could be directly and precisely assessed using specific DNA markers such as propidium iodide followed by FACS analysis and looking at a switch toward higher DNA content.

Unfortunately, in our hands, cells do not tolerate the GBD-PAK1 reporter very well, making the study of active Rac1 localisation more challenging. This could be a consequence of the tight interaction between Rac1 and the probe that would therefore block Rac1 signalling to other effectors. We also tried to optimise a Rac1-GTP antibody for immunofluorescence using various fixation conditions and antibody concentrations but the staining was not convincing enough to go further down this road.

The excessive spreading is directly correlated with an increase of adhesion sites underneath the growing lamellipodium. Indeed, knockout cells show more total focal adhesions and integrin-engaged focal adhesions (Phospho-Paxillin positive focal adhesion) compared with control cells. Rac1 has previously been linked to focal adhesion formation under different conditions. Guo *et al* (Guo et al., 2006) showed than Rac1$^{-/-}$ MEFs have a normal expression level of adhesion-related proteins (Vinculin, FAK, pFAK, Src and pSrc) but failed to interact with each other. Indeed, Vinculin and FAK both pulled-down with Src in wild-type cells but failed to do so upon loss of Rac1. This is reflected at the cellular level by the absence of p-FAK and Vinculin-positive focal adhesions.

However, according to Steffen *et al* (Steffen et al.), Rac1 is not essential for focal adhesion formation as Rac1$^{fl/fl}$ and Rac1$^{-/-}$ have a similar number of Vinculin-positive focal adhesion per cell area and adhesions showed a similar size. The discrepancy between these two datasets is probably due to the difference in the spreading area discussed above. It is difficult to distinguish the direct effects of Rac1 on focal adhesion formation or whether the increase in number of focal adhesions is just a passive event downstream of Rac1-

driven lamellipodium formation. Indeed, extension of the lamellipodia should engage more integrins in complex with the ECM resulting in more focal adhesions (Chen et al., 2003).
In our hands, we observed that *fam49b*-knockout cells show increased spreading, correlating with more focal adhesions. However, precise data analysis, notably by standardising the focal adhesion number to the cell area reveals the absence of statistical difference between conditions. The same result is obtained when looking at the total focal adhesion area reported to the global cell area. This would tend to suggest that increase of Rac1 activity following FAM49B loss does not really affect focal adhesion in our system and the observed difference in numbers is mostly related to the extreme difference in morphology. An easy way to test this hypothesis would be to use micropatterns that would allow cells to be constrained to a specific morphology and stained for focal adhesion markers. In this setup, a difference in focal adhesion number or focal adhesion area would be directly linked to Rac1 activity, independently of the cell shape. This would probably be the most direct way to investigate Rac1-driven focal adhesion formation upon FAM49B loss. Finally, at this point, it is too early to conclude whether FAM49B directly regulates focal adhesion, independently of Rac1.

Another striking feature was the shape of the focal adhesions, which were longer and more linear. Once again, we cannot exclude that cell shape had any influence on focal adhesion morphology. Adhesions seem to stretch radially from the nucleus out to the leading edge and form mature focal adhesions (> 5µm). Those can either be mature elongated focal adhesions or fibrillar adhesions. The latter are characterised by the presence of specific markers such as αSMA and Tensin, the absence of phospho-Paxillin Y118 staining and are very often localised in the central region of the cell (Geiger and Yamada, 2011). In *fam49b*-knockout cells, these long focal adhesions are negative for both αSMA and Tensin (not shown) and positive for phospho-Paxillin Y118. Also, they mostly accumulate at the edge of the cell. Together we conclude that these structures are different from fibrillar adhesions.
Elongated focal adhesions can however be formed if the rate of disassembly is slower than the rate of assembly. Data from the FAAS have highlighted the relative stability of those long adhesions. A more quantitative way to analyse focal adhesion turnover would be to look at the fluorescence recovery of Paxillin-GFP transfected cells by FRAP.
Finally, James Bear's lab suggested that one function of the lamellipodium is to spatially organise focal adhesions and promote their alignment. This results in a global coherence in their organisation relative to the lamellipodium, although mechanisms allowing this have

not been addressed (Wu et al., 2012). Our data confirmed that knockdown cells with broader lamellipodia realigned their focal adhesions compared with control cells.

Given the close relation between lamellipodia and filopodia formation, we analysed Fascin by immunofluorescence staining, in FAM49B-depleted cells. These cells are highly enriched in long filopodia that emerged from the lamellipodia. Interestingly, treatment with a CDC42-inhibitor or double knockout FAM49B and CDC42 does not rescue this phenotype, meaning that filopodia formation is independent of CDC42 activity. This observation should really make us challenge the accepted dogma found in most of the textbooks, in which Rac1 stimulates lamellipodia and CDC42 strictly promotes filopodia (Takenawa and Miki, 2001).

Three distinct models were proposed to explain the regulation of lamellipoda and filopodia. The "parallel pathway model" (the actual dogma) suggests that lamellipodia are regulated by Rac1/Scar/WAVE complex whereas CDC42 activates WASP proteins to induce filopodia (Takenawa and Miki, 2001). The "cascade pathway model" proposed however that Scar/WAVE and WASPs protein, downstream effector of Rac1 and CDC42 respectively, together stimulate lamellipodia formation and that filopodia result from external cues signalling to the lamellipodium (Biyasheva et al., 2004). Using *D. melanogaster* tissue cultured cells, the Borisy lab provided a refinement of the model (Biyasheva et al., 2004). The refined cascade model still depicts Scar/WAVE as the main driver of lamellipodia extension downstream of Rac1. However, CDC42 appears to have a double function, as WASP RNAi does not affect filopodia formation or lamellipodia, suggesting that WASP plays other actin-related cellular effects. Meanwhile, CDC42 may signal to the lamellipodium in order to induce filopodia formation and this was hypothesised to be dependent on specific effector, such as IRSp53 and the Diaphaneous-related formin Drf3 (Biyasheva et al., 2004). This is also supported by another study in *n-wasp*-knockout ES-derived fibroblast-like cells that are still able to form filopodia, although the filopodia number is decreased compared to the control (Snapper et al., 2001). Microinjection of active $CDC42^{Q61L}$ into *n-wasp*-knockout cells further increases filopodia number. This reveals that CDC42 can induce filopodia formation, independently of N-WASP and would tend to confirm the Borisy model.

However, in our case, we showed that CDC42 was not involved in the increase of filopodia formation upon FAM49B loss. Since the relationship between Rac1, CDC42 and filopodia is not as strict as it was previously described, it would be interesting to see whether an increase of Rac1 activity could enhance filopodia numbers. In *D. discoideum*, active Rac1 was shown to interact with the *D.discoideum* Dia2, which in turn localises to filopodia tips

and regulates their formation (Schirenbeck et al., 2005). Moreover, MEF cells expressing dominant negative $Rac1^{T17N}$ spreading on fibronectin showed a decrease of 50 % in the number of filopodia (Johnston et al., 2008). Similarly, neurons transfected with $Rac1^{T17N}$ showed a reduction in filopodia numbers in the axon, and this phenotype was not observed using $Cdc42^{T17N}$ (Spillane et al., 2012). In this report, authors showed that increase of Rac1 activity following nerve growth factor stimulation was dependent on PI3K-WAVE1-Cortactin pathways, inducing filopodia formation. We also noticed that knockout cells are not only more prone to form filopodia, but filopodia are also longer. In light of this observation, it would be interesting to look at activity of actin-nucleators, such as Arp2/3, Ena/VASP and Formin protein and their ability to be responsible for the increased of filopodia number and length in knockout cells. Together, we hypothesised that increase Rac1 activity in FAM49B-depleted cells is enough to promote filopodia formation. FRET imaging of the CDC42 reporter transfected into our knockout cells would allow us to confirm our CDC42 inhibition data.

Finally, in order to distinguish the difference of morphology of the cell, the use of micropatterns could be interesting. In this analysis, an increase of filopodia number/length could be directly linked to the loss of FAM49B, independent of the increase of the lamellipodia extension.

Actin-based protrusions have been correlated with a more invasive phenotype (Jacquemet et al., 2015) and allow cells to steer during migration. In parallel, Rac1 and Rac3 (Chan et al., 2005) have been linked to tumour invasion in glioblastoma and breast cancer cell lines. We then hypothesised that our FAM49B-depleted cell lines with high Rac1 activity would show pro-invasive phenotypes.

We directly tested this hypothesis using a range of 2D, 3D-like and 3D invasion assays showing in all cases that loss of FAM49B increased cell migration and invasion. This phenotype would correlate with higher Rac1 activity and an increase of actin-based protrusions able to drive cell migration. We were surprised by this global increase in 2D cell migration. Indeed, cell polarisation and the ability to define a front and a rear, with different actin dynamics, is a crucial feature to achieve an effective migration. This is in sharp contrast with the fried-egg phenotype obtained with FAM49B-depleted cells, which formed this un-polarised rounded shape (fried-egg). Frequently, we could see immobile cells switching from a uniform lamellipodium to a more polarised C-shape phenotype that represents the main feature responsible for the increase of cell migration. We then hypothesised that C-shape and fried-egg shape are actually the same but depict two different states of activation of the same cell. Breaking the symmetry has been previously

reported as important for migration in cell fragments (Verkhovsky et al., 1999) and in experiment where inhibitors were locally added using a micropipette (Kaverina et al., 2000).

This increase in cell migration and invasion highlights an interesting question regarding the role of FAM49B during cancer progression and metastasis. It is worth noticing that unlike *fam49a*, *fam49b* gene is co-amplified with the oncogene *c-myc* in ovarian and breast cancer (cBioPortal). At this point, it is difficult to conclude anything about the relevance of this amplification and to directly translate it at the cellular level. Indeed, *fam49b* and *c-myc* genes are sitting next to each other on chromosome 8. *c-myc* is one of the most commonly amplified oncogenes upon cancer initiation and cells are highly dependent on it to mediate proliferation, survival and transcription (Lin et al., 2012). Given this wide implication, FAM49B might just be passively selected and be a passenger from the *c-myc* amplification. Precise analysis is then required to see whether *fam49b* expression correlates with the c-*Myc* status of different ovarian and breast cancer cell lines. If this were the case, it would be interesting to analyses the effect of FAM49B loss on the invasiveness of these cells.

However, we would expect from our data that amplification of FAM49B would decrease cell migration, which seems in contradiction with the ovarian cancer genome analysis. An easy way to potentially explain this discrepancy can be highlighted in few points: 1) Different cell types might respond differently to FAM49B. 2) There is no direct relation of DNA/protein and a genomic amplification might not be translated at the protein level. 3) Signalling pathways might be different between isolated cells and collective cell migration. Despite the increase of cell migration seen in our assays, *fam49* knockout *D. discoideum* cells show a slower speed in an under agarose assay. Furthermore, migrating *fam49b*-knockout melanoblasts also migrated slower compared to wild-type cells (see section 6.2.2). These two observations would suggest that in a 3D environment, the loss of FAM49B might not be pro-invasive. Since cell migration is a complex event reflecting directionality, adhesion, protrusion rate and the cell compression, migration speed on its own is not very informative and only reflects the sum of how these parameters behaved. In our 2D random migration assay, cells were sparsely seeded and individual track reports cell migration. This is the only way to say whether intrinsic signalling makes a cell go faster/slower, as it is not influenced by the environment. However, it is well established that coordination between adhesion and migration is crucial for cell migration. In line with this observation, different cell types might emphasise slight modifications in one part of the mechanism, resulting in a differential speed. For example, *D. discoideum*, fish

keratocytes and neutrophils are well known for their fast migration, resulting from weak adhesions to the substratum. As a consequence, cell speed is limited by how fast the actin turns over and the cell polarity. However, mammalian cells from tissues are characterised by low speed, typically one to two orders of magnitude slower than the cell types mentioned above. This is the consequence of strong dependence to adhesion formation and turnover, together representing the main limiting factors.

In order to complete the analysis of FAM49B functions, it would be informative to perform some biochemical assay to look at the direct role of FAM49B during actin polymerisation. To do so, pyrene fluorescent assay could be performed and analysis of the fluorescence emission would give us direct readout of FAM49B effects in an *in vitro* setting.

It will also be important to work out the most basic function of FAM49B during invasion. Despite the contradicting results obtained in 2D and 3D environment, we could try to constrain control or knockout cells between two layers of agarose, similarly to the *D. discoideum* experiment and measure cell speed and directionality. Here, we hypothesise that knockout cells behave differently if they are in a constraint environment. Other *in vivo* experiments could be done in order to answer this question. Subcutaneous injection of control or *fam49b*-knockout melanoma cells into nude mice and monitoring of tumour growth and invasion could be informative. Alternatively, in collaboration with Karthic Swaminathan, I developed an ear injection assay to look at invasion of cancer cells stably expressing GFP-Lifeact *in vivo* using 2-photon microscopy. Finally, switching to a cancer mouse model, and looking at the effect of genetic loss of *fam49b* during cancer progression would definitively give us more insight about the role of FAM49B in cancer biology. For example, based on the Machesky lab's expertise, we could investigate the role of FAM49B in a pancreatic cancer mouse model as all the tool and mouse strains have already been developed..

6 Taking step towards FAM49B's *in vivo* functions using more physiologically relevant models

6.1 Introduction

Encouraged by our previous findings, we initiated the investigation of FAM49B using more complex models. This allowed us to monitor cell behaviour in a more physiologically relevant environment. For example, studying FAM49B using *ex vivo* protocols or directly in an animal with a complete ECM matrix and an immune system, should provide insight about FAM49B's biological relevance. To do so, a wide-range of methods and systems was applied.

As we here claim a close relationship between FAM49B and Rac1, we used a 3D-organoid model, in which Rac1 has previously been implicated as an important regulator of cystogenesis. Early on, it was shown that an autocrine loop involving Rac1 and the ECM, was able to signal directly to the cyst in order to regulate its organisation and polarity (O'Brien et al., 2001). Specific Rac1-GAPs, such as Chimaerin have also been linked to Rac1 polarisation resulting in an apico-basal gradient, which has been imaged using FRET reporter probes (Mack et al., 2012; Yagi et al., 2012a; Yagi et al., 2012b) (**Figure 6-1 - A**). In all these studies, increase of Rac1 activity and loss of Rac1 polarisation lead to a multi-lumen phenotype and an accumulation of cells inside the lumen. This model is a great tool for us to monitor the potential effect of FAM49B on 3D epithelial organisation.

One example of a system for study of individual cell migration in a physiological setting is the migration of melanoblasts through mouse embryo skin. We have optimised a method to image migrating melanoblasts from the developing skin of mouse embryo. Skin explants have been successfully used in the past by our lab to look at Rac1 and Cdc42 requirement during melanoblast development (Li et al., 2011; Mort et al., 2010; Woodham et al., 2017).

Finally, *D. melanogaster* is a quick and straightforward genetic model to study actin dynamics and we used it to confirm some of our *in cellulo* data.

In this chapter, I describe experiments that go beyond the role of FAM49B *in cellulo* and extrapolate to a more universal role in cells but also at the level of the whole organism.

6.2 Results

6.2.1 FAM49B is crucial during epithelial cell cyst polarisation using a Rac1-dependent mechanism

Cell polarisation is a fundamental event that results in plasma membrane segregation into an apical and a basolateral domain, which are functionally and morphologically different. It happens in all epithelial cells and maintains specific signalling molecules at one side of the cell. For example, intestinal epithelial cells are characterised by an apical brush-like zone, facing the intestine lumen and specialised in the absorption of nutrients. Similar structures cover most body surfaces in direct contact with the extracellular environment. On the other side, the basolateral domain allows cell-cell and cell-matrix interaction. Physical separation between these domains is mediated by the apical junctional complex composed by the zonula occludens, zonula adherens and macula adherens. Specific protein delivery to one end or the other is a complex event mediated by the Rab family proteins and is beyond the scope of this thesis.

For this work, we used Madin–Darby canine kidney (MDCK) cells that have the property to form spheroid-like structures when grown in 3D and mimic a simplified epithelium. This multi step process starts with one non-polarised cell that undergoes several mitotic events (**Figure 6-1 - A**). From the 2-cell stage onwards, intense and highly regulated trafficking events lead to the relocalisation of the apical markers to the apical membrane initiation site (AMIS). At this stage, the lumen is not fully formed and only becomes visible upon active pumping of ions and water into the lumen, while the cyst continues to expand.

Given the great model provided by MDCK cells, stable *fam49b*-knockdown cells were created by shRNA-lentiviral infection. To do so, human shRNA were aligned against the dog genome and matching oligos were selected. Puromycin selection followed by western blot analysis confirmed *fam49b* knockdown and shRNA cell lines number 2 and 4 (FAM49B level reduced by ~90% compared to control) were selected for further analysis (**Figure 6-1 - B**). Control or knockdown MDCK cells were plated on a Matrigel-coated chamber as a single cell suspension and grown 5 days in low Matrigel concentration. At this stage, cysts were fixed and stained for the apical marker Podocalyxin1/gp135 (Pdx1/gp135), F-actin and nuclei, before imaging using a confocal microscope (**Figure 6-2 - A**).

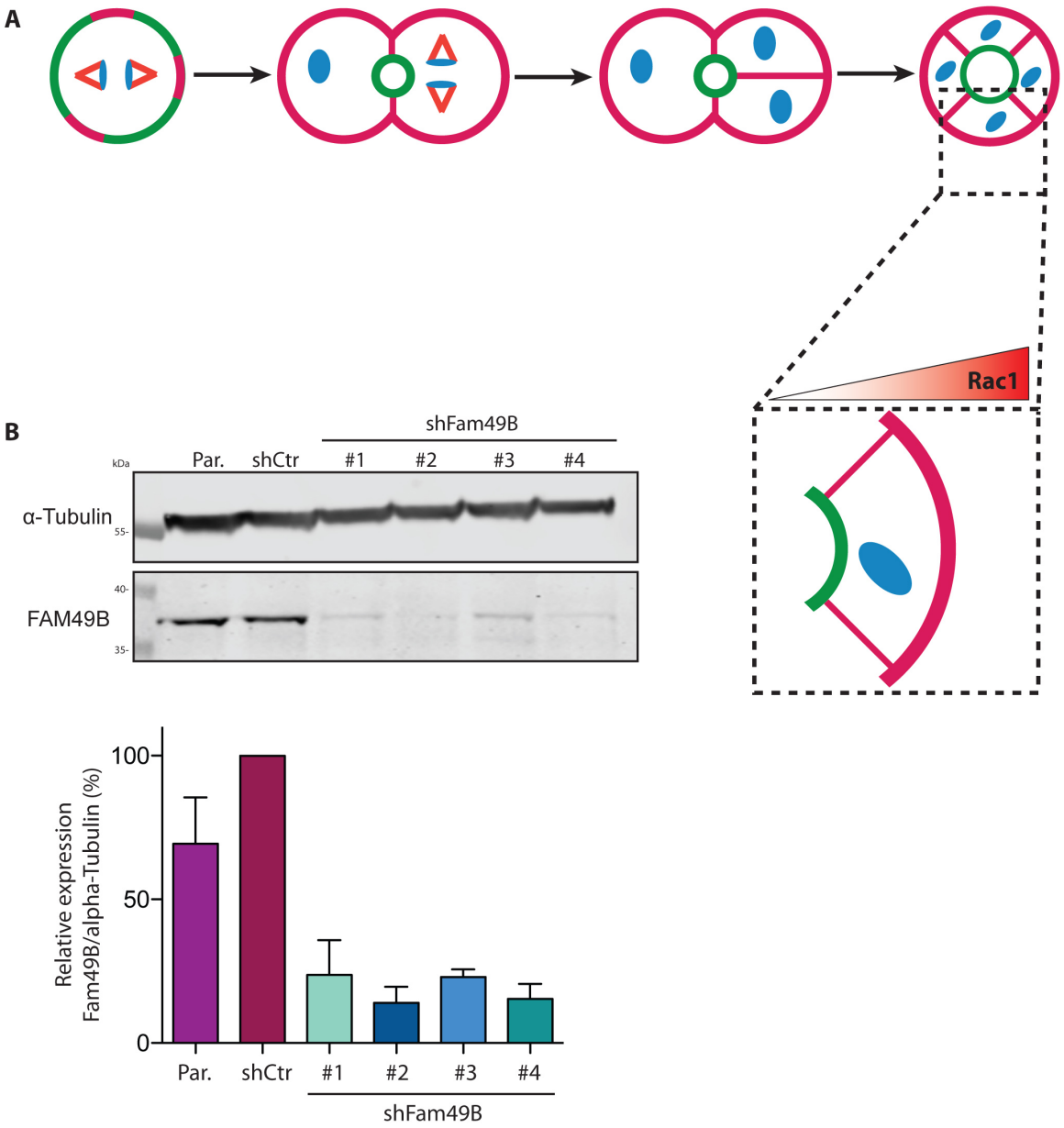

Figure 6-1: MDCK cyst development and knockdown cell lines generation
A – Schematic representation of early steps during lumen organisation in MDCK cyst development. Non-polarised single cell undergoes multiple mitotic events during which apical markers (green) get endocytosed and trafficked to the AMIS where they form the expanding apical domain. Magenta lines denote apico-basal membranes. Red lines represent microtubule spindle and nuclei are blue. Inset is a graphical representation of Rac1 gradient running from the apical to the baso-lateral membranes. *Inspired from Overeem et al (Overeem et al., 2015).*

B – Western blot analysis of parental (Par.), shControl (shCtr) or shFam49B MDCK cells. Membranes were blotted against FAM49B and α-Tubulin. Molecular weights are displayed on the side. Bar graph represents quantification of FAM49B expression of 3 independent experiments and S.E.M is displayed.

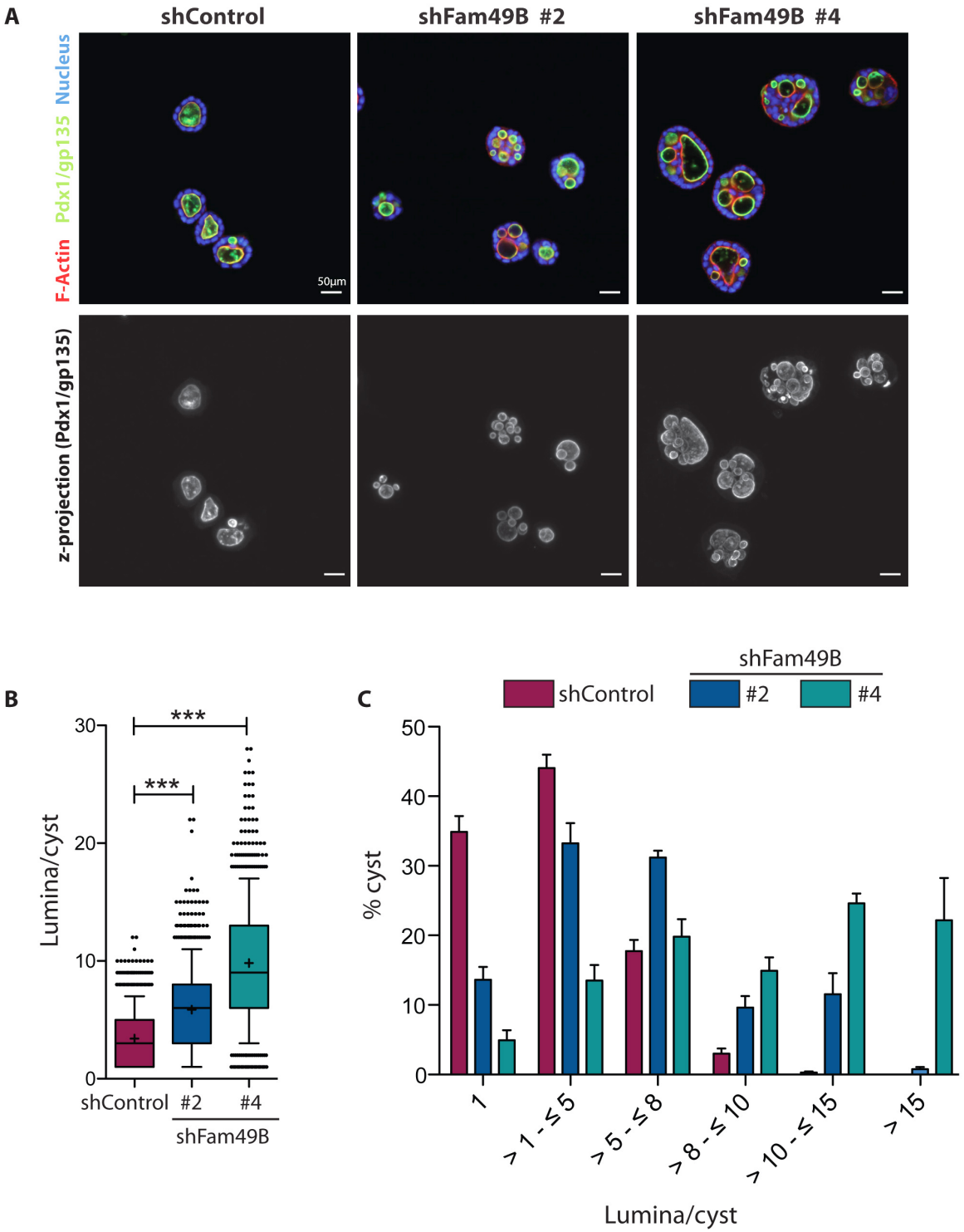

Figure 6-2: Loss of FAM49B causes a multilumen phenotype in MDCK cysts
A – Immunofluorescence of Control or *fam49b*-knockdown MDCK cysts grown in 3D. Cyst were fixed after 5 days and stained for Pdx1/gp135 (green), F-actin (red) and nuclei (blue). Top row is a confocal section across different cysts and bottom row represents Z-maximal projection intensity of the Pdx1/gp135 staining. Scale bare = 50 µm

B – Whisker-plot representing the number of lumen per cyst. Whiskers show 10th and 90th percentile. Cross shows the mean from 4 independent experiments. Error bar represent S.E.M. One-way ANOVA with Dunn's multiple comparison test was performed. *** p<0.001

C - Bar plot representing the distribution of cysts with a specific number of lumen from 4 independent experiments. Error bar represent S.E.M.

Unlike control cysts, *fam49b*-knockdown cysts are characterised by an enrichment of multiple small lumens, filling the middle of the cyst. This multilumen phenotype is even clearer if we take a z-stack running throughout the entire cyst and process the pictures using the maximum-z projection tool for the Pdx1/gp135 channel. Precise quantification reveals that control cysts have on average 2 lumina/cyst, compared to 6 and 9 lumina for FAM49B-depleted cysts (shRNA #2 and #4 respectively) (**Figure 6-2 - B**). Moreover, only 20% of the control cysts have more than 5 lumina whereas this phenotype was observed in 55 and 90% of the knockdown cyst with shRNA #2 and #4 respectively. Frequently, cysts containing more than 20 lumina were found, especially for shRNA #4 (**Figure 6-2 – B & C**).

It is well established that orientation of the mitotic spindle during cell division is fundamental to maintain the polarity of the cyst. Indeed a very regulated crosstalk between polarity markers and the cell division machinery assures a symmetrical division. However, defect in maintaining this polarity results in spindle misorientation and multi-lumen phenotype (**Figure 6-3 – A & B**). For example, LGN protein, a regulator of G-protein signalling, accumulates at the basolateral side of dividing cells and the current model suggests they are required for the capture and the stabilisation of astral microtubules (Peyre et al., 2011). In order to visualise the microtubule spindle, cysts were stained for tubulin and the angle formed by the mitotic spindle and the apico-basal axis was measured across multiple dividing cells (**Figure 6-3 - C**). On average, control cysts form a 70 degrees angle and this value goes down to ~40 degrees upon FAM49B loss. Similarly, only 25-30% of the knockdown cysts have an angle above 45 degrees, which is the accepted threshold value to consider a mitotic event as normal (Rodriguez-Fraticelli et al., 2010) (**Figure 6-3 – D & E**). Interestingly, staining for Ki-67 revealed that knockdown cysts are more proliferative, a feature that was not observed for cells plated on a 2D surface (**Figure 6-4**). This suggests that FAM49B might have differential functions between 2D and 3D environment.

As previously mentioned, Rac1 has been involved as a key player during cyst polarisation, by creating a signalling gradient, increasing from the apical to the basolateral membrane (**Figure 6-1 – A**). My hypothesis is that FAM49B-deficient MDCK cells have higher Rac1 activity and are not able to form this gradient anymore, resulting in abnormal signalling pathways downstream of Rac1, which are important for normal cystogenesis. If Rac1 was involved in the FAM49B-dependent multilumen phenotype, down-regulation of Rac1 should be able to rescue this phenotype. We tested this hypothesis by treating growing

cysts with different Rac1 inhibitors. EHT1864 is a pan-Rac inhibitor that binds to Rac1 (Rac1a and Rac1b) at low concentration and Rac2 and Rac3 at higher molarity. (Desire et al., 2005; Shutes et al., 2007). Binding to Rac destabilises the nucleotide interaction and interferes with the nucleotide-exchange process, inducing the blockage of further interaction with GEF and Rac effectors. (Shutes et al., 2007). Cysts were treated with 50 nM of EHT1864, a concentration that targets Rac1a and Rac1b over other Rac isoforms. Rac1 inhibition partially reverted the multi-lumen phenotype caused by FAM49B loss (**Figure 6-5 – A**). This rescue was confirmed using a second Rac1 inhibitor, NSC23766 that prevents GEF-mediated Rac1 activation (Gao et al., 2004). In either case, lumen number was decreased by a 2-fold factor and reached similar values (**Figure 6-5 – B & C**). We concluded that FAM49B is important for regulating Rac1 activity during epithelial cyst formation, which has direct consequences for the polarisation of the epithelium.

Altered Rac1 signalling should also directly affect downstream Rac1 effectors. Based on the 2D staining of our CrispR cells, the WRC seems to be a good initial candidate to look at. Cysts were stained for WAVE2 and Pdx1/gp135 and z-stacks were obtained by confocal microscopy (**Figure 6-6 - A**). Maximal intensity projection reveals that WAVE2 localised at the cell-cell junction (basolateral domain) in control cysts, similar to what is already published for the WRC localisation in monolayer of epithelial cells (Yamazaki et al., 2007). However, we found that upon FAM49B-depletion, WAVE2 relocalised to the apical membrane and colocalised with Pdx1. Indeed, pixel intensity measurements show that Pdx1/gp135 and WAVE2 staining co-varied in knockdown cysts to a much greater extent than in control cysts (**Figure 6-6 - A & B**). Thus the regulation of Rac1 activity is important for WAVE2 localisation. In turn, WAVE2 regulates localised branched actin polymerisation at cell-cell junctions and helps to define the polarity of epithelial cells.

Together, these results on 3D cyst polarisation suggest that FAM49B-mediated Rac1 regulation is important for normal organoid formation, especially establishment of the apico-basolateral axis.

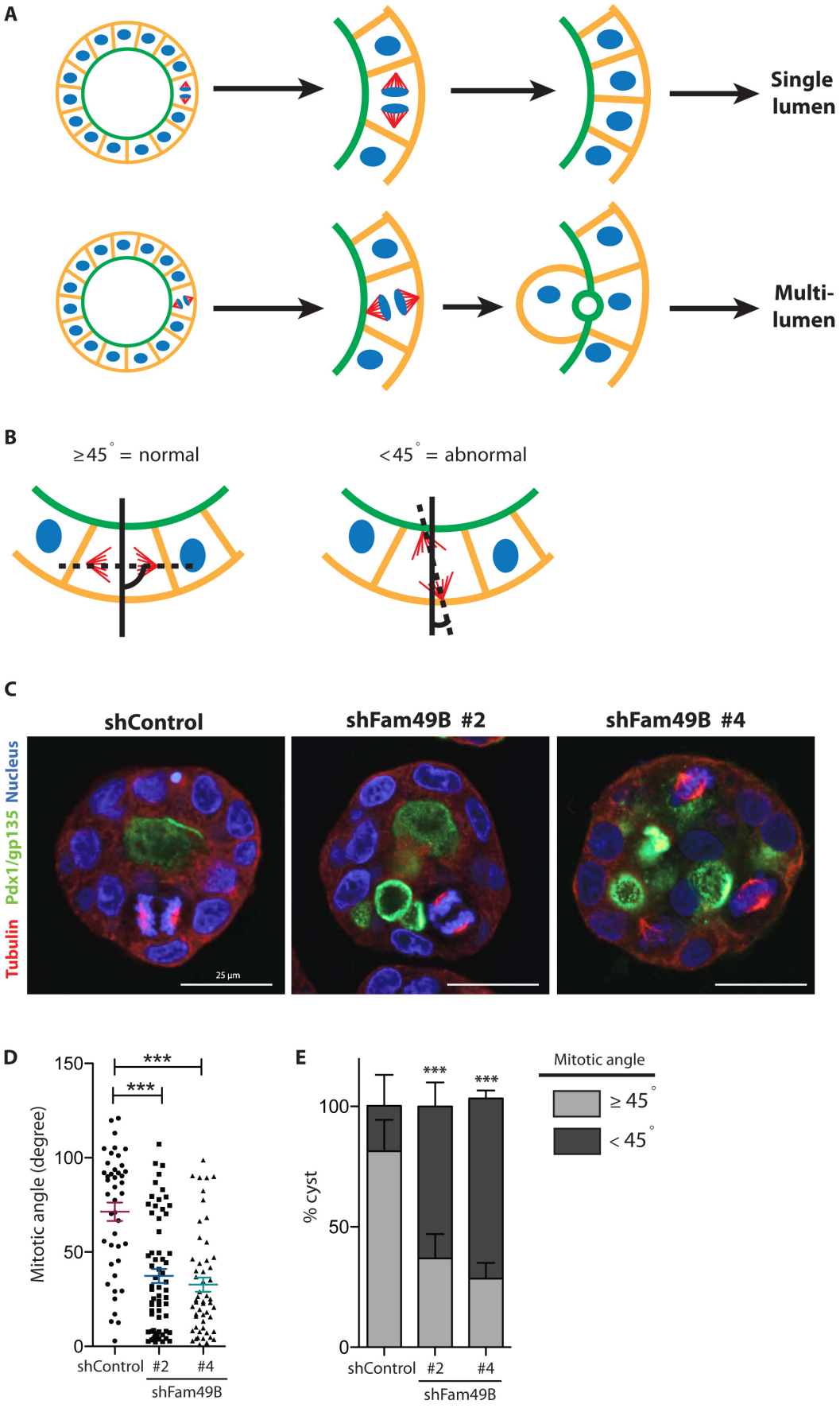

Figure 6-3: Microtubule spindle orientation is affected in *fam49b*-knockdown MDCK cells, probably responsible for the multilumen phenotype

A – Schematic representation of how microtubule spindle misorientation can lead to multilumen phenotype. Green = apical membrane, Orange = basolateral membrane, Blue = nuclei and Red = microtubule spindle

B – Schematic representation of normal and abnormal mitotic events. Angle formed between the apico-basal axis (full black line) and the mitotic axis (dotted black line) was measured in each condition. Green = apical membrane, Orange = basolateral membrane and Red = microtubule spindle. For simplification, nuclei were omitted.

C - Immunofluorescence of Control or *fam49b*-knockdown MDCK cysts grown in 3D. Cyst were fixed after 5 days and stained for Pdx1/gp135 (green), Tubulin (red) and nuclei (blue). Scale bar = 25 µm

D – E – Mitotic angle was quantified from 3 independent experiments and plotted as a scatter plot (D). One-way ANOVA with Dunn's multiple comparison test was performed. *** $p<0.001$. Angles were divided as greater or lower than 45 degrees and plotted as a bar graph in E. Two-tailed Chi-square test (95% confidence) was applied for each condition compared with the control cells. *** $p<0.001$. Error bars represent S.E.M.

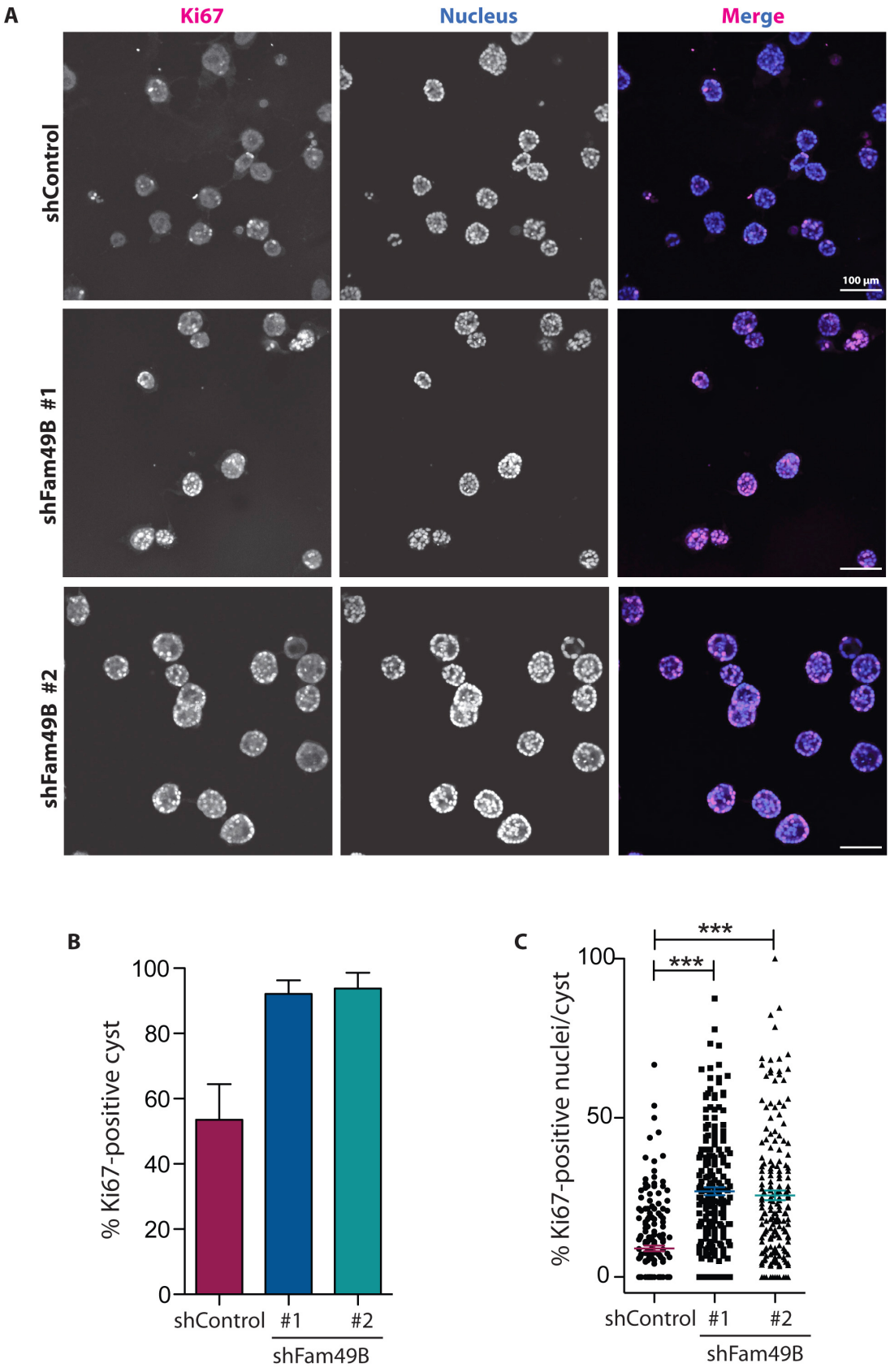

Figure 6-4: Loss of FAM49B increases proliferaton of 3D-cultured cysts
A - Immunofluorescence of Control or *fam49b*-knockdown MDCK cysts grown in 3D. Cyst were fixed after 5 days and stained for Ki-67 (magental) and nuclei (blue). Scale bar = 100 µm

B – C – Quantification of number of proliferating cysts (B) and number of proliferating cells per cyst (C) obtained from 3 independent experiments. S.E.M is displayed on each graph.

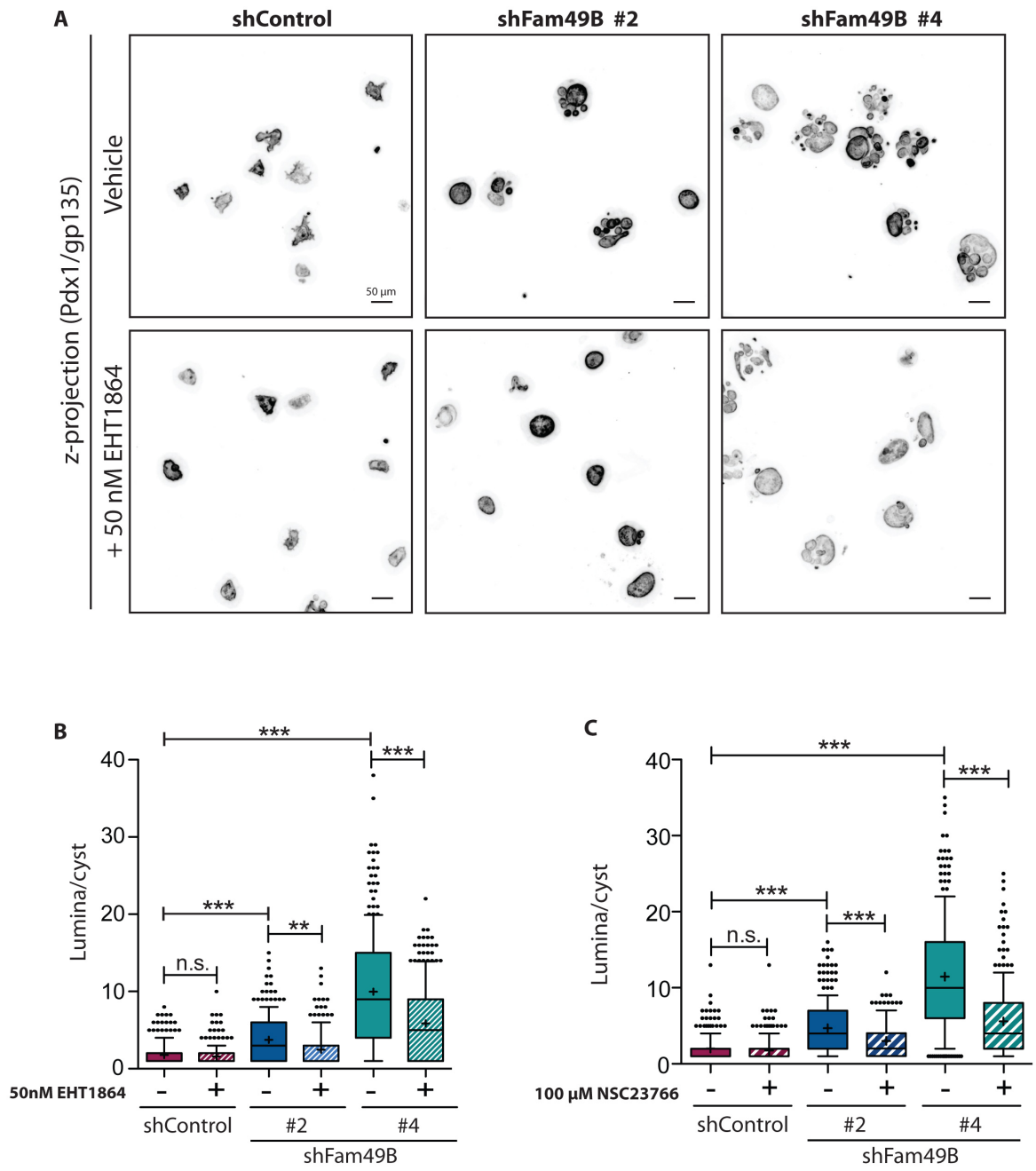

Figure 6-5: Inhibition of Rac1 signalling partially rescues the loss of FAM49B during cystogenesis

A – Immunofluorescence of control or *fam49b*-knockdown MDCK cysts grown during 5 days, treated or not with 50 nM EHT1864 and stained for Pdx1/gp135. Pictures represent maximum intensity projection of z-stack running across the entire cyst volume. Scale bar = 25 µm

B – C – Number of lumina from control or *fam49b*-knockdown cysts treated or not with 50nM EHT1864 (B) or 100 µM NSC23766 (C). Whisker plots represent 10-90 percentile, mean (cross) and S.E.M from 3 independent experiments. One-Way ANOVA with Dunn's post-test was applied between vehicle-treated knockdown cysts and vehicle-treated control cysts. Two-tailed t-test was applied to untreated versus treated cysts. n.s. $p>0.05$, ** $p\leq0.01$, *** $p\leq0.001$

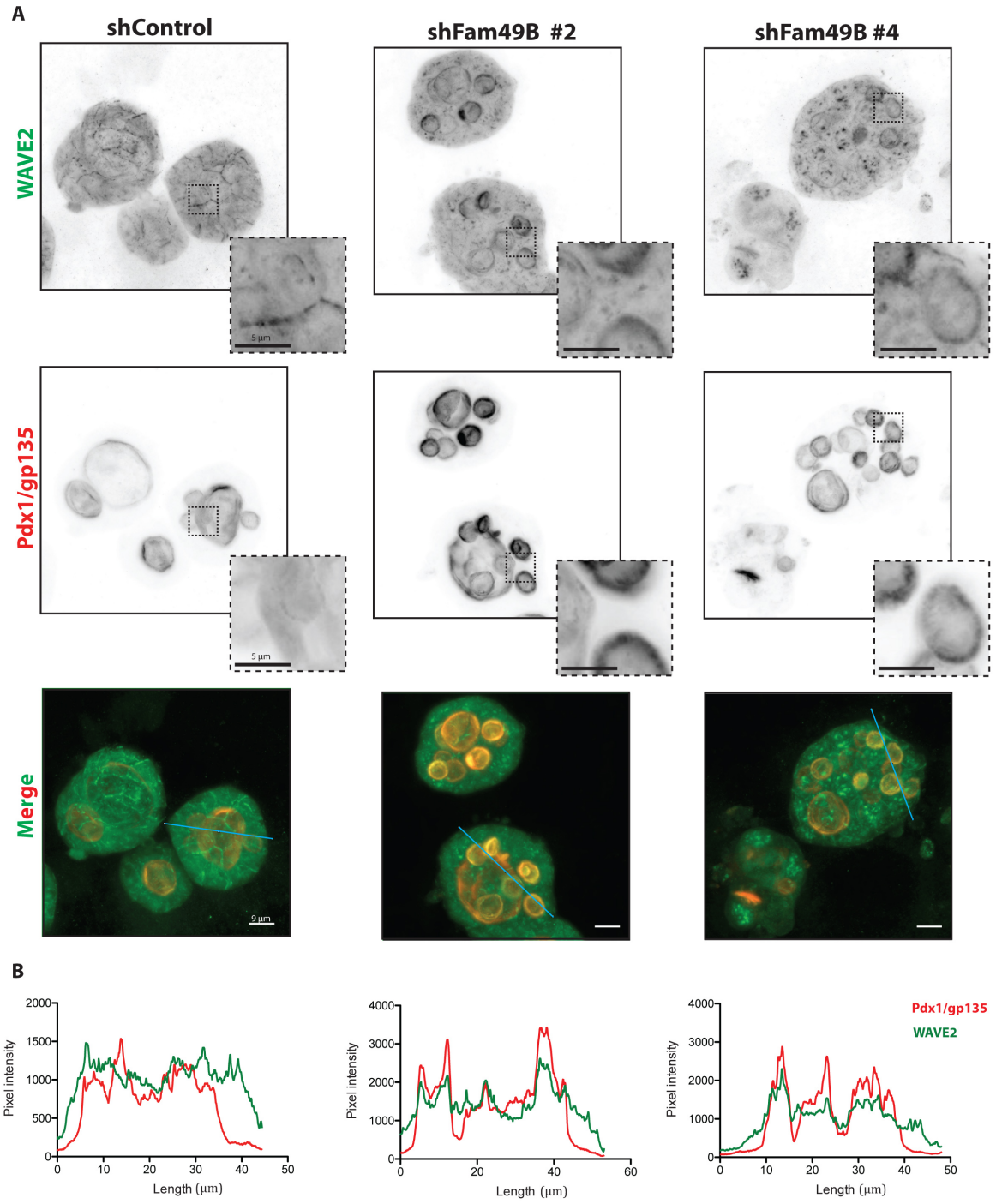

Figure 6-6: WRC localisation in MDCK cysts is affected following FAM49B loss
A – Immunofluorescence of *fam49b*-knockdown MDCK cysts grown during 5 days and stained for WAVE2 (green) and Pdx1/gp135 (red). Inverted LUT images for each individual channel and the merge picture are displayed. Scale bar = 9 µm. Insets provide a magnified view of the dotted square area. Scale bar = 5 µm.

B – Surface profile plot of both Pdx1/gp135 (red) and WAVE2 (green) staining intensity across the blue line represented on the merge picture in A. Note the different units scale for Control compared to knockdown conditions.

6.2.2 FAM49B regulates melanoblast migration using an *ex vivo* skin explant model

Very dynamic migration processes occur during embryo development, which are crucial for the position and the architecture of the future organs. In the lab, former colleagues refined a method published by Mort *et al* (Mort et al., 2010) in order to get high-resolution movies from migrating melanoblasts. Melanoblasts are the precursors of melanocytes that represent the specialised melanin-secreting cells in adult skin. They originate from a transient pluripotent population arising at embryonic day 10 (E10) around the dorsal neural tube, where they start their journey. Briefly, melanoblast differentiation is regulated by simultaneous signalling involving the Wnt pathway, the transient activation of Sox10 and Pax3, and the down regulation of FoxD3 (Silver et al., 2006) Together, these signals drive the expression of melanocyte-specific genes such as tyrosinase, downstream of the activation of MITF, a key transcription factor for the melanocytic lineage. At this point, they received sufficient information to migrate to their final destination.

The melanoblast journey has been studied for years and still, precise signalling pathways are missing. Our current understanding suggests that melanoblasts follow a dorsolateral path, making their way between the dorsal surface of the somite and the ectoderm. Following a proliferation step in the staging area, melanoblasts migrate into the dermis, just underneath the basement membrane from E11.5-E13.5. At this stage, few cells have already crossed the epidermal basement membrane but most, if not all melanoblasts reside in the epidermis by E15.5. Specifically, cells gather in structures called hair follicles where they will play their function from birth onward. Another population of pluripotent neural crest cells migrate ventrally, between the lateral sides of the neural tube and the somites, and develop into nervous structures, medulla of the adrenal glands. Specific population of cells derived from the Schwann cells may also differentiate into melanocytes of the skin (Adameyko et al., 2009).

This brief description is enough to understand why embryo skin is a perfect model for a lab working on cell migration. The superficiality of migrating cells makes the imaging easier and allows testing the effect of the genetic depletion of a gene in an *ex vivo* setup.

During this journey, melanoblasts use highly dynamic pseudopods to migrate through the tight layer of keratinocytes and pull their cell body forward. This crawling between keratinocytes and the basement membrane crossing seems to be independent from the activity of metalloproteinases and does not rely on invadopodia. Indeed, depletion of N-WASP, a key protein for invadopodia function does not alter fur colour (Li et al., 2011).

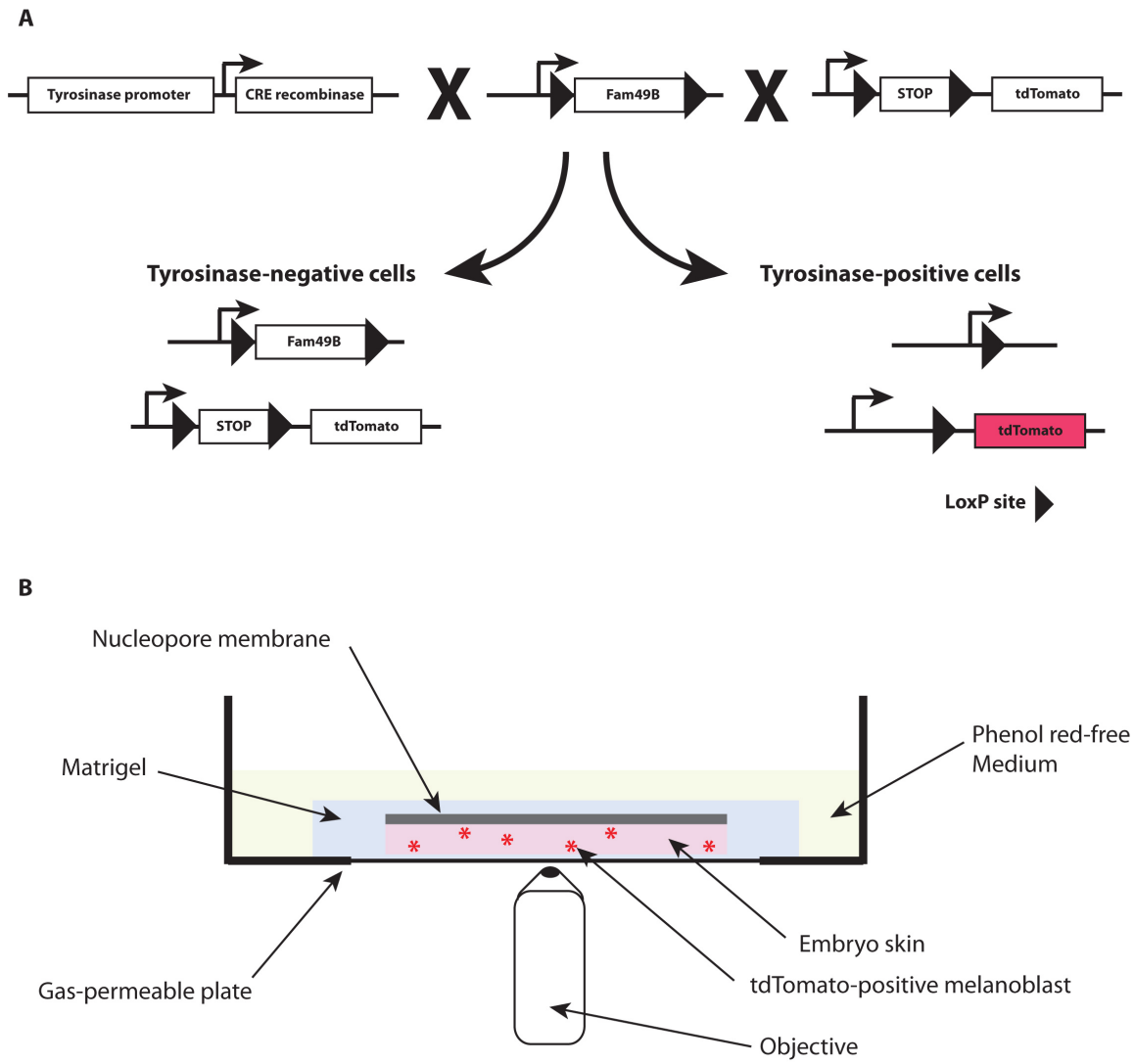

Figure 6-7: Tool and setup for studying *ex vivo* melanoblast migration
A – Development of a transgenic approach to achieve genetic depletion of *fam49b* gene at the same time as expression of the tdTomato reporter in the melanoblast lineage. Melanoblast-specific Tyrosine expression leads to the recombination of the LoxP sites at each end of the *fam49b* gene and the STOP codon. This results in expression of the reporter alongside to the loss of *fam49b* transgene.

B – Skin explant setup to achieve high-resolution imaging. Embryo skin was overlaid with a nucleopore membrane. Matrigel was added on the top of the skin and allowed to polymerise 30 min before adding Phenol red-free media.

We took the advantage of our floxed-*fam49b* mouse to investigate FAM49B functions during melanoblast migration. To do so, the *fam49b*$^{fl/fl}$ mouse was crossed with other transgenic strains in order to get a Tyr::CRE *fam49b*$^{fl/fl}$ LSL-tdTomato mouse. Basically, only cells expressing Tyrosinase will be able to produce the Cre enzyme, recombine the *fam49b* transgene and allow the removal of the Lox-STOP-Lox sequence (**Figure 6-7 – A**). As a consequence, tdTomato is only driven in the melanoblast lineage.

Timed matings were set up and embryos were harvested at E14.5. Embryos were dissected and the skin was isolated, flipped, flattened, placed with the epidermis side down and sandwiched between the gas permeable plate and the nucleopore membrane. Pure Matrigel was overlaid onto the skin in order to immobilise the skin and this setup was kept moist by filling the well with phenol red-free medium (**Figure 6-7 – B**). Skin explants from *fam49b*$^{fl/fl}$, *fam49b*$^{fl/-}$ and *fam49b*$^{-/-}$ were imaged every 5min using confocal microscopy during 4h.

Migrating melanoblasts exhibit a common morphology with a round cell body, extending at least one dynamic pseudopod. Preliminary quantification by manual tracking of tdTomato-positive cells from two different litters revealed a strong defect in migration for FAM49B-recombined melanoblasts (**Figure 6-8 – A-B**). Homozygote *fam49b* knockout cells migrate half as fast compared with control whereas heterozygotes have an intermediate phenotype (**Figure 6-8 – C**). Similarly to our *in cellulo* and *D. discoideum* work, FAM49B-depleted melanoblasts looked less polarised and much rounder, although cell size does not seem affected (**Figure 6-9 – A**). Knockout melanoblasts more frequently lack a pseudopod (16% for *fam49b*$^{fl/fl}$ *versus* 33% for *fam49b*$^{-/-}$ cells). In the same line, 50% of the wild type cells extend two or more pseudopods and this value is as low as 24% for knockout cells (**Figure 6-9 – B**). This reduction in pseudopod numbers was accompanied by a slight decrease in the pseudopod length (**Figure 6-9 – C**). Preliminary quantification suggests that *fam49b*-knockout pseudopods are more unstable, with an average lifetime of 50 min compared to 100 min for wild type cells (**Figure 6-9 – D**). From the movie analysis, it was also quite clear that knockout cells with an extending protrusion frequently displayed patchy and enlarged portions of pseudopod (**Figure 6-9 – A**) that contrast with the homogeneous and slender pseudopods formed by control cells. This phenotype might reflect membrane bursts throughout the pseudopod related to increasing Rac1 activity. Moreover, once a pseudopod is formed, knockout cells seem to fail to pull their cell body forward. This can result from the lack of coordination between membrane extension and physical traction and the ability of the cell to form potent and efficient protrusions. Therefore, FAM49B is important for controling pseudopod number, dynamics and morphology, probably resulting in the defect in migration observed in the spider plot.

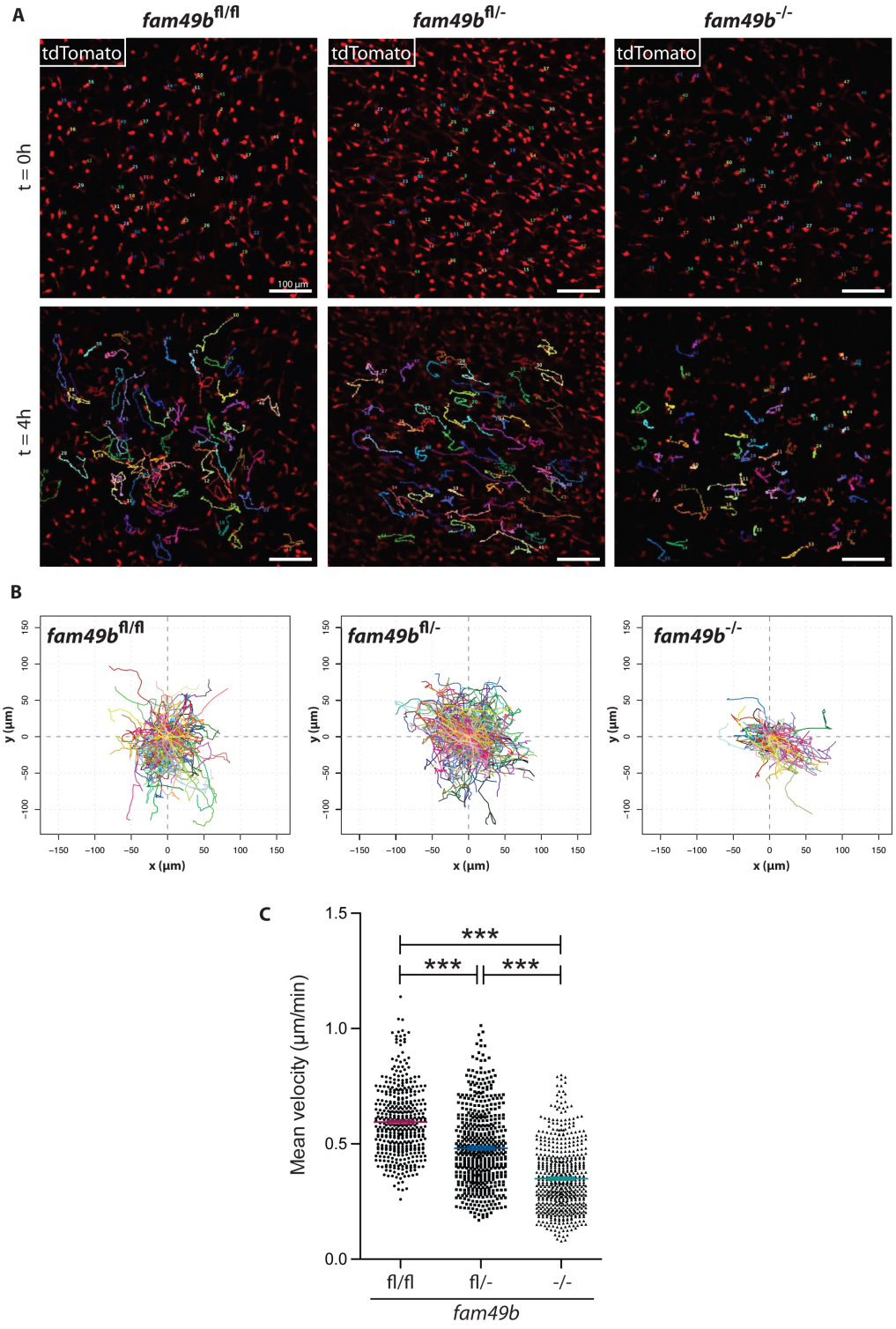

Figure 6-8: Loss of FAM49B impairs melanoblast migration (preliminary experiment)
A – Representative confocal pictures from a 4h timelapse movie. Still pictures have been extracted from the begging/end of each movie from wild-type (*fam49b*$^{fl/fl}$), heterozygote (*fam49b*$^{fl/-}$) and homozygote (*fam49b*$^{-/-}$) melanoblasts. Tracking from tdTomato-positive melanoblasts has been overlaid on the last image.

B – Spider plots combining tracks from technical replicates of 3 *fam49b*$^{fl/fl}$, 5 *fam49b*$^{fl/-}$ and 4 *fam49b*$^{-/-}$ embryo skins (respectively 419 cells, 540 cells, 569 cells), over 4h of movie. Embryos came from 2 independent litters.

C - Quantification of cell speed from technical replicates of 3 *fam49b*$^{fl/fl}$, 5 *fam49b*$^{fl/-}$ and 4 *fam49B*$^{-/-}$ embryo skins (respectively 419 cells, 540 cells, 569 cells), over 4h of movies. Embryos came from 2 independent litters. One-Way ANOVA with Dunn's post-test was applied. *** $p<0.001$

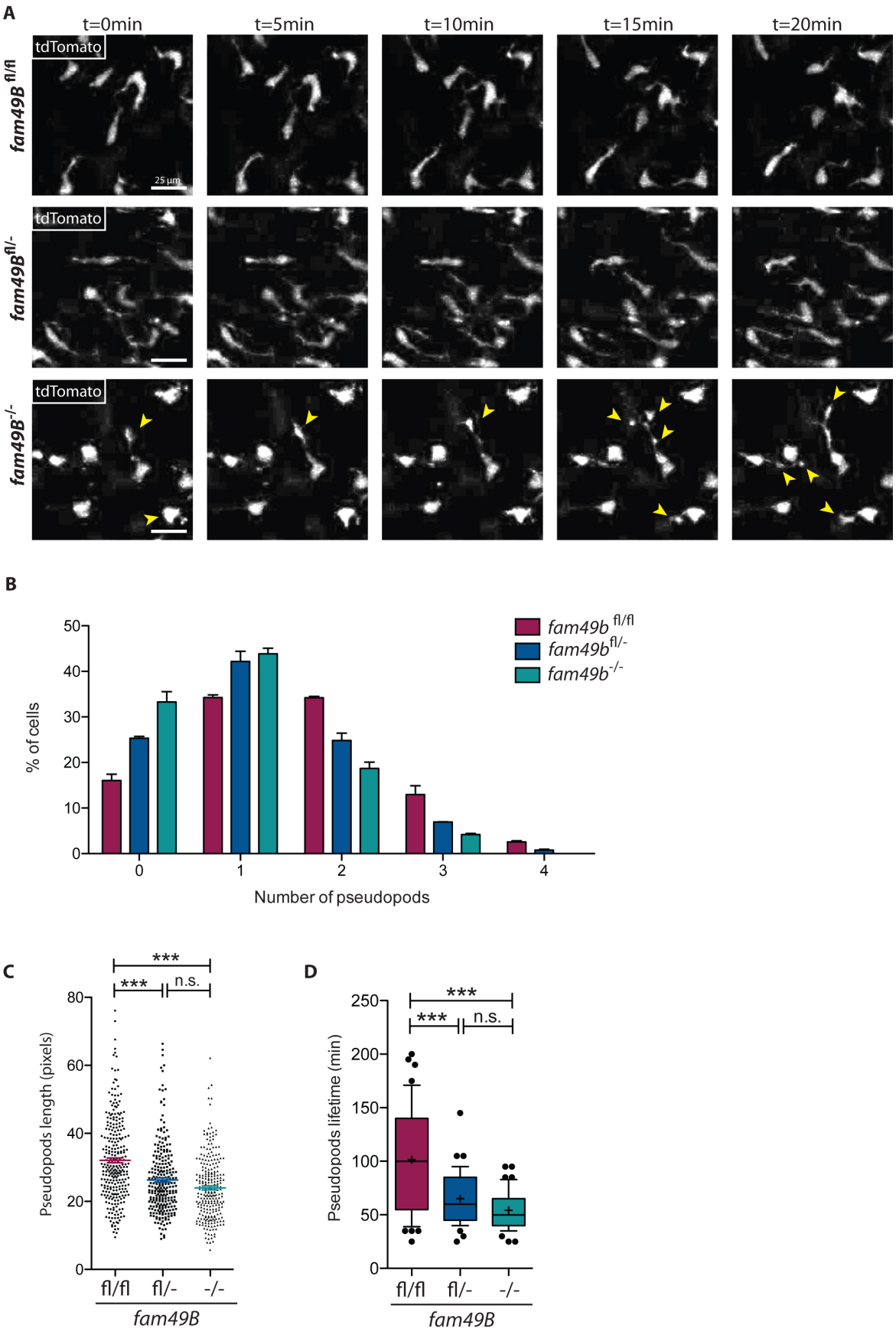

Figure 6-9: FAM49B-deficient melanoblasts have altered shape and pseudopod dynamics
A – Representative stills from a skin explant movie. tdTomato-positive melanoblasts from *fam49b*$^{fl/fl}$, *fam49b*$^{fl/-}$ and *fam49b*$^{-/-}$ skins were imaged every 5 min. Yellow arrowhead represents burst of the plasma membrane. Scale bar = 25 µm.

B – Manual quantification of pseudopod number across 2 independent litters (3-4 mice/genotype with 2 technical replicates), representing >700 cells per genotype. Error bars represent S.E.M.

C – Manual quantification of pseudopod length for each genotype. Scatter plot summarises data from 2 independent litters (3-4 mice/genotype with 2 technical replicate), representing >250 pseudopods per condition. S.E.M is displayed and One-Way ANOVA with Dunn's post-test was applied. n.s. $p>0.05$, *** $p<0.001$ (1 pixel = 0.6274978 µm).

D – Preliminary quantification of pseudopod lifetime. Pseudopods were tracked from their initiation until their retraction or split. Whisker plot summarises quantification from 1 mouse per genotype (2 technical replicate), representing 45 pseudopods. 10-90 percentile, mean (cross) and S.E.M are shown. One-Way ANOVA with Dunn's post-test was applied. n.s. $p>0.05$, *** $p<0.001$

6.2.3 fam49b-knockdown affects embryonic haemocyte membrane protrusion and dynamics in *D. melanogaster*

D. melanogaster (*Dm*) was used as an alternative model to study FAM49 *in vitro* and *in vivo*. Development of *D. melanogaster* follows three distinct stages referred to as larval, pupal and adult. Once hatched, the egg undergoes 3 larval instar stages, known as L1, L2, L3 before transiting to the pupal stage. This step allows the outgrowth and the development of the adult organs during a process called metamorphosis, resulting in an adult fly. In total, the life cycle lasts between 10-12 days and is dependent on the ambient temperature. During development, specific cell lineages will differentiate and colonise adult tissues. For example, embryonic haemocytes are the embryonic blood cells and originate from the procephalic and thoracic mesoderm (early and late development) before spreading across the embryo by using some pre-defined paths (Wood and Jacinto, 2007). In a healthy fly, blood cells are composed at 95% by plasmocytes (hereafter referred to as haemocytes). The remaining 5% is divided between crystal cells and lamellocytes. The latter is absent from a healthy fly and has only been found upon parasite infection of the larva. Haemocytes are the professional phagocytes and their function can be related to the mammalian macrophages. Indeed, they patrol across the developing embryos and later on in the adult fly in order to clear pathogens or apoptotic debris. As a consequence, they are crucial elements for the fly immune system (Wood and Jacinto, 2007).

Because of their function of scanning the environment, embryonic plasmocytes have to be extremely motile and they have been used as a tool to study cell migration and actin/microtubule dynamics. Also they are easily accessible as they circulate within the hemolymph and can be isolated by simple dissection.

Because of their motility capacity dependent on Rac1 activation (Paladi and Tepass, 2004; Stramer et al., 2005), we used *D. melanogaster* haemocytes as a tool to study the effect of FAM49 loss. Specific conditional knockdown of *D. melanogaster fam49* gene was based

on the GAL4/UAS system and obtained from the Vienna Drosophila RNAi Centre. GAL4 is a transcription factor and will be expressed accordingly to the promoter it has been placed under. Since the main effector sequence of GAL4 is the UAS, reporter gene or RNAi can be placed downstream of a UAS sequence and will be expressed in the GAL4-positive population. Fly lines containing a UAS-Scramble (Ctr) or UAS-FAM49 RNAi oligos (and #2) were crossed with Tub>GAL4 flies and recombinants were selected. Tubulin promoter drives a constitutive depletion of FAM49. Knockdown of *fam49* gene from L3 stage larvae was evaluated by qRT-PCR and reported to the ribosomal-related protein Rpl32 as housekeeping transcript. Mutants #1 and #2 showed a 6-fold reduction in *fam49* gene expression following RNAi targeting. (**Figure 6-10 – A**). Interestingly, mutant #2 stopped developing at the pupal stage and the mechanisms leading to this early lethality have not been further investigated. However, mutant #1 flies looked viable and fertile.

Hemolymph from L3 larvae of control or mutants flies was isolated and plated on a glass coverslip for 20 min. Cells were fixed, stained for F-actin and analysed by confocal microscopy (**Figure 6-10 – B**).

The first striking feature was the number of isolated cells from the *fam49*-knockdown larvae compared with control. On average, dissection of the same number of larvae resulted to 2.5 times more cells in the knockdown condition (**Figure 6-10 – B**). On glass, control cells appeared quite round with a strong cortical actin staining from which emerged few short filopodia. In contrast, FAM49-depleted cells widely spread a large lamellipodium, full of filopodia, although this phenotype tends to be subtler in mutant #2. Similarly to our previous work using other models, mutant cells are bigger (**Figure 6-10 – C)** and this difference was maintained during a time-course experiment (**Figure 6-10 - D**). The exact same phenotypes were also observed using a Tub-Gal4>UAS-LifeAct-GFP line (**Figure 6-11**). This increase of spreading was finally confirmed by live imaging of isolated haemocytes, plated on glass-bottom dish. DIC imaging allowed us some insight about protrusion dynamics. Movies and kymograph showed that control cells eventually do spread but with a much slower dynamism compared to the *fam49*-knockdown (**Figure 6-12 – A - B**). At some point, both cell type reached a state where lamellipodium is at its maximal extension. However, FAM49-depleted cells have a more steady lamellipodium compared with the instability of the control cells.

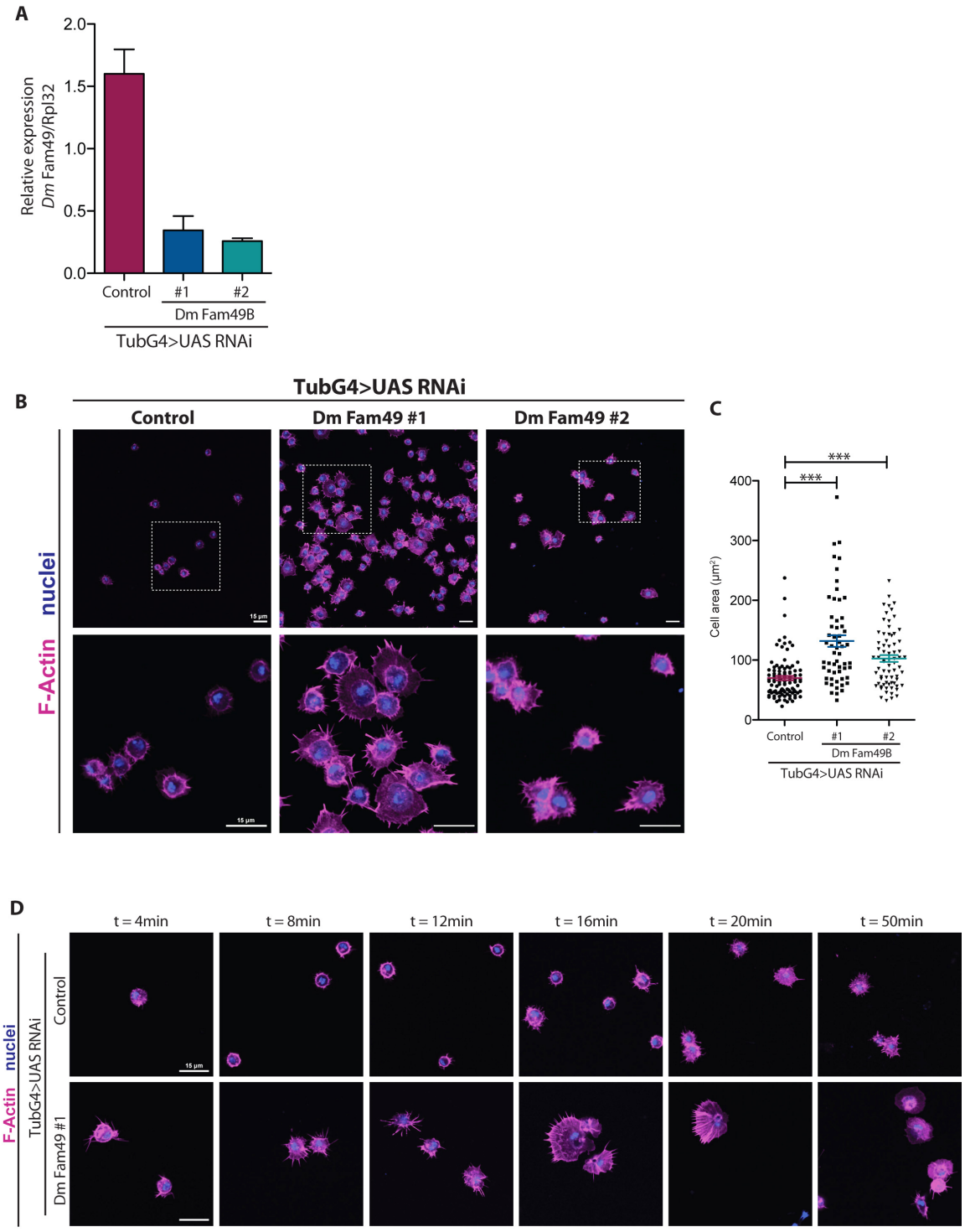

Figure 6-10: *fam49*-knockdown haemocytes recapitulate mammalian phenotype
A – Expression level of *D. melanogaster fam49b* gene in control or knockdown L3 larvae, using Tubulin promoter as driver (TubG4). Quantification represents qRT-PCR data from 3 independent experiments. Mean ± S.E.M is displayed.

B-C – Immunofluorescence of isolated haemocytes extracted from three L3 larvae of each condition. Cells were plated on glass coverslip, fixed after 20 min and stained for F-actin (magenta) and nuclei (blue). Bottom row is a magnified view from the dotted square area. Scale bar = 15 µm. Manual quantification of the cell area for each condition is shown as a scatter plot with mean ± S.E.M. One-way ANOVA with Dunn's post-test was performed. *** p<0.001.

D – Immunofluorescences from a timecourse experiment. Cells were plated on glass coverslip, fixed at each timepoint and stained for F-actin (magenta) and nuclei (blue). Scale bar = 15 µm

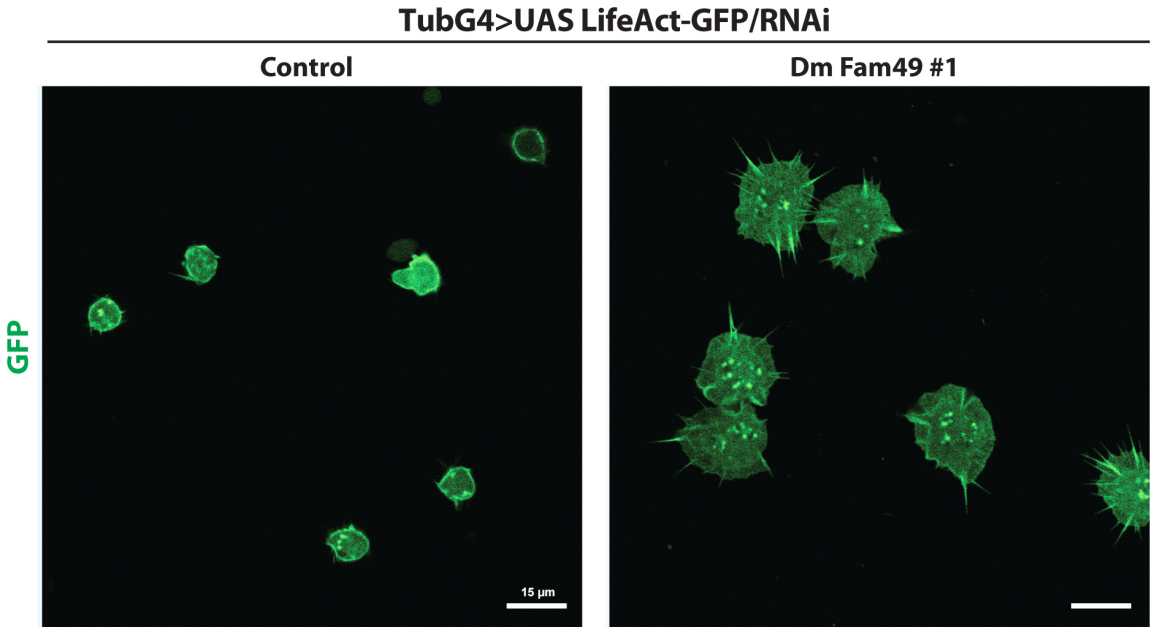

Figure 6-11: *fam49*-knockdown haemocytes extend larger actin-based protrusions
Still pictures of haemocytes expressing UAS-LifeAct-GFP and UAS-RNAi, under the control of TubGal4 (TubG4) promoter were plated on glass, left spreading for 20 min and live-imaged by confocal microscopy. Scale bar = 15 µm

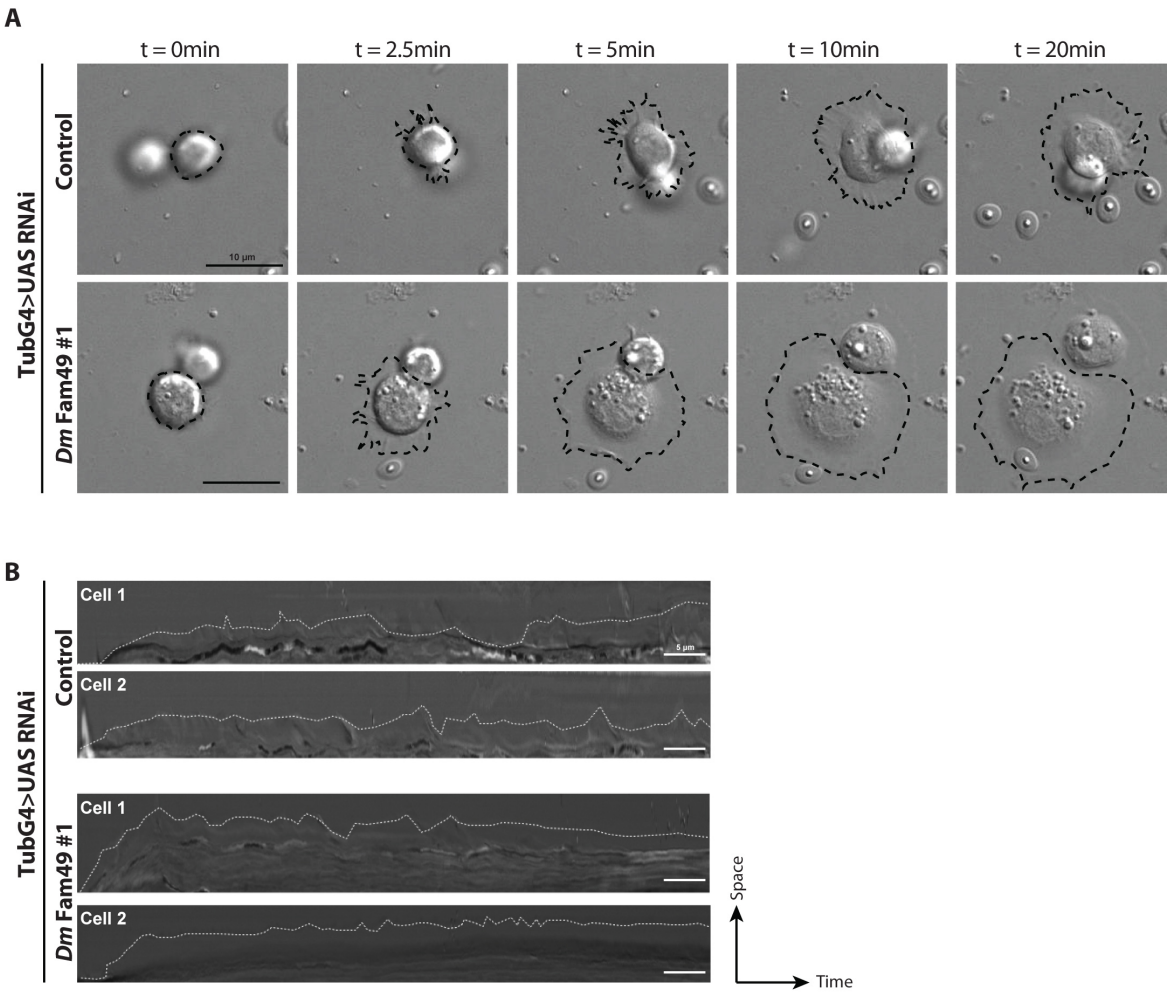

Figure 6-12: Effect of *fam49b*-knockdown on haemocyte spreading
A - Stills extracted from a DIC movie. Control or knockdown haemocytes were plated on a glass-bottom dish and imaged while they were adhering/spreading. Cell edges were highlighted by a black dotted line. Scale bar = 10 µm.

B – Kymograph analysis of spreading haemocytes. Cell edges were highlighted by a white dotted line. Time is shown on the x-axis and space on the y-axis Scale bar = 5 µm

As mentioned in the introductory paragraph, haemocytes are the major immune cells in *D. melanogaster* and can be activated upon a wide range of stimuli (infection, inflammation). In such a situation, naïve haemocytes get activated and undergo a profound re-arrangement of their morphology that could also explain the phenotype we observed. This is even more relevant because FAM49 is depleted across the whole body and might lead to inflammation of some tissues followed by the recruitment and activation of the haemocytes.

To rule out this possibility and ascertain whether loss of FAM49 was directly responsible for this phenotype, we performed haemocyte-specific *fam49*-knockdown by using the hemolectin-driven GAL4 line (hml-G4). Hemolectin is only expressed in plasmatocytes and crystal cells and is totally absent from lamellocytes after wasp infection or *L. boulardi* parasitation. It is expressed throughout the larval stages until the end of the puparisation, before strongly decreasing in the adult fly (Goto et al., 2003). In parallel of the RNAi, GFP was also expressed as a reporter. Isolated cells displayed a similar phenotype as previously described, so we conclude that cell enlargement and filopodia formation was specific to the loss of FAM49 and independent from external factors (**Figure 6-13**).

Given the striking phenotype in 2D, we hypothesised that cell shape will also be affected *in vivo*. Short movies from the hml-G4>UAS-RNAi/GFP L3 larvae were acquired using ligh sheet imaging (LSFM) (**Figure 6-14**). This technique allows a less phototoxic way of imaging living organisms by illumination of a thin slice of the sample. Unfortunately, only one larva of each condition was imaged during the trial-time of this microscope at the Beatson but it gave us some exciting preliminary videos that have to be further confirmed by more analysis and bigger sampling. Control haemocytes displayed a very smooth-edged phenotype with only few rare and not very active protrusions (yellow arrowheads). However, cells lacking FAM49 protrude actively and have a total different morphology. Cell body is enriched in vesicle-like structures and generally speaking, cells looked in an active state. Further work and collaboration will aim to confirm this phenotype and more careful analysis of cell behaviour and protrusion features is required.

.

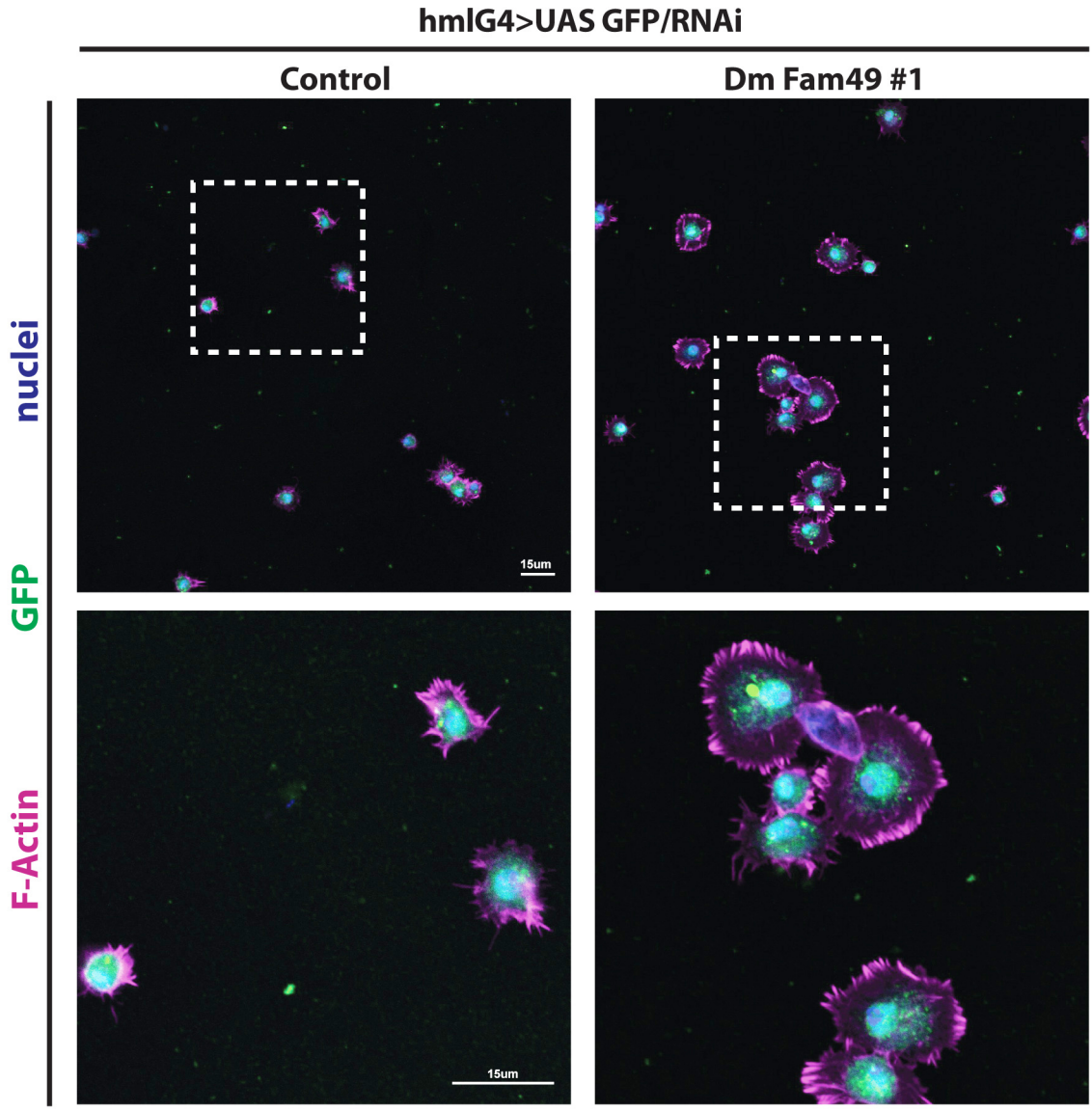

Figure 6-13: Specific depletion of *fam49b* in the haemocyte lineage leads to increase lamellipodia extension and filopodia
Immunofluorescence of isolated haemocytes extracted from three L3 larvae of each condition. Cells were plated on glass coverslip, fixed after 20 min and stained for F-actin (magenta) and nuclei (blue). Hml promoter drives the expression of GFP (green) in haemocytes containing the control or FAM49 RNAi. Bottom row shows magnified views from the dotted square area. Scale bar = 15 µm.

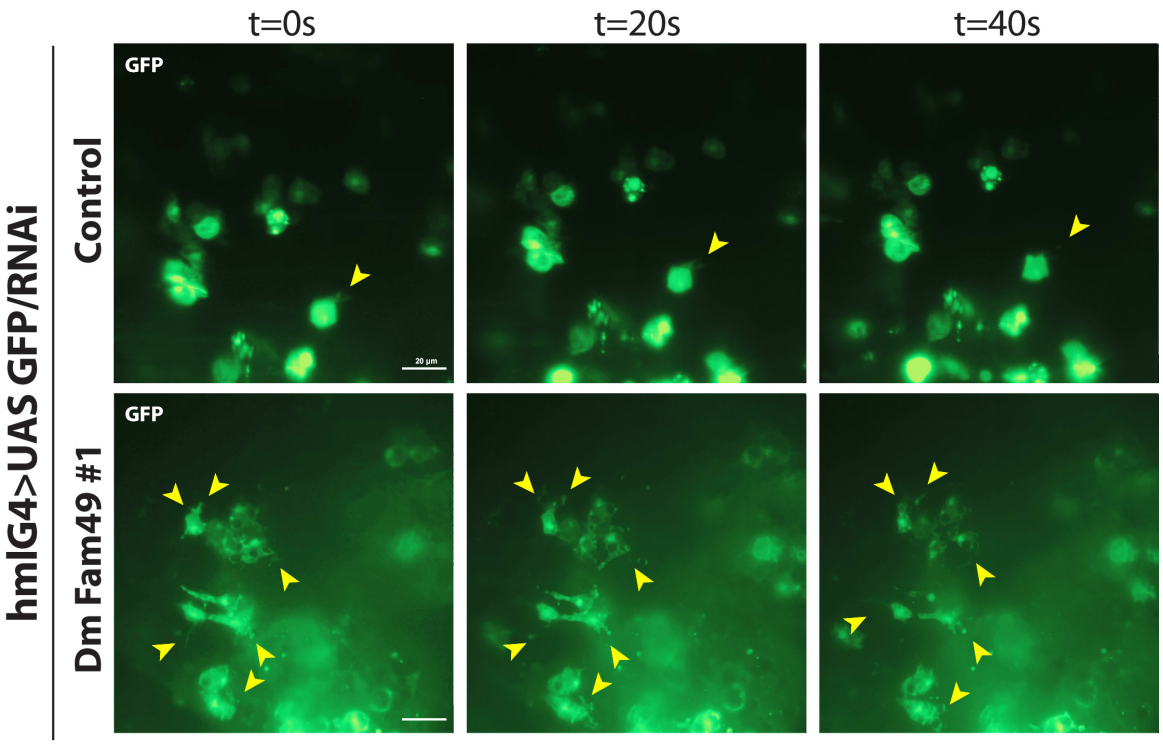

Figure 6-14: *In vivo* LSFM imaging reveals abnormality in pseudopods morphology of L3 larva haemocytes specifically knockdown for *fam49*
hmlGal4>UAS-GFP/RNAi L3 larvae were immobilised in an agarose plug and imaged every 20 seconds using light sheet microscopy. GFP-expressing haemocytes were imaged from one of the epidermal-muscular pocket located on the lateral side of the larva. Yellow arrowheads highlight active protrusions. Scale bar = 20 µm

6.3 Discussion

In this chapter, we tried to address the role of FAM49B using more complex physiological models, which have been previously used to study Rac1.

The MDCK organoid model turned out to be a great tool and gave us new insights about the potential role of FAM49B during cyst formation. Together, we hypothesised that FAM49B might play a role in the establishment of Rac1 gradient across the cyst. Rac1 has been previously shown to be required for proper organisation of the cyst architecture (Mack et al., 2012; O'Brien et al., 2001; Yagi et al., 2012a; Yagi et al., 2012b). Establishment of Rac1 gradient seems to be a fundamental step during cystogenesis and Mack et al (Mack et al., 2012) proposed an elegant model of differential recruitment of the Rac-GEF Tiam1 by distinct proteins along the cyst. According to their model, low Rac1 activity at the lumen is dependent on a Par3-mediated inhibition of Tiam1 whereas this GEF gets recruited and activated by β2-syntrophin at the basolateral side. Here, we propose that FAM49B might also be involved in the differential Rac1 activity and as a consequence, allows to restrict the spatial activation of the WRC at the apical membrane. Indeed, WAVE2 switches from a basolateral to an apical localisation upon FAM49B loss and correlates with a multilumen phenotype. This was rescued by chemical inhibition of Rac1

In this model, it would be interesting to measure Rac1 activity using FLIM/FRET imaging and we hypothesise that Rac1 activity would be much higher at the apical domain in *fam49b*-knockdown cysts. This model also implies FAM49B to be more enriched at the apical domain, or at least to have a differential activity between apical and basolateral membrane. This can be linked to the myristoylation/palmitoylation state of the protein. Genetic tools, such as membrane targeting using a dimeriser or optogenetic systems based on light-induced clusterisation (Nguyen et al., 2016) could allow us to affect localisation of one protein to one side of the cyst or the other. For example, techniques using FKBP-FRB and rapamycin (Banaszynski et al., 2005; Inobe and Nukina, 2016) would be useful to ask whether the mislocalisation of FAM49/WRC/Rac1 is sufficient to disrupt cell polarity. We could also directly address whether Rac1 accumulation at the basolateral domain would restore Rac1 gradient across the cyst following FAM49B loss.

The fundamental question here would be to understand the initial defect leading to this multilumen phenotype. *De novo* apical lumen formation has been investigated in different systems and basically two models have been proposed. The cavitation model results from apoptotic event occurring in the centre of a mass of cell and was shown to take place in mammary and salivary tissues (Aranda et al., 2006). However, in most of the tissues and

particularly in the MDCK-derived cysts grown in Matrigel, apoptosis does not seem to be required for apical lumen formation (Martin-Belmonte et al., 2008). Instead, the hollowing model establishes a coordination between cell division and trafficking events that lead to the formation of the apical membrane initiation site (AMIS) (Bryant et al., 2010). This is a key step that will drive and organise the primary polarity of the growing cyst. Relocalisation of apical protein is dependent on Rab11-mediated endocytosis and specific microtubule-dependent delivery (Casanova et al., 1999). This process has also been shown to be coupled to the WRC and Rac1 at the early stages of the cyst formation (Mangan et al., 2016). WRC-dependent actin polymerisation is crucial for proper localisation of Cingulin, a tight-junction protein, to the primary apical lumen during mid-body formation. This requirement towards the WRC for the mid-body formation is interesting as multi-lumen phenotype can also arise from defect in mid-body position (Lujan et al., 2016).

In this model, we can hypothesise that loss of WRC restriction during cytokinesis upon FAMB-knockout might abnormally orientate the midbody. This mispositioning might enhance the defect in the microtubule-spindle orientation even further. This could be easily addressed by staining 48h-cultured cysts and record the localisation of early midbody markers such as Cep55 and MKLP1/KIF23.

Mangan *et al* (Mangan et al., 2016) also showed that Rac1 inhibition during the 1st cell division results in a multilumen phenotype. This observation combined with our and others data would suggest that the actual level of Rac1 activity is not important for lumen formation. However, the differential activity in Rac1 signalling between apical and basolateral domain is. Indeed, having too much Rac1 at the apical side or not enough at the basolateral side would compromise the formation of the gradient and leads to defect in endocytosis-delivery to the AMIS. Based on Mangan's work, it would be interesting to perform a timecourse experiment at earlier timepoint in order to see whether loss of FAM49B affects trafficking and AMIS formation. Preliminary results showed that after 48h, cysts already presented apical accumulation of WAVE2. This points toward an early effect of FAM49B on WAVE2 localisation. Interestingly, we noticed that control cysts with a multi lumen phenotype at 48h (not shown) or 5 days (**Figure 6-6**), don't show a defect in WAVE2 localisation. This observation suggests that apical targeting of WAVE2 is not enough to drive the multilumen phenotype. Finally, Rab11 staining at early timepoint (12h, 24h, 48h) should also give us more details about the potential endosomal defects in knockdown cysts.

As a follow up for this part, *in vivo* FAM49B study in epithelial tissues has already started. Floxed FAM49B mouse was crossed with the Pdx1-CRE mouse. Pdx1 gene is expressed

by early pancreatic progenitors and is then considered as a multipotent pancreatic stem cells marker (Offield et al., 1996). Some leakiness of Pdx1 promoter has also been reported in the gastro-intestinal tract and some parts of the central nervous system (Schonhoff et al., 2004; Song et al., 2010). Laura's lab has a strong background in the pancreatic model, which is the reason we chose this system. The exocrine part of the pancreas is formed by pancreatic ducts ending as a secretory gland formed by acinar cell (see chapter 8). These structures are covered by a columnar epithelium allowing the secretion of digestive enzymes. As any epithelium, establishment of cell polarity is essential for pancreatic functions and would allow us to confirm the data obtained with the MDCK cysts, using an *in vivo* model. Pancreata from FAM49B$^{fl/fl}$ or FAM49B$^{-/-}$ mice were analysed by western blot and showed a strong reduction in FAM49B signal (not shown). Preliminary data showed that Pdx1-CRE *fam49b*-null mice are viable and don't have any growth defect compared to their wild-type littermates. Haematoxylin/Eosin staining of pancreas from 15-weeks old mice does not present any obvious morphology and organisational defect upon FAM49B loss. There are two possible explanations for this result. First, FAM49B is dispensable for pancreatic development from E8.5 onwards. Then, it has been reported that the Cre recombinase can show mosaic expression across the targeted organs (Gannon et al., 2000; Gu et al., 2002a). It could be possible that only a small proportion of ductal epithelial cells get recombined, not leading to enough depletion to see a phenotype. Unfortunately, FAM49B antibody has not been optimised for IHC on tissue yet. However, it showed a weak staining in CrispR control CHL1 embedded in an agarose-plug, which was lost in *fam49b*-CrispR knockout cells.

Finally, studying FAM49B during PDAC progression would also be a project to consider. Specific pancreatic depletion of Rac1 has been shown to reduce/stop pre-malignant lesion (acino-ductal metaplasia, PanIN) and cancer progression in both a KRas^{G12D} slow pancreatic model or a KRas^{G12D} and p53^{R172H} aggressive model. (Heid et al., 2011). This, combined to the fact that only one mouse showed advanced PanIN lesions, suggest an early and fundamental function of Rac1 in PDAC development. In either model, we would hypothesise that loss of FAM49B would lead to higher Rac1 activity, leading to increase tumour burden and invasion. Recently, major findings obtained from genomic analysis of human pancreatic tumours characterised four main subclasses of cancer correlating with histopathological features (Squamous, ADEX, Immunogenic, Pancreatic progenitor). (Bailey et al., 2016). Data from over 450 human samples reveal than the 4 subtypes express relatively high amount of FAM49B. Moreover, FAM49B expression correlates with survival: Indeed, high FAM49B expression leads to a poor outcome (p-value=0.016) in this cohort of patients (internal communication). However, it isn't yet possible to

interpret this in the context of Rac1 in PDAC. Further *in vivo* studies would be required to find out the specific roles of FAM49B and the potential crosstalk FAM49B/Rac1 in this context.

Ex vivo skin explant provided a contrasting model to epithelial organisation as melanoblasts migrate individually in the skin. This model allowed us to directly address FAM49B functions in individually migrating cells during development. Specific knockout in the melanoblast lineage and imaging at E14.5 suggests a function of FAM49B in migration, although depletion of the protein led to less migration, which was quite unexpected based on our *in vitro* data. A quick and easy way to detect melanoblast migration defect is to look at the colour coat of the mouse after weaning. Indeed, if a white-belly phenotype appears, it would suggest a migration defect at the embryonic stage. This has already been shown after Rac1 or Cdc42 depletion in Black6 background mice (Li et al., 2011; Woodham et al., 2017). Despite the reduced migration observed in this assay, we have not noticed any white-belly phenotype, suggesting that FAM49B-null melanoblasts are still able to complete their journey to the ventral part of the embryo. This means these cells might overcome the loss of FAM49B by alternative pathways. It would be informative to picture the melanoblast journey at different stages of the embryo development. An easy way to do so would be to use the DCT::LacZ reporter combined with our Tyr-Cre::FAM49B$^{fl/fl}$. Briefly, this gene allows the expression of the β-galactosidase, an enzyme that will only be expressed in DCT-positive cells (another marker of the melanoblast lineage). Incubation with X-Gal, the substrate of the β-galactosidase, will result in its conversion into a blue metabolite that can be visualised. This technique should allow us to spot any abnormality during melanoblast migration from the back up to the belly, and might explain why no white belly phenotype is observed despite a slower migration. Meanwhile, proliferation of these cells will be assessed *in vivo* by BrdU injection and staining. Indeed, migration defect could be compensated by an increase of proliferation.

Analysis of our skin explant movies revealed that pseudopod dynamics was also affected in FAM49B-null melanoblasts. Pseudopods were shorter and short-lived compared to control. As a comparison, migrating melanoblasts navigate using short and long protrusions and Rac1 was shown to control the formation and the frequency of the long protrusions that are the main drivers for the cell persistence and speed. (Li et al., 2011). Further analysis should allow us to determine whether FAM49B and Rac1 are playing a dual function during this process.

Moreover, we frequently observed bursts of td-Tomato signal along the pseudopod. This may reflect uncontrolled Rac1 activity resulting in membrane extension. In order to test this hypothesis, our Tyr-Cre::FAM49B$^{fl/fl}$, LSL-tdTomato mouse will be crossed with the Raichu Rac FRET reporter knock-in mouse (Johnsson et al., 2014). Tyrosinase-positive cells will express recombined FAM49B gene along with the Rac-FRET reporter and skin explant would be performed the same way as previously described but using a FLIM-FRET microscope. With this setup, we should find out more about the potential crosstalk between FAM49B and Rac1 during melanoblast migration. FRET efficiency from migrating melanoblasts could be measured as well as Rac1 activity during membrane bursts.

Similarly to our mammalian work, primary haemocytes isolated from *fam49*-knockdown *Drosophilia* (whole body or haemocyte-specific) extend a broader lamellipodium compared with control cells. It also contained lot of filopodia-like structure. This would tend to point toward a link between FAM49 and Rac1. Overexpression of Rac1 has also been shown to release the sessile population of haemocytes from the epidermis resulting in a 3-3.5-fold increase of circulating cells (Williams et al., 2006; Zettervall et al., 2004). We observed a similar hyper-recruitment to the hemolymph in our *fam49*-knockdown larvae. This effect had previously been shown to require the Drosophila Jun-kinase-homologue, called Bsk. Together they regulate lamellipodium extension and focal adhesion turnover, leading to increase mobility (Williams et al., 2006). However, signals leading to their release into the circulation have not been investigated. Drosophila would be a useful system to study genetic interaction between FAM49 and Rac1. Dominant negative Rac1 mutant showed important developmental defects leading to lethality (Harden et al., 1995). We could overcome this by driving dominant Rac1 expression into the haemocytes and look at potential rescue of the phenotype. This observation would suggest that Rac1 is important for FAM49 functions.

Imaging haemocyte morphology and migration *in vivo* would also be a project to follow up. Our results are too preliminary to conclude anything but more sophisticated models could be used. Haemocytes are becoming a powerful system for migration study, especially *in vivo*. Because of their immune functions, different groups have induced haemocyte recruitment after epithelium wounding using UV laser ablation. Haemocytes switch from a random to a directed migration after wounding (Moreira et al., 2011) and this chemotaxis seem to be dependent on PI3K (Wood et al., 2006). PI3K is potent activator of Rho family GTPase and a positive feedback loop exists downstream of the GTPase (Yang et al., 2012). Our hypothesis is that haemocyte-specific *fam49*-knockdown

would reinforce and unbalance this feedback loop resulting in Rac1 activity mis-regulation and defect in directed migration.

7 Conclusions, working model and future directions

The aim of my thesis was to work out the cellular role of a previously un-studied protein (FAM49B), which we now believe, is the first discovered negative regulator of cell protrusion. We carried out this analysis using a range of biological systems combining biochemistry, *in vitro*, *in cellulo* and *in vivo* data. Our current hypothesis suggests that FAM49B directly competes with active Rac1 for binding to the Scar/WAVE complex. This competition results in spatial regulation of Scar/WAVE activity in restricted and highly polarised patches, which are required for F-actin polymerisation and membrane protrusion. The direct interaction between active Rac1 and FAM49B makes this protein totally distinct from other negative regulators of actin branching such as Arpin, which acts downstream of the Scar/WAVE complex and does not interact with Rac1, although its functions are Rac1-dependent (Dang et al., 2013). In the absence of FAM49B, the Scar/WAVE complex cannot be constrained anymore and is free to diffuse around the cell membrane, which causes loss of pseudopod formation. We also show that FAM49B was required for different biological processes linked to actin dynamics and cell motility. Importantly, FAM49B is dispensable, although cells tend to dislike excessive amount of the protein, suggesting that regulation of FAM49B expression is tightly regulated to avoid any excess of the protein that could be toxic for the cell. Based on our mathematical model, the amount of FAM49B required for restricting the activator has to be just above the activator level at its edge. If we lose this higher level of inhibitor, the activator will enter into a positive feedback loop and expand across the entire cell. Biological data and modelling of FAM49B function led to the working model described in **Figure 7-1**.

We are currently prioritising 3 major projects that should give us a better understanding of FAM49 proteins:

1) FAM49B activation and regulation
2) Elucidating FAM49B structure
3) What are the other biological processes regulated by FAM49B?

As previously mentioned, the N-terminus part of FAM49B seems to be involved the protein regulation. This flexible part of the protein starts with a short alpha helix and then is followed by a predicted unfolded region. Pull-downs with Rac1 have only been successful using a construct truncated for the first ~35 amino acids. Anh Le, a PhD student in the lab has also confirmed the importance of these residues by using the FAM49B's DUF1394 domain with or without the N-terminus part. He has nicely shown that the alpha

helix and the unfolded region have an inhibitory effect on active Rac1 binding. This region contains the myristoylated residue and one putative S-acylated cysteine. Together, our hypothesis is that the protein is auto-inhibited by the N-terminus part, which folds over the RBD of the protein. Posttranslational modifications or myristoyl-switch would cause the following: Protein targeting to the membrane with concomitant unfolding of the N-terminal region, opening of the protein structure in order to expose the internal RBD, and finally, binding of the protein to Rac1. The signalling pathways that lead to FAM49B activation still remain elusive, although we may hypothesise that it is dependent on the regulation of the N-myristoyl-transferases and protein acyltransfereases. In order to get more information relative to the activation state and whether the protein switch from a cytosolic to a membrane localisation, we are developing our recombinant FAM49B protein that is being used for antibody production and purification. We hope to get a specific antibody against the endogenous protein that we could use for immunofluorescence. To do so, soluble protein and inclusion body were obtained and injected into rabbits. We are now about to start the purification of the total IgG and anti-FAM49B antibody using affinity purification and glycine elution.

The FAM49B structure presented throughout this thesis has been generated using i-TASSER. This tool generates tertiary structure prediction based on the primary structure of the protein. It uses sequence homology between the query protein and the sequences of structural templates from the protein database, and then reassembles each fragment to obtain a 3D structure prediction. Despite different conditions and screening tray set up, attempts to crystallise the protein have failed. We have now started a collaboration with Prof. Matthias Geyer in order to test more buffer conditions and also increase our yield of protein. The medium-term plan for this part would be to obtain a crystal good enough for X-ray diffraction and solve the structure of FAM49B. Solving the structure of the co-crystal FAM49B-Rac1 would be very informative and would allow us to design compounds, which could stabilise/destabilise this complex. A *Kd* of 20 μM is at the edge of co-purification so we would rather try to purify $Rac1^{Q61L}$ alone and set up crystal trays with stoichiometric amounts of either FAM49B or RBD.

This work on FAM49B is not restricted to its role on cell migration. Proteomics analysis of FAM49B gave a broader picture of potential new interacting proteins. Briefly, triplicate samples of COS-7 cells expressing GFP, GFP-FAM49B, FAM49B-GFP and GFP-RBD were used for a GFP-Trap pulldown and sent for LC-MS/MS analysis. Selected hits are displayed in appendix 6 based on the Label-free quantification (LFQ intensity). Data were

processed and the relative abundance of each protein compared with the GFP sample were analysed in order to get statistical value. Unlike the full-length protein that only shows a robust and consistent interaction with few proteins (10 proteins for FAM49B-GFP and 20 proteins for GFP-FAM49B), RBD-GFP interacts with over than 200 candidates. This massive difference in number of interacting proteins between the full length and the truncated construct is interesting and currently, 2 options are foreseen. Although unlikely, the first hypothesis would be that the RBD is not properly folded and forms aggregates, which interact with diverse proteins. However, cells respond to protein misfolding by recruitment of chaperones and none have been found in this screen. This implied that we can be fairly confident about the specificity of interaction. The second option would be that this construct represents an active form of FAM49B that binds to more effectors than the auto inhibited full-length protein. Once again, it seems that cells cannot handle very well this construct as we found a lot of subunits of the 26S proteasome, suggesting that cell tried to get rid of the excess protein. Among other interesting hits, FAM49A interacted with the 3 constructs, suggesting that its minimum-binding domain lies within the Rac-binding region and can form a heterodimer. Endogenous Rac protein (the MS was unable to differentiate between Rac isoforms) was statistically enriched in GFP-RBD and GFP-FAM49B, although, Cdc42 and RhoA have also been found as a significant interactor of GFP-RBD and would tend to contradict our GST-pulldown data. However, internal communication from Prof. Ivan Dikic shed a light on this potential interaction between FAM49 and RhoGTPases. Indeed his group found that FAM49A directly interacts with FAM49B and Cdc42. So Cdc42 might just be an indirect interactor of FAM49B, mediated by FAM49A. At the moment, the relation to RhoA is still being investigated. Other Ras-related GTPases such as Rab, Ral were also found and could might interesting candidates to look at. Of particular interest was Rab5C that has been linked to Rac1-dependent cell motility and was specifically found in GFP-RBD (Chen et al., 2014b). Interesting candidates will be individually confirmed by pulldown and immunofluorescence and should allow us to find out more about the biological functions of FAM49B.

To conclude, based on the mechanism of activation and the description of the functions of FAM49B during cell migration, we proposed to name this new protein CYRI-B. This stands for Cyfip-related Rac1-interacting protein B.

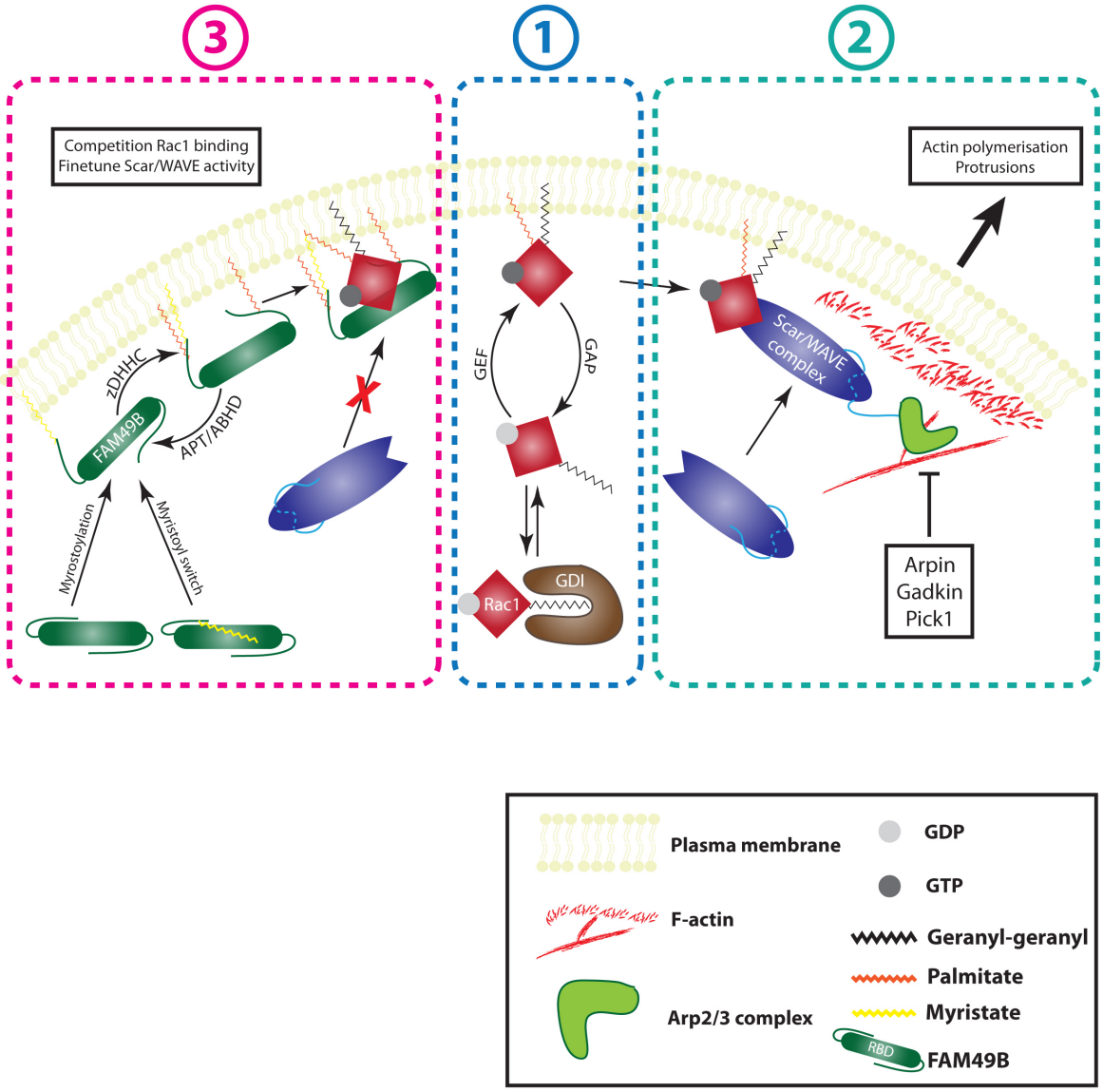

Figure 7-1: Working model of FAM49B functions during cell protrusion
1 – Following cell stimulation (growth factor, integrin signalling,..), GDP-Rac1 gets released from the GDI and activated by GEF resulting to the nucleotide exchange.

2 – GTP-Rac1 interacts with diverse effectors, for example, Scar/WAVE complex. Activation of the Scar/WAVE complex leads to the expulsion of the VCA tail from the core of the complex and stimulation of Arp2/3-dependent actin polymerisation, resulting *in fine* to actin-based protrusions. Arpin, Gadkin and Pick1 have previously been described as negative regulators of protrusion formation and actin branching, directly acting at the level of the Arp2/3 complex.

3 – Cytosolic autonihibitted FAM49B gets recruited to the plasma membrane following direct myristoylation or myristoyl switch. This weak membrane binding is strengthened by additional palmitoylation mediated by zDHHCs (active at the membrane or endomembrane followed by protein trafficking to the membrane). Protein modifications result to release the auto-inhibition from the N/C terminus of FAM49B and expose the RBD. Binding to active Rac1 blocks the Scar/WAVE complex activation. Reversibility of the palmitoylation (by APT or ABHD depalmitoylases) might regulate stable association to the plasma membrane and Rac1 interaction.

8 The bundling protein Fascin 1 increases pre-malignant lesions during pancreatic cancer progression

8.1 Introduction

Located in the upper left side of the abdomen, the pancreas is a glandular organ that has a dual function during digestion. The exocrine part is formed by acinar cells, which are specialised in the secretion of important digestive enzymes required for proper nutrient absorption by the small intestine. Pancreatic tubules directly connecting each acinus merge into a main pancreatic duct that connects the pancreas to the duodenum. The endocrine part is formed by the Islets of Langerhans and that are sparsely distributed across the exocrine pancreas. Islets are composed of α, β, δ, and γ cells, which are specialised in hormone secretion and work together using endocrine, paracrine and autocrine loops to tightly control the glucose level in the blood stream. Briefly, α cells secrete glucagon, responsible for conversion of glycogen into glucose and its discharge by the liver into the blood stream. On the other side, β cells are insulin-producing cells that act to decrease glucose by stimulating glycogenesis and lipogenesis. These two cell types are both negatively regulated by somastotastin, a peptide secreted by δ cells. Finally, γ cells are predominantly restricted to the head of the pancreas and release pancreatic polypeptides, stimulating gastric secretion and also regulating α and β cells. Together endocrine and exocrine pancreas functions assure coordination between food intake and energy storage/release during fasting periods.

Pancreatic cancer is the 11th most frequent cancer in the UK, although it represents the 5th most common cause of cancer-related death. Familial predisposition to develop pancreatic cancer only accounts for 2-10% (Hruban et al., 2010) whereas external factors and lifestyle, such as smoking and obesity, have been correlated with 37% of the cases (Cancer Research UK, http://www.cancerresearchuk.org/health-professional/cancer-statistics/statistics-by-cancer-type/pancreatic-cancer, August 2017). However, only 1% of patients diagnosed with a pancreatic cancer will survive beyond 10 years, making pancreatic cancer the cancer with the poorest survival rate. Even more alarming is that survival has remained stable over the last 40 years and reveals a lack of understanding about the molecular mechanisms. These poor statistics can be explained by the late diagnosis of pancreatic cancer. Indeed, 8 out of 10 patients in the UK were diagnosed with a late stage in 2014, resulting in more challenging surgery and a more aggressive line of

treatment. (Cancer Research UK, http://www.cancerresearchuk.org/health-professional/cancer-statistics/statistics-by-cancer-type/pancreatic-cancer, August 2017). Frequently, cancer has already spread across the body before the onset of clinical symptoms. These observations raise the question about early detection during pancreatic cancer and push researchers and clinicians to identify key proteins initiating the first stage of this cancer.

Histopathological features reveal a progressive evolution of pancreatic cancer, starting from pancreatic lesions (pancreatic intraepithelial neoplasia - PanIN1-3) to a fully developed cancer (hereafter referred to as pancreatic ductal adenocarcinoma – PDAC) (Yachida and Iacobuzio-Donahue, 2013). PDAC represents the most frequent type of pancreatic cancer, although other sub-types exist but are not of our interest. As mentioned by its name, it develops from ductal cells. Briefly, PanIN1 are subdivided into 1A (flat epithelial lesion characterised by mucin accumulation above the nucleus) and 1B (same as 1A but with papillary or pseudostratified structures). PanIN2 can be flat or papillary and show a loss of nuclear polarity correlating with morphological defects of the nucleus. Finally, PanIN3 show several cytological defects, with abnormal mitoses, nuclear irregularity, budding of cell clusters into the lumen and necrosis and is the last characterised lesion before the PDAC (John Hopkins university http://pathology.jhu.edu/pancreas/professionals/DuctLesions.php, August 2017). Other lesions, not directly related to ductal cells have been frequently noticed in patients and mouse models. To cite few, pancreatic cysts are commonly observed in patients with no pancreatic history (13.5%) and are thought to be precursor lesions. Classification of cyst types is out of the focus and we will just refer cystic structures as cysts, regardless to their origin or localisation. Finally, acinar to ductal metaplasia (ADM) corresponds to a metaplastic switch leading to the formation of ductal structures within acini. These lesions have been linked to an increased risk of developing PDAC in both mouse models and human (Lowenfels et al., 1993; Wagner et al., 1998). Origins of ADM are not well understood but matrix metalloproteinase-7 has been shown to regulate ADM formation, although other factors might be involved (Crawford et al., 2002).

PanIN formation correlates with an accumulation of various genetic alterations such as increase in gene copy number or gene expression, point mutation, epigenetic abnormality, etc. (Hansel et al., 2003). Sequencing effort has allowed identification of key driver genes and revealed mutation of K-Ras in 95% of cases (Almoguera et al., 1988). In particular, one hot spot mutation leads to the substitution of Gly12 to an Asp although other missense mutations have also been reported (Kalthoff et al., 1993). K-Ras belongs to the Ras-GTPase family and is involved in intracellular signalling. This mutation affects the

intrinsic GTPase activity, resulting in a higher proportion of molecules in the GTP-bound form. This dominant active form directly signals to downstream effectors such as the MAPK pathway, PI3K, mTOR and AKT which together, promote cell survival, proliferation and invasion (di Magliano and Logsdon, 2013). K-Ras has also been found highly mutated in early lesions, so it is thought to be the activator event (Yanagisawa et al., 1993). Based on the two-hits hypothesis proposed by Knudson, cancer initiation requires multiple hits (Knudson, 1971). In agreement with this model, K-Ras mutation is followed in 50-75% of cases by the alteration of the TP53 gene (encoding p53), mainly through a missense mutation at the hot spot Arg172 (Olivier et al., 2002; Redston et al., 1994). The fact that cancer cells preferentially mutate TP53 reflects a potential growth advantage compared to the deletion of the gene. p53 is the master regulator of cell cycle by controlling the G1-S or-G2-M transition. Upon DNA damage, TP53 lifetime increases and it accumulates in the nucleus where it stimulates transcription of key genes involved in cell arrest and apoptosis (Lakin and Jackson, 1999).

This brief introduction about the main genetic features occurring during pancreatic cancer is crucial to understand the mouse models that have been created to study PDAC. The different models have in common to mimic the evolution of the human disease, in terms of timing and histopathology. PDAC models differ about targeted genes and promoter used upstream of the CRE-recombinase (Guerra and Barbacid, 2013). The most widely used model (KPC model) is based on the concomitant expression of the two main driver mutations, K-Ras^{G12D} and p53^{R172H} under the control of a Pdx1-CRE driver (Hingorani et al., 2005; Morton et al., 2010). This model reflects the human disease as mutation of TP53 highly correlates with distant lymph node metastasis in human samples based, whereas metastasis-free lymph nodes had weaker p53 staining (Morton et al., 2010). TP53 status also correlates with ability to metastasise and mutated TP53 drives more aggressive cancer compared to mice harbouring the null allele (Lang et al., 2004; Olive et al., 2004). The KPC mouse model develops PanIN and PDAC and is highly metastatic with a median survival of 5 months (Hingorani et al., 2005).

For this project, we aimed to look at early pancreatic lesions so we used a slower version of this model by using Pdx1-CRE::K-Ras^{G12D} mice (KC model). These mice form fully penetrant PanIN lesions, developing into a long latency PDAC that will lead to the sacrifice of the mouse within 12-16 months (Hingorani et al., 2003). This mouse model was used to look at the effect of Fascin overexpression during pancreatic cancer progression. Fascin is one of the most well known actin binding proteins, involved in actin filament bundling and predominantly localised in filopodia, In mammals, three isoforms

have been described with different expression profiles. Unlike Fascin 2 and 3 that localise in the retina and testis respectively, Fascin 1 is ubiquitously expressed in a wide variety of tissues and will be referred to as Fascin throughout this chapter. Fascin is a globular protein formed by four β-trefoil subdomains (F1-4), organised in 2 main lobes (Lobe 1 = F1-F2 and Lobe 2 = F3-F4) (Sedeh et al., 2010). Its actin binding function comes from 2 actin-binding sites (Kabsch et al., 1990) that have been biochemically characterised using alanine-scanning mutagenesis. ABS1 extend between the N and C-terminus of the protein (F1 and F4) whereas ABS2 has been localised opposite to ABS1 (F1 and F2) (Jansen et al., 2011; Ono et al., 1997; Yang et al., 2013). Fascin regulation is based on the activity of Protein Kinase C (PKC) that specifically phosphorylates Ser39. This residue belongs to the ABS1 and the current dogma suggests that Ser39 phosphorylation impedes filament binding and therefore inhibits Fascin activity (Ono et al., 1997). Independently of its function as an actin-binding protein, Fascin also binds to microtubules (MT) and regulates MT dynamics under specific conditions (nocodazole washout) (Villari et al., 2015). *In vitro* and *in cellulo* experiments suggest a MT-binding site within the ABS2 and regulated by phosphorylation of a Ser274 on F2.

Disruption of the Fascin gene is viable and mice only show a slight abnormality in brain development and angiogenesis, which is not fatal. Moreover, the mendelian ratio at birth is respected, although early lethality was frequently observed in homozygote mice within the 48h post birth (Ma et al., 2013b; Yamakita et al., 2009). Moreover, Fascin-knockout MEFs have reduced filopodia number and are shorter-lived compared to wild-type cells (Yamakita et al., 2009). Previously, we discussed about the role of filopodia during invasion and migration (Jacquemet et al., 2015), so Fascin is a good candidate to look at during cell migration and invasion. During melanoblast migration, Tyr-CRE::fscn$^{-/-}$ mice showed a defect in coat pigmentation, characterised by a white belly phenotype and pale paws and tails (Ma et al., 2013a). This was a direct consequence of slower melanoblast migration and a defect in pseudopod formation during embryogenesis. Also, Fascin-null melanoma cells are delayed in their cell cycle (G1 blockage) (Ma et al., 2013a). Finally, a large amount of literature suggests Fascin as a pro-tumorigenic factor in breast cancer

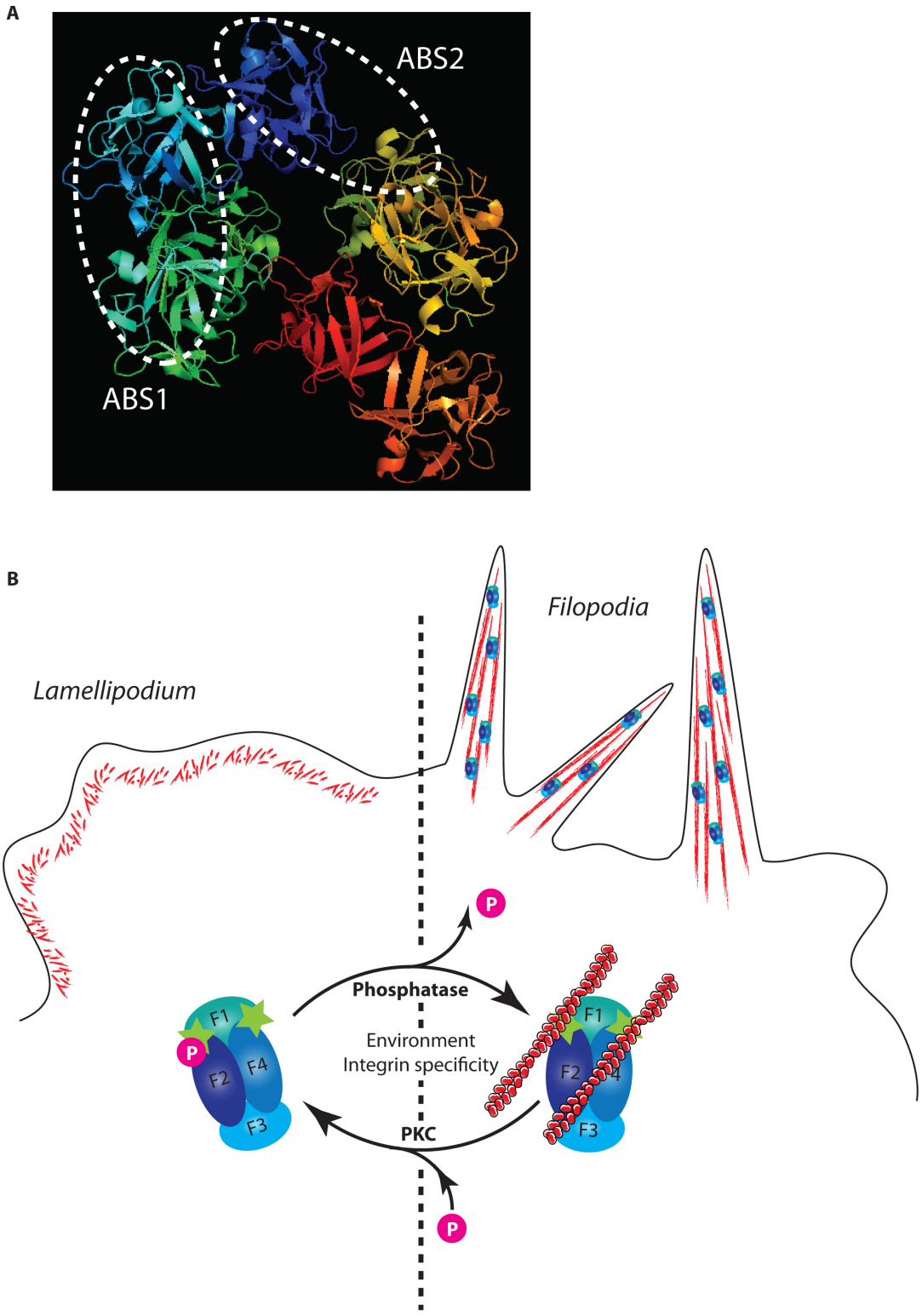

Figure 8-1: Introduction to Fascin, an actin-bundling protein
A – PyMol representation of human Fascin structure (PDB 3P53) (Jansen et al., 2011). Actin-Binding site 1 and 2 (ABS1 and ABS2) are highlighted.

B – Schematic representation of Fascin regulation. Fascin is composed of 4 domains (F1-4) organised in a globular shape. F-actin binding is mediated via at least 2 actin-binding sites (green stars) located between F1-F2 and F1-F4. Fascin forms 7nm-spaced actin bundles and organises filopodia formation. Under specific integrin activation/environmental cues, Protein Kinase C (PKC) phosphorylates Ser39 within the ABS1 and abrogates actin binding. Phosphatase(s) involved in the activation of the protein are unknown.

(Barnawi et al., 2016; Xing et al., 2011) and pancreatic cancer (Li et al., 2014). Using a KPC mouse model, Li and co-workers made a major step forward to understand the involvement of Fascin during PDAC evolution. Specific depletion of Fascin in acinar cells significantly improves survival, reduces tumour burden and strongly inhibits both local and distant metastasis. Finally, ChIP experiments, Western blot and RNA expression data showed a Slug-dependent regulation of Fascin.

However, loss of Fascin does not affect PanIN formation in a KC model. Both wild-type and Fascin-KO mice developed PanIN1 at 4 months (Li et al., 2014). We decided to specifically address the effect of Fascin overexpression on early lesion formation using a KC model and forcing its expression. Indeed, Fascin expression has been shown to correlate with survival and can be considered as a prognostic marker (Li et al., 2014). Based on these data, our main hypothesis here is that forcing Fascin expression should increase tumour burden at early timepoints.

8.2 Results

8.2.1 Fascin overexpression does not affect pancreatic functions

ROSA26-LSL-Fascin1 mouse was obtained from Douglas Strathdee's group and bred with our KC model (Pdx1-CRE::K-Ras^{G12D}). Pdx1 expression arises from E8.5 in pancreatic pluripotent cells and results in the specific expression of the CRE-recombinase in these cells, allowing genetic recombination of the different transgenes. Other cell types or tissues don't undergo any recombination event, maintaining the Lox-STOP-Lox sequence in front of the Fascin transgene. For clarity, genotypes will be referred as K-Ras WT or Het and Fascin Pos or Neg, always mentioning the K-Ras status first. Mice included in each cohort were Pdx1-Cre positive. Our initial experimental design was based on a small cohort (3-9 mice) of each genotype that were aged and sacrificed at 6 weeks, 15 weeks or 6 months. Physiological parameters such as body and pancreas weight, pancreatic profile and number of metastases was recorded. In addition, histological analyses were performed for different proliferation markers, tissue architecture based on Haematoxylin/Eosin staining, and immune cell infiltration.

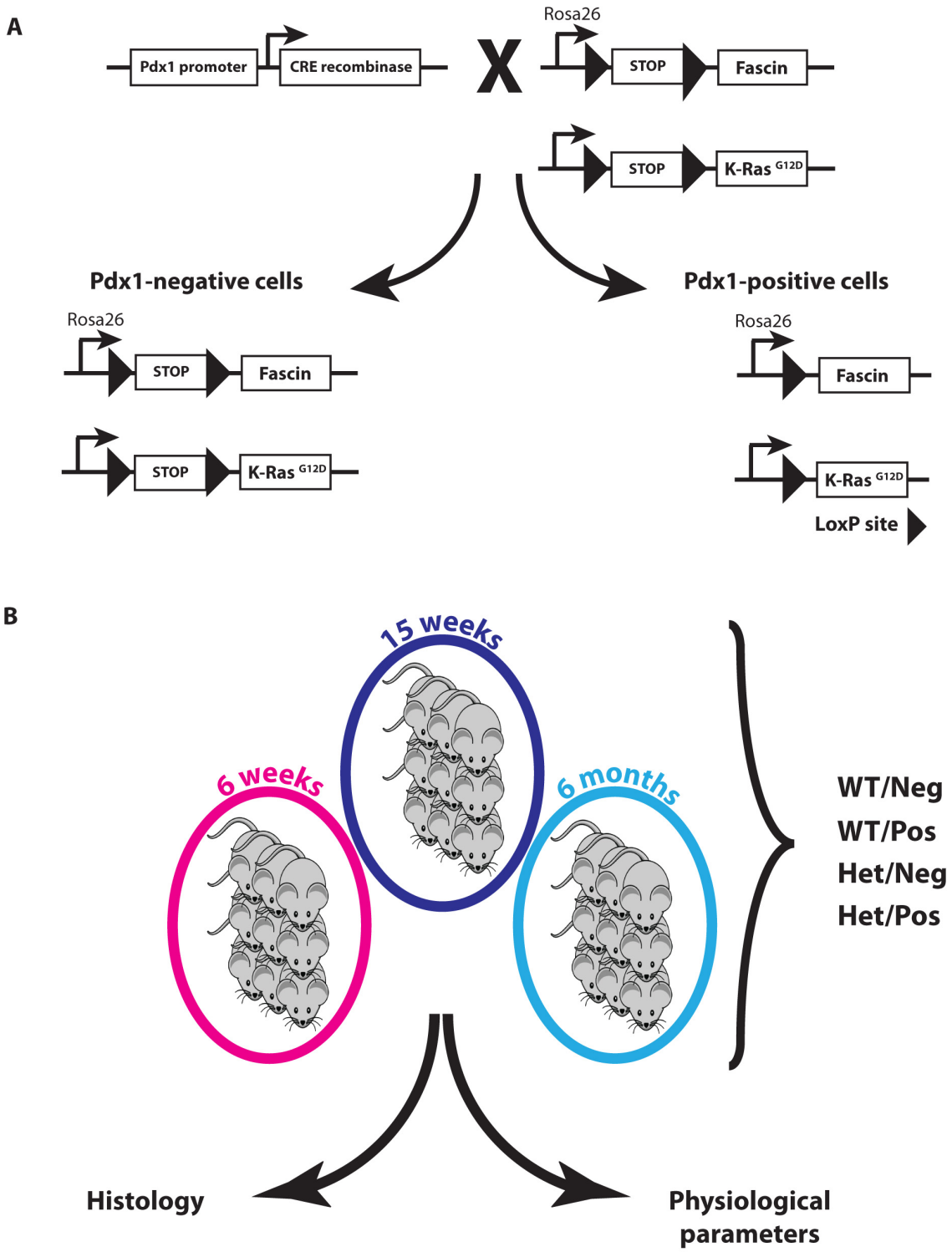

Figure 8-2: KC model used for this study and experimental design
A – Schematic of the gene targeting strategy to study Fascin overexpression in a pancreatic KC model. Cre-recombinase is placed under the pancreatic-specific Pdx1 promoter, leading to the specific excision of the Lox-STOP-Lox sequence from the Rosa-Fascin-Tg and K-Ras^{G12D} knock-in mouse.

B – Representation of the experimental design, with mice cohorts and analyses performed. All mice used were Cre-positive. Genotypes are represented with the K-Ras status first, followed by the Fascin status.

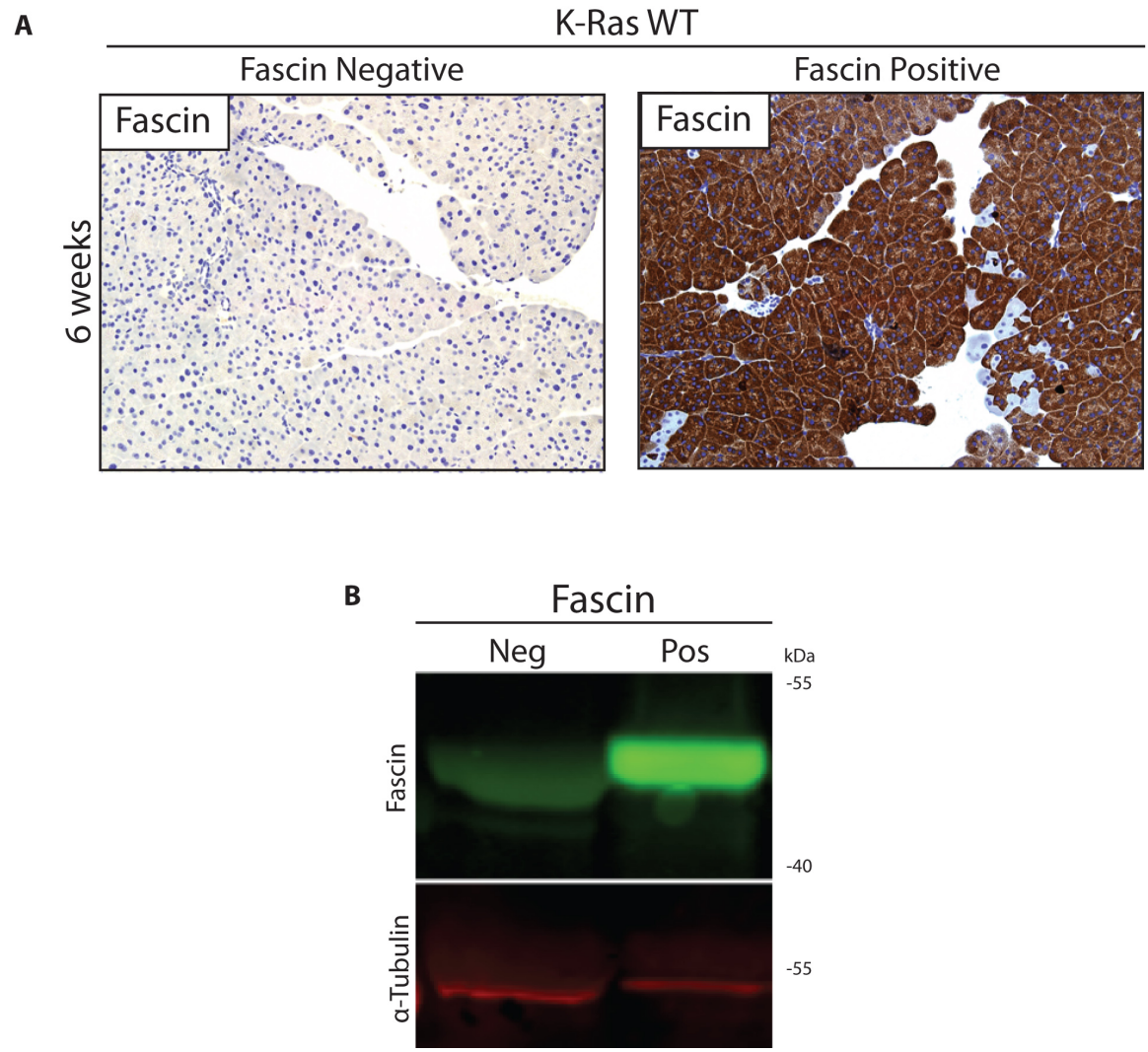

Figure 8-3: Validation of the Fascin KC model
A - Immunohistochemistry analysis of Fascin expression in a WT/Neg (left) and WT/Pos (right) pancreas at 6 weeks of age. Fascin is brown and nuclei are blue.

B – Western Blot analysis from a tissue lysate of a WT/Neg and WT/Pos pancreas at 6 weeks of age. Membrane was blotted against Fascin (green) and α-Tubulin (red). Molecular weights are displayed on the side.

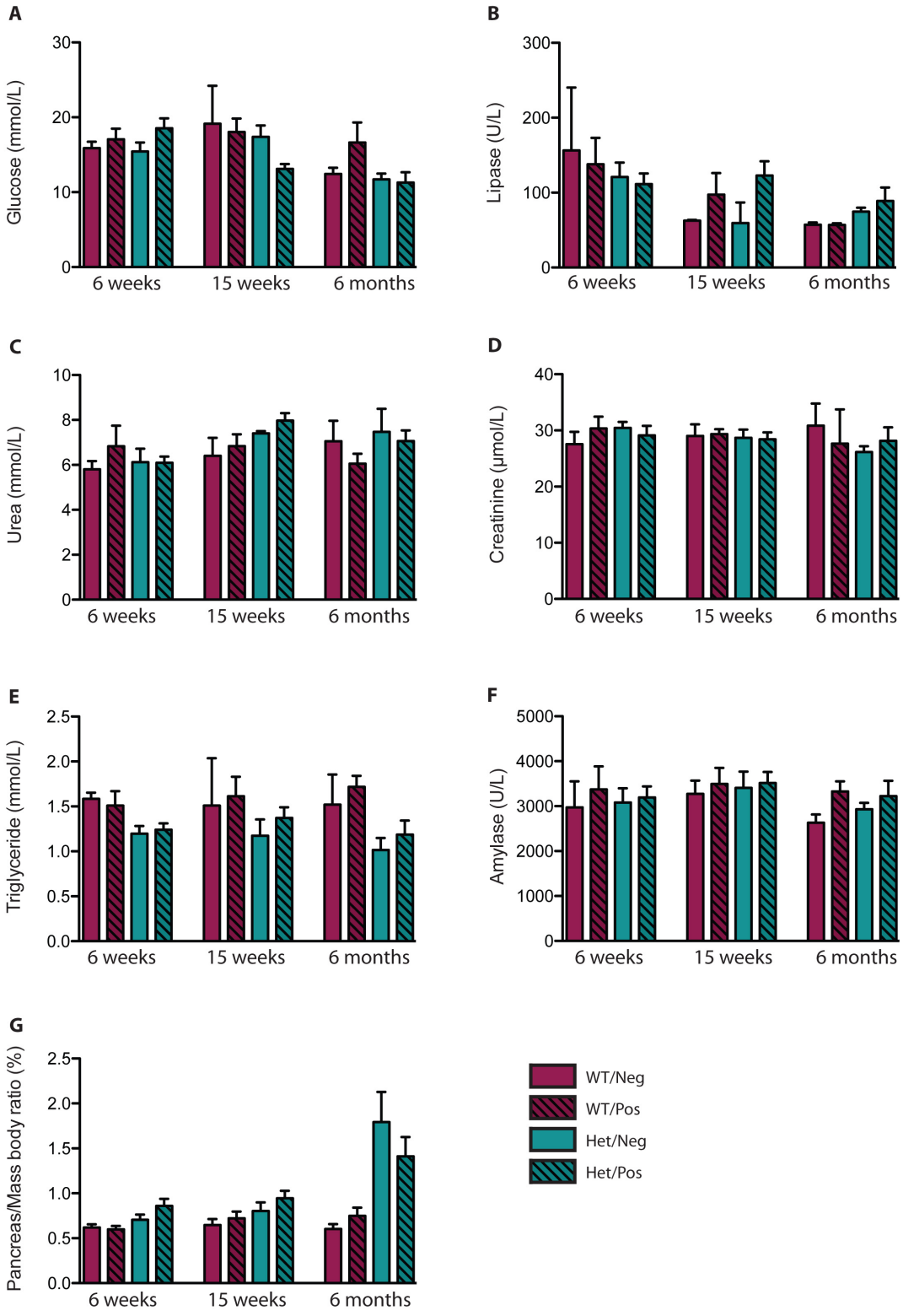

Figure 8-4: Physiological parameters from the 4 cohorts at different time points
A-F – Results from the pancreatic profile obtained after terminal bleeding. Serum was collected and sent to the veterinary school for analysis.

G – Pancreas versus body mass ratio obtained by reporting the weight of the pancreas at the time of sacrifice to the total animal weight.

***6 weeks**: 9 mice/cohort – **15 weeks**: WT/Neg = 3 mice, WT/Pos = 9 mice, Het/Neg = 3 mice, Het/Pos = 6 mice – **6 months**: 6 mice/cohort*

Error bars represent S.E.M.

Fascin expression of WT/Neg and WT/Pos pancreata of 6 weeks old mice were analysed by immunohistochemistry (IHC) and Western blot. In both cases, we were able to confirm a strong increase of Fascin expression in the pancreas. IHC revealed that expression of the CRE was mosaic, as already described for the same model. WT/Neg mice did not show any staining and this observation is in line with the reported transient expression of Fascin during development in epithelial tissues (Zhang et al., 2008b).

The pancreatic profile of each mouse was obtained from a blood sample at the time of sacrifice and pancreatic enzymes concentration was analysed. Differences observed between cohorts were statistically non-significant, probably reflecting the variability of the population. Therefore, Fascin overexpression in a wild-type background or a KC model did not affect pancreatic functions. Moreover, all sacrificed mice were healthy at each timepoint.

The pancreas/body weight ratio is a reporter of PDAC formation. Tumours are characterised by a dense necrotic core characterised by a lot of fibrosis, which together are heavier than the normal tissue. Mice bearing mutated K-Ras showed a 3-fold increase in this ratio, but no differences were observed when Fascin was overexpressed. This suggests that K-Ras drives initial lesion formation but Fascin does not affect it.

8.2.2 Fascin overexpression increases pre-malignant lesions at an early time point

Initial observations were made using H&E staining, in order to analyse the tissue architecture on a small cohort of mice. This included any types of lesion and reflects the tumour burden between conditions, without classification of the PanIN sub-classes. This value corresponds to the percentage of lesion area over the total tissue surface. Histology analysis of 6-week old pancreata did not show any lesions in WT/Neg or WT/Pos mice. However, Het/Pos mice show extensive lesions compared to the Het/Neg counterparts and this is reflected by a 10-fold increase of the tumour burden ratio. The lesions are still small and minor compared to the total pancreas but may be the initial seeds driving PDAC formation. In this situation, Fascin and mutated K-Ras have a synergic effect as Fascin alone (i.e. in a K-Ras ^{WT} background) does not affect lesion initiation. When we extended our analysis to the 15-week and 6-month cohorts, the difference between these two genotypes was lost and suggests that the effect of K-Ras might over take the effect mediated by Fascin. However, the difference between K-Ras ^{WT} and K-Ras ^{Het} mice was more and more pronounced at later time points. Few lesions or only few of them were observed in K-Ras ^{WT} whether Fascin was overexpressed or not. This reinforced all the

published data focusing on the central role of mutated K-Ras during PDAC development. We also hypothesise that Fascin is not important for lesion initiation at later timepoint as mutated K-Ras alone is enough to increase the area affected by pancreatic lesions.

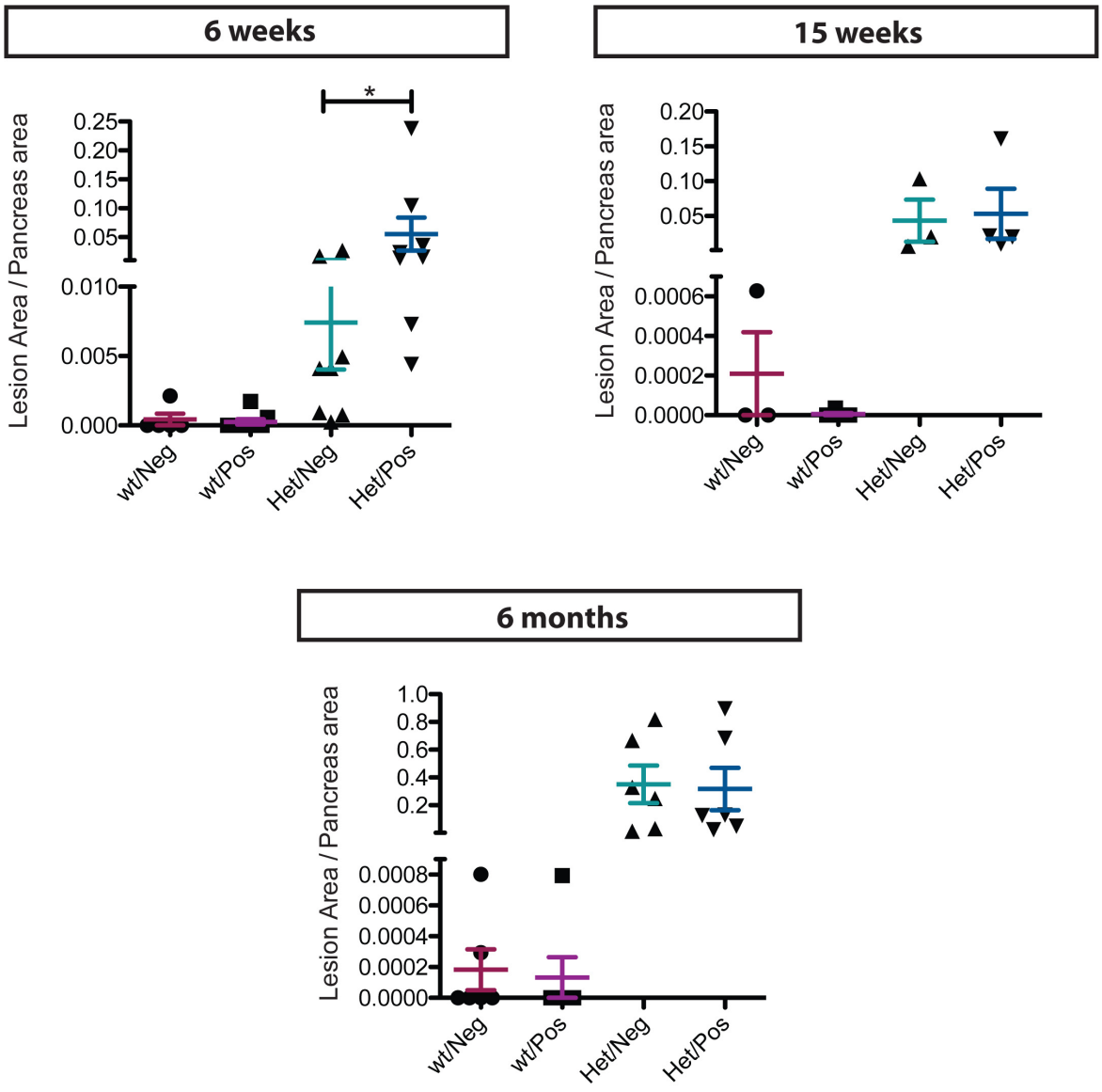

Figure 8-5: Fascin expression increases pancreatic tumour burden at an early time point
Scatter plot representing the area of abnormal pancreatic structures (ADM, PanIN, PDAC) relative to the area of the section at each time point. Medium and S.E.M are represented. Mann Whitney test was applied. * $p<0.05$.

***6 weeks**: WT/Neg = 5 mice, WT/Pos = 9 mice, Het/Neg = 8 mice, Het/Pos = 8 mice*
***15 weeks**: WT/Neg = 3 mice, WT/Pos = 7 mice, Het/Neg = 3 mice, Het/Pos = 4 mice*
***6 months**: 6 mice/cohort*

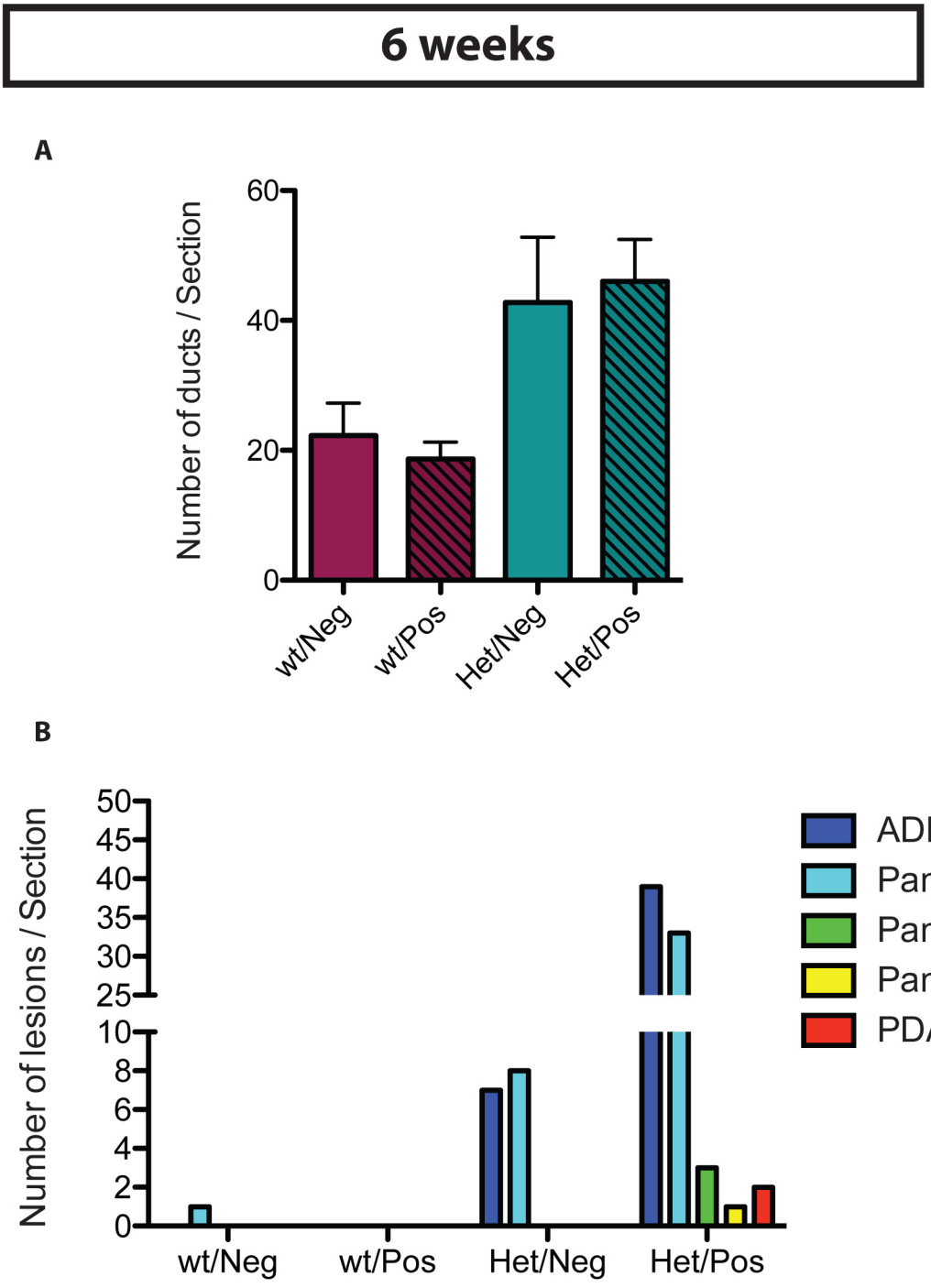

Figure 8-6: Classification of the different lesions observed in the 6-week cohort
A – Manual counting of the number of ducts observed for each pancreas section. Bar plot represent quantification of WT/Neg = 4 mice, WT/Pos = 9 mice, Het/Neg = 5 mice, Het/Pos = 8 mice. Error bars represent S.E.M.

B – Ranking of the pancreatic lesion according to their microscopic features

In order to characterise this phenotype, pancreata were precisely analysed and each lesion/duct ranked according to their type, starting from ADM to PDAC. This refinement of the previous quantification was restricted to the 6-weeks cohort as no differences were observed at later time points. Although the duct numbers were similar between each comparative cohort *(WT/Neg vs WT/Pos = 20 ducts/section and Het/Neg vs Het/Pos = 45 ducts/section)*, lesion types were different. Unlike Het/Neg mice that only show some ADM and PanIN1, Het/Pos cohort develops a wide range of lesions and notably, 2 pancreata out of 8 had a small PDAC. Also, the proportion of ADM and PanIN1 was 5-fold higher.

For further characterisation, 2h before sacrifice, mice were injected with BrdU, a specific marker of cells during S-phase. In combination IHC against Ki-67, another proliferative marker that accumulates in all actively cycling cells was performed, excluding resting cells (G0). In addition, tissues were also stained by IHC against a key regulator of apoptosis, cleaved Caspase-3. This staining is specific to the fragmented protein and not the full length. This truncation occurs at Asp175 by activation of upstream Caspases (Caspase 8 and 9) and activates downstream apoptotic pathways. In order to standardise our quantification method, seven random fields were taken across each pancreas and positive cells were manually counted according to their localisation (duct or acini). We did not observe any significant difference in proliferation of ductal cells, although there may be a trend towards more proliferation. No differences in proliferation of acinar cells or in apoptosis (acini and duct) were significant at 6 weeks. We did not observe any difference in proliferation and apoptosis at 15 weeks and 6 months by BrdU/Ki-67 and cleaved Caspase-3 staining. A larger sample size would be required to confirm an effect of Fascin overexpression on ductal cell proliferation.

Overall we can conclude that Fascin overexpression accelerates development of early pancreatic ductal lesions. Higher grade lesions (PanIN2 and PanIN3) arise more frequently and may also end in PDAC formation. However, at 6 weeks of age, PDAC is too small to be diagnostic using apparent symptoms. Also, it is worth highlighting that Fascin overexpression alone, with no initial “hit” (K-Ras mutation) is not enough to initiate the aforementioned effects.

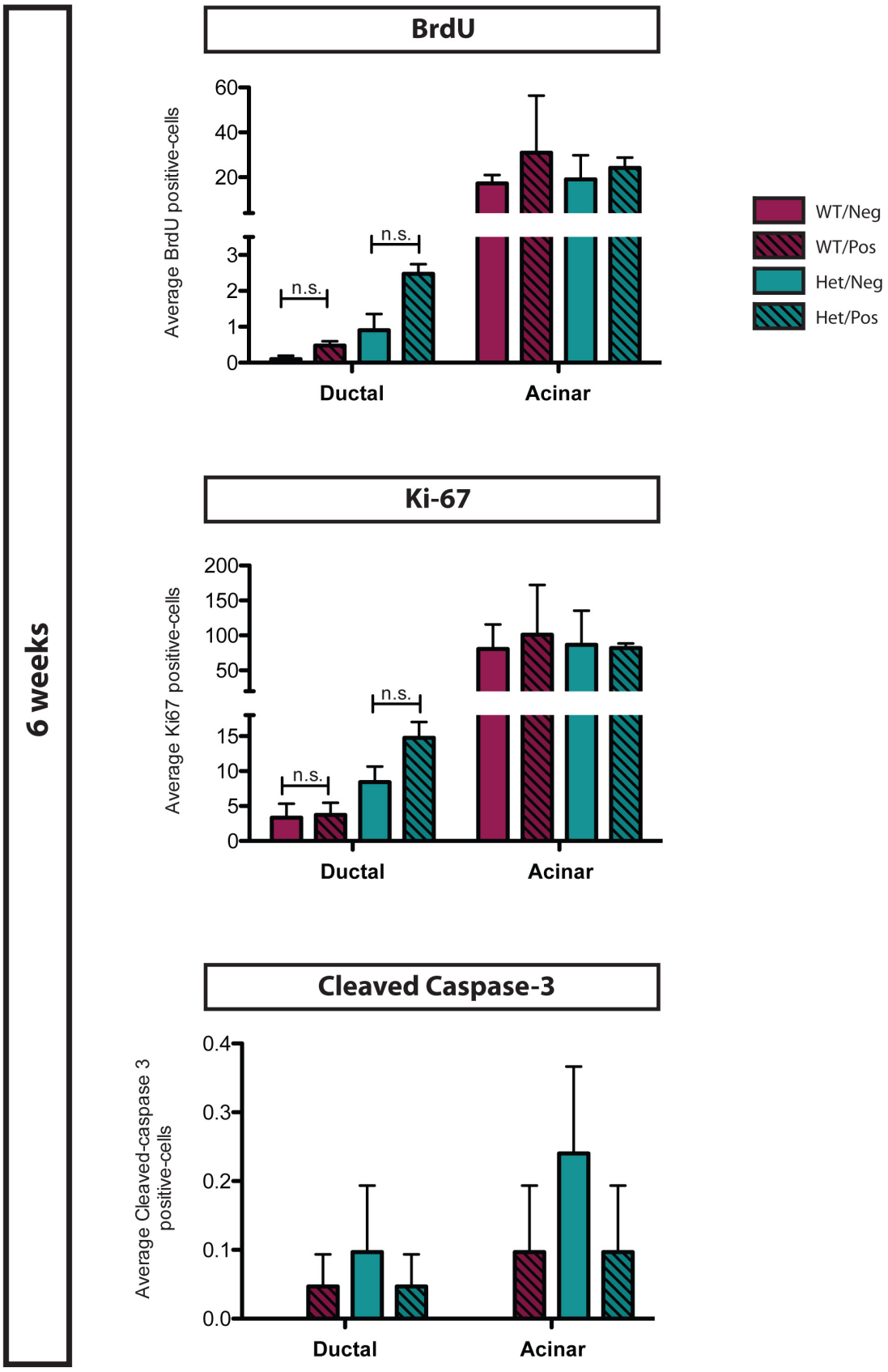

Figure 8-7: Histology analysis of 6-week old pancreata
BrdU, Ki-67 and Cleaved Caspase-3 stained were performed by IHC. Positive cells were counted and attributed to an acinar or ductal localisation. Bar plots represent an average number of positive cells across seven random fields. Error bars represent S.E.M. Mann Whitney test was applied. n.s. $p>0.05$.

3 pancreas/genotype were quantified.

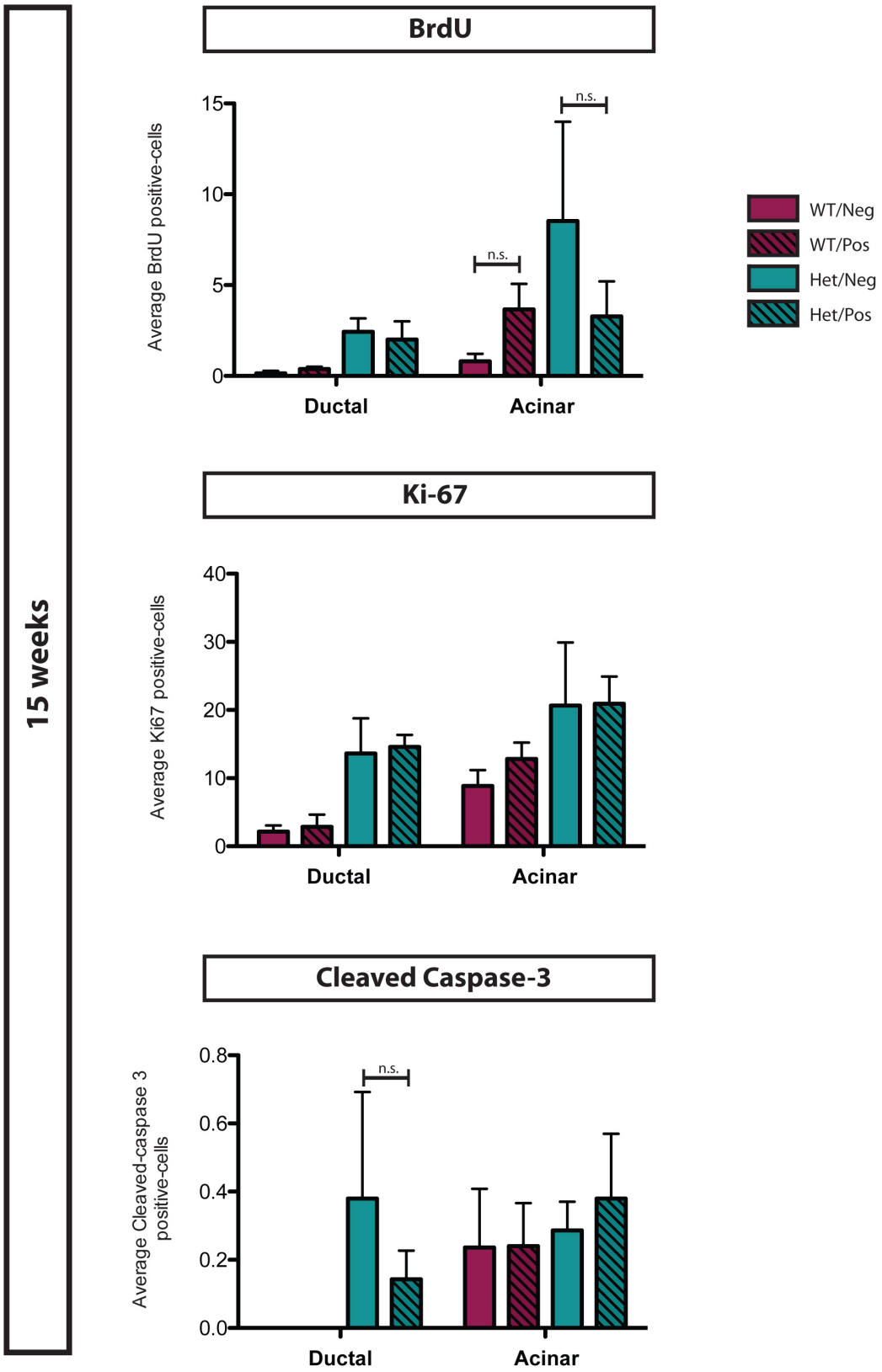

Figure 8-8: Histology analysis of 15-week old pancreata
BrdU, Ki-67 and Cleaved Caspase-3 stained were performed by IHC. Positive cells were counted and attributed to an acinar or ductal localisation. Bar plots represent an average number of positive cells across seven random fields Error bars represent S.E.M. Mann Whitney test was applied. n.s. $p>0.05$

3 pancreas/genotype were quantified.

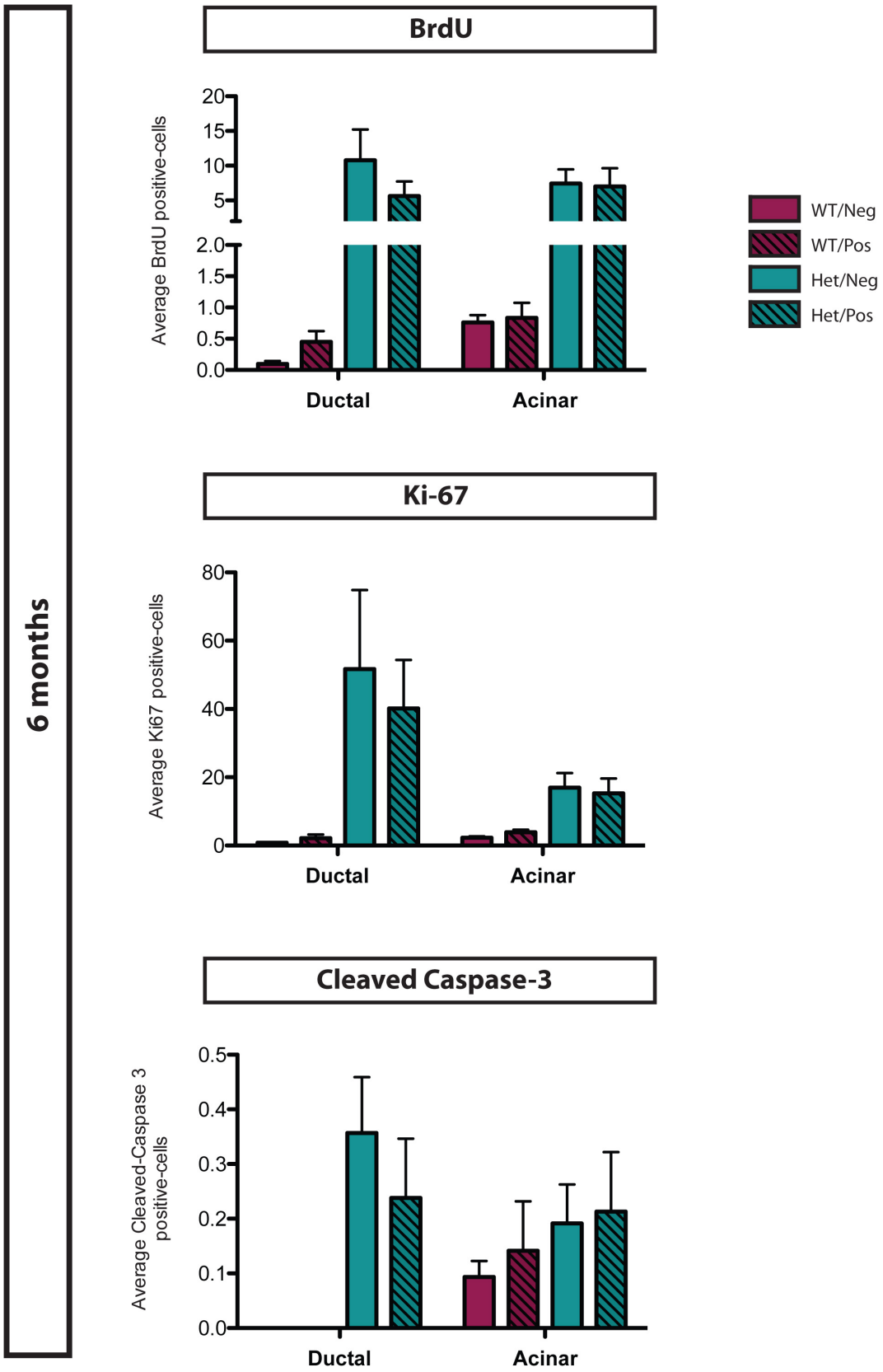

gure 8-9: Histology analysis of 6-month old pancreata
BrdU, Ki-67 and Cleaved Caspase-3 stained were performed by IHC. Positive cells were counted and attributed to an acinar or ductal localisation. Bar plots represent an average number of positive cells across seven random fields. Error bars represent S.E.M. Mann Whitney test was applied.

6 pancreas/genotype were quantified.

8.3 Discussion, Future directions and Conclusion

The data presented here suggest that Fascin is not crucial for early lesion formation but might synergise the effects mediated by K-Ras in a slow pancreatic cancer mouse model. Following the observation that Het/Pos mice were developing earlier lesions, we started a small cohort to look at 4 weeks old pups. This cohort is still on-going but the smaller size of the mice makes the terminal bleeding for pancreatic profile more difficult. Also, because blood sample analyses were normal at 6 weeks, we decided to not perform pancreatic profile analysis at 4 weeks. From the macroscopic analysis of the 4-week old cohort, Het/Pos mice have an enlarged pancreas compared to Het/Neg mice (Pancreas/body mass ratio = 0.9 ± 0.05 versus 0.55 ± 0.06 – S.E.M). Interestingly, out of 8 mice, one developed a small PDAC and one had a hyperplasic pancreas. However, none of these features were observed in the 4 control mice that we analysed.

On its own, Fascin cannot drive lesion formation and only amplifies the effect of an initial hit. In our case, we looked at K-Ras but the phenotype related to K-Ras is too strong and may quickly overtake the effect of Fascin. To overcome this, we could switch to a pancreatitis model. Indeed, chronic inflammation also increases the risk of developing PDAC (Lowenfels et al., 1993). In an *in vivo* model, this protocol includes daily injection of Caerulein from 4 weeks old for 2 weeks. Dosage varies according to the different study but ranges from 50-400ng/g. Caerulein is a cholecystokinin (CCK) analogue that stimulates secretion of pancreatic enzymes. However, to understand the Caerulein-induced inflammation, it is important to look at the mechanism of action of CCK. CCK binds to a high and low affinity population of receptor. When CCK concentration is within the physiological range, it binds to high affinity receptors and stimulates exocytosis of granules containing pancreatic enzymes. Whenever the concentration rises, high-affinity receptors get saturated and CCK binds to low-affinity receptors, which inhibits enzyme secretion as they get trapped within the acinar cells (Saluja et al., 1985). Despite this storage as precursor enzymes, it is unknown how pro-peptides get activated and what is the mechanisms linking accumulation of inactive zymogens and pancreatitis. However, this acute response seeds the soil for an initial tumour burden, making it possible to study the role of Fascin during PanIN initiation. Alternative PDAC models could also been investigated. A model not requiring K-Ras has been developed by Wagner et al (Wagner et al., 2001) and is based on the overexpression of TGF-α under the elastase promoter and the deletion of TP53. Other models using a different promoter for the Cre recombinase expression have also different latency and could be useful for our purposes (Guerra and Barbacid, 2013).

We saw a trend towards more proliferation at 6 weeks in the Het/Pos cohort but this quantification was only done on a pilot cohort. Since this time, more pancreata have been sampled and we will complete our Ki-67 and BrdU counting. This effect on proliferation is however interesting as Li *et al* showed a direct relationship between the transcription factor Slug and Fascin (Li et al., 2014). Slug is a major regulator EMT regulator and has been linked to loss of cell-cell contacts and proliferation, although the exact effects seem to be cancer-type dependent (Emadi Baygi et al., 2010; Liu et al., 2010). The hypothesis here would be that Fascin might act on Slug expression using a feedback loop and affect downstream proliferation of ductal and acinar cells. IHC staining and western blot against Slug will be performed in our different cohorts at 6 weeks could suggest a potential loop of regulation.

Finally, 6-week old pancreata were stained for immune cell infiltration. The GPI-anchored protein Ly-6G and the glycoprotein F4/80 were used as specific markers for neutrophils and macrophages respectively. Het/Pos pancreata showed increased infiltration of neutrophils and macrophages (data not shown) but this has not been properly quantified yet. Because of the irregular and diffuse staining and in order to be more transparent and precise, we are planning to use the HALO software that includes analysis of pixel intensity and shape in a semi-automatic manner. This should help us to determine whether mice develop an inflammation response during PanIN progression and address whether Fascin overexpressing induces any recruitment of immune cells following PanIN development.

In conclusion, following the work of a previous PhD student looking at the role of Fascin during PDAC develop at late stage, we developed a project to investigate the effects of Fascin during early pancreatic development. We found that Fascin overexpressing mice had a higher tumour background, as early as 6 weeks of age and this correlates with a slight but non-significant increase in proliferation, although this might be linked to the size of the population in this cohort. Preliminary data even suggest an effect of Fascin overexpression at 4 weeks. We are hoping in the future to look deeper into the mechanisms driving this phenotype. This project is part of a bigger project co-lead by Nikki Paul, a post-doc in the lab. Together, we are planning to investigate the global modification of the proteome by laser dissection and mass spectrometry between our different cohorts. These data should be useful to understand the biology early development of lesions and potentially use Fascin as an early prognostic marker in patient biopsies.

9 References

Abella, J.V., C. Galloni, J. Pernier, D.J. Barry, S. Kjaer, M.F. Carlier, and M. Way. 2016. Isoform diversity in the Arp2/3 complex determines actin filament dynamics. *Nat Cell Biol*. 18:76-86.

Abercrombie, M., J.E. Heaysman, and S.M. Pegrum. 1970. The locomotion of fibroblasts in culture. 3. Movements of particles on the dorsal surface of the leading lamella. *Exp Cell Res*. 62:389-398.

Abu Taha, A., M. Taha, J. Seebach, and H.J. Schnittler. 2014. ARP2/3-mediated junction-associated lamellipodia control VE-cadherin-based cell junction dynamics and maintain monolayer integrity. *Mol Biol Cell*. 25:245-256.

Adameyko, I., F. Lallemend, J.B. Aquino, J.A. Pereira, P. Topilko, T. Muller, N. Fritz, A. Beljajeva, M. Mochii, I. Liste, D. Usoskin, U. Suter, C. Birchmeier, and P. Ernfors. 2009. Schwann cell precursors from nerve innervation are a cellular origin of melanocytes in skin. *Cell*. 139:366-379.

Akhmanova, A., and M.O. Steinmetz. 2015. Control of microtubule organization and dynamics: two ends in the limelight. *Nat Rev Mol Cell Biol*. 16:711-726.

Alanko, J., A. Mai, G. Jacquemet, K. Schauer, R. Kaukonen, M. Saari, B. Goud, and J. Ivaska. 2015. Integrin endosomal signalling suppresses anoikis. *Nat Cell Biol*. 17:1412-1421.

Almoguera, C., D. Shibata, K. Forrester, J. Martin, N. Arnheim, and M. Perucho. 1988. Most human carcinomas of the exocrine pancreas contain mutant c-K-ras genes. *Cell*. 53:549-554.

Amann, K.J., and T.D. Pollard. 2001. Direct real-time observation of actin filament branching mediated by Arp2/3 complex using total internal reflection fluorescence microscopy. *Proc Natl Acad Sci U S A*. 98:15009-15013.

Aranda, V., T. Haire, M.E. Nolan, J.P. Calarco, A.Z. Rosenberg, J.P. Fawcett, T. Pawson, and S.K. Muthuswamy. 2006. Par6-aPKC uncouples ErbB2 induced disruption of polarized epithelial organization from proliferation control. *Nat Cell Biol*. 8:1235-1245.

Ardern, H., E. Sandilands, L.M. Machesky, P. Timpson, M.C. Frame, and V.G. Brunton. 2006. Src-dependent phosphorylation of Scar1 promotes its association with the Arp2/3 complex. *Cell Motil Cytoskeleton*. 63:6-13.

Arias-Salgado, E.G., S. Lizano, S. Sarkar, J.S. Brugge, M.H. Ginsberg, and S.J. Shattil. 2003. Src kinase activation by direct interaction with the integrin beta cytoplasmic domain. *Proc Natl Acad Sci U S A*. 100:13298-13302.

Babuta, M., M.S. Mansuri, S. Bhattacharya, and A. Bhattacharya. 2015. The Entamoeba histolytica, Arp2/3 Complex Is Recruited to Phagocytic Cups through an Atypical Kinase EhAK1. *PLoS Pathog*. 11:e1005310.

Bailey, P., D.K. Chang, K. Nones, A.L. Johns, A.M. Patch, M.C. Gingras, D.K. Miller, A.N. Christ, T.J. Bruxner, M.C. Quinn, C. Nourse, L.C. Murtaugh, I. Harliwong, S. Idrisoglu, S. Manning, E. Nourbakhsh, S. Wani, L. Fink, O. Holmes, V. Chin, M.J. Anderson, S. Kazakoff, C. Leonard, F. Newell, N. Waddell, S. Wood, Q. Xu, P.J. Wilson, N. Cloonan, K.S. Kassahn, D. Taylor, K. Quek, A. Robertson, L. Pantano, L. Mincarelli, L.N. Sanchez, L. Evers, J. Wu, M. Pinese, M.J. Cowley, M.D. Jones, E.K. Colvin, A.M. Nagrial, E.S. Humphrey, L.A. Chantrill, A. Mawson, J. Humphris, A. Chou, M. Pajic, C.J. Scarlett, A.V. Pinho, M. Giry-Laterriere, I. Rooman, J.S. Samra, J.G. Kench, J.A. Lovell, N.D. Merrett, C.W. Toon, K. Epari, N.Q. Nguyen, A. Barbour, N. Zeps, K. Moran-Jones, N.B. Jamieson, J.S. Graham, F. Duthie, K. Oien, J. Hair, R. Grutzmann, A. Maitra, C.A. Iacobuzio-Donahue, C.L. Wolfgang, R.A. Morgan, R.T. Lawlor, V. Corbo, C. Bassi, B. Rusev, P. Capelli, R. Salvia, G. Tortora, D. Mukhopadhyay, G.M. Petersen, I. Australian Pancreatic Cancer Genome, D.M. Munzy, W.E. Fisher, S.A. Karim, J.R. Eshleman, R.H. Hruban, C. Pilarsky, J.P. Morton, O.J. Sansom, A. Scarpa, E.A. Musgrove, U.M. Bailey, O. Hofmann, R.L. Sutherland, D.A. Wheeler, A.J. Gill, R.A. Gibbs, J.V. Pearson, et al. 2016. Genomic analyses identify molecular subtypes of pancreatic cancer. *Nature*. 531:47-52.

Banaszynski, L.A., C.W. Liu, and T.J. Wandless. 2005. Characterization of the FKBP.rapamycin.FRB ternary complex. *J Am Chem Soc*. 127:4715-4721.

Banno, A., B.T. Goult, H. Lee, N. Bate, D.R. Critchley, and M.H. Ginsberg. 2012. Subcellular localization of talin is regulated by inter-domain interactions. *J Biol Chem*. 287:13799-13812.

Barber, M.A., A. Hendrickx, M. Beullens, H. Ceulemans, D. Oxley, S. Thelen, M. Thelen, M. Bollen, and H.C. Welch. 2012. The guanine-nucleotide-exchange factor P-Rex1 is activated by protein phosphatase 1alpha. *Biochem J*. 443:173-183.

Barnawi, R., S. Al-Khaldi, G. Majed Sleiman, A. Sarkar, A. Al-Dhfyan, F. Al-Mohanna, H. Ghebeh, and M. Al-Alwan. 2016. Fascin Is Critical for the Maintenance of Breast Cancer Stem Cell Pool Predominantly via the Activation of the Notch Self-Renewal Pathway. *Stem Cells*. 34:2799-2813.

Bartel, P., C.T. Chien, R. Sternglanz, and S. Fields. 1993. Elimination of false positives that arise in using the two-hybrid system. *Biotechniques*. 14:920-924.

Bastos, R.N., X. Penate, M. Bates, D. Hammond, and F.A. Barr. 2012. CYK4 inhibits Rac1-dependent PAK1 and ARHGEF7 effector pathways during cytokinesis. *J Cell Biol*. 198:865-880.

Bianco, A., M. Poukkula, A. Cliffe, J. Mathieu, C.M. Luque, T.A. Fulga, and P. Rorth. 2007. Two distinct modes of guidance signalling during collective migration of border cells. *Nature*. 448:362-365.

Biyasheva, A., T. Svitkina, P. Kunda, B. Baum, and G. Borisy. 2004. Cascade pathway of filopodia formation downstream of SCAR. *J Cell Sci*. 117:837-848.

Blanchoin, L., T.D. Pollard, and S.E. Hitchcock-DeGregori. 2001. Inhibition of the Arp2/3 complex-nucleated actin polymerization and branch formation by tropomyosin. *Curr Biol*. 11:1300-1304.

Blaser, H., S. Eisenbeiss, M. Neumann, M. Reichman-Fried, B. Thisse, C. Thisse, and E. Raz. 2005. Transition from non-motile behaviour to directed migration during early PGC development in zebrafish. *J Cell Sci*. 118:4027-4038.

Blaser, H., M. Reichman-Fried, I. Castanon, K. Dumstrei, F.L. Marlow, K. Kawakami, L. Solnica-Krezel, C.P. Heisenberg, and E. Raz. 2006. Migration of zebrafish primordial germ cells: a role for myosin contraction and cytoplasmic flow. *Dev Cell*. 11:613-627.

Bonaccorso, C.M., M. Spatuzza, B. Di Marco, A. Gloria, G. Barrancotto, A. Cupo, S.A. Musumeci, S. D'Antoni, B. Bardoni, and M.V. Catania. 2015. Fragile X mental retardation protein (FMRP) interacting proteins exhibit different expression patterns during development. *Int J Dev Neurosci*. 42:15-23.

Bos, J.L., H. Rehmann, and A. Wittinghofer. 2007. GEFs and GAPs: critical elements in the control of small G proteins. *Cell*. 129:865-877.

Bridgewater, R.E., J.C. Norman, and P.T. Caswell. 2012. Integrin trafficking at a glance. *J Cell Sci*. 125:3695-3701.

Brooks, S.P., M. Coccia, H.R. Tang, N. Kanuga, L.M. Machesky, M. Bailly, M.E. Cheetham, and A.J. Hardcastle. 2010. The Nance-Horan syndrome protein encodes a functional WAVE homology domain (WHD) and is important for co-ordinating actin remodelling and maintaining cell morphology. *Hum Mol Genet*. 19:2421-2432.

Brown, M.C., J.A. Perrotta, and C.E. Turner. 1996. Identification of LIM3 as the principal determinant of paxillin focal adhesion localization and characterization of a novel motif on paxillin directing vinculin and focal adhesion kinase binding. *J Cell Biol*. 135:1109-1123.

Bryant, D.M., A. Datta, A.E. Rodriguez-Fraticelli, J. Peranen, F. Martin-Belmonte, and K.E. Mostov. 2010. A molecular network for de novo generation of the apical surface and lumen. *Nat Cell Biol*. 12:1035-1045.

Bugalhao, J.N., L.J. Mota, and I.S. Franco. 2015. Bacterial nucleators: actin' on actin. *Pathog Dis*. 73:ftv078.

Burbelo, P.D., D. Drechsel, and A. Hall. 1995. A conserved binding motif defines numerous candidate target proteins for both Cdc42 and Rac GTPases. *J Biol Chem*. 270:29071-29074.

Carlier, M.F., D. Pantaloni, and E.D. Korn. 1984. Evidence for an ATP cap at the ends of actin filaments and its regulation of the F-actin steady state. *J Biol Chem*. 259:9983-9986.

Carmona, G., U. Perera, C. Gillett, A. Naba, A.L. Law, V.P. Sharma, J. Wang, J. Wyckoff, M. Balsamo, F. Mosis, M. De Piano, J. Monypenny, N. Woodman, R.E. McConnell, G. Mouneimne, M. Van Hemelrijck, Y. Cao, J. Condeelis, R.O. Hynes, F.B. Gertler, and M. Krause. 2016. Lamellipodin promotes invasive 3D cancer cell migration via regulated interactions with Ena/VASP and SCAR/WAVE. *Oncogene*. 35:5155-5169.

Casanova, J.E., X. Wang, R. Kumar, S.G. Bhartur, J. Navarre, J.E. Woodrum, Y. Altschuler, G.S. Ray, and J.R. Goldenring. 1999. Association of Rab25 and Rab11a with the apical recycling system of polarized Madin-Darby canine kidney cells. *Mol Biol Cell*. 10:47-61.

Case, L.B., and C.M. Waterman. 2015. Integration of actin dynamics and cell adhesion by a three-dimensional, mechanosensitive molecular clutch. *Nat Cell Biol*. 17:955-963.

Cetera, M., G.R. Ramirez-San Juan, P.W. Oakes, L. Lewellyn, M.J. Fairchild, G. Tanentzapf, M.L. Gardel, and S. Horne-Badovinac. 2014. Epithelial rotation promotes the global alignment of contractile actin bundles during Drosophila egg chamber elongation. *Nat Commun*. 5:5511.

Chamberlain, L.H., and M.J. Shipston. 2015. The physiology of protein S-acylation. *Physiol Rev*. 95:341-376.

Chan, A.Y., S.J. Coniglio, Y.Y. Chuang, D. Michaelson, U.G. Knaus, M.R. Philips, and M. Symons. 2005. Roles of the Rac1 and Rac3 GTPases in human tumor cell invasion. *Oncogene*. 24:7821-7829.

Charras, G.T., C.K. Hu, M. Coughlin, and T.J. Mitchison. 2006. Reassembly of contractile actin cortex in cell blebs. *J Cell Biol*. 175:477-490.

Chen, B., K. Brinkmann, Z. Chen, C.W. Pak, Y. Liao, S. Shi, L. Henry, N.V. Grishin, S. Bogdan, and M.K. Rosen. 2014a. The WAVE regulatory complex links diverse receptors to the actin cytoskeleton. *Cell*. 156:195-207.

Chen, C.S., J.L. Alonso, E. Ostuni, G.M. Whitesides, and D.E. Ingber. 2003. Cell shape provides global control of focal adhesion assembly. *Biochem Biophys Res Commun*. 307:355-361.

Chen, H.Y., C.H. Shen, Y.T. Tsai, F.C. Lin, Y.P. Huang, and R.H. Chen. 2004. Brk activates rac1 and promotes cell migration and invasion by phosphorylating paxillin. *Mol Cell Biol*. 24:10558-10572.

Chen, L., G. Liao, R.R. Waclaw, K.A. Burns, D. Linquist, K. Campbell, Y. Zheng, and C.Y. Kuan. 2007. Rac1 controls the formation of midline commissures and the competency of tangential migration in ventral telencephalic neurons. *J Neurosci*. 27:3884-3893.

Chen, P.I., K. Schauer, C. Kong, A.R. Harding, B. Goud, and P.D. Stahl. 2014b. Rab5 isoforms orchestrate a "division of labor" in the endocytic network; Rab5C modulates Rac-mediated cell motility. *PLoS One*. 9:e90384.

Chen, X.J., A.J. Squarr, R. Stephan, B. Chen, T.E. Higgins, D.J. Barry, M.C. Martin, M.K. Rosen, S. Bogdan, and M. Way. 2014c. Ena/VASP proteins cooperate with the WAVE complex to regulate the actin cytoskeleton. *Dev Cell*. 30:569-584.

Chen, Z., D. Borek, S.B. Padrick, T.S. Gomez, Z. Metlagel, A.M. Ismail, J. Umetani, D.D. Billadeau, Z. Otwinowski, and M.K. Rosen. 2010. Structure and control of the actin regulatory WAVE complex. *Nature*. 468:533-538.

Cherfils, J., and M. Zeghouf. 2013. Regulation of small GTPases by GEFs, GAPs, and GDIs. *Physiol Rev*. 93:269-309.

Choi, C.K., M. Vicente-Manzanares, J. Zareno, L.A. Whitmore, A. Mogilner, and A.R. Horwitz. 2008. Actin and alpha-actinin orchestrate the assembly and maturation of nascent adhesions in a myosin II motor-independent manner. *Nat Cell Biol*. 10:1039-1050.

Chorev, D.S., O. Moscovitz, B. Geiger, and M. Sharon. 2014. Regulation of focal adhesion formation by a vinculin-Arp2/3 hybrid complex. *Nat Commun*. 5:3758.

Chorzalska, A., I. Salloum, H. Shafqat, S. Khan, P. Marjon, D. Treaba, C. Schorl, J. Morgan, C.R. Bryke, V. Falanga, T.C. Zhao, J. Reagan, E. Winer, A.J. Olszewski, A.S. Al-Homsi, N. Kouttab, and P.M. Dubielecka. 2014. Low expression of Abelson interactor-1 is linked to acquired drug resistance in Bcr-Abl-induced leukemia. *Leukemia*. 28:2165-2177.

Clark, E.S., A.S. Whigham, W.G. Yarbrough, and A.M. Weaver. 2007. Cortactin is an essential regulator of matrix metalloproteinase secretion and extracellular matrix degradation in invadopodia. *Cancer Res*. 67:4227-4235.

Clarke, S. 1992. Protein isoprenylation and methylation at carboxyl-terminal cysteine residues. *Annu Rev Biochem*. 61:355-386.

Coccia, M., S.P. Brooks, T.R. Webb, K. Christodoulou, I.O. Wozniak, V. Murday, M. Balicki, H.A. Yee, T. Wangensteen, R. Riise, A.K. Saggar, S.M. Park, N. Kanuga, P.J. Francis, E.R. Maher, A.T. Moore, I.M. Russell-Eggitt, and A.J. Hardcastle. 2009. X-linked cataract and Nance-Horan syndrome are allelic disorders. *Hum Mol Genet*. 18:2643-2655.

Conde, C., and A. Caceres. 2009. Microtubule assembly, organization and dynamics in axons and dendrites. *Nat Rev Neurosci*. 10:319-332.

Cooke, R. 1975. The role of the bound nucleotide in the polymerization of actin. *Biochemistry*. 14:3250-3256.

Cote, J.F., and K. Vuori. 2002. Identification of an evolutionarily conserved superfamily of DOCK180-related proteins with guanine nucleotide exchange activity. *J Cell Sci*. 115:4901-4913.

Couto, A., N.A. Mack, L. Favia, and M. Georgiou. 2017. An apicobasal gradient of Rac activity determines protrusion form and position. *Nat Commun*. 8:15385.

Cox, J., M.Y. Hein, C.A. Luber, I. Paron, N. Nagaraj, and M. Mann. 2014. Accurate proteome-wide label-free quantification by delayed normalization and maximal peptide ratio extraction, termed MaxLFQ. *Mol Cell Proteomics*. 13:2513-2526.

Cox, J., and M. Mann. 2008. MaxQuant enables high peptide identification rates, individualized p.p.b.-range mass accuracies and proteome-wide protein quantification. *Nat Biotechnol*. 26:1367-1372.

Cox, J., N. Neuhauser, A. Michalski, R.A. Scheltema, J.V. Olsen, and M. Mann. 2011. Andromeda: a peptide search engine integrated into the MaxQuant environment. *J Proteome Res*. 10:1794-1805.

Crawford, H.C., C.R. Scoggins, M.K. Washington, L.M. Matrisian, and S.D. Leach. 2002. Matrix metalloproteinase-7 is expressed by pancreatic cancer precursors and regulates acinar-to-ductal metaplasia in exocrine pancreas. *J Clin Invest*. 109:1437-1444.

Cunningham, C.C. 1995. Actin polymerization and intracellular solvent flow in cell surface blebbing. *J Cell Biol*. 129:1589-1599.

Dahl, J.P., J. Wang-Dunlop, C. Gonzales, M.E. Goad, R.J. Mark, and S.P. Kwak. 2003. Characterization of the WAVE1 knock-out mouse: implications for CNS development. *J Neurosci*. 23:3343-3352.

Dai, Z., R.C. Quackenbush, K.D. Courtney, M. Grove, D. Cortez, G.W. Reuther, and A.M. Pendergast. 1998. Oncogenic Abl and Src tyrosine kinases elicit the ubiquitin-dependent degradation of target proteins through a Ras-independent pathway. *Genes Dev*. 12:1415-1424.

Dang, I., R. Gorelik, C. Sousa-Blin, E. Derivery, C. Guerin, J. Linkner, M. Nemethova, J.G. Dumortier, F.A. Giger, T.A. Chipysheva, V.D. Ermilova, S. Vacher, V. Campanacci, I. Herrada, A.G. Planson, S. Fetics, V. Henriot, V. David, K. Oguievetskaia, G. Lakisic, F. Pierre, A. Steffen, A. Boyreau, N. Peyrieras, K. Rottner, S. Zinn-Justin, J. Cherfils, I. Bieche, A.Y. Alexandrova, N.B. David, J.V. Small, J. Faix, L. Blanchoin, and A. Gautreau. 2013. Inhibitory signalling to the Arp2/3 complex steers cell migration. *Nature*. 503:281-284.

Davidson, A.J., and R.H. Insall. 2011. Actin-based motility: WAVE regulatory complex structure reopens old SCARs. *Curr Biol*. 21:R66-68.

Dayel, M.J., E.A. Holleran, and R.D. Mullins. 2001. Arp2/3 complex requires hydrolyzable ATP for nucleation of new actin filaments. *Proc Natl Acad Sci U S A*. 98:14871-14876.

De La Cruz, E.M., A. Mandinova, M.O. Steinmetz, D. Stoffler, U. Aebi, and T.D. Pollard. 2000. Polymerization and structure of nucleotide-free actin filaments. *J Mol Biol*. 295:517-526.

de Lanerolle, P., and L. Serebryannyy. 2011. Nuclear actin and myosins: life without filaments. *Nat Cell Biol*. 13:1282-1288.

DeMali, K.A., C.A. Barlow, and K. Burridge. 2002. Recruitment of the Arp2/3 complex to vinculin: coupling membrane protrusion to matrix adhesion. *J Cell Biol*. 159:881-891.

Derivery, E., J. Fink, D. Martin, A. Houdusse, M. Piel, T.E. Stradal, D. Louvard, and A. Gautreau. 2008. Free Brick1 is a trimeric precursor in the assembly of a functional wave complex. *PLoS One*. 3:e2462.

Derivery, E., B. Lombard, D. Loew, and A. Gautreau. 2009a. The Wave complex is intrinsically inactive. *Cell Motil Cytoskeleton*. 66:777-790.

Derivery, E., C. Sousa, J.J. Gautier, B. Lombard, D. Loew, and A. Gautreau. 2009b. The Arp2/3 activator WASH controls the fission of endosomes through a large multiprotein complex. *Dev Cell*. 17:712-723.

Desai, R.A., L. Gao, S. Raghavan, W.F. Liu, and C.S. Chen. 2009. Cell polarity triggered by cell-cell adhesion via E-cadherin. *J Cell Sci*. 122:905-911.

Desire, L., J. Bourdin, N. Loiseau, H. Peillon, V. Picard, C. De Oliveira, F. Bachelot, B. Leblond, T. Taverne, E. Beausoleil, S. Lacombe, D. Drouin, and F. Schweighoffer. 2005. RAC1 inhibition targets amyloid precursor protein processing by gamma-secretase and decreases Abeta production in vitro and in vivo. *J Biol Chem*. 280:37516-37525.

di Magliano, M.P., and C.D. Logsdon. 2013. Roles for KRAS in pancreatic tumor development and progression. *Gastroenterology*. 144:1220-1229.

Didry, D., M.F. Carlier, and D. Pantaloni. 1998. Synergy between actin depolymerizing factor/cofilin and profilin in increasing actin filament turnover. *J Biol Chem*. 273:25602-25611.

Didsbury, J., R.F. Weber, G.M. Bokoch, T. Evans, and R. Snyderman. 1989. rac, a novel ras-related family of proteins that are botulinum toxin substrates. *J Biol Chem*. 264:16378-16382.

Djakovic, S., J. Dyachok, M. Burke, M.J. Frank, and L.G. Smith. 2006. BRICK1/HSPC300 functions with SCAR and the ARP2/3 complex to regulate epidermal cell shape in Arabidopsis. *Development*. 133:1091-1100.

Dovas, A., and J.R. Couchman. 2005. RhoGDI: multiple functions in the regulation of Rho family GTPase activities. *Biochem J*. 390:1-9.

Doyle, A.D., and K.M. Yamada. 2016. Mechanosensing via cell-matrix adhesions in 3D microenvironments. *Exp Cell Res*. 343:60-66.

Dubielecka, P.M., K.I. Ladwein, X. Xiong, I. Migeotte, A. Chorzalska, K.V. Anderson, J.A. Sawicki, K. Rottner, T.E. Stradal, and L. Kotula. 2011. Essential role for Abi1 in embryonic survival and WAVE2 complex integrity. *Proc Natl Acad Sci U S A*. 108:7022-7027.

Duchek, P., K. Somogyi, G. Jekely, S. Beccari, and P. Rorth. 2001. Guidance of cell migration by the Drosophila PDGF/VEGF receptor. *Cell*. 107:17-26.

Duleh, S.N., and M.D. Welch. 2010. WASH and the Arp2/3 complex regulate endosome shape and trafficking. *Cytoskeleton (Hoboken)*. 67:193-206.

Eden, S., R. Rohatgi, A.V. Podtelejnikov, M. Mann, and M.W. Kirschner. 2002. Mechanism of regulation of WAVE1-induced actin nucleation by Rac1 and Nck. *Nature*. 418:790-793.

Emadi Baygi, M., Z.S. Soheili, F. Essmann, A. Deezagi, R. Engers, W. Goering, and W.A. Schulz. 2010. Slug/SNAI2 regulates cell proliferation and invasiveness of metastatic prostate cancer cell lines. *Tumour Biol*. 31:297-307.

Escobar, B., G. de Carcer, G. Fernandez-Miranda, A. Cascon, J.J. Bravo-Cordero, M.C. Montoya, M. Robledo, M. Canamero, and M. Malumbres. 2010. Brick1 is an essential regulator of actin cytoskeleton required for embryonic development and cell transformation. *Cancer Res*. 70:9349-9359.

Etienne-Manneville, S., and A. Hall. 2002. Rho GTPases in cell biology. *Nature*. 420:629-635.

Faroudi, M., M. Hons, A. Zachacz, C. Dumont, R. Lyck, J.V. Stein, and V.L. Tybulewicz. 2010. Critical roles for Rac GTPases in T-cell migration to and within lymph nodes. *Blood*. 116:5536-5547.

Ferguson, K.M., M.A. Lemmon, J. Schlessinger, and P.B. Sigler. 1995. Structure of the high affinity complex of inositol trisphosphate with a phospholipase C pleckstrin homology domain. *Cell*. 83:1037-1046.

Fetics, S., A. Thureau, V. Campanacci, M. Aumont-Nicaise, I. Dang, A. Gautreau, J. Perez, and J. Cherfils. 2016. Hybrid Structural Analysis of the Arp2/3 Regulator Arpin Identifies Its Acidic Tail as a Primary Binding Epitope. *Structure*. 24:252-260.

Fiegen, D., L.C. Haeusler, L. Blumenstein, U. Herbrand, R. Dvorsky, I.R. Vetter, and M.R. Ahmadian. 2004. Alternative splicing of Rac1 generates Rac1b, a self-activating GTPase. *J Biol Chem*. 279:4743-4749.

Filic, V., M. Marinovic, J. Faix, and I. Weber. 2012. A dual role for Rac1 GTPases in the regulation of cell motility. *J Cell Sci*. 125:387-398.

Finn, R.D., A. Bateman, J. Clements, P. Coggill, R.Y. Eberhardt, S.R. Eddy, A. Heger, K. Hetherington, L. Holm, J. Mistry, E.L. Sonnhammer, J. Tate, and M. Punta. 2014. Pfam: the protein families database. *Nucleic Acids Res*. 42:D222-230.

Formstecher, E., S. Aresta, V. Collura, A. Hamburger, A. Meil, A. Trehin, C. Reverdy, V. Betin, S. Maire, C. Brun, B. Jacq, M. Arpin, Y. Bellaiche, S. Bellusci, P. Benaroch, M. Bornens, R. Chanet, P. Chavrier, O. Delattre, V. Doye, R. Fehon, G. Faye, T. Galli, J.A. Girault, B. Goud, J. de Gunzburg, L. Johannes, M.P. Junier, V. Mirouse, A. Mukherjee, D. Papadopoulo, F. Perez, A. Plessis, C. Rosse, S. Saule, D. Stoppa-Lyonnet, A. Vincent, M. White, P. Legrain, J. Wojcik, J. Camonis, and L. Daviet. 2005. Protein interaction mapping: a Drosophila case study. *Genome Res*. 15:376-384.

Fraley, S.I., Y. Feng, R. Krishnamurthy, D.H. Kim, A. Celedon, G.D. Longmore, and D. Wirtz. 2010. A distinctive role for focal adhesion proteins in three-dimensional cell motility. *Nat Cell Biol*. 12:598-604.

Frank, M.J., and L.G. Smith. 2002. A small, novel protein highly conserved in plants and animals promotes the polarized growth and division of maize leaf epidermal cells. *Curr Biol*. 12:849-853.

Frank, R. 2002. The SPOT-synthesis technique. Synthetic peptide arrays on membrane supports--principles and applications. *J Immunol Methods*. 267:13-26.

Friedl, P., and K. Wolf. 2010. Plasticity of cell migration: a multiscale tuning model. *J Cell Biol*. 188:11-19.

Fritz, R.D., and O. Pertz. 2016. The dynamics of spatio-temporal Rho GTPase signaling: formation of signaling patterns. *F1000Res*. 5.

Fromont-Racine, M., J.C. Rain, and P. Legrain. 1997. Toward a functional analysis of the yeast genome through exhaustive two-hybrid screens. *Nat Genet*. 16:277-282.

Fujii, M., K. Kawai, Y. Egami, and N. Araki. 2013. Dissecting the roles of Rac1 activation and deactivation in macropinocytosis using microscopic photo-manipulation. *Sci Rep*. 3:2385.

Gandhi, M., B.A. Smith, M. Bovellan, V. Paavilainen, K. Daugherty-Clarke, J. Gelles, P. Lappalainen, and B.L. Goode. 2010. GMF is a cofilin homolog that binds Arp2/3 complex to stimulate filament debranching and inhibit actin nucleation. *Curr Biol*. 20:861-867.

Ganesan, S., S.M. Ameer-Beg, T.T. Ng, B. Vojnovic, and F.S. Wouters. 2006. A dark yellow fluorescent protein (YFP)-based Resonance Energy-Accepting Chromoprotein (REACh) for Forster resonance energy transfer with GFP. *Proc Natl Acad Sci U S A*. 103:4089-4094.

Gannon, M., P.L. Herrera, and C.V. Wright. 2000. Mosaic Cre-mediated recombination in pancreas using the pdx-1 enhancer/promoter. *Genesis*. 26:143-144.

Gao, Y., J.B. Dickerson, F. Guo, J. Zheng, and Y. Zheng. 2004. Rational design and characterization of a Rac GTPase-specific small molecule inhibitor. *Proc Natl Acad Sci U S A*. 101:7618-7623.

Gautier, J.J., M.E. Lomakina, L. Bouslama-Oueghlani, E. Derivery, H. Beilinson, W. Faigle, D. Loew, D. Louvard, A. Echard, A.Y. Alexandrova, B. Baum, and A. Gautreau. 2011. Clathrin is required for Scar/Wave-mediated lamellipodium formation. *J Cell Sci*. 124:3414-3427.

Gautreau, A., H.Y. Ho, J. Li, H. Steen, S.P. Gygi, and M.W. Kirschner. 2004. Purification and architecture of the ubiquitous Wave complex. *Proc Natl Acad Sci U S A*. 101:4379-4383.

Gawden-Bone, C., Z. Zhou, E. King, A. Prescott, C. Watts, and J. Lucocq. 2010. Dendritic cell podosomes are protrusive and invade the extracellular matrix using metalloproteinase MMP-14. *J Cell Sci*. 123:1427-1437.

Gaynor, E.C., C.Y. Chen, S.D. Emr, and T.R. Graham. 1998. ARF is required for maintenance of yeast Golgi and endosome structure and function. *Mol Biol Cell*. 9:653-670.

Gefen, A., and D. Weihs. 2016. Cytoskeleton and plasma-membrane damage resulting from exposure to sustained deformations: A review of the mechanobiology of chronic wounds. *Med Eng Phys*. 38:828-833.

Geiger, B., and K.M. Yamada. 2011. Molecular architecture and function of matrix adhesions. *Cold Spring Harb Perspect Biol*. 3.

Gerard, A., G. Patino-Lopez, P. Beemiller, R. Nambiar, K. Ben-Aissa, Y. Liu, F.J. Totah, M.J. Tyska, S. Shaw, and M.F. Krummel. 2014. Detection of rare antigen-presenting cells through T cell-intrinsic meandering motility, mediated by Myo1g. *Cell*. 158:492-505.

Gilli, F., R.L. Lindberg, P. Valentino, F. Marnetto, S. Malucchi, A. Sala, M. Capobianco, A. di Sapio, F. Sperli, L. Kappos, R.A. Calogero, and A. Bertolotto. 2010. Learning from nature: pregnancy changes the expression of inflammation-related genes in patients with multiple sclerosis. *PLoS One*. 5:e8962.

Goley, E.D., A. Rammohan, E.A. Znameroski, E.N. Firat-Karalar, D. Sept, and M.D. Welch. 2010. An actin-filament-binding interface on the Arp2/3 complex is critical for nucleation and branch stability. *Proc Natl Acad Sci U S A*. 107:8159-8164.

Goley, E.D., S.E. Rodenbusch, A.C. Martin, and M.D. Welch. 2004. Critical conformational changes in the Arp2/3 complex are induced by nucleotide and nucleation promoting factor. *Mol Cell*. 16:269-279.

Goode, B.L., and M.J. Eck. 2007. Mechanism and function of formins in the control of actin assembly. *Annu Rev Biochem*. 76:593-627.

Gorleku, O.A., A.M. Barns, G.R. Prescott, J. Greaves, and L.H. Chamberlain. 2011. Endoplasmic reticulum localization of DHHC palmitoyltransferases mediated by lysine-based sorting signals. *J Biol Chem*. 286:39573-39584.

Gorzalczany, Y., N. Sigal, M. Itan, O. Lotan, and E. Pick. 2000. Targeting of Rac1 to the phagocyte membrane is sufficient for the induction of NADPH oxidase assembly. *J Biol Chem*. 275:40073-40081.

Goto, A., T. Kadowaki, and Y. Kitagawa. 2003. Drosophila hemolectin gene is expressed in embryonic and larval hemocytes and its knock down causes bleeding defects. *Dev Biol*. 264:582-591.

Grebecki, A., L. Grebecka, and A. Wasik. 2001. Minipodia and rosette contacts are adhesive organelles present in free-living amoebae. *Cell Biol Int*. 25:1279-1283.

Gu, G., J. Dubauskaite, and D.A. Melton. 2002a. Direct evidence for the pancreatic lineage: NGN3+ cells are islet progenitors and are distinct from duct progenitors. *Development*. 129:2447-2457.

Gu, Y., M.C. Byrne, N.C. Paranavitana, B. Aronow, J.E. Siefring, M. D'Souza, H.F. Horton, L.A. Quilliam, and D.A. Williams. 2002b. Rac2, a hematopoiesis-specific Rho GTPase, specifically regulates mast cell protease gene expression in bone marrow-derived mast cells. *Mol Cell Biol*. 22:7645-7657.

Guerra, C., and M. Barbacid. 2013. Genetically engineered mouse models of pancreatic adenocarcinoma. *Mol Oncol*. 7:232-247.

Guo, F., M. Debidda, L. Yang, D.A. Williams, and Y. Zheng. 2006. Genetic deletion of Rac1 GTPase reveals its critical role in actin stress fiber formation and focal adhesion complex assembly. *J Biol Chem*. 281:18652-18659.

Haataja, L., J. Groffen, and N. Heisterkamp. 1997. Characterization of RAC3, a novel member of the Rho family. *J Biol Chem*. 272:20384-20388.

Han, S.P., Y. Gambin, G.A. Gomez, S. Verma, N. Giles, M. Michael, S.K. Wu, Z. Guo, W. Johnston, E. Sierecki, R.G. Parton, K. Alexandrov, and A.S. Yap. 2014. Cortactin scaffolds Arp2/3 and WAVE2 at the epithelial zonula adherens. *J Biol Chem*. 289:7764-7775.

Hanahan, D., and R.A. Weinberg. 2011. Hallmarks of cancer: the next generation. *Cell*. 144:646-674.

Hancock, J.F., and A. Hall. 1993. A novel role for RhoGDI as an inhibitor of GAP proteins. *EMBO J*. 12:1915-1921.

Hansel, D.E., S.E. Kern, and R.H. Hruban. 2003. Molecular pathogenesis of pancreatic cancer. *Annu Rev Genomics Hum Genet*. 4:237-256.

Harden, N., H.Y. Loh, W. Chia, and L. Lim. 1995. A dominant inhibitory version of the small GTP-binding protein Rac disrupts cytoskeletal structures and inhibits developmental cell shape changes in Drosophila. *Development*. 121:903-914.

Heasman, S.J., and A.J. Ridley. 2008. Mammalian Rho GTPases: new insights into their functions from in vivo studies. *Nat Rev Mol Cell Biol*. 9:690-701.

Heid, I., C. Lubeseder-Martellato, B. Sipos, P.K. Mazur, M. Lesina, R.M. Schmid, and J.T. Siveke. 2011. Early requirement of Rac1 in a mouse model of pancreatic cancer. *Gastroenterology*. 141:719-730, 730 e711-717.

Helgeson, L.A., and B.J. Nolen. 2013. Mechanism of synergistic activation of Arp2/3 complex by cortactin and N-WASP. *Elife*. 2:e00884.

Herrmann, H., H. Bar, L. Kreplak, S.V. Strelkov, and U. Aebi. 2007. Intermediate filaments: from cell architecture to nanomechanics. *Nat Rev Mol Cell Biol*. 8:562-573.

Herrmann, H., S.V. Strelkov, P. Burkhard, and U. Aebi. 2009. Intermediate filaments: primary determinants of cell architecture and plasticity. *J Clin Invest*. 119:1772-1783.

Heuser, J.E., and M.W. Kirschner. 1980. Filament organization revealed in platinum replicas of freeze-dried cytoskeletons. *J Cell Biol*. 86:212-234.

Hieb, A.R., S. D'Arcy, M.A. Kramer, A.E. White, and K. Luger. 2012. Fluorescence strategies for high-throughput quantification of protein interactions. *Nucleic Acids Res*. 40:e33.

Higgs, H.N., and T.D. Pollard. 1999. Regulation of actin polymerization by Arp2/3 complex and WASp/Scar proteins. *J Biol Chem*. 274:32531-32534.

Hingorani, S.R., E.F. Petricoin, A. Maitra, V. Rajapakse, C. King, M.A. Jacobetz, S. Ross, T.P. Conrads, T.D. Veenstra, B.A. Hitt, Y. Kawaguchi, D. Johann, L.A. Liotta, H.C. Crawford, M.E. Putt, T. Jacks, C.V. Wright, R.H. Hruban, A.M. Lowy, and D.A. Tuveson. 2003. Preinvasive and invasive ductal pancreatic cancer and its early detection in the mouse. *Cancer Cell*. 4:437-450.

Hingorani, S.R., L. Wang, A.S. Multani, C. Combs, T.B. Deramaudt, R.H. Hruban, A.K. Rustgi, S. Chang, and D.A. Tuveson. 2005. Trp53R172H and KrasG12D cooperate to promote chromosomal instability and widely metastatic pancreatic ductal adenocarcinoma in mice. *Cancer Cell*. 7:469-483.

Hodge, R.G., and A.J. Ridley. 2016. Regulating Rho GTPases and their regulators. *Nat Rev Mol Cell Biol*. 17:496-510.

Hoeller, O., and R.R. Kay. 2007. Chemotaxis in the absence of PIP3 gradients. *Curr Biol*. 17:813-817.

Hofbauer, S.W., P.W. Krenn, S. Ganghammer, D. Asslaber, U. Pichler, K. Oberascher, R. Henschler, M. Wallner, H. Kerschbaum, R. Greil, and T.N. Hartmann. 2014. Tiam1/Rac1 signals contribute to the proliferation and chemoresistance, but not motility, of chronic lymphocytic leukemia cells. *Blood*. 123:2181-2188.

Hoffmann, B., and C. Schafer. 2010. Filopodial focal complexes direct adhesion and force generation towards filopodia outgrowth. *Cell Adh Migr*. 4:190-193.

Hruban, R.H., M.I. Canto, M. Goggins, R. Schulick, and A.P. Klein. 2010. Update on familial pancreatic cancer. *Adv Surg*. 44:293-311.

Humphries, J.D., P. Wang, C. Streuli, B. Geiger, M.J. Humphries, and C. Ballestrem. 2007. Vinculin controls focal adhesion formation by direct interactions with talin and actin. *J Cell Biol*. 179:1043-1057.

Ibarra, N., S.L. Blagg, F. Vazquez, and R.H. Insall. 2006. Nap1 regulates Dictyostelium cell motility and adhesion through SCAR-dependent and -independent pathways. *Curr Biol*. 16:717-722.

Innocenti, M., E. Frittoli, I. Ponzanelli, J.R. Falck, S.M. Brachmann, P.P. Di Fiore, and G. Scita. 2003. Phosphoinositide 3-kinase activates Rac by entering in a complex with Eps8, Abi1, and Sos-1. *J Cell Biol*. 160:17-23.

Innocenti, M., A. Zucconi, A. Disanza, E. Frittoli, L.B. Areces, A. Steffen, T.E. Stradal, P.P. Di Fiore, M.F. Carlier, and G. Scita. 2004. Abi1 is essential for the formation and activation of a WAVE2 signalling complex. *Nat Cell Biol*. 6:319-327.

Inobe, T., and N. Nukina. 2016. Rapamycin-induced oligomer formation system of FRB-FKBP fusion proteins. *J Biosci Bioeng*. 122:40-46.

Isambert, H., P. Venier, A.C. Maggs, A. Fattoum, R. Kassab, D. Pantaloni, and M.F. Carlier. 1995. Flexibility of actin filaments derived from thermal fluctuations. Effect of bound nucleotide, phalloidin, and muscle regulatory proteins. *J Biol Chem*. 270:11437-11444.

Ismail, A.M., S.B. Padrick, B. Chen, J. Umetani, and M.K. Rosen. 2009. The WAVE regulatory complex is inhibited. *Nat Struct Mol Biol*. 16:561-563.

Itoh, R.E., K. Kurokawa, Y. Ohba, H. Yoshizaki, N. Mochizuki, and M. Matsuda. 2002. Activation of rac and cdc42 video imaged by fluorescent resonance energy transfer-based single-molecule probes in the membrane of living cells. *Mol Cell Biol*. 22:6582-6591.

Jacquemet, G., H. Hamidi, and J. Ivaska. 2015. Filopodia in cell adhesion, 3D migration and cancer cell invasion. *Curr Opin Cell Biol*. 36:23-31.

Jansen, S., A. Collins, C. Yang, G. Rebowski, T. Svitkina, and R. Dominguez. 2011. Mechanism of actin filament bundling by fascin. *J Biol Chem*. 286:30087-30096.

Jia, D., T.S. Gomez, Z. Metlagel, J. Umetani, Z. Otwinowski, M.K. Rosen, and D.D. Billadeau. 2010. WASH and WAVE actin regulators of the Wiskott-Aldrich syndrome protein (WASP) family are controlled by analogous structurally related complexes. *Proc Natl Acad Sci U S A*. 107:10442-10447.

Johnsson, A.K., Y. Dai, M. Nobis, M.J. Baker, E.J. McGhee, S. Walker, J.P. Schwarz, S. Kadir, J.P. Morton, K.B. Myant, D.J. Huels, A. Segonds-Pichon, O.J. Sansom, K.I. Anderson, P. Timpson, and H.C. Welch. 2014. The Rac-FRET mouse reveals tight spatiotemporal control of Rac activity in primary cells and tissues. *Cell Rep*. 6:1153-1164.

Johnston, S.A., J.P. Bramble, C.L. Yeung, P.M. Mendes, and L.M. Machesky. 2008. Arp2/3 complex activity in filopodia of spreading cells. *BMC Cell Biol*. 9:65.

Jordan, P., R. Brazao, M.G. Boavida, C. Gespach, and E. Chastre. 1999. Cloning of a novel human Rac1b splice variant with increased expression in colorectal tumors. *Oncogene*. 18:6835-6839.

Kabsch, W., H.G. Mannherz, D. Suck, E.F. Pai, and K.C. Holmes. 1990. Atomic structure of the actin:DNase I complex. *Nature*. 347:37-44.

Kalthoff, H., W. Schmiegel, C. Roeder, D. Kasche, A. Schmidt, G. Lauer, H.G. Thiele, G. Honold, K. Pantel, G. Riethmuller, and et al. 1993. p53 and K-RAS alterations in pancreatic epithelial cell lesions. *Oncogene*. 8:289-298.

Kang, H., M.J. Bradley, B.R. McCullough, A. Pierre, E.E. Grintsevich, E. Reisler, and E.M. De La Cruz. 2012. Identification of cation-binding sites on actin that drive polymerization and modulate bending stiffness. *Proc Natl Acad Sci U S A*. 109:16923-16927.

Kardash, E., M. Reichman-Fried, J.L. Maitre, B. Boldajipour, E. Papusheva, E.M. Messerschmidt, C.P. Heisenberg, and E. Raz. 2010. A role for Rho GTPases and cell-cell adhesion in single-cell motility in vivo. *Nat Cell Biol*. 12:47-53; sup pp 41-11.

Kaverina, I., O. Krylyshkina, M. Gimona, K. Beningo, Y.L. Wang, and J.V. Small. 2000. Enforced polarisation and locomotion of fibroblasts lacking microtubules. *Curr Biol*. 10:739-742.

Kawahara, R., J.G. Bollinger, C. Rivera, A.C. Ribeiro, T.B. Brandao, A.F. Paes Leme, and M.J. MacCoss. 2016. A targeted proteomic strategy for the measurement of oral cancer candidate biomarkers in human saliva. *Proteomics*. 16:159-173.

Keely, P.J., J.K. Westwick, I.P. Whitehead, C.J. Der, and L.V. Parise. 1997. Cdc42 and Rac1 induce integrin-mediated cell motility and invasiveness through PI(3)K. *Nature*. 390:632-636.

Kelleher, J.F., S.J. Atkinson, and T.D. Pollard. 1995. Sequences, structural models, and cellular localization of the actin-related proteins Arp2 and Arp3 from Acanthamoeba. *J Cell Biol*. 131:385-397.

Keller, H., and P. Eggli. 1998. Protrusive activity, cytoplasmic compartmentalization, and restriction rings in locomoting blebbing Walker carcinosarcoma cells are related to detachment of cortical actin from the plasma membrane. *Cell Motil Cytoskeleton*. 41:181-193.

Kelly, A.E., H. Kranitz, V. Dotsch, and R.D. Mullins. 2006. Actin binding to the central domain of WASP/Scar proteins plays a critical role in the activation of the Arp2/3 complex. *J Biol Chem*. 281:10589-10597.

Kim, A.S., L.T. Kakalis, N. Abdul-Manan, G.A. Liu, and M.K. Rosen. 2000. Autoinhibition and activation mechanisms of the Wiskott-Aldrich syndrome protein. *Nature*. 404:151-158.

Kim, H.J., A.B. DiBernardo, J.A. Sloane, M.N. Rasband, D. Solomon, B. Kosaras, S.P. Kwak, and T.K. Vartanian. 2006. WAVE1 is required for oligodendrocyte morphogenesis and normal CNS myelination. *J Neurosci*. 26:5849-5859.

Kinosian, H.J., L.A. Selden, L.C. Gershman, and J.E. Estes. 2004. Non-muscle actin filament elongation from complexes of profilin with nucleotide-free actin and divalent cation-free ATP-actin. *Biochemistry*. 43:6253-6260.

Kinsella, B.T., R.A. Erdman, and W.A. Maltese. 1991. Carboxyl-terminal isoprenylation of ras-related GTP-binding proteins encoded by rac1, rac2, and ralA. *J Biol Chem*. 266:9786-9794.

Kitamura, T., Y. Kitamura, K. Yonezawa, N.F. Totty, I. Gout, K. Hara, M.D. Waterfield, M. Sakaue, W. Ogawa, and M. Kasuga. 1996. Molecular cloning of p125Nap1, a protein that associates with an SH3 domain of Nck. *Biochem Biophys Res Commun*. 219:509-514.

Kleuss, C., and E. Krause. 2003. Galpha(s) is palmitoylated at the N-terminal glycine. *EMBO J*. 22:826-832.

Knudson, A.G., Jr. 1971. Mutation and cancer: statistical study of retinoblastoma. *Proc Natl Acad Sci U S A*. 68:820-823.

Kobayashi, K., S. Kuroda, M. Fukata, T. Nakamura, T. Nagase, N. Nomura, Y. Matsuura, N. Yoshida-Kubomura, A. Iwamatsu, and K. Kaibuchi. 1998. p140Sra-1 (specifically Rac1-associated protein) is a novel specific target for Rac1 small GTPase. *J Biol Chem*. 273:291-295.

Koronakis, V., P.J. Hume, D. Humphreys, T. Liu, O. Horning, O.N. Jensen, and E.J. McGhie. 2011. WAVE regulatory complex activation by cooperating GTPases Arf and Rac1. *Proc Natl Acad Sci U S A*. 108:14449-14454.

Krause, M., and A. Gautreau. 2014. Steering cell migration: lamellipodium dynamics and the regulation of directional persistence. *Nat Rev Mol Cell Biol*. 15:577-590.

Krause, M., J.D. Leslie, M. Stewart, E.M. Lafuente, F. Valderrama, R. Jagannathan, G.A. Strasser, D.A. Rubinson, H. Liu, M. Way, M.B. Yaffe, V.A. Boussiotis, and F.B. Gertler. 2004. Lamellipodin, an Ena/VASP ligand, is implicated in the regulation of lamellipodial dynamics. *Dev Cell*. 7:571-583.

Kraynov, V.S., C. Chamberlain, G.M. Bokoch, M.A. Schwartz, S. Slabaugh, and K.M. Hahn. 2000. Localized Rac activation dynamics visualized in living cells. *Science*. 290:333-337.

Krugmann, S., I. Jordens, K. Gevaert, M. Driessens, J. Vandekerckhove, and A. Hall. 2001. Cdc42 induces filopodia by promoting the formation of an IRSp53:Mena complex. *Curr Biol*. 11:1645-1655.

Krummel, M.F., F. Bartumeus, and A. Gerard. 2016. T cell migration, search strategies and mechanisms. *Nat Rev Immunol*. 16:193-201.

Kunda, P., G. Craig, V. Dominguez, and B. Baum. 2003. Abi, Sra1, and Kette control the stability and localization of SCAR/WAVE to regulate the formation of actin-based protrusions. *Curr Biol*. 13:1867-1875.

Kurisu, S., and T. Takenawa. 2009. The WASP and WAVE family proteins. *Genome Biol*. 10:226.

Kurokawa, K., R.E. Itoh, H. Yoshizaki, Y.O. Nakamura, and M. Matsuda. 2004. Coactivation of Rac1 and Cdc42 at lamellipodia and membrane ruffles induced by epidermal growth factor. *Mol Biol Cell*. 15:1003-1010.

Lakin, N.D., and S.P. Jackson. 1999. Regulation of p53 in response to DNA damage. *Oncogene*. 18:7644-7655.

Lammermann, T., B.L. Bader, S.J. Monkley, T. Worbs, R. Wedlich-Soldner, K. Hirsch, M. Keller, R. Forster, D.R. Critchley, R. Fassler, and M. Sixt. 2008. Rapid leukocyte migration by integrin-independent flowing and squeezing. *Nature*. 453:51-55.

Lang, G.A., T. Iwakuma, Y.A. Suh, G. Liu, V.A. Rao, J.M. Parant, Y.A. Valentin-Vega, T. Terzian, L.C. Caldwell, L.C. Strong, A.K. El-Naggar, and G. Lozano. 2004. Gain of function of a p53 hot spot mutation in a mouse model of Li-Fraumeni syndrome. *Cell*. 119:861-872.

Law, A.L., A. Vehlow, M. Kotini, L. Dodgson, D. Soong, E. Theveneau, C. Bodo, E. Taylor, C. Navarro, U. Perera, M. Michael, G.A. Dunn, D. Bennett, R. Mayor, and M. Krause. 2013. Lamellipodin and the Scar/WAVE complex cooperate to promote cell migration in vivo. *J Cell Biol*. 203:673-689.

Le Clainche, C., D. Didry, M.F. Carlier, and D. Pantaloni. 2001. Activation of Arp2/3 complex by Wiskott-Aldrich Syndrome protein is linked to enhanced binding of ATP to Arp2. *J Biol Chem*. 276:46689-46692.

Le, J., E.L. Mallery, C. Zhang, S. Brankle, and D.B. Szymanski. 2006. Arabidopsis BRICK1/HSPC300 is an essential WAVE-complex subunit that selectively stabilizes the Arp2/3 activator SCAR2. *Curr Biol*. 16:895-901.

Lebensohn, A.M., and M.W. Kirschner. 2009. Activation of the WAVE complex by coincident signals controls actin assembly. *Mol Cell*. 36:512-524.

LeClaire, L.L., 3rd, M. Baumgartner, J.H. Iwasa, R.D. Mullins, and D.L. Barber. 2008. Phosphorylation of the Arp2/3 complex is necessary to nucleate actin filaments. *J Cell Biol*. 182:647-654.

Lemonidis, K., M.W. Werno, J. Greaves, C. Diez-Ardanuy, M.C. Sanchez-Perez, C. Salaun, D.M. Thomson, and L.H. Chamberlain. 2015. The zDHHC family of S-acyltransferases. *Biochem Soc Trans*. 43:217-221.

Leng, Y., J. Zhang, K. Badour, E. Arpaia, S. Freeman, P. Cheung, M. Siu, and K. Siminovitch. 2005. Abelson-interactor-1 promotes WAVE2 membrane translocation and Abelson-mediated tyrosine phosphorylation required for WAVE2 activation. *Proc Natl Acad Sci U S A*. 102:1098-1103.

Li, A., Y. Ma, X. Yu, R.L. Mort, C.R. Lindsay, D. Stevenson, D. Strathdee, R.H. Insall, J. Chernoff, S.B. Snapper, I.J. Jackson, L. Larue, O.J. Sansom, and L.M. Machesky. 2011. Rac1 drives melanoblast organization during mouse development by orchestrating pseudopod- driven motility and cell-cycle progression. *Dev Cell*. 21:722-734.

Li, A., J.P. Morton, Y. Ma, S.A. Karim, Y. Zhou, W.J. Faller, E.F. Woodham, H.T. Morris, R.P. Stevenson, A. Juin, N.B. Jamieson, C.J. MacKay, C.R. Carter, H.Y. Leung, S. Yamashiro, K. Blyth, O.J. Sansom, and L.M. Machesky. 2014. Fascin is regulated by slug, promotes progression of pancreatic cancer in mice, and is associated with patient outcomes. *Gastroenterology*. 146:1386-1396 e1381-1317.

Li, R.A., D. Traver, T. Matthes, and J.Y. Bertrand. 2016. Ndrg1b and fam49ab modulate the PTEN pathway to control T-cell lymphopoiesis in the zebrafish. *Blood*. 128:3052-3060.

Li, Y., N. Clough, X. Sun, W. Yu, B.L. Abbott, C.J. Hogan, and Z. Dai. 2007. Bcr-Abl induces abnormal cytoskeleton remodeling, beta1 integrin clustering and increased cell adhesion to fibronectin through the Abl interactor 1 pathway. *J Cell Sci*. 120:1436-1446.

Lin, C.Y., J. Loven, P.B. Rahl, R.M. Paranal, C.B. Burge, J.E. Bradner, T.I. Lee, and R.A. Young. 2012. Transcriptional amplification in tumor cells with elevated c-Myc. *Cell*. 151:56-67.

Linder, S. 2007. The matrix corroded: podosomes and invadopodia in extracellular matrix degradation. *Trends Cell Biol*. 17:107-117.

Lindsay, C.R., S. Lawn, A.D. Campbell, W.J. Faller, F. Rambow, R.L. Mort, P. Timpson, A. Li, P. Cammareri, R.A. Ridgway, J.P. Morton, B. Doyle, S. Hegarty, M. Rafferty, I.G. Murphy, E.W. McDermott, K. Sheahan, K. Pedone, A.J. Finn, P.A. Groben, N.E. Thomas, H. Hao, C. Carson, J.C. Norman, L.M. Machesky, W.M. Gallagher, I.J. Jackson, L. Van Kempen, F. Beermann, C. Der, L. Larue, H.C. Welch, B.W. Ozanne, and O.J. Sansom. 2011. P-Rex1 is required for efficient melanoblast migration and melanoma metastasis. *Nat Commun*. 2:555.

Lindsay, C.R., A. Li, W. Faller, B. Ozanne, H. Welch, L.M. Machesky, and O.J. Sansom. 2015. A Rac1-independent role for P-Rex1 in melanoblasts. *J Invest Dermatol*. 135:314-318.

Linkner, J., G. Witte, T. Stradal, U. Curth, and J. Faix. 2011. High-resolution X-ray structure of the trimeric Scar/WAVE-complex precursor Brk1. *PLoS One*. 6:e21327.

Liu, J., B. Uygur, Z. Zhang, L. Shao, D. Romero, C. Vary, Q. Ding, and W.S. Wu. 2010. Slug inhibits proliferation of human prostate cancer cells via downregulation of cyclin D1 expression. *Prostate*. 70:1768-1777.

Lomakina, M.E., F. Lallemand, S. Vacher, N. Molinie, I. Dang, W. Cacheux, T.A. Chipysheva, V.D. Ermilova, L. de Koning, T. Dubois, I. Bieche, A.Y. Alexandrova, and A. Gautreau. 2016. Arpin downregulation in breast cancer is associated with poor prognosis. *Br J Cancer*. 114:545-553.

Lowenfels, A.B., P. Maisonneuve, G. Cavallini, R.W. Ammann, P.G. Lankisch, J.R. Andersen, E.P. Dimagno, A. Andren-Sandberg, and L. Domellof. 1993. Pancreatitis and the risk of pancreatic cancer. International Pancreatitis Study Group. *N Engl J Med*. 328:1433-1437.

Lujan, P., G. Varsano, T. Rubio, M.L. Hennrich, T. Sachsenheimer, M. Galvez-Santisteban, F. Martin-Belmonte, A.C. Gavin, B. Brugger, and M. Kohn. 2016. PRL-3 disrupts epithelial architecture by altering the post-mitotic midbody position. *J Cell Sci*. 129:4130-4142.

Luo, L., T.K. Hensch, L. Ackerman, S. Barbel, L.Y. Jan, and Y.N. Jan. 1996. Differential effects of the Rac GTPase on Purkinje cell axons and dendritic trunks and spines. *Nature*. 379:837-840.

Luo, L., Y.J. Liao, L.Y. Jan, and Y.N. Jan. 1994. Distinct morphogenetic functions of similar small GTPases: Drosophila Drac1 is involved in axonal outgrowth and myoblast fusion. *Genes Dev*. 8:1787-1802.

Ma, Y., A. Li, W.J. Faller, S. Libertini, F. Fiorito, D.A. Gillespie, O.J. Sansom, S. Yamashiro, and L.M. Machesky. 2013a. Fascin 1 is transiently expressed in mouse melanoblasts during development and promotes migration and proliferation. *Development*. 140:2203-2211.

Ma, Y., L.E. Reynolds, A. Li, R.P. Stevenson, K.M. Hodivala-Dilke, S. Yamashiro, and L.M. Machesky. 2013b. Fascin 1 is dispensable for developmental and tumour angiogenesis. *Biol Open*. 2:1187-1191.

Machacek, M., L. Hodgson, C. Welch, H. Elliott, O. Pertz, P. Nalbant, A. Abell, G.L. Johnson, K.M. Hahn, and G. Danuser. 2009. Coordination of Rho GTPase activities during cell protrusion. *Nature*. 461:99-103.

Machesky, L.M., S.J. Atkinson, C. Ampe, J. Vandekerckhove, and T.D. Pollard. 1994. Purification of a cortical complex containing two unconventional actins from Acanthamoeba by affinity chromatography on profilin-agarose. *J Cell Biol*. 127:107-115.

Machesky, L.M., and R.H. Insall. 1998. Scar1 and the related Wiskott-Aldrich syndrome protein, WASP, regulate the actin cytoskeleton through the Arp2/3 complex. *Curr Biol*. 8:1347-1356.

Machesky, L.M., R.D. Mullins, H.N. Higgs, D.A. Kaiser, L. Blanchoin, R.C. May, M.E. Hall, and T.D. Pollard. 1999. Scar, a WASp-related protein, activates nucleation of actin filaments by the Arp2/3 complex. *Proc Natl Acad Sci U S A*. 96:3739-3744.

Mack, N.A., and M. Georgiou. 2014. The interdependence of the Rho GTPases and apicobasal cell polarity. *Small GTPases*. 5:10.

Mack, N.A., A.P. Porter, H.J. Whalley, J.P. Schwarz, R.C. Jones, A.S. Khaja, A. Bjartell, K.I. Anderson, and A. Malliri. 2012. beta2-syntrophin and Par-3 promote an apicobasal Rac activity gradient at cell-cell junctions by differentially regulating Tiam1 activity. *Nat Cell Biol*. 14:1169-1180.

Madasu, Y., C. Yang, M. Boczkowska, K.A. Bethoney, A. Zwolak, G. Rebowski, T. Svitkina, and R. Dominguez. 2015. PICK1 is implicated in organelle motility in an Arp2/3 complex-independent manner. *Mol Biol Cell*. 26:1308-1322.

Mangan, A.J., D.V. Sietsema, D. Li, J.K. Moore, S. Citi, and R. Prekeris. 2016. Cingulin and actin mediate midbody-dependent apical lumen formation during polarization of epithelial cells. *Nat Commun*. 7:12426.

Marei, H., and A. Malliri. 2017. Rac1 in human diseases: The therapeutic potential of targeting Rac1 signaling regulatory mechanisms. *Small GTPases*. 8:139-163.

Maritzen, T., M.R. Schmidt, V. Kukhtina, V.A. Higman, H. Strauss, R. Volkmer, H. Oschkinat, C.G. Dotti, and V. Haucke. 2010. A novel subtype of AP-1-binding motif within the palmitoylated trans-Golgi network/endosomal accessory protein Gadkin/gamma-BAR. *J Biol Chem*. 285:4074-4086.

Maritzen, T., T. Zech, M.R. Schmidt, E. Krause, L.M. Machesky, and V. Haucke. 2012. Gadkin negatively regulates cell spreading and motility via sequestration of the actin-nucleating ARP2/3 complex. *Proc Natl Acad Sci U S A*. 109:10382-10387.

Martin, A.C., M. Kaschube, and E.F. Wieschaus. 2009. Pulsed contractions of an actin-myosin network drive apical constriction. *Nature*. 457:495-499.

Martin, A.C., M.D. Welch, and D.G. Drubin. 2006. Arp2/3 ATP hydrolysis-catalysed branch dissociation is critical for endocytic force generation. *Nat Cell Biol*. 8:826-833.

Martin, A.C., X.P. Xu, I. Rouiller, M. Kaksonen, Y. Sun, L. Belmont, N. Volkmann, D. Hanein, M. Welch, and D.G. Drubin. 2005. Effects of Arp2 and Arp3 nucleotide-binding pocket mutations on Arp2/3 complex function. *J Cell Biol*. 168:315-328.

Martin, B.R., C. Wang, A. Adibekian, S.E. Tully, and B.F. Cravatt. 2011. Global profiling of dynamic protein palmitoylation. *Nat Methods*. 9:84-89.

Martin, K., A. Reimann, R.D. Fritz, H. Ryu, N.L. Jeon, and O. Pertz. 2016. Spatio-temporal co-ordination of RhoA, Rac1 and Cdc42 activation during prototypical edge protrusion and retraction dynamics. *Sci Rep*. 6:21901.

Martin-Belmonte, F., W. Yu, A.E. Rodriguez-Fraticelli, A.J. Ewald, Z. Werb, M.A. Alonso, and K. Mostov. 2008. Cell-polarity dynamics controls the mechanism of lumen formation in epithelial morphogenesis. *Curr Biol*. 18:507-513.

Mason, F.M., M. Tworoger, and A.C. Martin. 2013. Apical domain polarization localizes actin-myosin activity to drive ratchet-like apical constriction. *Nat Cell Biol*. 15:926-936.

Matos, P., J.G. Collard, and P. Jordan. 2003. Tumor-related alternatively spliced Rac1b is not regulated by Rho-GDP dissociation inhibitors and exhibits selective downstream signaling. *J Biol Chem*. 278:50442-50448.

Matos, P., and P. Jordan. 2006. Rac1, but not Rac1B, stimulates RelB-mediated gene transcription in colorectal cancer cells. *J Biol Chem*. 281:13724-13732.

May, R.C., E. Caron, A. Hall, and L.M. Machesky. 2000. Involvement of the Arp2/3 complex in phagocytosis mediated by FcgammaR or CR3. *Nat Cell Biol*. 2:246-248.

Meinhardt, H. 1999. Orientation of chemotactic cells and growth cones: models and mechanisms. *J Cell Sci*. 112 (Pt 17):2867-2874.

Michaelson, D., J. Silletti, G. Murphy, P. D'Eustachio, M. Rush, and M.R. Philips. 2001. Differential localization of Rho GTPases in live cells: regulation by hypervariable regions and RhoGDI binding. *J Cell Biol*. 152:111-126.

Miki, H., S. Suetsugu, and T. Takenawa. 1998. WAVE, a novel WASP-family protein involved in actin reorganization induced by Rac. *EMBO J*. 17:6932-6941.

Miki, H., H. Yamaguchi, S. Suetsugu, and T. Takenawa. 2000. IRSp53 is an essential intermediate between Rac and WAVE in the regulation of membrane ruffling. *Nature*. 408:732-735.

Milburn, M.V., L. Tong, A.M. deVos, A. Brunger, Z. Yamaizumi, S. Nishimura, and S.H. Kim. 1990. Molecular switch for signal transduction: structural differences between active and inactive forms of protooncogenic ras proteins. *Science*. 247:939-945.

Miller, C.T., G. Chen, T.G. Gharib, H. Wang, D.G. Thomas, D.E. Misek, T.J. Giordano, J. Yee, M.B. Orringer, S.M. Hanash, and D.G. Beer. 2003. Increased C-CRK proto-oncogene expression is associated with an aggressive phenotype in lung adenocarcinomas. *Oncogene*. 22:7950-7957.

Miyamoto, Y., J. Yamauchi, and A. Tanoue. 2008. Cdk5 phosphorylation of WAVE2 regulates oligodendrocyte precursor cell migration through nonreceptor tyrosine kinase Fyn. *J Neurosci*. 28:8326-8337.

Moreira, C.G., J.C. Regan, A. Zaidman-Remy, A. Jacinto, and S. Prag. 2011. Drosophila hemocyte migration: an in vivo assay for directional cell migration. *Methods Mol Biol*. 769:249-260.

Moriyama, K., and I. Yahara. 2002. Human CAP1 is a key factor in the recycling of cofilin and actin for rapid actin turnover. *J Cell Sci*. 115:1591-1601.

Mort, R.L., L. Hay, and I.J. Jackson. 2010. Ex vivo live imaging of melanoblast migration in embryonic mouse skin. *Pigment Cell Melanoma Res*. 23:299-301.

Morton, J.P., P. Timpson, S.A. Karim, R.A. Ridgway, D. Athineos, B. Doyle, N.B. Jamieson, K.A. Oien, A.M. Lowy, V.G. Brunton, M.C. Frame, T.R. Evans, and O.J. Sansom. 2010. Mutant p53 drives metastasis and overcomes growth arrest/senescence in pancreatic cancer. *Proc Natl Acad Sci U S A*. 107:246-251.

Mullins, R.D., J.A. Heuser, and T.D. Pollard. 1998. The interaction of Arp2/3 complex with actin: nucleation, high affinity pointed end capping, and formation of branching networks of filaments. *Proc Natl Acad Sci U S A*. 95:6181-6186.

Mullins, R.D., W.F. Stafford, and T.D. Pollard. 1997. Structure, subunit topology, and actin-binding activity of the Arp2/3 complex from Acanthamoeba. *J Cell Biol*. 136:331-343.

Murakoshi, H., S.J. Lee, and R. Yasuda. 2008. Highly sensitive and quantitative FRET-FLIM imaging in single dendritic spines using improved non-radiative YFP. *Brain Cell Biol*. 36:31-42.

Murphy, D.A., and S.A. Courtneidge. 2011. The 'ins' and 'outs' of podosomes and invadopodia: characteristics, formation and function. *Nat Rev Mol Cell Biol*. 12:413-426.

Myant, K.B., P. Cammareri, E.J. McGhee, R.A. Ridgway, D.J. Huels, J.B. Cordero, S. Schwitalla, G. Kalna, E.L. Ogg, D. Athineos, P. Timpson, M. Vidal, G.I. Murray, F.R. Greten, K.I. Anderson, and O.J. Sansom. 2013. ROS production and NF-kappaB activation triggered by RAC1 facilitate WNT-driven intestinal stem cell proliferation and colorectal cancer initiation. *Cell Stem Cell*. 12:761-773.

Nagarajan, N.A., F. Gonzalez, and N. Shastri. 2012. Nonclassical MHC class Ib-restricted cytotoxic T cells monitor antigen processing in the endoplasmic reticulum. *Nat Immunol*. 13:579-586.

Nakao, S., A. Platek, S. Hirano, and M. Takeichi. 2008. Contact-dependent promotion of cell migration by the OL-protocadherin-Nap1 interaction. *J Cell Biol*. 182:395-410.

Nalbant, P., L. Hodgson, V. Kraynov, A. Toutchkine, and K.M. Hahn. 2004. Activation of endogenous Cdc42 visualized in living cells. *Science*. 305:1615-1619.

Napoli, I., V. Mercaldo, P.P. Boyl, B. Eleuteri, F. Zalfa, S. De Rubeis, D. Di Marino, E. Mohr, M. Massimi, M. Falconi, W. Witke, M. Costa-Mattioli, N. Sonenberg, T. Achsel, and C. Bagni. 2008. The fragile X syndrome protein represses activity-dependent translation through CYFIP1, a new 4E-BP. *Cell*. 134:1042-1054.

Narayanan, A., L.L. LeClaire, 3rd, D.L. Barber, and M.P. Jacobson. 2011. Phosphorylation of the Arp2 subunit relieves auto-inhibitory interactions for Arp2/3 complex activation. *PLoS Comput Biol*. 7:e1002226.

Nassar, N., G.R. Hoffman, D. Manor, J.C. Clardy, and R.A. Cerione. 1998. Structures of Cdc42 bound to the active and catalytically compromised forms of Cdc42GAP. *Nat Struct Biol*. 5:1047-1052.

Navarro-Lerida, I., S. Sanchez-Perales, M. Calvo, C. Rentero, Y. Zheng, C. Enrich, and M.A. Del Pozo. 2012. A palmitoylation switch mechanism regulates Rac1 function and membrane organization. *EMBO J*. 31:534-551.

Nayal, A., D.J. Webb, C.M. Brown, E.M. Schaefer, M. Vicente-Manzanares, and A.R. Horwitz. 2006. Paxillin phosphorylation at Ser273 localizes a GIT1-PIX-PAK complex and regulates adhesion and protrusion dynamics. *J Cell Biol*. 173:587-589.

Neilson, M.P., J.A. Mackenzie, S.D. Webb, and R.H. Insall. 2010. Use of the parameterised finite element method to robustly and efficiently evolve the edge of a moving cell. *Integr Biol (Camb)*. 2:687-695.

Nguyen, M.K., C.Y. Kim, J.M. Kim, B.O. Park, S. Lee, H. Park, and W.D. Heo. 2016. Optogenetic oligomerization of Rab GTPases regulates intracellular membrane trafficking. *Nat Chem Biol*. 12:431-436.

Nimnual, A.S., L.J. Taylor, M. Nyako, H.H. Jeng, and D. Bar-Sagi. 2010. Perturbation of cytoskeleton dynamics by the opposing effects of Rac1 and Rac1b. *Small GTPases*. 1:89-97.

Nobes, C.D., and A. Hall. 1995. Rho, rac, and cdc42 GTPases regulate the assembly of multimolecular focal complexes associated with actin stress fibers, lamellipodia, and filopodia. *Cell*. 81:53-62.

O'Brien, L.E., T.S. Jou, A.L. Pollack, Q. Zhang, S.H. Hansen, P. Yurchenco, and K.E. Mostov. 2001. Rac1 orientates epithelial apical polarity through effects on basolateral laminin assembly. *Nat Cell Biol*. 3:831-838.

Oda, T., T. Aihara, and K. Wakabayashi. 2016. Early nucleation events in the polymerization of actin, probed by time-resolved small-angle x-ray scattering. *Sci Rep*. 6:34539.

Offield, M.F., T.L. Jetton, P.A. Labosky, M. Ray, R.W. Stein, M.A. Magnuson, B.L. Hogan, and C.V. Wright. 1996. PDX-1 is required for pancreatic outgrowth and differentiation of the rostral duodenum. *Development*. 122:983-995.

Oguro-Ando, A., C. Rosensweig, E. Herman, Y. Nishimura, D. Werling, B.R. Bill, J.M. Berg, F. Gao, G. Coppola, B.S. Abrahams, and D.H. Geschwind. 2015. Increased CYFIP1 dosage alters cellular and dendritic morphology and dysregulates mTOR. *Mol Psychiatry*. 20:1069-1078.

Oikawa, T., H. Yamaguchi, T. Itoh, M. Kato, T. Ijuin, D. Yamazaki, S. Suetsugu, and T. Takenawa. 2004. PtdIns(3,4,5)P3 binding is necessary for WAVE2-induced formation of lamellipodia. *Nat Cell Biol*. 6:420-426.

Olive, K.P., D.A. Tuveson, Z.C. Ruhe, B. Yin, N.A. Willis, R.T. Bronson, D. Crowley, and T. Jacks. 2004. Mutant p53 gain of function in two mouse models of Li-Fraumeni syndrome. *Cell*. 119:847-860.

Olivier, M., R. Eeles, M. Hollstein, M.A. Khan, C.C. Harris, and P. Hainaut. 2002. The IARC TP53 database: new online mutation analysis and recommendations to users. *Hum Mutat*. 19:607-614.

Olson, M.F. 2016. Rho GTPases, their post-translational modifications, disease-associated mutations and pharmacological inhibitors. *Small GTPases*:1-13.

Ono, S., Y. Yamakita, S. Yamashiro, P.T. Matsudaira, J.R. Gnarra, T. Obinata, and F. Matsumura. 1997. Identification of an actin binding region and a protein kinase C phosphorylation site on human fascin. *J Biol Chem*. 272:2527-2533.

Otterbein, L.R., P. Graceffa, and R. Dominguez. 2001. The crystal structure of uncomplexed actin in the ADP state. *Science*. 293:708-711.

Overeem, A.W., D.M. Bryant, and I.S.C. van. 2015. Mechanisms of apical-basal axis orientation and epithelial lumen positioning. *Trends Cell Biol*. 25:476-485.

Paladi, M., and U. Tepass. 2004. Function of Rho GTPases in embryonic blood cell migration in Drosophila. *J Cell Sci*. 117:6313-6326.

Paluch, E., M. Piel, J. Prost, M. Bornens, and C. Sykes. 2005. Cortical actomyosin breakage triggers shape oscillations in cells and cell fragments. *Biophys J*. 89:724-733.

Panbianco, C., and M. Gotta. 2011. Coordinating cell polarity with cell division in space and time. *Trends Cell Biol*. 21:672-680.

Parsons, J.T., A.R. Horwitz, and M.A. Schwartz. 2010. Cell adhesion: integrating cytoskeletal dynamics and cellular tension. *Nat Rev Mol Cell Biol*. 11:633-643.

Pathania, M., E.C. Davenport, J. Muir, D.F. Sheehan, G. Lopez-Domenech, and J.T. Kittler. 2014. The autism and schizophrenia associated gene CYFIP1 is critical for the maintenance of dendritic complexity and the stabilization of mature spines. *Transl Psychiatry*. 4:e374.

Peng, J., B.J. Wallar, A. Flanders, P.J. Swiatek, and A.S. Alberts. 2003. Disruption of the Diaphanous-related formin Drf1 gene encoding mDia1 reveals a role for Drf3 as an effector for Cdc42. *Curr Biol*. 13:534-545.

Pertz, O., L. Hodgson, R.L. Klemke, and K.M. Hahn. 2006. Spatiotemporal dynamics of RhoA activity in migrating cells. *Nature*. 440:1069-1072.

Peyre, E., F. Jaouen, M. Saadaoui, L. Haren, A. Merdes, P. Durbec, and X. Morin. 2011. A lateral belt of cortical LGN and NuMA guides mitotic spindle movements and planar division in neuroepithelial cells. *J Cell Biol*. 193:141-154.

Pinner, S., and E. Sahai. 2008. PDK1 regulates cancer cell motility by antagonising inhibition of ROCK1 by RhoE. *Nat Cell Biol*. 10:127-137.

Polgar, N., and B. Fogelgren. 2017. Regulation of Cell Polarity by Exocyst-Mediated Trafficking. *Cold Spring Harb Perspect Biol*.

Pollitt, A.Y., and R.H. Insall. 2009. Loss of Dictyostelium HSPC300 causes a scar-like phenotype and loss of SCAR protein. *BMC Cell Biol*. 10:13.

Porter, A.P., A. Papaioannou, and A. Malliri. 2016. Deregulation of Rho GTPases in cancer. *Small GTPases*. 7:123-138.

Poukkula, M., M. Hakala, N. Pentinmikko, M.O. Sweeney, S. Jansen, J. Mattila, V. Hietakangas, B.L. Goode, and P. Lappalainen. 2014. GMF promotes leading-edge dynamics and collective cell migration in vivo. *Curr Biol*. 24:2533-2540.

Prols, F., Sagar, and M. Scaal. 2016. Signaling filopodia in vertebrate embryonic development. *Cell Mol Life Sci*. 73:961-974.

Qin, J., Y. Xie, B. Wang, M. Hoshino, D.W. Wolff, J. Zhao, M.A. Scofield, F.J. Dowd, M.F. Lin, and Y. Tu. 2009. Upregulation of PIP3-dependent Rac exchanger 1 (P-Rex1) promotes prostate cancer metastasis. *Oncogene*. 28:1853-1863.

Quaresma, M., M.P. Coleman, and B. Rachet. 2015. 40-year trends in an index of survival for all cancers combined and survival adjusted for age and sex for each cancer in England and Wales, 1971-2011: a population-based study. *Lancet*. 385:1206-1218.

Rakeman, A.S., and K.V. Anderson. 2006. Axis specification and morphogenesis in the mouse embryo require Nap1, a regulator of WAVE-mediated actin branching. *Development*. 133:3075-3083.

Ran, F.A., P.D. Hsu, J. Wright, V. Agarwala, D.A. Scott, and F. Zhang. 2013. Genome engineering using the CRISPR-Cas9 system. *Nat Protoc*. 8:2281-2308.

Redston, M.S., C. Caldas, A.B. Seymour, R.H. Hruban, L. da Costa, C.J. Yeo, and S.E. Kern. 1994. p53 mutations in pancreatic carcinoma and evidence of common involvement of homocopolymer tracts in DNA microdeletions. *Cancer Res*. 54:3025-3033.

Ridley, A.J., H.F. Paterson, C.L. Johnston, D. Diekmann, and A. Hall. 1992. The small GTP-binding protein rac regulates growth factor-induced membrane ruffling. *Cell*. 70:401-410.

Roberts, P.J., N. Mitin, P.J. Keller, E.J. Chenette, J.P. Madigan, R.O. Currin, A.D. Cox, O. Wilson, P. Kirschmeier, and C.J. Der. 2008. Rho Family GTPase modification and dependence on CAAX motif-signaled posttranslational modification. *J Biol Chem*. 283:25150-25163.

Robinson, R.C., K. Turbedsky, D.A. Kaiser, J.B. Marchand, H.N. Higgs, S. Choe, and T.D. Pollard. 2001. Crystal structure of Arp2/3 complex. *Science*. 294:1679-1684.

Rocca, D.L., S. Martin, E.L. Jenkins, and J.G. Hanley. 2008. Inhibition of Arp2/3-mediated actin polymerization by PICK1 regulates neuronal morphology and AMPA receptor endocytosis. *Nat Cell Biol*. 10:259-271.

Rodal, A.A., O. Sokolova, D.B. Robins, K.M. Daugherty, S. Hippenmeyer, H. Riezman, N. Grigorieff, and B.L. Goode. 2005. Conformational changes in the Arp2/3 complex leading to actin nucleation. *Nat Struct Mol Biol*. 12:26-31.

Rodnick-Smith, M., S.L. Liu, C.J. Balzer, Q. Luan, and B.J. Nolen. 2016. Identification of an ATP-controlled allosteric switch that controls actin filament nucleation by Arp2/3 complex. *Nat Commun*. 7:12226.

Rodriguez-Boulan, E., and I.G. Macara. 2014. Organization and execution of the epithelial polarity programme. *Nat Rev Mol Cell Biol*. 15:225-242.

Rodriguez-Fraticelli, A.E., S. Vergarajauregui, D.J. Eastburn, A. Datta, M.A. Alonso, K. Mostov, and F. Martin-Belmonte. 2010. The Cdc42 GEF Intersectin 2 controls mitotic spindle orientation to form the lumen during epithelial morphogenesis. *J Cell Biol*. 189:725-738.

Rohatgi, R., H.Y. Ho, and M.W. Kirschner. 2000. Mechanism of N-WASP activation by CDC42 and phosphatidylinositol 4, 5-bisphosphate. *J Cell Biol*. 150:1299-1310.

Rojas, A.M., G. Fuentes, A. Rausell, and A. Valencia. 2012. The Ras protein superfamily: evolutionary tree and role of conserved amino acids. *J Cell Biol*. 196:189-201.

Romero, S., C. Le Clainche, D. Didry, C. Egile, D. Pantaloni, and M.F. Carlier. 2004. Formin is a processive motor that requires profilin to accelerate actin assembly and associated ATP hydrolysis. *Cell*. 119:419-429.

Rottner, K., A. Hall, and J.V. Small. 1999. Interplay between Rac and Rho in the control of substrate contact dynamics. *Curr Biol*. 9:640-648.

Rotty, J.D., C. Wu, and J.E. Bear. 2013. New insights into the regulation and cellular functions of the ARP2/3 complex. *Nat Rev Mol Cell Biol*. 14:7-12.

Roy, A., A. Kucukural, and Y. Zhang. 2010. I-TASSER: a unified platform for automated protein structure and function prediction. *Nat Protoc*. 5:725-738.

Royal, I., N. Lamarche-Vane, L. Lamorte, K. Kaibuchi, and M. Park. 2000. Activation of cdc42, rac, PAK, and rho-kinase in response to hepatocyte growth factor differentially regulates epithelial cell colony spreading and dissociation. *Mol Biol Cell*. 11:1709-1725.

Saluja, A., I. Saito, M. Saluja, M.J. Houlihan, R.E. Powers, J. Meldolesi, and M. Steer. 1985. In vivo rat pancreatic acinar cell function during supramaximal stimulation with caerulein. *Am J Physiol*. 249:G702-710.

Schachtner, H., M. Weimershaus, V. Stache, N. Plewa, D.F. Legler, U.E. Hopken, and T. Maritzen. 2015. Loss of Gadkin Affects Dendritic Cell Migration In Vitro. *PLoS One*. 10:e0143883.

Scheidig, A.J., C. Burmester, and R.S. Goody. 1999. The pre-hydrolysis state of p21(ras) in complex with GTP: new insights into the role of water molecules in the GTP hydrolysis reaction of ras-like proteins. *Structure*. 7:1311-1324.

Schiff, P.B., J. Fant, and S.B. Horwitz. 1979. Promotion of microtubule assembly in vitro by taxol. *Nature*. 277:665-667.

Schirenbeck, A., T. Bretschneider, R. Arasada, M. Schleicher, and J. Faix. 2005. The Diaphanous-related formin dDia2 is required for the formation and maintenance of filopodia. *Nat Cell Biol*. 7:619-625.

Schnelzer, A., D. Prechtel, U. Knaus, K. Dehne, M. Gerhard, H. Graeff, N. Harbeck, M. Schmitt, and E. Lengyel. 2000. Rac1 in human breast cancer: overexpression, mutation analysis, and characterization of a new isoform, Rac1b. *Oncogene*. 19:3013-3020.

Schonhoff, S.E., M. Giel-Moloney, and A.B. Leiter. 2004. Neurogenin 3-expressing progenitor cells in the gastrointestinal tract differentiate into both endocrine and non-endocrine cell types. *Dev Biol*. 270:443-454.

Schoumacher, M., R.D. Goldman, D. Louvard, and D.M. Vignjevic. 2010. Actin, microtubules, and vimentin intermediate filaments cooperate for elongation of invadopodia. *J Cell Biol*. 189:541-556.

Schwob, E., and R.P. Martin. 1992. New yeast actin-like gene required late in the cell cycle. *Nature*. 355:179-182.

Sedeh, R.S., A.A. Fedorov, E.V. Fedorov, S. Ono, F. Matsumura, S.C. Almo, and M. Bathe. 2010. Structure, evolutionary conservation, and conformational dynamics of Homo sapiens fascin-1, an F-actin crosslinking protein. *J Mol Biol*. 400:589-604.

Sept, D., and J.A. McCammon. 2001. Thermodynamics and kinetics of actin filament nucleation. *Biophys J*. 81:667-674.

Serrels, B., A. Serrels, V.G. Brunton, M. Holt, G.W. McLean, C.H. Gray, G.E. Jones, and M.C. Frame. 2007. Focal adhesion kinase controls actin assembly via a FERM-mediated interaction with the Arp2/3 complex. *Nat Cell Biol*. 9:1046-1056.

Shahapure, R., F. Difato, A. Laio, G. Bisson, E. Ercolini, L. Amin, E. Ferrari, and V. Torre. 2010. Force generation in lamellipodia is a probabilistic process with fast growth and retraction events. *Biophys J*. 98:979-988.

Sharili, A.S., F.N. Kenny, M.K. Vartiainen, and J.T. Connelly. 2016. Nuclear actin modulates cell motility via transcriptional regulation of adhesive and cytoskeletal genes. *Sci Rep*. 6:33893.

Shi, Y., K. Alin, and S.P. Goff. 1995. Abl-interactor-1, a novel SH3 protein binding to the carboxy-terminal portion of the Abl protein, suppresses v-abl transforming activity. *Genes Dev*. 9:2583-2597.

Shutes, A., C. Onesto, V. Picard, B. Leblond, F. Schweighoffer, and C.J. Der. 2007. Specificity and mechanism of action of EHT 1864, a novel small molecule inhibitor of Rac family small GTPases. *J Biol Chem*. 282:35666-35678.

Silva, J.M., E. Ezhkova, J. Silva, S. Heart, M. Castillo, Y. Campos, V. Castro, F. Bonilla, C. Cordon-Cardo, S.K. Muthuswamy, S. Powers, E. Fuchs, and G.J. Hannon. 2009. Cyfip1 is a putative invasion suppressor in epithelial cancers. *Cell*. 137:1047-1061.

Silver, D.L., L. Hou, and W.J. Pavan. 2006. The genetic regulation of pigment cell development. *Adv Exp Med Biol*. 589:155-169.

Singh, A., A.E. Karnoub, T.R. Palmby, E. Lengyel, J. Sondek, and C.J. Der. 2004. Rac1b, a tumor associated, constitutively active Rac1 splice variant, promotes cellular transformation. *Oncogene*. 23:9369-9380.

Snapper, S.B., F. Takeshima, I. Anton, C.H. Liu, S.M. Thomas, D. Nguyen, D. Dudley, H. Fraser, D. Purich, M. Lopez-Ilasaca, C. Klein, L. Davidson, R. Bronson, R.C. Mulligan, F. Southwick, R. Geha, M.B. Goldberg, F.S. Rosen, J.H. Hartwig, and F.W. Alt. 2001. N-WASP deficiency reveals distinct pathways for cell surface projections and microbial actin-based motility. *Nat Cell Biol*. 3:897-904.

Snyder, J.T., K.L. Rossman, M.A. Baumeister, W.M. Pruitt, D.P. Siderovski, C.J. Der, M.A. Lemmon, and J. Sondek. 2001. Quantitative analysis of the effect of phosphoinositide interactions on the function of Dbl family proteins. *J Biol Chem*. 276:45868-45875.

Sokolova, O.S., A. Chemeris, S. Guo, S.L. Alioto, M. Gandhi, S. Padrick, E. Pechnikova, V. David, A. Gautreau, and B.L. Goode. 2017. Structural Basis of Arp2/3 Complex Inhibition by GMF, Coronin, and Arpin. *J Mol Biol*. 429:237-248.

Song, J., Y. Xu, X. Hu, B. Choi, and Q. Tong. 2010. Brain expression of Cre recombinase driven by pancreas-specific promoters. *Genesis*. 48:628-634.

Spence, H.J., P. Timpson, H.R. Tang, R.H. Insall, and L.M. Machesky. 2012. Scar/WAVE3 contributes to motility and plasticity of lamellipodial dynamics but not invasion in three dimensions. *Biochem J*. 448:35-42.

Spillane, M., A. Ketschek, C.J. Donnelly, A. Pacheco, J.L. Twiss, and G. Gallo. 2012. Nerve growth factor-induced formation of axonal filopodia and collateral branches involves the intra-axonal synthesis of regulators of the actin-nucleating Arp2/3 complex. *J Neurosci*. 32:17671-17689.

Squarr, A.J., K. Brinkmann, B. Chen, T. Steinbacher, K. Ebnet, M.K. Rosen, and S. Bogdan. 2016. Fat2 acts through the WAVE regulatory complex to drive collective cell migration during tissue rotation. *J Cell Biol*. 212:591-603.

Sriram, G., and R.B. Birge. 2010. Emerging roles for crk in human cancer. *Genes Cancer*. 1:1132-1139.

Stam, J.C., E.E. Sander, F. Michiels, F.N. van Leeuwen, H.E. Kain, R.A. van der Kammen, and J.G. Collard. 1997. Targeting of Tiam1 to the plasma membrane requires the cooperative function of the N-terminal pleckstrin homology domain and an adjacent protein interaction domain. *J Biol Chem*. 272:28447-28454.

Stanganello, E., A.I. Hagemann, B. Mattes, C. Sinner, D. Meyen, S. Weber, A. Schug, E. Raz, and S. Scholpp. 2015. Filopodia-based Wnt transport during vertebrate tissue patterning. *Nat Commun*. 6:5846.

Steffen, A., M. Ladwein, G.A. Dimchev, A. Hein, L. Schwenkmezger, S. Arens, K.I. Ladwein, J. Margit Holleboom, F. Schur, J. Victor Small, J. Schwarz, R. Gerhard, J. Faix, T.E. Stradal, C. Brakebusch, and K. Rottner. 2013. Rac function is crucial for cell migration but is not required for spreading and focal adhesion formation. *J Cell Sci*. 126:4572-4588.

Steffen, A., K. Rottner, J. Ehinger, M. Innocenti, G. Scita, J. Wehland, and T.E. Stradal. 2004. Sra-1 and Nap1 link Rac to actin assembly driving lamellipodia formation. *EMBO J*. 23:749-759.

Stehn, J.R., N.K. Haass, T. Bonello, M. Desouza, G. Kottyan, H. Treutlein, J. Zeng, P.R. Nascimento, V.B. Sequeira, T.L. Butler, M. Allanson, T. Fath, T.A. Hill, A. McCluskey, G. Schevzov, S.J. Palmer, E.C. Hardeman, D. Winlaw, V.E. Reeve, I. Dixon, W. Weninger, T.P. Cripe, and P.W. Gunning. 2013. A novel class of anticancer compounds targets the actin cytoskeleton in tumor cells. *Cancer Res*. 73:5169-5182.

Stovold, C.F., T.H. Millard, and L.M. Machesky. 2005. Inclusion of Scar/WAVE3 in a similar complex to Scar/WAVE1 and 2. *BMC Cell Biol*. 6:11.

Stramer, B., W. Wood, M.J. Galko, M.J. Redd, A. Jacinto, S.M. Parkhurst, and P. Martin. 2005. Live imaging of wound inflammation in Drosophila embryos reveals key roles for small GTPases during in vivo cell migration. *J Cell Biol*. 168:567-573.

Strzelecka-Golaszewska, H., E. Prochniewicz, and W. Drabikowski. 1978. Interaction of actin with divalent cations. 1. The effect of various cations on the physical state of actin. *Eur J Biochem*. 88:219-227.

Suetsugu, S., S. Kurisu, T. Oikawa, D. Yamazaki, A. Oda, and T. Takenawa. 2006. Optimization of WAVE2 complex-induced actin polymerization by membrane-bound IRSp53, PIP(3), and Rac. *J Cell Biol*. 173:571-585.

Sugihara, K., N. Nakatsuji, K. Nakamura, K. Nakao, R. Hashimoto, H. Otani, H. Sakagami, H. Kondo, S. Nozawa, A. Aiba, and M. Katsuki. 1998. Rac1 is required for the formation of three germ layers during gastrulation. *Oncogene*. 17:3427-3433.

Sumida, G.M., and S. Yamada. 2015. Rho GTPases and the downstream effectors actin-related protein 2/3 (Arp2/3) complex and myosin II induce membrane fusion at self-contacts. *J Biol Chem*. 290:3238-3247.

Sun, X., C. Li, C. Zhuang, W.C. Gilmore, E. Cobos, Y. Tao, and Z. Dai. 2009. Abl interactor 1 regulates Src-Id1-matrix metalloproteinase 9 axis and is required for invadopodia formation, extracellular matrix degradation and tumor growth of human breast cancer cells. *Carcinogenesis*. 30:2109-2116.

Suraneni, P., B. Rubinstein, J.R. Unruh, M. Durnin, D. Hanein, and R. Li. 2012. The Arp2/3 complex is required for lamellipodia extension and directional fibroblast cell migration. *J Cell Biol*. 197:239-251.

Svitkina, T.M., E.A. Bulanova, O.Y. Chaga, D.M. Vignjevic, S. Kojima, J.M. Vasiliev, and G.G. Borisy. 2003. Mechanism of filopodia initiation by reorganization of a dendritic network. *J Cell Biol*. 160:409-421.

Svitkina, T.M., A.B. Verkhovsky, K.M. McQuade, and G.G. Borisy. 1997. Analysis of the actin-myosin II system in fish epidermal keratocytes: mechanism of cell body translocation. *J Cell Biol*. 139:397-415.

Takenawa, T., and H. Miki. 2001. WASP and WAVE family proteins: key molecules for rapid rearrangement of cortical actin filaments and cell movement. *J Cell Sci*. 114:1801-1809.

Tang, H., A. Li, J. Bi, D.M. Veltman, T. Zech, H.J. Spence, X. Yu, P. Timpson, R.H. Insall, M.C. Frame, and L.M. Machesky. 2013. Loss of Scar/WAVE complex promotes N-WASP- and FAK-dependent invasion. *Curr Biol*. 23:107-117.

Teng, Y., A. Bahassan, D. Dong, L.E. Hanold, X. Ren, E.J. Kennedy, and J.K. Cowell. 2016a. Targeting the WASF3-CYFIP1 Complex Using Stapled Peptides Suppresses Cancer Cell Invasion. *Cancer Res*. 76:965-973.

Teng, Y., H. Qin, A. Bahassan, N.G. Bendzunas, E.J. Kennedy, and J.K. Cowell. 2016b. The WASF3-NCKAP1-CYFIP1 Complex Is Essential for Breast Cancer Metastasis. *Cancer Res*. 76:5133-5142.

Thamilselvan, V., and M.D. Basson. 2005. The role of the cytoskeleton in differentially regulating pressure-mediated effects on malignant colonocyte focal adhesion signaling and cell adhesion. *Carcinogenesis*. 26:1687-1697.

Thinon, E., R.A. Serwa, M. Broncel, J.A. Brannigan, U. Brassat, M.H. Wright, W.P. Heal, A.J. Wilkinson, D.J. Mann, and E.W. Tate. 2014. Global profiling of co- and post-translationally N-myristoylated proteomes in human cells. *Nat Commun*. 5:4919.

Thompson, G., D. Owen, P.A. Chalk, and P.N. Lowe. 1998. Delineation of the Cdc42/Rac-binding domain of p21-activated kinase. *Biochemistry*. 37:7885-7891.

Ti, S.C., C.T. Jurgenson, B.J. Nolen, and T.D. Pollard. 2011. Structural and biochemical characterization of two binding sites for nucleation-promoting factor WASp-VCA on Arp2/3 complex. *Proc Natl Acad Sci U S A*. 108:E463-471.

Tian, Q., Y. Li, R. Kousar, H. Guo, F. Peng, Y. Zheng, X. Yang, Z. Long, R. Tian, K. Xia, H. Lin, and Q. Pan. 2017. A novel NHS mutation causes Nance-Horan Syndrome in a Chinese family. *BMC Med Genet*. 18:2.

Tinevez, J.Y., U. Schulze, G. Salbreux, J. Roensch, J.F. Joanny, and E. Paluch. 2009. Role of cortical tension in bleb growth. *Proc Natl Acad Sci U S A*. 106:18581-18586.

Toutain, A., A.D. Ayrault, and C. Moraine. 1997. Mental retardation in Nance-Horan syndrome: clinical and neuropsychological assessment in four families. *Am J Med Genet*. 71:305-314.

UniProt, C. 2010. The Universal Protein Resource (UniProt) in 2010. *Nucleic Acids Res*. 38:D142-148.

Uruno, T., J. Liu, P. Zhang, Y. Fan, C. Egile, R. Li, S.C. Mueller, and X. Zhan. 2001. Activation of Arp2/3 complex-mediated actin polymerization by cortactin. *Nat Cell Biol*. 3:259-266.

Veltman, D.M., and R.H. Insall. 2010. WASP family proteins: their evolution and its physiological implications. *Mol Biol Cell*. 21:2880-2893.

Verkhovsky, A.B., T.M. Svitkina, and G.G. Borisy. 1999. Self-polarization and directional motility of cytoplasm. *Curr Biol*. 9:11-20.

Verma, S., S.P. Han, M. Michael, G.A. Gomez, Z. Yang, R.D. Teasdale, A. Ratheesh, E.M. Kovacs, R.G. Ali, and A.S. Yap. 2012. A WAVE2-Arp2/3 actin nucleator apparatus supports junctional tension at the epithelial zonula adherens. *Mol Biol Cell*. 23:4601-4610.

Vetter, I.R., and A. Wittinghofer. 2001. The guanine nucleotide-binding switch in three dimensions. *Science*. 294:1299-1304.

Vignjevic, D., S. Kojima, Y. Aratyn, O. Danciu, T. Svitkina, and G.G. Borisy. 2006. Role of fascin in filopodial protrusion. *J Cell Biol*. 174:863-875.

Villari, G., A. Jayo, J. Zanet, B. Fitch, B. Serrels, M. Frame, B.M. Stramer, B.T. Goult, and M. Parsons. 2015. A direct interaction between fascin and microtubules contributes to adhesion dynamics and cell migration. *J Cell Sci*. 128:4601-4614.

Vincent, S., P. Jeanteur, and P. Fort. 1992. Growth-regulated expression of rhoG, a new member of the ras homolog gene family. *Mol Cell Biol*. 12:3138-3148.

Vojtek, A.B., and S.M. Hollenberg. 1995. Ras-Raf interaction: two-hybrid analysis. *Methods Enzymol*. 255:331-342.

Wagner, A.R., Q. Luan, S.L. Liu, and B.J. Nolen. 2013. Dip1 defines a class of Arp2/3 complex activators that function without preformed actin filaments. *Curr Biol*. 23:1990-1998.

Wagner, M., F.R. Greten, C.K. Weber, S. Koschnick, T. Mattfeldt, W. Deppert, H. Kern, G. Adler, and R.M. Schmid. 2001. A murine tumor progression model for pancreatic cancer recapitulating the genetic alterations of the human disease. *Genes Dev*. 15:286-293.

Wagner, M., H. Luhrs, G. Kloppel, G. Adler, and R.M. Schmid. 1998. Malignant transformation of duct-like cells originating from acini in transforming growth factor transgenic mice. *Gastroenterology*. 115:1254-1262.

Walcott, S., D.H. Kim, D. Wirtz, and S.X. Sun. 2011. Nucleation and decay initiation are the stiffness-sensitive phases of focal adhesion maturation. *Biophys J*. 101:2919-2928.

Wang, L., K. Tabu, T. Kimura, M. Tsuda, H. Linghu, M. Tanino, S. Kaneko, H. Nishihara, and S. Tanaka. 2007. Signaling adaptor protein Crk is indispensable for malignant feature of glioblastoma cell line KMG4. *Biochem Biophys Res Commun*. 362:976-981.

Wang, Y., and M.A. McNiven. 2012. Invasive matrix degradation at focal adhesions occurs via protease recruitment by a FAK-p130Cas complex. *J Cell Biol*. 196:375-385.

Weaver, A.M., J.E. Heuser, A.V. Karginov, W.L. Lee, J.T. Parsons, and J.A. Cooper. 2002. Interaction of cortactin and N-WASp with Arp2/3 complex. *Curr Biol*. 12:1270-1278.

Weaver, A.M., A.V. Karginov, A.W. Kinley, S.A. Weed, Y. Li, J.T. Parsons, and J.A. Cooper. 2001. Cortactin promotes and stabilizes Arp2/3-induced actin filament network formation. *Curr Biol*. 11:370-374.

Weber, A., J. Northrop, M.F. Bishop, F.A. Ferrone, and M.S. Mooseker. 1987. Kinetics of actin elongation and depolymerization at the pointed end. *Biochemistry*. 26:2537-2544.

Wegner, A. 1976. Head to tail polymerization of actin. *J Mol Biol*. 108:139-150.

Welch, H.C., W.J. Coadwell, L.R. Stephens, and P.T. Hawkins. 2003. Phosphoinositide 3-kinase-dependent activation of Rac. *FEBS Lett*. 546:93-97.

Welch, M.D., A.H. DePace, S. Verma, A. Iwamatsu, and T.J. Mitchison. 1997. The human Arp2/3 complex is composed of evolutionarily conserved subunits and is localized to cellular regions of dynamic actin filament assembly. *J Cell Biol*. 138:375-384.

Welch, M.D., J. Rosenblatt, J. Skoble, D.A. Portnoy, and T.J. Mitchison. 1998. Interaction of human Arp2/3 complex and the Listeria monocytogenes ActA protein in actin filament nucleation. *Science*. 281:105-108.

Wells, C.M., M. Walmsley, S. Ooi, V. Tybulewicz, and A.J. Ridley. 2004. Rac1-deficient macrophages exhibit defects in cell spreading and membrane ruffling but not migration. *J Cell Sci*. 117:1259-1268.

Wennerberg, K., K.L. Rossman, and C.J. Der. 2005. The Ras superfamily at a glance. *J Cell Sci*. 118:843-846.

Wheeler, T.J., J. Clements, and R.D. Finn. 2014. Skylign: a tool for creating informative, interactive logos representing sequence alignments and profile hidden Markov models. *BMC Bioinformatics*. 15:7.

Whelan, D.R., and T.D. Bell. 2015. Image artifacts in single molecule localization microscopy: why optimization of sample preparation protocols matters. *Sci Rep*. 5:7924.

Williams, K.E., O. Miroshnychenko, E.B. Johansen, R.K. Niles, R. Sundaram, K. Kannan, M. Albertolle, Y. Zhou, N. Prasad, P.M. Drake, L.C. Giudice, S.C. Hall, H.E. Witkowska, G.M. Buck Louis, and S.J. Fisher. 2015. Urine, peritoneal fluid and omental fat proteomes of reproductive age women: Endometriosis-related changes and associations with endocrine disrupting chemicals. *J Proteomics*. 113:194-205.

Williams, M.J., M.L. Wiklund, S. Wikman, and D. Hultmark. 2006. Rac1 signalling in the Drosophila larval cellular immune response. *J Cell Sci*. 119:2015-2024.

Wilson, C., and C. Gonzalez-Billault. 2015. Regulation of cytoskeletal dynamics by redox signaling and oxidative stress: implications for neuronal development and trafficking. *Front Cell Neurosci*. 9:381.

Wilson, J.P., A.S. Raghavan, Y.Y. Yang, G. Charron, and H.C. Hang. 2011. Proteomic analysis of fatty-acylated proteins in mammalian cells with chemical reporters reveals S-acylation of histone H3 variants. *Mol Cell Proteomics*. 10:M110 001198.

Winograd-Katz, S.E., R. Fassler, B. Geiger, and K.R. Legate. 2014. The integrin adhesome: from genes and proteins to human disease. *Nat Rev Mol Cell Biol*. 15:273-288.

Winter-Vann, A.M., and P.J. Casey. 2005. Post-prenylation-processing enzymes as new targets in oncogenesis. *Nat Rev Cancer*. 5:405-412.

Wood, W., C. Faria, and A. Jacinto. 2006. Distinct mechanisms regulate hemocyte chemotaxis during development and wound healing in Drosophila melanogaster. *J Cell Biol*. 173:405-416.

Wood, W., and A. Jacinto. 2007. Drosophila melanogaster embryonic haemocytes: masters of multitasking. *Nat Rev Mol Cell Biol*. 8:542-551.

Woodham, E.F., N.R. Paul, B. Tyrrell, H.J. Spence, K. Swaminathan, M.R. Scribner, E. Giampazolias, A. Hedley, W. Clark, F. Kage, D.J. Marston, K.M. Hahn, S.W. Tait, L. Larue, C.H. Brakebusch, R.H. Insall, and L.M. Machesky. 2017. Coordination by Cdc42 of Actin, Contractility, and Adhesion for Melanoblast Movement in Mouse Skin. *Curr Biol*. 27:624-637.

Worthylake, D.K., K.L. Rossman, and J. Sondek. 2000. Crystal structure of Rac1 in complex with the guanine nucleotide exchange region of Tiam1. *Nature*. 408:682-688.

Wright, M.H., W.P. Heal, D.J. Mann, and E.W. Tate. 2010. Protein myristoylation in health and disease. *J Chem Biol*. 3:19-35.

Wu, C., S.B. Asokan, M.E. Berginski, E.M. Haynes, N.E. Sharpless, J.D. Griffith, S.M. Gomez, and J.E. Bear. 2012. Arp2/3 is critical for lamellipodia and response to extracellular matrix cues but is dispensable for chemotaxis. *Cell*. 148:973-987.

Wu, C., E.M. Haynes, S.B. Asokan, J.M. Simon, N.E. Sharpless, A.S. Baldwin, I.J. Davis, G.L. Johnson, and J.E. Bear. 2013. Loss of Arp2/3 induces an NF-kappaB-dependent, nonautonomous effect on chemotactic signaling. *J Cell Biol*. 203:907-916.

Xing, P., J.G. Li, F. Jin, T.T. Zhao, Q. Liu, H.T. Dong, and X.L. Wei. 2011. Fascin, an actin-bundling protein, promotes breast cancer progression in vitro. *Cell Biochem Funct*. 29:303-310.

Yachida, S., and C.A. Iacobuzio-Donahue. 2013. Evolution and dynamics of pancreatic cancer progression. *Oncogene*. 32:5253-5260.

Yae, K., V.W. Keng, M. Koike, K. Yusa, M. Kouno, Y. Uno, G. Kondoh, T. Gotow, Y. Uchiyama, K. Horie, and J. Takeda. 2006. Sleeping beauty transposon-based phenotypic analysis of mice: lack of Arpc3 results in defective trophoblast outgrowth. *Mol Cell Biol*. 26:6185-6196.

Yagi, S., M. Matsuda, and E. Kiyokawa. 2012a. Chimaerin suppresses Rac1 activation at the apical membrane to maintain the cyst structure. *PLoS One*. 7:e52258.

Yagi, S., M. Matsuda, and E. Kiyokawa. 2012b. Suppression of Rac1 activity at the apical membrane of MDCK cells is essential for cyst structure maintenance. *EMBO Rep*. 13:237-243.

Yam, P.T., C.A. Wilson, L. Ji, B. Hebert, E.L. Barnhart, N.A. Dye, P.W. Wiseman, G. Danuser, and J.A. Theriot. 2007. Actin-myosin network reorganization breaks symmetry at the cell rear to spontaneously initiate polarized cell motility. *J Cell Biol*. 178:1207-1221.

Yamakita, Y., F. Matsumura, and S. Yamashiro. 2009. Fascin1 is dispensable for mouse development but is favorable for neonatal survival. *Cell Motil Cytoskeleton*. 66:524-534.

Yamazaki, D., T. Oikawa, and T. Takenawa. 2007. Rac-WAVE-mediated actin reorganization is required for organization and maintenance of cell-cell adhesion. *J Cell Sci*. 120:86-100.

Yanagisawa, A., K. Ohtake, K. Ohashi, M. Hori, T. Kitagawa, H. Sugano, and Y. Kato. 1993. Frequent c-Ki-ras oncogene activation in mucous cell hyperplasias of pancreas suffering from chronic inflammation. *Cancer Res*. 53:953-956.

Yang, H.W., M.G. Shin, S. Lee, J.R. Kim, W.S. Park, K.H. Cho, T. Meyer, and W.D. Heo. 2012. Cooperative activation of PI3K by Ras and Rho family small GTPases. *Mol Cell*. 47:281-290.

Yang, N., O. Higuchi, K. Ohashi, K. Nagata, A. Wada, K. Kangawa, E. Nishida, and K. Mizuno. 1998. Cofilin phosphorylation by LIM-kinase 1 and its role in Rac-mediated actin reorganization. *Nature*. 393:809-812.

Yang, S., F.K. Huang, J. Huang, S. Chen, J. Jakoncic, A. Leo-Macias, R. Diaz-Avalos, L. Chen, J.J. Zhang, and X.Y. Huang. 2013. Molecular mechanism of fascin function in filopodial formation. *J Biol Chem*. 288:274-284.

Yang, X., D. Dormann, A.E. Munsterberg, and C.J. Weijer. 2002. Cell movement patterns during gastrulation in the chick are controlled by positive and negative chemotaxis mediated by FGF4 and FGF8. *Dev Cell*. 3:425-437.

Yokota, Y., C. Ring, R. Cheung, L. Pevny, and E.S. Anton. 2007. Nap1-regulated neuronal cytoskeletal dynamics is essential for the final differentiation of neurons in cerebral cortex. *Neuron*. 54:429-445.

Yoshizaki, H., Y. Ohba, K. Kurokawa, R.E. Itoh, T. Nakamura, N. Mochizuki, K. Nagashima, and M. Matsuda. 2003. Activity of Rho-family GTPases during cell division as visualized with FRET-based probes. *J Cell Biol*. 162:223-232.

Yu, W., X. Sun, N. Clough, E. Cobos, Y. Tao, and Z. Dai. 2008. Abi1 gene silencing by short hairpin RNA impairs Bcr-Abl-induced cell adhesion and migration in vitro and leukemogenesis in vivo. *Carcinogenesis*. 29:1717-1724.

Zettervall, C.J., I. Anderl, M.J. Williams, R. Palmer, E. Kurucz, I. Ando, and D. Hultmark. 2004. A directed screen for genes involved in Drosophila blood cell activation. *Proc Natl Acad Sci U S A*. 101:14192-14197.

Zhang, C., E.L. Mallery, J. Schlueter, S. Huang, Y. Fan, S. Brankle, C.J. Staiger, and D.B. Szymanski. 2008a. Arabidopsis SCARs function interchangeably to meet actin-related protein 2/3 activation thresholds during morphogenesis. *Plant Cell*. 20:995-1011.

Zhang, F.R., L.H. Tao, Z.Y. Shen, Z. Lv, L.Y. Xu, and E.M. Li. 2008b. Fascin expression in human embryonic, fetal, and normal adult tissue. *J Histochem Cytochem*. 56:193-199.

Zhang, Z., X. Liang, L. Gao, H. Ma, X. Liu, Y. Pan, W. Yan, H. Shan, Z. Wang, Y.H. Chen, and C. Ma. 2015. TIPE1 induces apoptosis by negatively regulating Rac1 activation in hepatocellular carcinoma cells. *Oncogene*. 34:2566-2574.

Zheng, Y., M.J. Hart, K. Shinjo, T. Evans, A. Bender, and R.A. Cerione. 1993. Biochemical comparisons of the Saccharomyces cerevisiae Bem2 and Bem3 proteins. Delineation of a limit Cdc42 GTPase-activating protein domain. *J Biol Chem*. 268:24629-24634.

Zhou, C., S. Licciulli, J.L. Avila, M. Cho, S. Troutman, P. Jiang, A.V. Kossenkov, L.C. Showe, Q. Liu, A. Vachani, S.M. Albelda, and J.L. Kissil. 2013. The Rac1 splice form Rac1b promotes K-ras-induced lung tumorigenesis. *Oncogene*. 32:903-909.

10 Appendices

FAM49 conservation

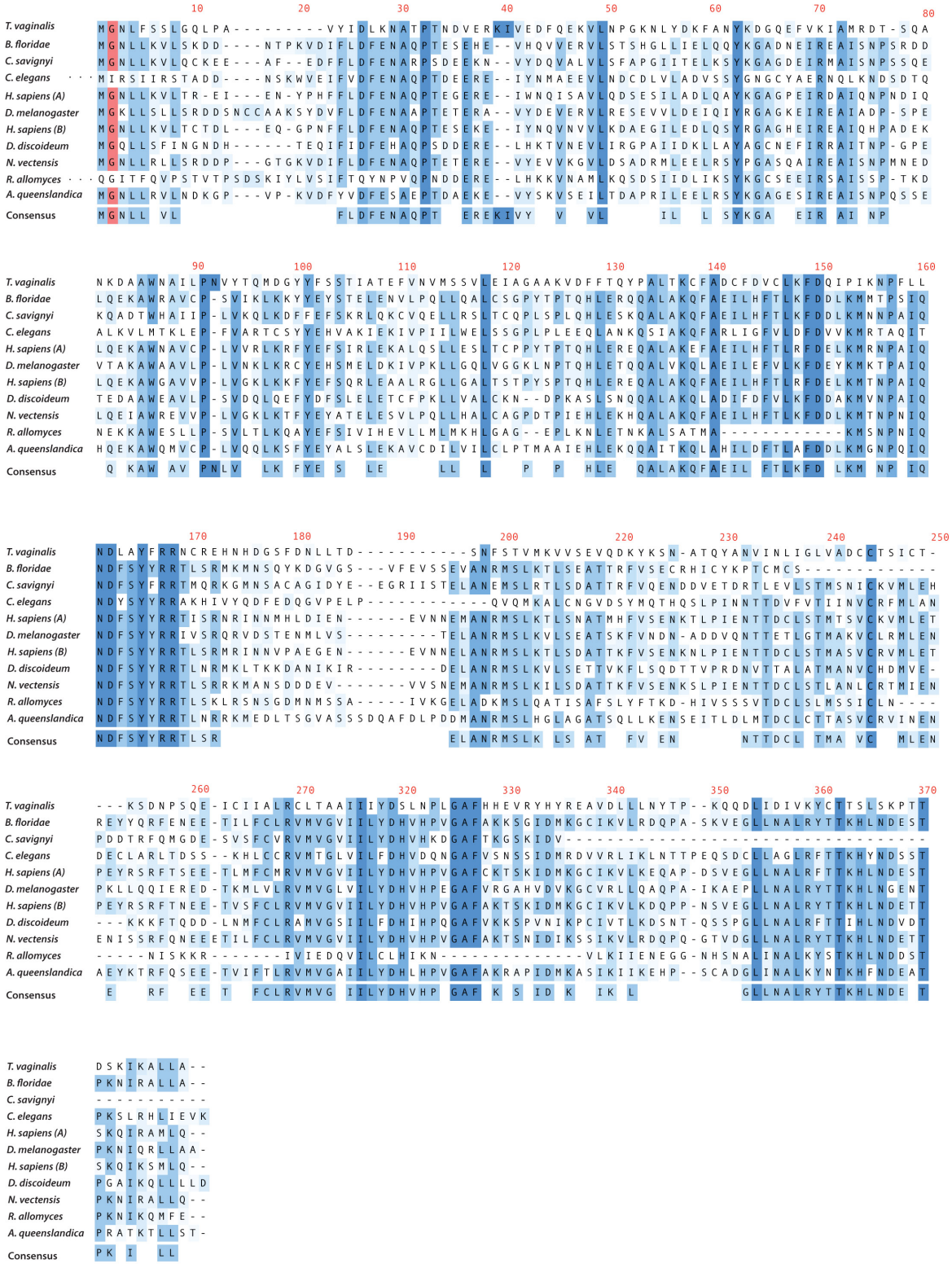

Appendix 1: Multi-alignment of FAM49

Sequences were obtained from Uniprot and correspond to the following UniProt ID: A2E1F1 (*Trichomonas vaginalis*), C3Y224 (*Branchiostoma floridae*), H2ZNC1 (*Ciona savignyi*), Q09387 (*Caenorhabditis elegans*), Q9H0Q0 (*Homo sapiens* FAM49A), Q7K1H0 (*Drosophila melanogaster*), Q9NUQ9 (Homo sapiens FAM49B), Q8T2H0 (Dictyostelium discoideum), A7SA43 (*Nematostella vectensis*), A0A075APQ0 (*Rozella allomycis*), I1F5T7 (*Amphimedon queenslandica*). Sequences

were aligned using macVector software. Red numbers above the first sequence highlight the residue position. A dash (-) represents a gap in the alignment, which might reflects deletion events during evolution. The bottom row highlights the 75% consensus sequence. Colour code represents the number of entries with similar amino acid at this position.

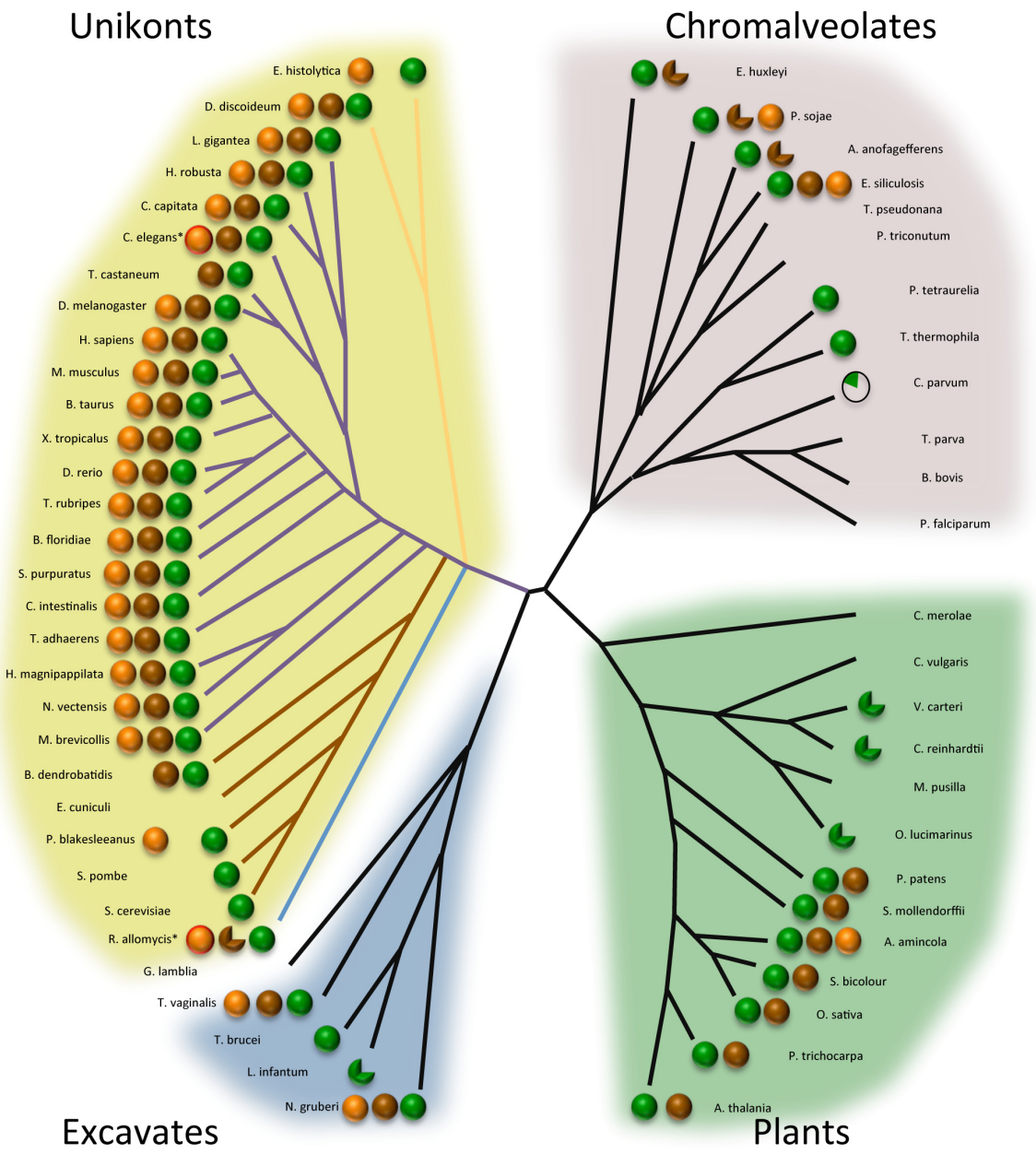

Appendix 2: Co-evolution of FAM49 with the actin-machinery
Phylogenetic tree representing the co-evolution of Arp2/3 (green), Scar/WAVE (brown) and FAM49 (orange) across the main phyla of the eukaryotic tree. Each superfamily is represented with a specific background colour: Excavates (blue), Unikonts (yellow), chromalveolates (pink) and plants (green). Branch length is not proportional to the evolution distance between organisms. Incomplete circles represent the lack of some subunits in the protein complex. Asterisk * correspond to the lack of putative N-myristoylation site on FAM49. In the Unikonts phylum, branch colours correspond to amoebazoa (yellow), metazoan (purple), fungi (brown) and *Rozella allomycis* (blue). This figure was inspired from (Veltman and Insall, 2010).

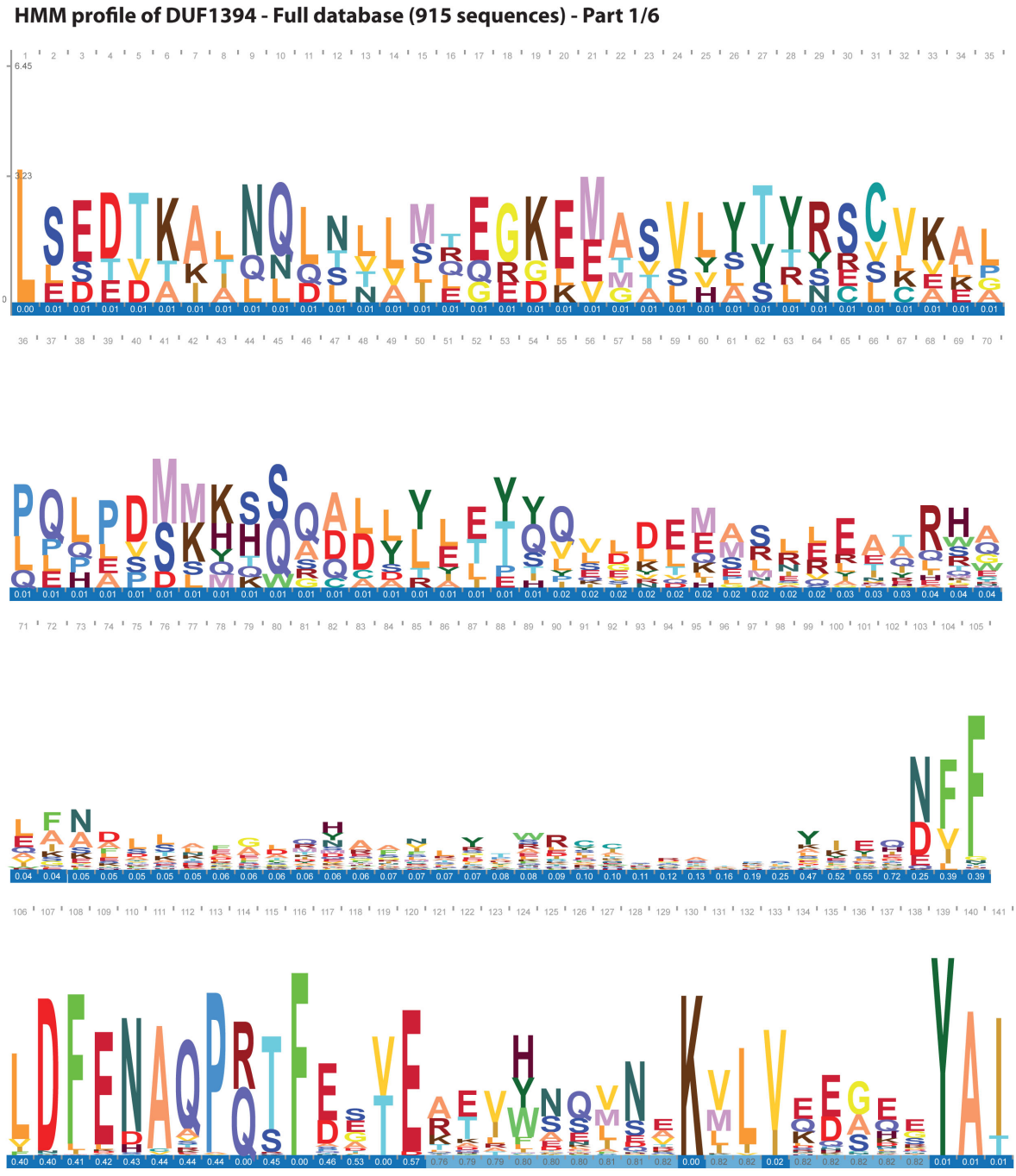

Appendix 3: Hidden Markov Model (HMM) representing the conservation of the DUF1394 domain from the "full Pfam database"

HMM profile of 915 sequences corresponding to the evolution of the DUF1394 domain and generated by Skylign. The height of the stack corresponds to the residue conservation at this position while the height of each letter reflects the frequency of the residue at this position. Each residue got assigned a colour according to the default parameters of the Skylign tool. Numbers above each sequence represent the cumulative number of residues used in the analysis. Numbers from the bottom row correspond to an occupancy score (Ranging from 0-1) and is defined as the probability of observing a letter at this position. The darker the colour, the lower the probability is, meaning that only a small proportion of sequences has a residue at this position in the alignment. The red line running across the sequence highlights the Rac1 Binding Domain (RBD).

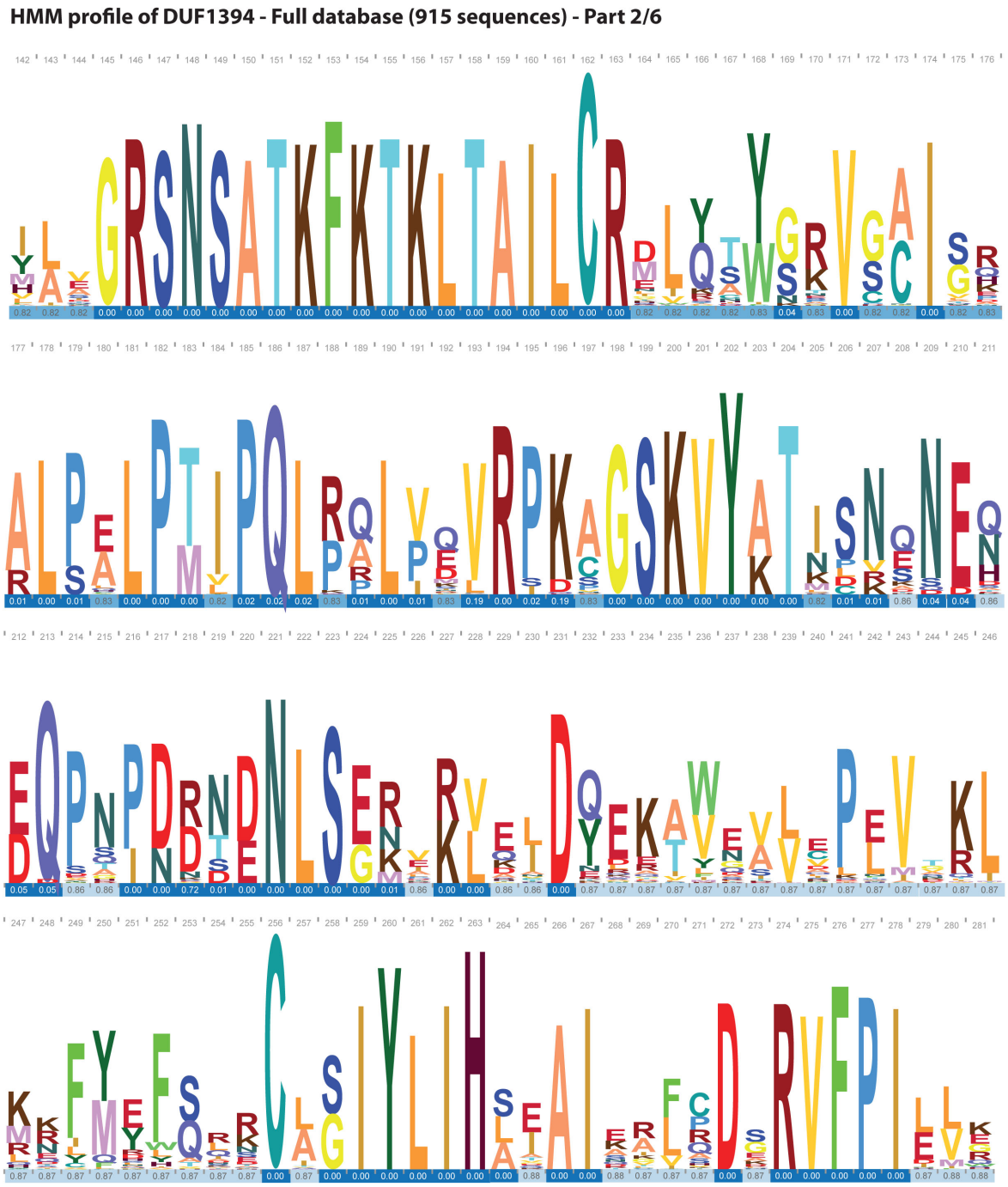

Appendix 3: Hidden Markov Model (HMM) representing the conservation of the DUF1394 domain from the "full Pfam database" (continued)

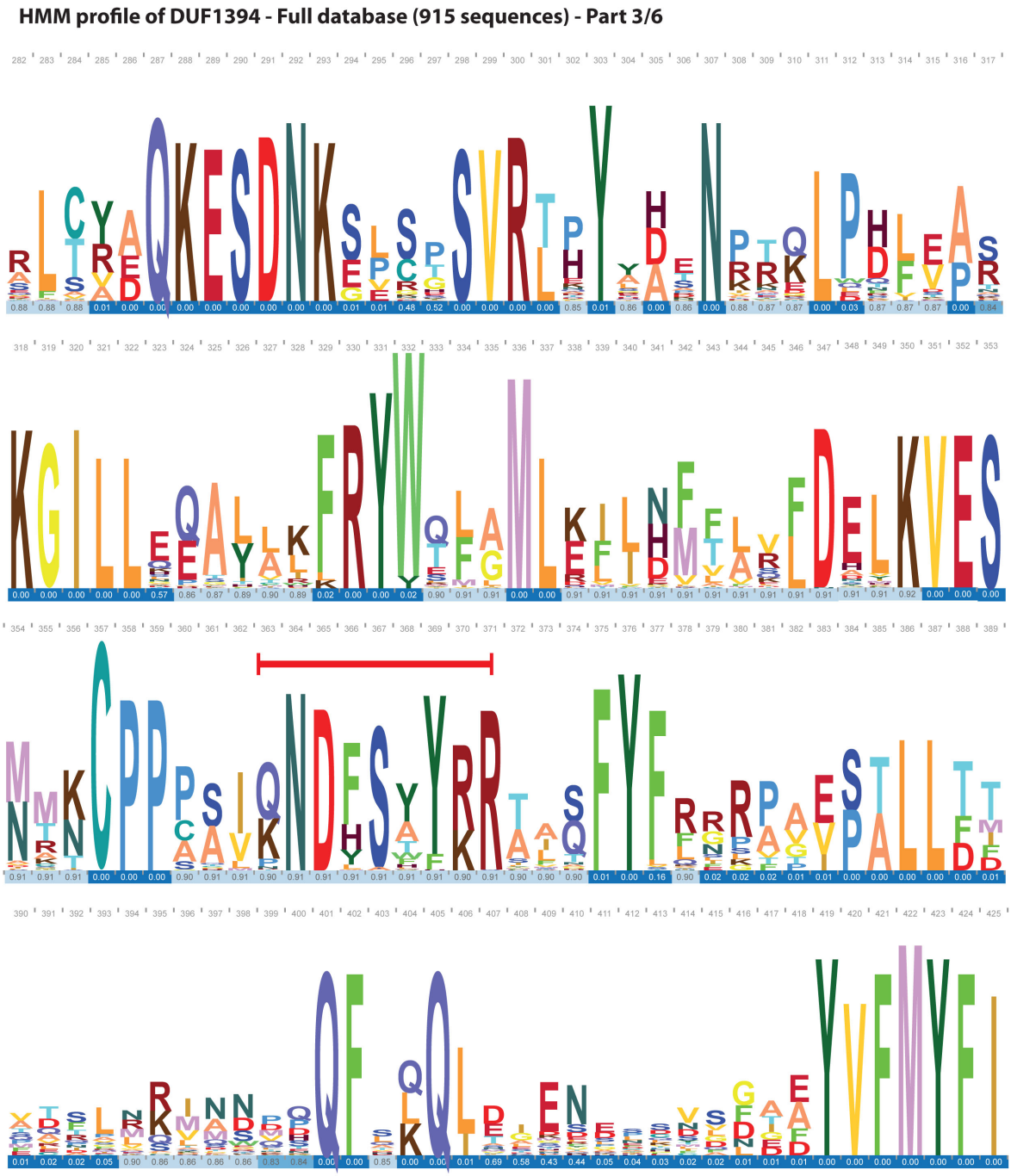

Appendix 3: Hidden Markov Model (HMM) representing the conservation of the DUF1394 domain from the "full Pfam database" (continued)

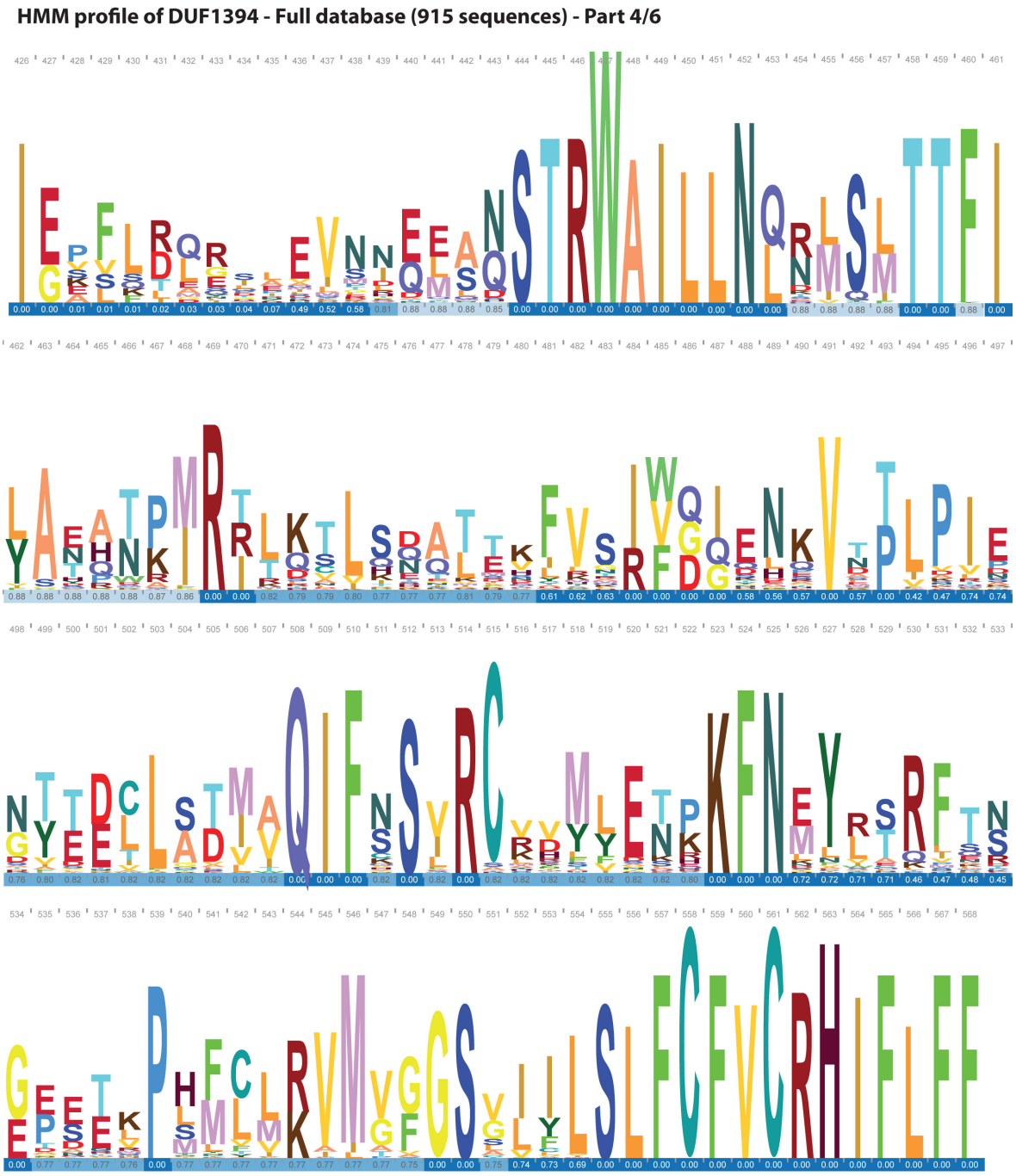

Appendix 3: Hidden Markov Model (HMM) representing the conservation of the DUF1394 domain from the "full Pfam database" (continued)

HMM profile of DUF1394 - Full database (915 sequences) - Part 5/6

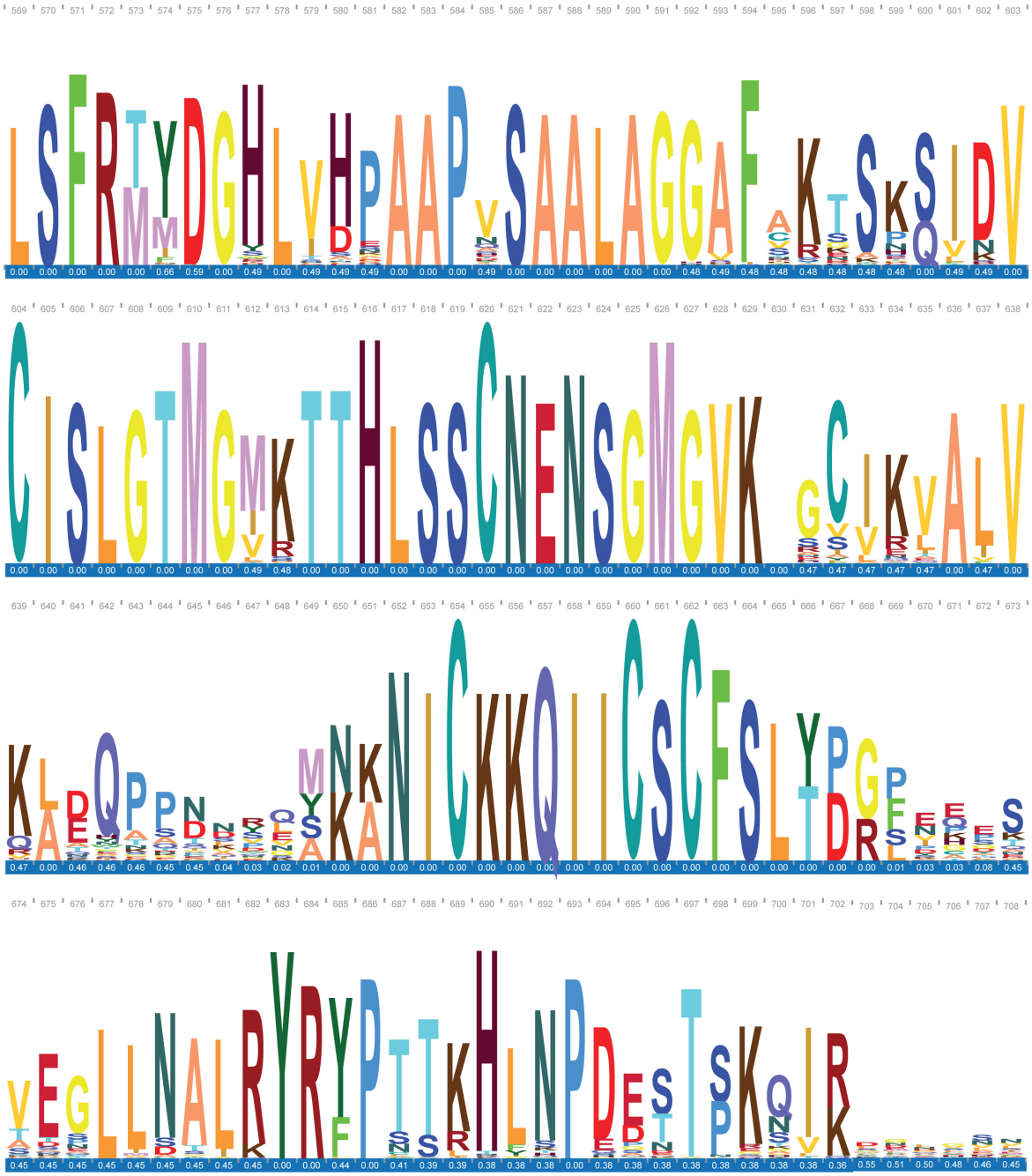

Appendix 3: Hidden Markov Model (HMM) representing the conservation of the DUF1394 domain from the "full Pfam database" (continued)

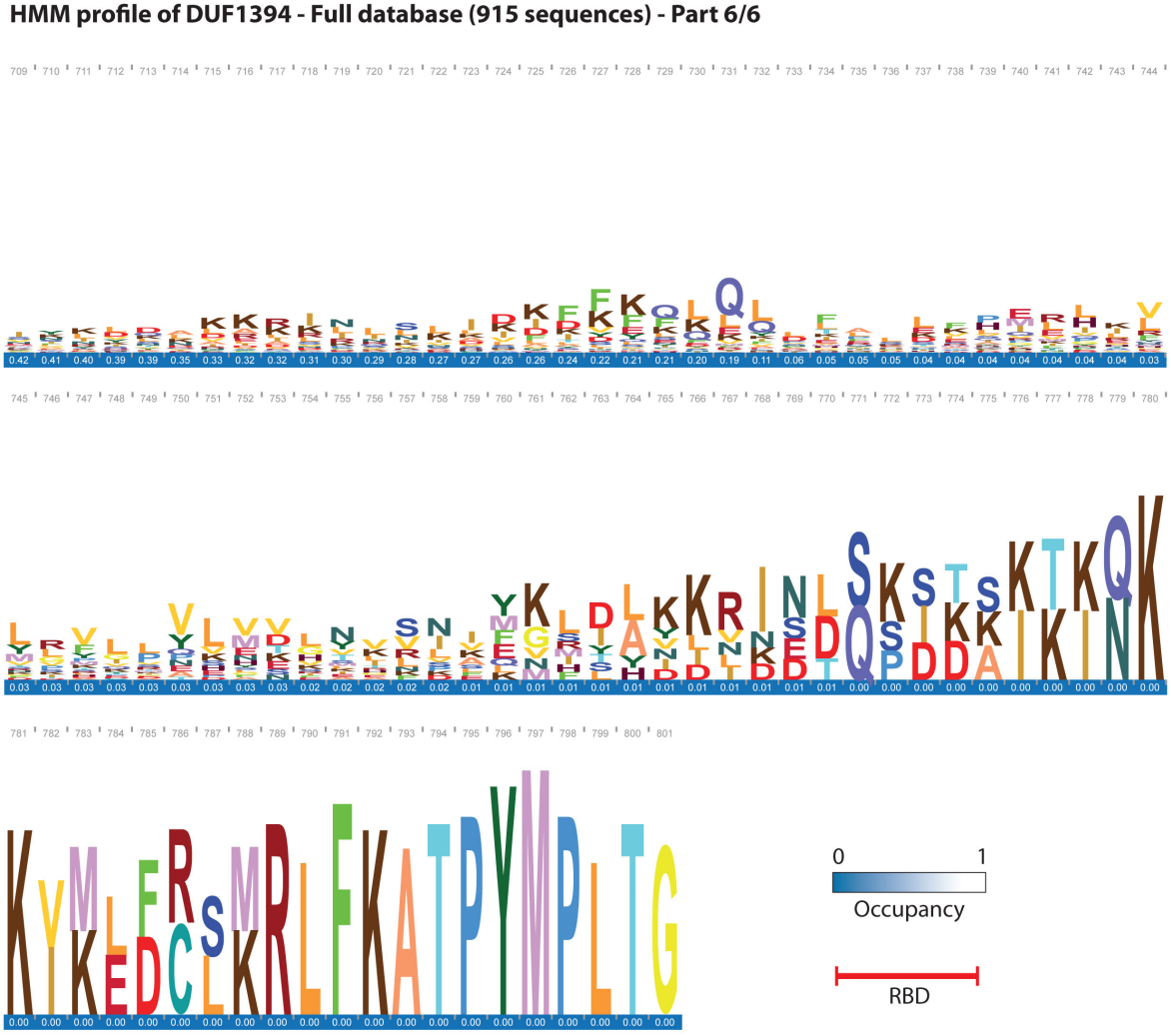

Appendix 3: Hidden Markov Model (HMM) representing the conservation of the DUF1394 domain from the "full Pfam database" (continued)

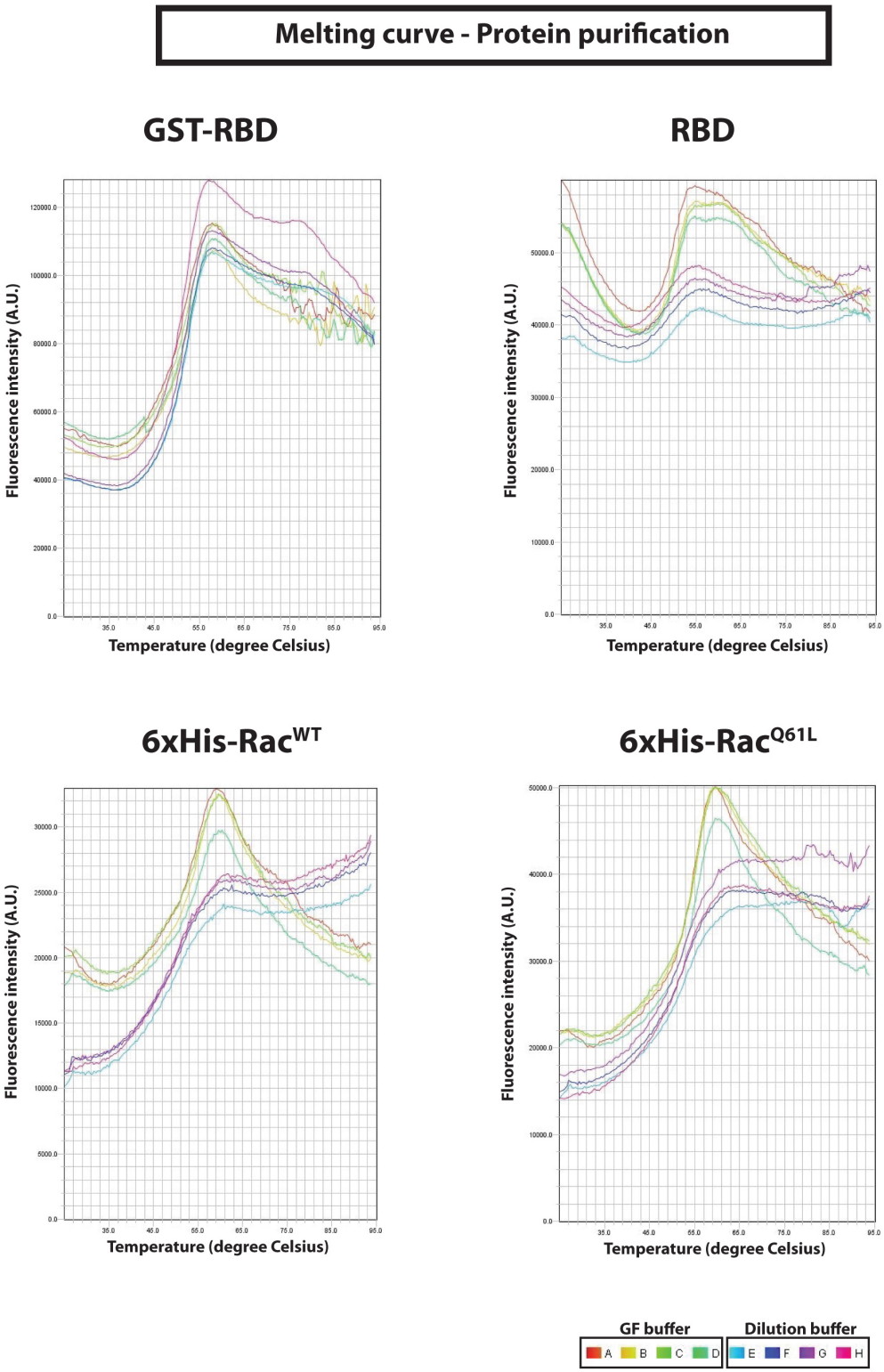

Appendix 4: Thermal shift assay

Protein folding was tested by thermal shift assay before being used for further analysis. Protein was mixed with a dye that specifically binds to hydrophobic (unfolded) regions before being diluted either in gel filtration buffer (GF buffer) or the buffer provided in the kit (dilution buffer). Four technical replicates were obtained and displayed with a specific colour to assess the variability of the assay. Temperature was then gradually increased, resulting in the denaturation of the protein, which exposes a larger hydrophobic surface. This is reflected by a rapid increase of the dye fluorescence and corresponds to the "protein melt". In this assay, GST-Rac1 binding domain, untagged Rac1 binding domain, Histidine-tagged wild-type or constitutively active Q61L Rac1 were tested.

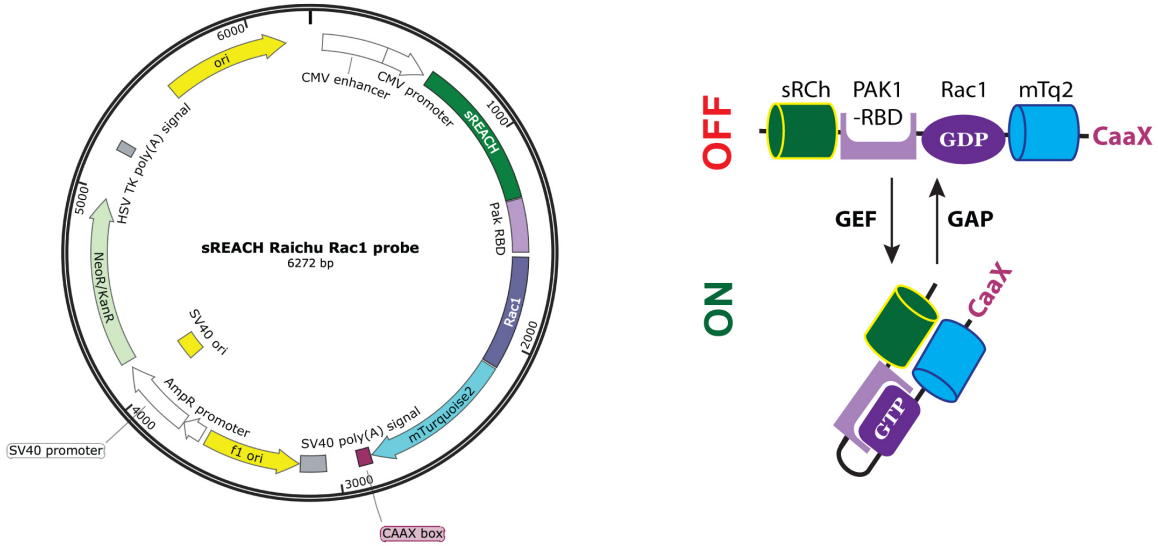

Appendix 5: Rac1 FRET probe
Vector map and graphical representation of the folding of the Rac1 FRET probe designed by Kirsty Martin (Martin et al, 2017). In an inactive state, GDP-loaded Rac1 cannot interact with the Rac1 binding domain of PAK1, resulting to an open conformation of the reporter. Upon GEF activity, GTP gets loaded onto Rac1, which in turn can bind to the PAK1 protein. This folding allows mTurquoise2 and sREACh to be in close proximity, allowing FRET.

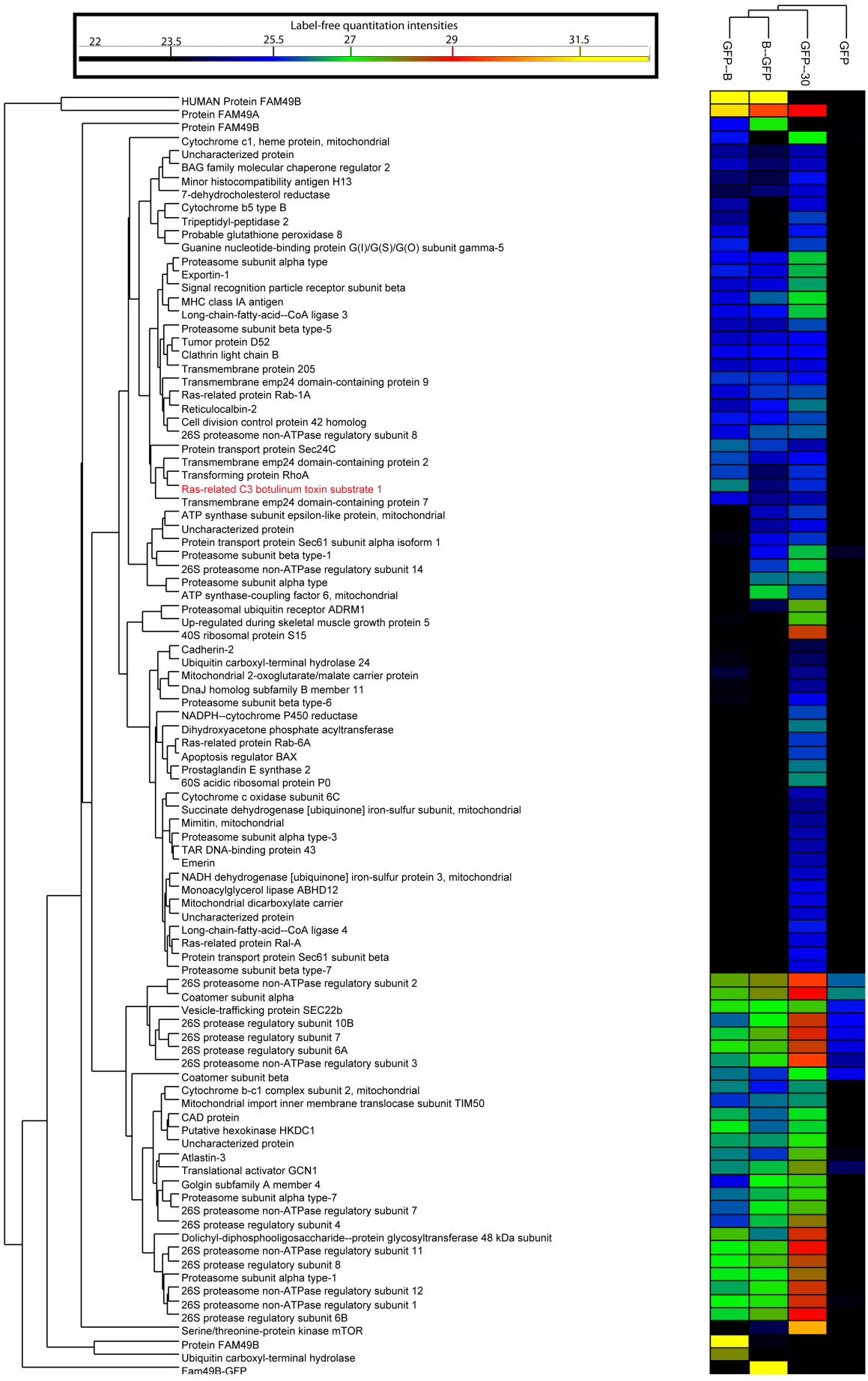

Appendix 6: Heat-map of selected putative FAM49B interactors identified by mass spectrometry

COS-7 cells were transfected with GFP, GFP-FAM49B, FAM49B-GFP or GFP-30-236 (corresponding to FAM49B-RBD and referred to as GFP-30) and GFP-trap was performed before tryptic digestion “on-beads” and LS-MS/MS analysis. Enriched candidates are presented according to the label-free quantitation intensities calculated by MaxQuant.

Rac1 is highlighted in red.

Appendix 7: Table of copyrights and permission

Publisher	Journal	Article title	Authors (Year)	Figures number in this thesis	Copyright permission	Order licence ID
Rockefeller University Press	J. Cell Biol.	Mechanism of filopodia initiation by reorganization of a dendritic network	Svitkina et al., (2003)	Figure 1-2 - B'	11654880	4144171126280
Rockefeller University Press	J. Cell Biol.	Analysis of the Actin–Myosin II System in Fish Epidermal Keratocytes: Mechanism of Cell Body Translocation	Svitkina et al., (1997)	Figure 1-2 - C' and D'	11654881	4144190077623
Nature Publishing Group	Nat. Rev. Mol. Cell Biol.	The 'ins' and 'outs' of podosomes and invadopodia: characteristics, formation and function	Murphy and Courtneidge (2001)	Figure 1-3 - B	Available on request	4144210907804
Nature Publishing Group	Nat. Cell Biol.	Integration of actin dynamics and cell adhesion by a three-dimensional, mechanosensitive molecular clutch	Case and Waterman (2015)	Figure 1-5	Available on request	4144230798965